Universiteit Leiden
The Netherlands

Semi-empirical approach to the simulation of molecule-surface reaction dynamcis

Migliorini, D.

Citation
Migliorini, D. (2019, March 14). *Semi-empirical approach to the simulation of molecule-surface reaction dynamcis*. Retrieved from https://hdl.handle.net/1887/69724

Version:	Not Applicable (or Unknown)
License:	Licence agreement concerning inclusion of doctoral thesis in the Institutional Repository of the University of Leiden
Downloaded from:	https://hdl.handle.net/1887/69724

Note: To cite this publication please use the final published version (if applicable).

Cover Page

Universiteit Leiden

Leiden University Repository

The handle http://hdl.handle.net/1887/69724 holds various files of this Leiden University dissertation.

Author: Migliorini, D.
Title: Semi-empirical approach to the simulation of molecule-surface reaction dynamcis
Issue Date: 2019-03-14

Semi-Empirical Approach to the Simulation of Molecule-Surface Reaction Dynamics

PROEFSCHRIFT

ter verkrijging van

de graad van Doctor aan de Universiteit Leiden,

op gezag van Rector Magnificus prof. mr. C. J. J. M. Stolker,

volgens besluit van het College voor Promoties

te verdedigen op donderdag 14 maart 2019

klokke 15:00 uur

door

Davide Migliorini

geboren te Crema, Italië, 1990

Promotiecommissie

Promoter:	Prof. dr. G. J. Kroes	
Overige leden:	Prof. dr. H. S. Overkleeft	
	Prof. dr. M. T. M. Koper	
	Prof. dr. C. Fonseca Guerra	
	Prof. dr. A. L. Utz	Tufts University, Medford, MA, USA
	Prof. dr. R. D. Beck	École Polytechnique Fédérale de Lausanne, Lausanne, CH
	Dr. M. Alducin	Centro de Física de Materiales, Donostia - San Sebastián, ES
	Dr. J. Meyer	

ISBN: 978-94-028-1392-0

The research reported in this thesis has been performed in the Theoretical Chemistry Group at the Leiden Institute of Chemistry (Einsteinweg 55, 2333 CC, Leiden NL). This work has been made possible by financial support by the Nederlandse Organisatie voor Wetenschappelijk Onderzoek (NWO) and by the European Research Council through an ERC-2013 advanced grant (Nr. 338580), and with computer time granted by NWO Exacte Wetenschappen, EW (NWO Physical Sciences Division).

In the beginning the Universe was created.
This had made a lot of people very angry
and been widely regarded as a bad move.

– *Douglas Adams.*

On the cover are reported the bond lenghts of the laser-off trajectory number 0059 for CHD_3 on Pt(211) and $\langle E_i \rangle = 58$ kJ/mol.

Contents

1 General Introduction **1**

1.1 Heterogeneous Catalysis 1

1.2 From Heterogeneous Catalysis to Surface Science (and Back) 3

1.3 Molecules on surfaces: Possibilities and Challenges 5

1.4 Aim of this Thesis 7

1.5 Main Results 9

1.6 Outlook 13

2 Methods and Theory: A Semi-Empirical Approach to Density Functional Theory **23**

2.1 Introduction 23

2.2 SRP Approach to DFT 25

2.2.1 Density Functional Theory 25

2.2.2 Plane Wave DFT 28

2.2.3 Exchange-Correlation Functional 29

2.2.4 Specific Reaction Parameter Functional 32

2.3 Semi-Empirical Strategy 34

2.4 Initial Condition Sampling 37

2.4.1 Molecular Beam 38

2.4.2 van der Waals Functionals and Residual Energy 43

2.4.3 Metal Surface Temperature 46

3 Application of van der Waals Functionals to the Calculation of Dissociative Adsorption of N_2 on W(110) for Static and Dynamic Systems 55

3.1 Introduction 56

3.2 Method 61

3.3 Results and Discussion 67

3.3.1 Static Results 67

3.3.2 AIMD Results 81

3.4 Summary and Conclusions 97

4 Surface Reaction Barriometry: Methane Dissociation on Flat and Stepped Transition Metal Surfaces 105

4.1 Introduction 106

4.2 Method 108

4.3 Results and Discussion 110

4.3.1 Theory-Experiment Comparison 110

4.3.2 Implications for Simulating Heterogeneous Catalysis 117

4.4 Summary and Conclusions 121

5 Methane on a Stepped Surface: Dynamical Insights on the Dissociation of CHD_3 on Pt(111) and Pt(211) 129

5.1 Introduction 130

5.2 Method 132

5.3 Results and Discussion 134

5.3.1 Transition States 136

5.3.2 Energy Transfer to Parallel Motion 141

5.3.3 Energy Transfer to Surface Phonons 148

5.3.4 Reaction Site and Dissociation Geometry 151

5.4 Summary and Conclusions 159

6 CHD_3 Dissociation on Pt(111): A Comparison of the Reaction Dynamics Based on the PBE Functional and on a Specific Reaction Parameter Functional 167

6.1 Introduction 168

6.2 Method 171

6.3 Results and Discussion 173

6.3.1 Surface Motion and Effective Barriers 177

6.3.2 Motion Across the Potential Energy Surface and the Minimum Energy Path 180

6.3.3 Molecule-Surface Interaction Times 185

6.3.4 Energy Transfer to the Surface 185

6.4 Summary and Conclusions 187

7 HOD on Ni(111): *Ab Initio* Molecular Dynamics Prediction of Molecular Beam Experiments 197

7.1 Introduction 198

7.2 Method 201

7.2.1 Electronic Structure Method 201

7.2.2 Dynamics Calculations 203

7.3 Results and Discussion 209

7.4 Summary and Conclusions 222

Samenvatting 233

Curriculum Vitae 239

List of Publications 241

Chapter 1

General Introduction

1.1 Heterogeneous Catalysis

Chemistry and chemical reactions play a central role in every aspect of our life: from the production of everyday materials like plastic or paper to the synthesis of medicines, from the complex metabolic cycles that sustain our body to the formation of new molecules in the interstellar medium. Chemical reactions, both in nature and in industrial processes can be facilitated and controlled using catalysts.

A catalyst is a substance that interacts with the reacting molecules and accelerates their conversion into products by providing an alternative mechanism which might be more complicated but is energetically favorable. The catalyst is then able to release the products and to return to its initial state without being modified or consumed, ready for the next catalytic cycle. In addition to increasing the conversion rate, using a catalyst may allow one to run the reaction under milder conditions and, in some cases, it can also provide selectivity, increasing the formation rate of one of the products over that of other possible and unwanted side products.

There are several different types of catalysts that can be catalogued according to their function, structure or phase. Among the most important and studied classes of catalysis we can identify three principal types of catalysis: biocatalysis, homogeneous catalysis and heterogeneous catalysis. Biocatalysis is performed by

enzymes which are proteins that act as highly specific catalysts and are involved in nearly all the metabolic processes playing a fundamental role in the biochemical reactions underlying life [1]. Homogeneous and heterogeneous catalysis, on the other hand, are defined on the basis of the phase of reactant and catalyst. The catalysis is defined as homogeneous if the reactant and the catalyst are in the same phase, which can be gaseous or more commonly liquid [2]. Finally, heterogeneous catalysis involves the presence of an interface and usually consists of a liquid or gaseous mixture reacting on a solid catalyst.

In heterogeneously catalyzed processes we often see that a transition metal based catalyst facilitates the reaction by stabilizing the molecular transition state (TS) and lowering the energy required for breaking a chemical bond [2–4], and by adsorbing the fragments that can subsequently desorb or undergo further transformation. The exploitation of heterogeneous catalysis is of extreme relevance to industry and one of the most important processes is the Haber-Bosch [3] production of ammonia (NH_3). This process takes place on an iron based catalyst [3] that promotes the cleavage of the molecular N_2 bond and subsequently the reaction with hydrogen to give ammonia:

$$N_2 + 3\ H_2 \rightleftharpoons 2\ NH_3. \tag{1.1}$$

This process has been designed by Fritz Haber, scaled up by Carl Bosch and is still today one of the main processes of ammonia production which is a fundamental building block in the synthesis of fertilizers.

Another process of great industrial relevance is steam reforming [2]. This process consists of the reforming of natural gas on a nickel based catalyst, giving as a result molecular hydrogen and carbon monoxide:

$$CH_4 + H_2O \rightleftharpoons CO + 3\ H_2. \tag{1.2}$$

The steam reforming reaction is one of the main industrial processes used for molecular hydrogen production and it can be coupled with a second process,

called the water-gas shift reaction [4], to increase the total hydrogen yield:

$$CO + H_2O \rightleftharpoons CO_2 + H_2. \tag{1.3}$$

A deep understanding of these catalytic processes is highly desirable and a large research effort has been made in this regard in past decades. Unfortunately, the high degree of complexity of these processes makes it extremely challenging to design and perform accurate experiments and theoretical simulations that can give insights in their overall behavior. In this Thesis we will study reactions that are important to the overall processes 1.1–1.3, in order to contribute to their understanding.

1.2 From Heterogeneous Catalysis to Surface Science (and Back)

Heterogeneously catalyzed processes, including the ones introduced in the previous Section, are usually complex multi-step processes which involve several different reactions and many molecular states. Moreover, at the industrial level, they are carried out on supported transition state metal particles which are usually poorly characterized, having different sizes and irregular shapes. Therefore, the different reaction steps can take place simultaneously and on many different sites on the catalyst. Furthermore, this kind of processes are often run at high temperature and pressure. Since most of the experimental techniques used to study surfaces rely on electrons, it is hard to perform *in situ* experiments to monitor the process under industrial conditions [5]. Moreover, it is hard to disentangle the many factors that come into play to define the mechanism and the results of these experiments. At the same time, accurate theoretical simulations of such processes in their entirety is far out of reach of present computational resources.

Microkinetic simulations [6, 7] can be used to obtain the rate of the overall process and the concentrations of reactants and products involved. In order to do

so, a set of kinetic equations needs to be defined including all the relevant reactions of the process as well as the energy of the relevant adsorption and transition states. Insights on the mechanism and on the energetics of the reactions of interest can be obtained by performing surface science experiments and theoretical simulations like the ones reported in this Thesis.

One way to tackle the study of these complicated processes is to reduce the complexity by dealing with one reaction step at the time and by using a clean single-cut metal surface to approximate the catalyst [8]. Focusing only on one (or a few) reaction steps is justified by the fact that heterogeneously catalyzed processes usually involve one or a few rate controlling steps [9] which control the overall rate of the process and therefore need to be described with high accuracy. The knowledge generated can then be used to understand the overall process and its mechanism. However, even though the contribution of surface science studies to understand heterogeneous catalysis is invaluable, several challenges needs to be faced and gaps still need to be filled in order to simulate real industrial conditions.

One of the main differences between surface science and heterogeneous catalysis concerns the pressure regime under which the processes are carried out (i.e., the so called "pressure gap" [10, 11]). While in typical industrial applications the processes take place at high temperature and pressure, surface science experiments are usually performed in ultra-high vacuum (UHV). Another important aspect to consider is the so called "materials gap" [10, 11] that arises from the difference in complexity between the ideal (and often low-index) metal surface used in experiments and simulations and the real industrial catalyst. In order to improve the description of the process, all the relevant metal facets that can be found on the catalyst should be accounted for and studied. Moreover, it can happen that the catalytic activity of a particle is higher than the sum of the catalytic activities of its facets [12]. This can be due to the presence of edges between the facets that, involving undercoordinated atoms, might facilitate one of the reactions in the process [13], but also to purely kinetic reasons, like the diffusion of adsorbed species from one facet to the other [12].

One of the main goals of surface science is to contribute to the quest of design-

ing new, more efficient and cleaner catalysts. In this regard, the synergy between experiment and theoretical simulations can provide the knowledge needed to develop new and accurate microkinetic models and to improve existing ones in order to work towards the systematic design of new catalysts.

1.3 Molecules on surfaces: Possibilities and Challenges

As mentioned before, a way to improve the understanding of heterogeneously catalyzed processes is to break them down into simple reaction steps and to investigate their behavior on well defined surfaces. The improvement in the accuracy and characterization of the experiments together with the increase of computational power, allows a comparison between experimental and theoretical results that is becoming more meaningful and insightful.

Using *ab initio* molecular dynamics (AIMD) simulations and molecular beam experiments it is now possible to investigate the behavior and the reactivity of a single reaction step of a much more complex catalytical process. As discussed in Chapter 2, this helps in reducing the complexity of the problem and obtaining important insights on a rate limiting step of the process. Synergy between experiments and theory is of invaluable importance since they can be used to obtain the same observable (i.e., the zero-coverage reaction probability S_0, studied in this Thesis) so that the comparison can give a measure of the accuracy of the theoretical model and help improve it, as discussed in Chapters 2 and 4. Moreover, performing theoretical simulations of the dissociative chemisorption of molecules on a surface can be exceptionally useful to understand the reaction mechanism, since it allows one to obtain atomic resolution of the process, which is extremely hard to achieve experimentally.

The possibility of monitoring the orientation, the internal energy and other dynamical features in “real time” during the reaction complements the information obtainable from experiments. Moreover, from the calculations it is possible

to compute important details of the underlying potential energy surface (PES) as, for example, energy barriers obtained by locating transition states (TSs) on the surface (see Figure 1.1).

Performing accurate calculations is important to being able to make meaningful comparisons with experiments. As discussed in Chapter 2, both the accuracy of the calculation and the computational cost of AIMD scale with the size of the simulation box and a compromise needs to be made. Along the same lines, it is possible to propagate the simulations only up to very few (i.e., $1 \sim 2$) picoseconds due to the high computational cost of AIMD. Moreover, in order to simulate the surface which, in principle, is infinite one needs to exploit its periodicity and represent it using a periodic metal slab. This allows one to keep the computational cost contained, but it has some drawbacks.

First of all, the unit cell has to be chosen large enough to minimize the interaction between the molecule and its first periodic replicas. Similarly, a sufficiently large vacuum space needs to be used to separate the metal slab from its periodic image. Although the computational resources available are constantly increasing, the necessity of limiting the cell size still forbids simulating the effects of isolated defects that might be important for some reactions. In addition, the limited amount of surface atoms can lead to a less accurate description of the energy dissipation.

Finally, high accuracy simulations are crucial to obtain qualitative answers from the comparison with the experiments. The work reported in this Thesis, together with the vast majority of theoretical studies in surface science, exploits density functional theory (DFT) to compute the electronic energy of the system. As extensively discussed on Chapter 2, the accuracy of DFT depends on the choice of the exchange-correlation functional (E_{XC}). The performance of a particular E_{XC} depends on the system under consideration and therefore it needs to be carefully selected. A method to systematically improve the accuracy of E_{XC} in a semi-empirical and system-specific way, by comparing the results of experiments and simulations, is at the heart of this Thesis and it will be discussed thoroughly in the following Sections and Chapters.

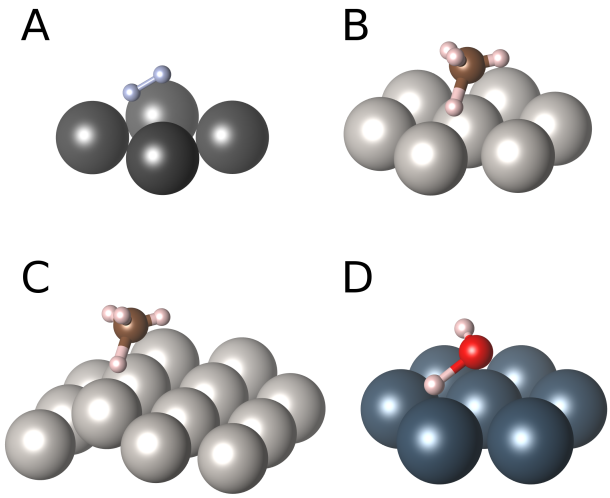

Figure 1.1: Examples of relevant transition states for the systems studied in this Thesis: (A) N_2 on W(110) studied in Chapter 3, (B) CH_4 on Pt(111) studied in Chapters 4, 5 and 6, (C) CH_4 on Pt(211) studied in Chapters 4 and 5 and (D) H_2O on Ni(111) studied in Chapter 7.

1.4 Aim of this Thesis

As discussed before, one of the main problems in the accurate simulation of the dissociative chemisorption of polyatomic molecules on a transition metal surface is the choice of the exchange correlation functional E_{XC} used to perform the DFT calculations. The main goal of this Thesis is twofold. Firstly, the static calculations and dynamical simulations reported can improve the understanding and give insights into catalytically relevant reactions. Secondly and most importantly, the main aim of this Thesis is to study how the choice of E_{XC} can influence the result of DFT calculations for molecules interacting with metal surfaces, and how developing a semi-empirical specific reaction parameter (SRP) functional [13–15] can improve the quality of said results and ultimately be used to accurately describe dissociative chemisorption reactions.

The aim of the work reported in the following Chapters of this Thesis is briefly summarized here in this Section.

Chapter 2 describes the basics of the DFT method and the semi-empirical

SRP approach that can be used to develop and test an accurate functional for a molecule-metal surface system. The Chapter reports and explains the different steps that are necessary to perform accurate AIMD simulations in order to obtain a good comparison with supersonic molecular beam experiments, which is at the heart of the semi-empirical SRP-DFT approach.

Chapter 3 reports a study aimed at testing the performance of the long-range van der Waals functional developed by Dion *et al.* (vdW-DF) [16] and its variant, called vdW-DF2, developed by Lee *et al.* [17]. It has been shown [13, 15, 18] that using a functional that models vdW interactions can improve the accuracy of DFT calculations for catalytically relevant systems. In the study reported in this Chapter, the vdW-DF and the vdW-DF2 functionals are tested for N_2 on W(110), a prototypical surface science system for which quantitative agreement between theory and experiments has not yet been achieved [19–22].

Chapter 4 focuses on the transferability of an SRP functional among chemically related systems. The SRP functional originally developed to describe the dissociative chemisorption of CHD_3 on Ni(111) [15] (called SRP32-vdW functional) is tested here on the dissociation of the same molecule on Pt(111) [13]. Most importantly, the work reported in Chapter 4 also studies the transferability among systems in which CHD_3 interacts with different facets of the same transition metal in order to go from the flat Pt(111) to more catalytically relevant and "defected" surfaces such as the stepped Pt(211) surface. The aim of this work is to provide a simple and systematic strategy to predict chemically accurate barriers for different surface sites of catalytically relevant systems.

Chapter 5 reports a study where the chemically accurate SRP32-vdW functional is used to obtain dynamically relevant features of the dissociative chemisorption of CHD_3 on the flat Pt(111) and on the stepped Pt(211) surfaces [23]. The aim of this work is to understand how the under-coordinated step site of the Pt(211) surface influences the reactivity and how the different topology of the surface can alter the dissociation dynamics.

Chapter 6 compares the performance of a standard GGA functional (i.e., PBE [24]) with that of the SRP32-vdW functional for CHD_3 on Pt(111) [13, 15]. The

aim of this Chapter is to investigate why the SRP32-vdW functional reproduces experiments whereas the PBE functional does not, even though the two functionals return a very similar geometry and energy for the minimum barrier [25].
Chapter 7 takes the first step in the development of an SRP functional for a different system for which chemical accuracy has not yet been achieved: HOD on Ni(111) [26]. Here the SRP functional developed for methane is used as an initial guess to obtain a prediction for plausible molecular beam experiments for this system. Another aim of this Chapter is to obtain useful dynamical insights on this relevant process while treating all the DOFs, including surface motion, in the simulation. Moreover, another important purpose of this work is to show that molecular beam experiments for HOD on Ni(111) can be accurately simulated (i.e., with reaction probabilies > 1 % for incidence energies achievable with molecular beams) in the hope to motivate other scientists to provide well-characterized experiments on this system. This would make it possible to eventually derive an accurate density functional for the investigated process.

1.5 Main Results

The main results of the work reported in the following Chapters of this Thesis are summarized in this Section.

Chapter 3 | Application of van der Waals Functionals to the Calculation of Dissociative Adsorption of N_2 on W(110) for Static and Dynamic Systems

In Chapter 3 we report a study of the static potential energy surface (PES) and of the reaction probability of N_2 on W(110). The study has been performed on a DFT level using functionals that include the correlation part developed by Dion *et al.* [16] (called vdW-DF) and its revised version (vdW-DF2) [17]. We find that using the vdW-DF2 functional improves the description of the molecule-surface interaction compared to GGA functionals like PBE and RPBE, by giving generally shallower molecular adsorption wells and barriers for the indirect reaction

and for the molecular desorption more similar to each other, as suggested by experiments [27]. The vdW-DF2 functional is then used to perform AIMD simulations of molecular beam experiments [28, 29] for which the agreement between experiment and theory is, at best, qualitative [19–22]. Despite the improvements in the description of the static PES, the reactivity computed through AIMD simulations does not depend much on the incidence energy (E_i), similarly to what was observed with PBE and RPBE [22], because of the competition between the direct and the indirect reaction mechanisms. The dependence of reaction on incident energy found experimentally [28, 29] is therefore not reproduced. The AIMD results show that the less deep molecular adsorption wells lead to a reduced indirect reaction probability, especially for normal incidence. However, the barrier for the direct dissociation computed with the vdW-DF2 functional might still be too large.

Chapter 4 | Surface Reaction Barriometry: Methane Dissociation on Flat and Stepped Transition Metal Surfaces

In Chapter 4 we study the transferability of the SRP32-vdW functional, which was initially developed to reproduce experiments for CHD_3 on Ni(111) with chemical accuracy [15]. In this Chapter we show that the same functional can be used to model the same reaction on a different low-index transition metal surface (i.e., Pt(111)) with chemical accuracy [13]. Furthermore, the SRP32-vdW functional is also transferable to methane interacting with the "defected" Pt(211) surface, which has under-coordinated step sites. The transferability of the SRP functional among systems in which a specific molecule interacts with different facets of the same metal allows us to define a semi-empirical protocol, which we call "reaction barriometry", that can help bridge the materials gap between surface science and heterogeneous catalysis. The strategy can be summarized as follows: (I) accurate molecular beam experiments are performed for a molecule dissociating over an ideal low index surface. (II) an SRP functional is developed for said system by comparing AIMD and experimental results. (III) the SRP functional is tested on a different experiment for the same system. (IV) the transferabil-

ity demonstrated in this Chapter can then be exploited to obtain chemically accurate barriers (i.e., with errors smaller than 4.2 kJ/mol) on all the relevant surface cuts of the metal studied, including stepped surfaces and, presumably, edges and corners of nanoparticles. The results can be used as a benchmark for future theoretical work, new methodological approximations and (hopefully) to perform accurate microkinetic simulations of catalytic processes proceeding over nanoparticles of the metal studied.

Chapter 5 | Methane on a Stepped Surface: Dynamical Insights on the Dissociation of CHD_3 on Pt(111) and Pt(211)

In Chapter 5 we report an extensive analysis of 12500 AIMD trajectories run performed using the SRP32-vdW functional on the flat Pt(111) and the stepped Pt(211) surface. The results show that, even though the difference in minimum barrier height results in a significantly different reactivity [23], the reaction mechanism is very similar on the two surfaces. This can be explained by the similar geometry of the TSs on the two surfaces and by the known absence of rotational steering [13, 15, 23, 30], which requires the molecules to be preoriented in a geometry similar to that of the TS in order to react. It has also been shown that the molecular trapping observed on the Pt(211) surface but not on the Pt(111) surface can partially be explained by the larger energy transfer to surface phonons on the stepped surface. In addition the geometry of the stepped surface promotes energy transfer to parallel motion, resulting in trapped molecules which retain a relatively large velocity parallel to the surface. Together with the long estimated trapping time (i.e., $\approx$ 43 ps), this suggests that experimentally the trapped molecules have time to explore a large portion of the surface and possibly to react by finding the most favorable geometry or even a higher order defect, like a kink.

Chapter 6 | CHD_3 Dissociation on Pt(111): a Comparison of the Reaction Dynamics Based on the PBE Functional and on a Specific Reaction Parameter Functional

In Chapter 6 we compare the performance of two density functionals on the description of the reaction of CHD_3 on Pt(111). The functionals under consideration are the well-known PBE [24] functional and the SRP32-vdW functional developed for CHD_3 on Ni(111) [15]. The TS associated with the minimum barrier has been computed with the two functionals. The calculations show a very similar barrier geometry and the same barrier height within 0.6 kJ/mol. However, while the SRP32-vdW functional reproduces molecular beam experiments with chemical accuracy [13], the PBE functional considerably overestimates the reaction probability [25]. We found that the van der Waals well described by the correlation part [16] of the SRP32-vdW functional, and not present with the PBE functional, accelerates the trajectories towards the surface, leaving the molecule less time to distort towards the TS geometry and leading to a larger energy transfer to the surface phonons. These factors play a role in lowering the reactivity computed using the SRP32-vdW functional with respect to that obtained using the PBE functional and therefore contribute to the improved agreement with the experimental results.

Chapter 7 | HOD on Ni(111): Ab Initio Molecular Dynamics Prediction of Molecular Beam Experiments

In Chapter 7 we report a predictive AIMD study for molecular beam experiments on the dissociative chemisorption of HOD on Ni(111) for which, at present, no experimental results are available. Our study improves the description of the system over previous theoretical work [31] by explicitly treating all the degrees of freedom of the surface through AIMD simulations and by using the SRP functional developed for CHD_3 (SRP32-vdW) [15] that models long-range vdW interactions [16, 32], which are important for this type of system [13, 15, 18]. The analysis of the trajectories confirmed the strong mode [33, 34] and bond [35]

selectivity of the reaction and suggested rotational steering plays an important role. Molecules have been observed to react regardless of their initial orientation, while the bonds were steered towards their orientation in the TS at the time of the dissociation. Most importantly, comparing our results with experiments performed on a similar system (D_2O on Ni(111) [36]), we find that the SRP32-vdW functional is a good starting point for developing an SRP functional for HOD on Ni(111). The comparison seems to suggest that the SRP32-vdW would overestimate the reactivity for the system studied. Therefore, when experimental results become available, the mixing parameter of the functional (which currently has a low value) can be increased to make the functional describe a more repulsive interaction so that the AIMD simulations reproduce the experimental results.

1.6 Outlook

In this Section the questions that remain open from the work presented in this Thesis are reported and discussed, together with an outlook on the possible directions in which this research could be developed in the future.

At present, the understanding of the dissociative chemisorption of N_2 on W(110) is still poor. In order to develop an SRP functional for the system, one would need a weighted average of two density functionals that, coupled with AIMD, are able to reproduce the shape of the experimental reactivity curve (i.e., its dependence on the collision energy, see Chapter 2). Once these two functionals have been identified, the procedure illustrated in Chapter 2 can be exploited to devise and test a semi-empirical functional that might be able to accurately reproduce molecular beam experiments, hence giving important dynamical insights on this reaction. Currently, neither standard GGA functionals such as PBE and RPBE [22] or a functional including van der Waals interactions like the vdW-DF2 [37] has been successful. In order to be able to accurately reproduce experiments for this system, one needs a functional able to properly describe both the dissociative chemisorption and the molecular adsorption and desorption processes observed. A problem with this is that the GGA functionals that de-

scribe molecular adsorption and dissociative adsorption well tend to differ. For instance, the RPBE functional does rather well at describing molecular adsorption [38], but tends to overestimate dissociative chemisorption barriers [14, 39]. A possible solution to this problem might be the development of a meta-GGA [40] based SRP functional. Further work would be needed to improve the understanding of N_2 on W(110), both on the theoretical side, as mentioned above, and on the experimental side. To the best of our knowledge there are only two molecular beam experiment results available for the system [28, 29] and they report rather different results, complicating the comparison with theoretical simulations. The availability of new and well characterized molecular beam experiments would help in the quest for a candidate SRP functional by allowing theoreticians to design better and more comparable AIMD simulations.

The transferability of the SRP functional discussed in Chapter 4 opens new possibilities to improve the accuracy of existing microkinetic simulations which rely on computed barrier heights to obtain reaction rates. The SRP functional can be exploited to compute chemically accurate barriers on different surface sites and defects that can be found in real catalytic conditions, therefore improving the quality of the description.

Further investigation is also required to fully understand the difference in reactivity observed for CHD_3 on Pt(111) using the PBE and the SRP32-vdW functionals, as described in Chapter 6. Using the modified Baule model [41] to estimate the dependence of the energy transfer (E_T) to the surface on the molecular collision energy and on the depth of the molecular adsorption well, suggests that only roughly half of the energy shift between the reaction probability curves can be explained with the larger E_T observed for the SRP32-vdW functional and due to the van der Waals interactions modeled by its correlation part. Further work might shed light on the dynamical effects behind what is left to explain of the difference in reactivity between the two functionals.

The work reported in Chapter 7 on HOD on Ni(111) represents the initial step to developing an accurate density functional for said system. In order to further proceed towards this goal, well characterized molecular beam experiments

are needed for conditions at which AIMD is applicable. As soon as experimental results become available, the SRP32-vdW functional used in our study [13, 15, 26] can be tuned to try to reproduce the experimental results with chemical accuracy. This could help improve the understanding of this catalytically relevant system.

Along the same line, having developed an SRP functional for CHD_3 on Pt and Ni surfaces, the next natural step in the line of work presented in this Thesis would be to tackle the dissociative chemisorption of CHD_3 on Pd(111) to test if the SRP32-vdW functional is transferable to yet another group X transition metal. Moreover, the transferability of said functional to other surface cuts could be tested on Pt surfaces with kinks, like the Pt(210) surface, to be used as a model system for nanoparticle corners. In the Theoretical Chemistry group of Leiden, work along these lines is already underway.

The SRP approach could also be extended to other different and, possibly, more complex reactions involved in catalytic processes. Besides the study discussed in Chapter 7 on HOD on Ni(111), other relevant processes of choice would be, for example, the dissociation of methanol (CH_3OH) or ammonia (NH_3) on a metal surface.

Having an SRP functional also allows one to obtain information on dynamically relevant features of a process, as shown in Chapters 5 and 7, but, unfortunately, at this stage AIMD can not accurately predict reactivities below 1% (see Chapter 2 for more details). This limitation can be circumvented by coupling high-dimensional PESs developed using a Neural Network method [42, 43], which also model surface motion [44–47], with chemically accurate SRP functionals. This will allow one to run a large number of computationally cheap quasi-classical trajectories and hence to obtain statistically significant results for low reaction probabilities.

Bibliography

[1] D. Voet and J. G. Voet, *Biochemistry, 4th edn.* John Wiley & Sons, 2011.

[2] I. Chorkendorff and J. W. Niemantsverdriet, *Concepts of Modern Catalysis and Kinetics.* Weinheim: Wiley-VCH, 2003.

[3] G. Ertl, "Surface Science and Catalysis-Studies on the Mechanism of Ammonia Synthesis: The P. H. Emmett Award Address," *Catal. Rev.*, vol. 21, pp. 201–223, 1980.

[4] C. Ratnasamy and J. P. Wagner, "Water Gas Shift Catalysis," *Catal. Rev.*, vol. 51, pp. 325–440, 2009.

[5] R. Imbihl, R. J. Behm, and R. Schlögl, "Bridging the Pressure and Material Gap in Heterogeneous Catalysis," *Phys. Chem. Chem. Phys.*, vol. 9, p. 3459, 2007.

[6] C. A. Wolcott, A. J. Medford, F. Studt, and C. T. Campbell, "Degree of Rate Control Approach to Computational Catalyst Screening," *J. Catal.*, vol. 330, pp. 197–207, 2015.

[7] Y. Xu, A. C. Lausche, S. G. Wang, T. S. Khan, F. Abild-Pedersen, F. Studt, J. K. Nørskov, and T. Bligaard, "In Silico Search for Novel Methane Steam Reforming Catalysts," *New J. Phys.*, vol. 15, p. 125021, 2013.

[8] M. K. Sabbe, M. F. Reyniers, and K. Reuter, "First-Principles Kinetic Modeling in Heterogeneous Catalysis: an Industrial Perspective on Best-Practice, Gaps and Needs," *Catal. Sci. Technol.*, vol. 2, pp. 2010–2024, 2012.

[9] C. Stegelmann, A. Andreasen, and C. T. Campbell, "Degree of Rate Control: How Much the Energies of Intermediates and Transition States Control Rates," *J. Am. Chem. Soc.*, vol. 131, pp. 8077–8082, 2009.

[10] H. J. Freund, H. Kuhlenbeck, J. Libuda, G. Rupprechter, M. Bäumer, and H. Hamann, "Bridging the Pressure and Materials Gaps between Cataly-

sis and Surface Science: Clean and Modified Oxide Surfaces," *Top. Catal.*, vol. 15, pp. 201–209, 2001.

[11] G. A. Somorjai, R. L. York, D. Butcher, and J. Y. Park, "The evolution of Model Catalytic Systems; Studies of Structure, Bonding and Dynamics from Single Crystal Metal Surfaces to Nanoparticles, and from Low Pressure ($<10^{-3}$ Torr) to High Pressure ($>10^{-3}$ Torr) to Liquid Interfaces," *Phys. Chem. Chem. Phys.*, vol. 9, pp. 3500–3513, 2007.

[12] V. P. Zhdanov, "Structure Gap in Heterogeneous Catalysis: Kinetic Aspects," *Phys. Rev. B*, vol. 64, p. 193406, 2001.

[13] D. Migliorini, H. Chadwick, F. Nattino, A. Gutiérrez-González, E. Dombrowski, E. A. High, H. Guo, A. L. Utz, B. Jackson, R. D. Beck, and G. J. Kroes, "Surface Reaction Barriometry: Methane Dissociation on Flat and Stepped Transition-Metal Surfaces," *J. Phys. Chem. Lett.*, vol. 8, pp. 4177–4182, 2017.

[14] C. Díaz, E. Pijper, R. A. Olsen, H. F. Busnengo, D. J. Auerbach, and G. J. Kroes, "Chemically Accurate Simulation of a Prototypical Surface Reaction: H_2 Dissociation on Cu(111)," *Science*, vol. 326, pp. 832–834, 2009.

[15] F. Nattino, D. Migliorini, G. J. Kroes, E. Dombrowski, E. A. High, D. R. Killelea, and A. L. Utz, "Chemically Accurate Simulation of a Polyatomic Molecule-Metal Surface Reaction," *J. Phys. Chem. Lett.*, vol. 7, pp. 2402–2406, 2016.

[16] M. Dion, H. Rydberg, E. Schröder, D. C. Langreth, and B. I. Lundqvist, "Van der Waals Density Functional for General Geometries," *Phys. Rev. Lett.*, vol. 92, p. 246401, 2004.

[17] K. Lee, É. D. Murray, L. Z. Kong, B. I. Lundqvist, and D. C. Langreth, "Higher-Accuracy van der Waals density functional," *Phys. Rev. B*, vol. 82, p. 081101, 2010.

[18] F. Nattino, D. Migliorini, M. Bonfanti, and G. J. Kroes, "Methane Dissociation on Pt(111): Searching for a Specific Reaction Parameter Density Functional," *J. Chem. Phys.*, vol. 144, p. 044702, 2016.

[19] M. Alducin, R. Díez Muiño, H. F. Busnengo, and A. Salin, "Why N_2 Molecules with Thermal Energy Abundantly Dissociate on W(100) and Not on W(110)," *Phys. Rev. Lett.*, vol. 97, p. 056102, 2006.

[20] M. Alducin, R. Díez Muiño, H. F. Busnengo, and A. Salin, "Low Sticking Probability in the Nonactivated Dissociation of N_2 Molecules on W(110)," *J. Chem. Phys.*, vol. 125, p. 144705, 2006.

[21] G. A. Bocan, R. Díez Muiño, M. Alducin, H. F. Busnengo, and A. Salin, "The Role of Exchange-Correlation Functionals in the Potential Energy Surface and Dynamics of N_2 Dissociation on W Surfaces," *J. Chem. Phys.*, vol. 128, p. 154704, 2008.

[22] F. Nattino, F. Costanzo, and G. J. Kroes, "N_2 Dissociation on W(110): An Ab Initio Molecular Dynamics Study on the Effect of Phonons," *J. Chem. Phys.*, vol. 142, p. 104702, 2015.

[23] D. Migliorini, H. Chadwick, and G. J. Kroes, "Methane on a Stepped Surface: Dynamical Insights on the Dissociation of CHD_3 on Pt(111) and Pt(211)," *J. Chem. Phys.*, vol. 149, p. 094701, 2018.

[24] J. P. Perdew, K. Burke, and M. Ernzerhof, "Generalized Gradient Approximation Made Simple," *Phys. Rev. Lett.*, vol. 77, pp. 3865–3868, 1996.

[25] H. Chadwick, D. Migliorini, and G. J. Kroes, "CHD_3 Dissociation on Pt(111): A Comparison of the Reaction Dynamics Based on the PBE Functional and on a Specific Reaction Parameter Functional," *J. Chem. Phys.*, vol. 149, p. 044701, 2018.

[26] D. Migliorini, F. Nattino, A. K. Tiwari, and G. J. Kroes, "HOD on Ni(111): Ab Initio Molecular Dynamics Prediction of Molecular Beam Experiments," *J. Chem. Phys.*, vol. 149, p. 244706, 2018.

[27] J. C. Lin, N. Shamir, Y. B. Zhao, and R. Gomer, "Adsorption, Desorption and Dissociation of N_2 on W(110)," *Surf. Sci.*, vol. 231, pp. 333–343, 1990.

[28] H. E. Pfnür, C. T. Rettner, J. Lee, R. J. Madix, and D. J. Auerbach, "Dynamics of the Activated Dissociative Chemisorption of N_2 on W(110): A Molecular Beam Study," *J. Chem. Phys.*, vol. 85, pp. 7452–7466, 1986.

[29] C. T. Rettner, E. K. Schweizer, and H. Stein, "Dynamics of the Chemisorption of N_2 on W(100): Precursor-Mediated and Activated Dissociation," *J. Chem. Phys.*, vol. 93, pp. 1442–1454, 1990.

[30] G. Füchsel, P. S. Thomas, J. den Uyl, Y. Öztürk, F. Nattino, H. D. Meyer, and G. J. Kroes, "Rotational Effects on the Dissociation Dynamics of CHD_3 on Pt(111)," *Phys. Chem. Chem. Phys.*, vol. 18, pp. 8174–8185, 2016.

[31] B. Jiang and H. Guo, "Towards an Accurate Specific Reaction Parameter Density Functional for Water Dissociation on Ni(111): RPBE versus PW91," *Phys. Chem. Chem. Phys.*, vol. 18, pp. 21817–21824, 2016.

[32] G. Román-Pérez and J. M. Soler, "Efficient Implementation of a van der Waals Density Functional: Application to Double-Wall Carbon Nanotubes," *Phys. Rev. Lett.*, vol. 103, p. 096102, 2009.

[33] T. H. Liu, B. N. Fu, and D. H. Zhang, "An Approximate Full-Dimensional Quantum Dynamics Study of the Mode Specificity in the Dissociative Chemisorption of D_2O on Rigid Cu(111)," *Phys. Chem. Chem. Phys.*, vol. 19, pp. 11960–11967, 2017.

[34] H. Seenivasan, B. Jackson, and A. K. Tiwari, "Water Dissociation on Ni(100), Ni(110), and Ni(111) Surfaces: Reaction Path Approach to Mode Selectivity," *J. Chem. Phys.*, vol. 146, p. 074705, 2017.

[35] T. H. Liu, Z. J. Zhang, J. Chen, B. N. Fu, and D. H. Zhang, "Mode Specificity of the Dissociative Chemisorption of HOD on Rigid Cu(111): an Approximate Full-Dimensional Quantum Dynamics Study," *Phys. Chem. Chem. Phys.*, vol. 18, pp. 26358–26364, 2016.

[36] P. M. Hundt, B. Jiang, M. E. van Reijzen, H. Guo, and R. D. Beck, "Vibrationally Promoted Dissociation of Water on Ni(111)," *Science*, vol. 344, pp. 504–507, 2014.

[37] D. Migliorini, F. Nattino, and G. J. Kroes, "Application of van der Waals Functionals to the Calculation of Dissociative Adsorption of N_2 on W(110) for Static and Dynamic Systems," *J. Chem. Phys.*, vol. 144, p. 084702, 2016.

[38] B. Hammer, L. B. Hansen, and J. K. Nørskov, "Improved Adsorption Energetics Within Density-Functional Theory Using Rrevised Perdew-Burke-Ernzerhof Functionals," *Phys. Rev. B*, vol. 59, pp. 7413–7421, 1999.

[39] M. Wijzenbroek and G. J. Kroes, "The Effect of the Exchange-Correlation Functional on H_2 Dissociation on Ru(0001)," *J. Chem. Phys.*, vol. 140, p. 084702, 2014.

[40] H. W. Peng, Z. H. Yang, J. P. Perdew, and J. W. Sun, "Versatile van der Waals Density Functional Based on a Meta-Generalized Gradient Approximation," *Phys. Rev. X*, vol. 6, p. 041005, 2016.

[41] B. Baule, "Theoretische Behandlung der Erscheinungen in verdünnten Gasen," *Ann. Phys.*, vol. 349, pp. 145–176, 1914.

[42] J. Behler and M. Parrinello, "Generalized Neural-Network Representation of High-Dimensional Potential-Energy Surfaces," *Phys. Rev. Lett.*, vol. 98, p. 146401, 2007.

[43] J. Behler, "Representing Potential Energy Surfaces by High-Dimensional Neural Network Potentials," *J. Phys. Condens. Matter*, vol. 26, p. 183001, 2014.

[44] K. Shakouri, J. Behler, J. Meyer, and G. J. Kroes, "Accurate Neural Network Description of Surface Phonons in Reactive Gas-Surface Dynamics: N_2 + Ru(0001)," *J. Phys. Chem. Lett.*, vol. 8, pp. 2131–2136, 2017.

[45] B. Kolb, X. Luo, X. Y. Zhou, B. Jiang, and H. Guo, "High-Dimensional Atomistic Neural Network Potentials for Molecule–Surface Interactions: HCl Scattering from Au(111)," *J. Phys. Chem. Lett.*, vol. 8, pp. 666–672, 2017.

[46] Q. H. Liu, X. Y. Zhou, L. S. Zhou, Y. L. Zhang, X. Luo, H. Guo, and B. Jiang, "Constructing High-Dimensional Neural Network Potential Energy Surfaces for Gas–Surface Scattering and Reactions," *J. Phys. Chem. C*, vol. 122, pp. 1761–1769, 2018.

[47] K. Shakouri, J. Belher, J. Meyer, and G. J. Kroes, "Analysis of Energy Dissipation Channels in a Benchmark System of Activated Dissociation: N_2 on Ru(0001)," *J. Phys. Chem. C*, vol. 122, pp. 23470–23480, 2018.

Chapter 2

Methods and Theory: A Semi-Empirical Approach to Density Functional Theory

Part of this Chapter is based on:

D. Migliorini *et al.*, *J. Chem. Phys. Lett.*, 8, 4177 (2017)
https://pubs.acs.org/doi/abs/10.1021/acs.jpclett.7b01905
which is reproduced with the permission of ACS Publications[1].

2.1 Introduction

Heterogeneous catalysis generally focuses on very complicated processes that involve many molecular states and several reaction steps taking place on irregular and highly corrugated transition metal catalysts. Today an accurate simulation of such processes in their entirety is far beyond computational possibility. However it has been shown that usually only a very few of the molecular states involved exhibit a large degree of rate control on the overall process [1] and this allows experiments and simulations to focus on single fundamental steps rather than on

[1] further permissions related to the material excerpted should be directed to the ACS.

the whole process. Often the catalytic system is modeled by a single reaction step involving a molecule dissociating on an ideal low-index metal surface.

Rate controlling states can be either molecular adsorption or transition states and they are crucial because a small change in their energy might dramatically affect the rate of the overall process. While molecular adsorption energies can be measured experimentally (i.e., using tempreature programmed desorption), it is more complicated to design experiments able to measure dissociative chemisorption barriers. Theoretical calculations can provide energy barriers (E_b) but the large number of atoms and the periodic representation [2] needed for this kind of system makes accurate full quantum chemical simulations unfeasible. The theoretical method of choice to simulate the dissociation of molecules on a metal surface while including all the relevant atoms is density functional theory (DFT) at the generalized gradient approximation (GGA) level. Unfortunately GGA-DFT is not accurate enough to calculate chemically accurate barriers (i.e., with errors smaller than 1 kcal/mol $\approx$ 4.2 kJ/mol) [3].

A way to improve DFT accuracy is to develop a semi-empirical specific reaction parameter (SRP) density functional. Recent theoretical work [4–6] and recent joint theoretical and experimental efforts [7, 8] have been successful in developing system-specific SRP functionals for several catalytically relevant systems [4–8] by comparing *ab initio* molecular dynamics (AIMD) simulations [9, 10] with supersonic molecular beam experiments.

In this Chapter the main steps needed to accurately simulate supersonic molecular beam experiments are reported and discussed in order to obtain an SRP functional for a polyatomic molecule dissociating on a transition metal surface. The Chapter is organized as follows: the basics of the DFT method and of the specific reaction parameter approach to DFT are explained in Section 2.2, the strategy to develop and test an SRP functional is reported in Section 2.3 and the procedure to accurately simulate molecular beam experiments is described in Section 2.4.

2.2 SRP Approach to DFT

DFT is a particularly convenient method to study catalytically relevant systems and surface science in general. The high complexity of these systems and the large number of degrees of freedom (DOFs) involved benefit from the favorable scaling of the computational cost of DFT ($\propto n^3$, where n is the total number of electrons), which is better than for correlated wavefunction-based methods. Moreover DFT offers an easy treatment of periodicity. This allows a full-dimensional treatment of larger systems (even for dynamical simulations, when coupled with classical time propagation), which are crucial to understand surface reactions. However this comes with the price of a lower accuracy due to the unknown analytical form of the exchange-correlation functional (E_{XC}), needed to obtain the energy of the system in the DFT approach. This problem of lack of accuracy for a molecule on a transition metal surface can be circumvented trough a semi-empirical approach by developing a specific reaction parameter density functional (SRP-DFT).

2.2.1 Density Functional Theory

The heart of the DFT method is formed by the Hohenberg-Kohn theorems [11]. The first theorem states that for a non-degenerate ground state (gs) all the properties of the system are determined by the electronic density (ρ_0). This implies that the gs wave function ($\Psi_0(\mathbf{r}_1, \mathbf{r}_2, ..., \mathbf{r}_n)$) can be expressed as a functional of the gs electronic density (ρ_0):

$$\Psi_0(\mathbf{r}_1, \mathbf{r}_2, ..., \mathbf{r}_n) = \Psi[\rho_0(\mathbf{r})], \tag{2.1}$$

and allows one to write the gs expectation value of any observable $\hat{O}$ as a functional of the density:

$$O_0 = O[\rho_0] = \langle \Psi[\rho_0(\mathbf{r})] \mid \hat{O} \mid \Psi[\rho_0(\mathbf{r})] \rangle. \tag{2.2}$$

This entails that the energy of the ground state is a functional of $\rho_0(\mathbf{r})$ as well. Moreover, the second Hohenberg-Kohn theorem states that, for a given system,

the energy $E[\rho']$ of a generic density ρ' cannot be lower than the gs energy $E[\rho_0]$:

$$E[\rho_0] = \langle \Psi[\rho_0(\mathbf{r})] \mid \hat{H} \mid \Psi[\rho_0(\mathbf{r})] \rangle \leq \langle \Psi[\rho'(\mathbf{r})] \mid \hat{H} \mid \Psi[\rho'(\mathbf{r})] \rangle = E[\rho'], \quad (2.3)$$

where $\hat{H}$ is the Hamiltonian for the given system that can be written as:

$$\hat{H} = \hat{T} + \hat{U} + \hat{V}. \quad (2.4)$$

Here $\hat{T}$ is the kinetic term, $\hat{U}$ is the electron-electron interaction term and $\hat{V}$ is the potential term due to the positively charged nuclei. In order to obtain the gs energy of the system, ideally one only has to minimize the functional:

$$E[\rho] = \langle \Psi[\rho] \mid \hat{T} + \hat{U} + \hat{V} \mid \Psi[\rho] \rangle. \quad (2.5)$$

However, in order to do so, analytical expressions for $\hat{T}$, $\hat{U}$ and $\hat{V}$ are needed.

The most common approach to solve the DFT problem and to obtain the gs energy has been proposed by Kohn and Sham [12]. The core idea of the Kohn-Sham (KS) method is to introduce a fictious system of non-interacting particles that has the same gs density of the real interacting system and to solve a set of single-particle Kohn-Sham (KS) equations:

$$\left[-\frac{1}{2}\nabla^2 + V_s(\mathbf{r}) \right] \varphi_i(\mathbf{r}) = \epsilon_i \varphi_i(\mathbf{r}). \quad (2.6)$$

Here the gs wavefunction Ψ_0 has been written as a Slater determinant of single particle KS orbitals $\varphi_i(\mathbf{r})$, and $V_s(\mathbf{r})$ is the so-called KS potential. Equation 2.6 is reported in atomic units, consistently with the rest of the equations in this Section.

In order to solve the KS Equation 2.6, one can use the kinetic energy for a system of non-interacting particles $T_s[\rho]$, the Hartree interaction energy $U_H[\rho]$ (i.e., the coulombic repulsion), while moving the contributions due to the interacting nature of the system into the so-called exchange-correlation energy term

E_{XC}, so that:

$$E[\rho] = T_s[\rho] + U_H[\rho] + E_{XC}[\rho] + V[\rho], \tag{2.7}$$

where

$$E_{XC} = (U - U_H) + (T - T_s). \tag{2.8}$$

Note that Equation 2.7 is formally correct but the analytical expression of E_{XC} is unknown. Therefore, in order to obtain an accurate value for the energy, a good approximation (i.e., analytical expression) of E_{XC} is needed. Some of the most important and widely used approximations for E_{XC} are reported and discussed in Section 2.2.3. Now it is possible to define the KS potential as:

$$V_s(\mathbf{r}) = \int d\mathbf{r}' \frac{\rho(\mathbf{r})}{|\mathbf{r} - \mathbf{r}'|} - \sum_N \frac{Z_N}{|\mathbf{r} - \mathbf{R}_N|} + V_{XC}(\mathbf{r}), \tag{2.9}$$

where the first term is the Hartree potential U_H, the second (V) is due to the interaction with the N nuclei in the system and $V_{XC}(\mathbf{r})$ is the derivative of $E_{XC}[\rho(\mathbf{r})]$ with respect to the density:

$$V_{XC}(\mathbf{r}) = \frac{\delta E_{XC}[\rho(\mathbf{r})]}{\delta \rho(\mathbf{r})}. \tag{2.10}$$

If V_s is defined as in Equation 2.9, from the solution of Equation 2.6 it is possible to recover the ground state density of the real correlated system as:

$$\rho_0(\mathbf{r}) = \sum_i f_i \mid \varphi_i(\mathbf{r}) \mid^2 . \tag{2.11}$$

where f_i are the occupation numbers. Note that $\rho_0(\mathbf{r})$ is the correct gs density if the exact analytical expression for E_{XC} would be known. The Kohn-Sham Equation 2.6 depend on the density $\rho(\mathbf{r})$ through $V_s(\mathbf{r})$ and $\rho(\mathbf{r})$ itself is obtained from the KS orbitals through Equation 2.11. Therefore, in order to optimize the KS orbitals $\varphi_i(\mathbf{r})$, the KS equations need to be solved self-consistently starting

from an initial guess of the density $\rho^{init}(\mathbf{r})$.

The KS approach shifts the problem from minimizing the energy functional to solving a set of non-interacting equations while, in principle, delivering the correct density ρ_0 (Equation 2.11) and energy $E[\rho_0]$ (Equation 2.7) of the real interacting and correlated system. As mentioned before, the overall accuracy of the method depends then on the quality of the approximation used to obtain the exchange-correlation contribution E_{XC} (see Section 2.2.3).

2.2.2 Plane Wave DFT

When it comes to describing periodic systems, it is possible to expand the KS orbitals according to Bloch's theorem in a set of plane waves that have the same periodicity as the system considered:

$$\varphi_j(\mathbf{r}, \mathbf{k}) = N \sum_G c_{j\mathbf{Gk}} e^{i(\mathbf{k}+\mathbf{G})\mathbf{r}}. \tag{2.12}$$

Here j runs over the KS orbitals, $\mathbf{k}$ is a vector in the irreducible Brillouin zone (IBZ), $\mathbf{G}$ is a reciprocal lattice vector and N is a normalization constant. Equation 2.12 has to be solved for the coefficients $c_{j\mathbf{Gk}}$. Performing a plane wave DFT calculation requires two "parameters": a grid of K-points in order to avoid having to integrate over all the IBZ, and a cut off on the kinetic energy of the plane waves (E_{cut}). This defines the size of the basis set as it will only include plane waves associated with a kinetic energy:

$$\frac{1}{2} \mid \mathbf{k} + \mathbf{G} \mid^2 \leq E_{cut}. \tag{2.13}$$

In order to obtain accurate results, the energy needs to be converged with respect to both the value of E_{cut} and the number of K-points.

In order to accurately reproduce the strongly oscillating wave function close to the nuclei one would need to use a very large value of E_{cut}, thus resulting in slowly converging calculations. This limitation can be circumvented by using pseudopotentials [13, 14] to explicitly treat only the valence electrons while re-

placing the strong Coulomb potential close to the nuclei with a weaker (effective) potential. This results in smoother wave functions close to the nuclei that can be described using a smaller value of E_{cut}, while approximately reproducing the all-electron wave functions at larger distances. Moreover the pseudopotentials can be designed to partially account for relativistic effects and, since only the chemically-relevant valence electrons are explicitly treated, they further reduce the calculation time.

The plane waves implementation of DFT has the advantage that the basis functions are inherently periodic and do not depend on the atomic positions but only on the size of the simulation box and on the value of E_{cut}. This avoids the basis-set superposition error (BSSE) and issues with systematic basis set convergence which are typical of atomic orbital based methods. On the other hand, it implies that increasing the box size will increase the computational cost even if the number of atoms is held constant. For surface simulations, this translates into a limitation of the size of the vacuum that can be use to separate the metal slab from its 1st periodic replica, which needs to be considered when long range interactions are included. A more detailed discussion is reported in Section 2.4.2.

2.2.3 Exchange-Correlation Functional

As mentioned before, the DFT approach is formally correct and it would return the exact ground state density and energy if an analytical expression for E_{XC} was known. Since the beginning of DFT, many different E_{XC} approximations have been proposed and applied to physically relevant systems. However the recipe for the universal exchange-correlation functional has not yet been found and any of the available approximations will perform better for some systems and worse for others.

The first form of E_{XC} is based on the assumption that the electrons behave as a homogeneous gas and it was proposed directly by Kohn and Sham [12] with

the name of local density approximation (LDA):

$$E_{XC}^{LDA}[\rho(\mathbf{r})] = \int \rho(\mathbf{r})\ \epsilon_{xc}^{LDA}[\rho(\mathbf{r})]\ d\mathbf{r}, \tag{2.14}$$

where ϵ_{xc}^{LDA} can be decomposed into the exchange part ϵ_x [15, 16]:

$$\epsilon_x = -\frac{3}{4}\left(\frac{3}{\pi}\ \rho(\mathbf{r})\right)^{1/3}, \tag{2.15}$$

and into the correlation part ϵ_c. The analytical expression of ϵ_c is known for the limits of high density (weak correlation) and low density (strong correlation). The two limits have then been connected by fitting results of Monte Carlo simulations [17].

The LDA approximation is based on the assumption that the electrons behave as a homogeneous gas and therefore it performs poorly when it comes to describe molecular bonds or molecule-surface interactions. This makes the LDA approximation not viable for heterogeneous catalysis where dissociation barrier heights are of fundamental importance and need to be calculated with high accuracy.

The next natural step to overcome the locality of this approximation is to include the gradient of the density ($\nabla\rho(\mathbf{r})$) in the expression of E_{XC}. The so-called semi-local generalized gradient approximation (GGA) functionals have a general form:

$$E_{XC}^{GGA}[\rho(\mathbf{r})] = \int \mathcal{F}[\ \rho(\mathbf{r}), \nabla\rho(\mathbf{r})\ ]\ d\mathbf{r}, \tag{2.16}$$

where E_{XC}^{GGA} can be decomposed into the sum of the exchange part (E_X^{GGA}) plus the correlation part (E_C^{GGA}). Two of the most used GGA functionals in surface science are the Perdew-Burke-Ernzerhof (PBE) [18, 19] and its revised version by Nørskov and coworkers (RPBE) [20]. The PBE and the RPBE functionals have the same correlation part:

$$E_C^{GGA}[\rho(\mathbf{r})] = \int \rho(\mathbf{r})\ \Big(\epsilon_c[\rho(\mathbf{r})] + H[\rho(\mathbf{r}), \nabla\rho(\mathbf{r})]\Big)\ d\mathbf{r}, \tag{2.17}$$

where the gradient contribution H is based on physical constraints.

For both PBE and RPBE the GGA exchange functional (E_X^{GGA}) has the general form:

$$E_X^{GGA}[\rho(\mathbf{r})] = \int \rho(\mathbf{r})\ \epsilon_x[\rho(\mathbf{r})]\ F(s)\ d\mathbf{r}, \tag{2.18}$$

where $F(s)$ is the enhancement factor of the LDA ϵ_x and depends on the reduced density gradient $s(\mathbf{r})$:

$$s(\mathbf{r}) = \frac{\mid \nabla\rho(\mathbf{r}) \mid}{[\ 2(3\pi^2)^{1/3}\rho(\mathbf{r})^{4/3}\ ]}. \tag{2.19}$$

The only difference between PBE [18] and RPBE [20] is in the expression of $F(s)$:

$$F^{PBE}(s) = 1 + k - \frac{k}{(1 + \mu s^2/k)}, \tag{2.20}$$

$$F^{RPBE}(s) = 1 + k(1 - e^{-\mu s^2/k}), \tag{2.21}$$

where k and μ are based on physical constants [18].

Several attempts have been made to improve further on the GGA approximation such as including the Laplacian of the electron density $\nabla^2\rho(\mathbf{r})$ (meta-GGA functionals) or adding fractions of the Hartree-Fock exchange (hybrid functionals). However these approximations are not suitable to effectively simulate molecules on surfaces due to, for instance, their high computational cost.

One of the pitfalls of the GGA approximation is that long range van der Waals interaction is not taken into account. Among the different approaches that have been proposed to overcome this limitation [21–24], one of the most interesting is the vdW-DF correlation functional developed by Dion *et al.* [24], which models the long range interaction based on the density of the system without semi-empirical parameters.

The vdW-DF approach consists in pairing a GGA exchange functional with a correlation ($E_C^{\text{vdW-DF}}$) that can model the van der Waals interaction. The ensuing correlation is defined as the sum of a local (LDA) part and a non local

(nl) contribution:

$$E_{XC}^{\text{vdW-DF}}[\rho(\mathbf{r})] = E_X^{GGA}[\rho(\mathbf{r})] + E_C^{LDA}[\rho(\mathbf{r})] + E_C^{nl}[\rho(\mathbf{r})], \tag{2.22}$$

where the non-local part of the correlation, which vanishes for a homogeneous density, is obtained through a double spatial integration over the density:

$$E_C^{nl}[\rho(\mathbf{r})] = \frac{1}{2}\iint d\mathbf{r}_1\ d\mathbf{r}_2\ \rho(\mathbf{r}_1)\Phi(q_1, q_2, r_{12})\rho(\mathbf{r}_2). \tag{2.23}$$

The kernel Φ depends on $r_{12} = |\mathbf{r}_1 - \mathbf{r}_2|$ and on q_1 and q_2 which, in turn, depend on ρ and on $\nabla\rho$ evaluated in $\mathbf{r}_1$ and $\mathbf{r}_2$.

Despite the complexity of $E_C^{nl}[\rho(\mathbf{r})]$, the kernel Φ can be tabulated and the integral can be very efficiently evaluated thanks to the implementation of Román-Pérez and Soler [25]. This makes the vdW-DF functional almost as fast to evaluate as any other standard GGA functional. Moreover the long range interaction is evaluated self-consistently on the density of the system without semi-empirical parameters [24, 26].

2.2.4 Specific Reaction Parameter Functional

The specific reaction parameter (SRP) approach to DFT is a semi-empirical method, originally proposed by Truhlar and coworkers [27]. Its implementation for molecules on surfaces allows us to develop a semi-empirical and system specific functional able to improve the accuracy of standard GGA functionals, which are in general not quantitative for these systems [3]. The SRP-DFT approach has been proven successful for different molecule-metal surface systems such as H_2 on Cu(111) [4], H_2 on Cu(100) [5], D_2 on Pt(111) [6] and recently CHD_3 on Ni(111) [7] and Pt(111) and Pt(211) [8]. The SRP strategy consists of selecting an experimental observable that depends on the minimum barrier height (i.e. the zero-coverage reaction probability S_0) and to choose two functionals that predict values that are systematically too high and too low compared to the experimental data. Note that the functionals of choice need to be able to reproduce

the shape of the reaction probability curve which depends on the distribution of energy barriers on the surface [28]. For many molecules reacting on a metal surface [4, 7, 8, 28–33] the GGA exchange functionals of choice are PBE [18] and RPBE [20], with the first known to usually underestimate and the second to overestimate barrier heights for these systems. The SRP exchange correlation functional (E_{XC}^{SRP}) is then defined as a linear combination of the chosen GGA functionals:

$$E_{XC}^{SRP} = x \cdot E_{XC}^{RPBE} + (1 - x) \cdot E_{XC}^{PBE}, \tag{2.24}$$

where x is an adjustable parameter that allows us to tune the performance of the functional in order to fit theoretical values of S_0 to a set of experimental results. Once the mixing parameter is identified, the SRP functional is tested and validated by simulating a different set of experimental data for the same system (more details are reported in Section 2.3).

The van der Waals interaction can be accounted for by replacing the PBE correlation functional present in PBE and RPBE by the vdW-DF correlation functional ($E_C^{\text{vdW-DF}}$) developed by Dion *et al.* [24, 25] and discussed in Section 2.2.3. This correlation functional has been shown to improve the description of weakly activated dissociation [28] while maintaining the same accuracy of [34], or improving the accuracy [7, 8] over that [33] achieved using Equation 2.24 for highly activated dissociation systems. Moreover, as mentioned before, the vdW-DF correlation functional is non-empirical being based on first principles [26]. The general formulation of the SRP functional used in most of the studies reported in this Thesis is based on a linear combination of the two GGA exchange functionals plus the vdW-DF correlation funtional:

$$E_{XC}^{SRP} = x \cdot E_{X}^{RPBE} + (1 - x) \cdot E_{X}^{PBE} + E_C^{\text{vdW-DF}}. \tag{2.25}$$

The SRP functional is constructed as much as possible [7] on the basis of non-empirical, constrained-based functionals (including the spin-scaling relationship,

the Lieb-Oxford bound, and the recovery of the uniform gas limit [18, 24] that should ensure applicability to metals [35]).

2.3 Semi-Empirical Strategy

The strategy and the steps needed to develop and test an SRP functional for a polyatomic molecule dissociating on a metal surface are reported in the following Sections. The discussion is mainly focused on the tri-deuterated methane molecule (CHD_3) which has been the center of most of the studies on which this Thesis is based. However, the same methodology should be applicable, in principle, to any molecule dissociating on a transition metal surface through σ-bond breaking [8].

The SRP functional used in most of the work reported in this Thesis has been developed by comparing an observable that depends on the minimum barrier height, the zero-coverage reaction probability (S_0), obtained from *ab initio* molecular dynamics (AIMD) calculations [9, 10] and from supersonic molecular beam experiments. For specific initial conditions, S_0 can be measured experimentally using the King and Wells beam reflectivity technique [36, 37] after a molecular beam impinges on an ideal low-index metal surface. The same quantity can then be obtained from the number of reacted molecules (N_{react}):

$$S_0 = N_{react}/N_{tot}, \tag{2.26}$$

in a set of N_{tot} AIMD trajectories where a single molecule impinges on the surface, prepared as described in Section 2.4 to accurately reproduce the experimental initial conditions.

AIMD allows the accurate simulation of dynamical processes within the framework of the Born-Oppenheimer approximation. This approximation assumes that, due to the different time scale, it is possible to separate the motion of the electrons from that of the nuclei, effectively treating the electrons as if they were moving in the potential generated by the nuclei. For each propagation step

the energy and the forces are evaluated on-the-fly at a DFT level without the need to fit a high dimensional Potential Energy Surface (PES), and then the positions of the ions are classically propagated according to Newton's equations of motion. Moreover the quasi-classical trajectory (QCT) approach can be exploited by imparting vibrational zero-point energy (ZPE) to the molecule. For the experimental conditions addressed in this Thesis, AIMD-QCT is the method of choice to effectively simulate molecular beam experiments and to test the validity of the semi-empirical SRP approach. The main reason to choose AIMD over a higher level of theory (i.e., quantum dynamics) [38, 39] is the possibility to include explicitly all the DOFs of the system in the simulation without any dynamical approximation. Not only is it possible to include all the molecular DOFs, but the surface atom motion, which is known to be important for the dissociation of polyatomic molecules (such as methane) on metal surfaces [40], is also accounted for. AIMD can also be extended to reactions affected by electron-hole pair excitation by including electronic friction [41].

The results of the AIMD simulations are compared with experimental results for a set of laser-off conditions (for which the initial molecular rovibrational distribution only depends on the nozzle temperature, see Section 2.4) and, through a trial and error procedure, the parameter x of Equation 2.25 is optimized until the AIMD results are in agreement with the experiments within chemical accuracy. The agreement between the results is verified by fitting the experimental data and by checking that, on average, the distance on the energy axis from the AIMD results to the experimental fit is smaller than 4.2 kJ/mol. Once chemical accuracy has been reached for the laser-off simulations, the candidate SRP functional is validated by simulating a different experiment for the same system. The SRP functional presented in this Thesis has been tested against state-resolved molecular beam experiments for which the molecules impinge on the surface after being selectively prepared in a specific rovibrational state through laser excitation.

In order to ensure a meaningful comparison between experiments and AIMD-QCT simulations, many aspects have to be considered, both on the experimental and on the theoretical side. First, the total energy of the molecule (translational

+ vibrational) has to be chosen above the minimum ZPE corrected barrier. This ensures the applicability of the QCT approach because under such conditions the reaction occurs in the classical "over-the-barrier" regime [9, 42]. Second, the molecular beams have to be produced using a nozzle temperature (T_n) as low as possible, for example by taking advantage of H_2 seeding, so that most of the molecules are in the vibrational ground state. This limits the deficiencies of the QCT method in describing the reactivity of coupled excited vibrational states (i.e., the CD vibrational states in CHD_3) due to artificial intramolecular vibrational energy redistribution (IVR) caused by the availability of resonant vibrations [7]. For the same reason the $\nu_1 = 1$ excited state of CHD_3 is a good choice to compare theoretical and experimental state selected reaction probabilities. This excited vibrational state possesses 95% of CH stretch character [43] and, due to the lack of Fermi resonances, energy imparted to this normal mode in the gas-phase remains localized on a time scale comparable with the collision time [7, 8, 44]. The reactivity of $\nu_1 = 1$ CHD_3 is therefore unlikely to be affected by IVR [9, 44]. Third, the surface temperature (T_s) has to be chosen well above the Debye temperature T_D of the metal bulk, which varies with the composition of the surface. At T_s larger than T_D quantum effects are not expected to significantly affect the molecule-surface energy exchange dynamics, making such conditions suitable for AIMD simulations. Specifically, for values of T_s higher than the Debye-Waller temperature the validity of a classical approach to dynamics calculations on scattering from a surface can be assessed by computing the argument to the Debye-Waller factor [45]:

$$2W = \frac{3p^2 T_s}{M_C k_b T_D^2}, \tag{2.27}$$

where p^2 is the average of the square of the change in momentum of a scattering molecule, M_C the mass of a surface atom and k_b the Boltzmann constant. Experience suggests that treating the surface vibrations classically works well for $T_s > T_D$ for values of $2W$ greater than 6 [46, 47] (note that $2W$ is a dimensionless quantity) and that under such conditions, the energy transfer to the surface

phonons should happen classically. Finally AIMD cannot be comfortably used to compute reaction probabilities smaller than 1%. This is due to the high computational cost of the method which, in light of present-day computational resources, limits the number of trajectories (N_{tot}) that can be used to simulate a single beam condition to $\approx$ 500-1000. This affects the accuracy of the results since the statistical error on S_0 representing the 68% confidence limits [48] depends on the reaction probability and on the total number of trajectories as:

$$\sigma_p = \sqrt{\frac{S_0(1 - S_0)}{N_{tot}}}. \tag{2.28}$$

This effectively reduces the statistical significance of low reaction probabilities computed with AIMD. However, once the SRP functional has been developed, in principle it is possible to couple it with an high dimensional PES approach that also describes the motion of the surface atoms (as demonstrated for N_2 + Ru(0001) [49]) allowing the accurate simulation of smaller S_0.

2.4 Initial Condition Sampling

In order to simulate a molecular beam experiment at an AIMD-QCT level it is important to accurately generate and sample the initial conditions of the system in order to have a fair comparison. In the work reported in this Thesis, we can distinguish between two classes of molecular beam experiments: laser-off and laser-on.

In laser-off experiments the molecules are accelerated according to the nozzle temperature (T_n) which defines the collision energy (E_i) distribution of the beam and the vibrational states as a Boltzmann distribution for that temperature. The rotational energy of the molecules is generally low as the number of intermolecular collisions during the expansion is high enough to dissipate it (rotational cooling). Therefore, in laser-off experiments, all the molecules are assumed to be in the rotational ground state. The experimental laser-off zero-coverage reactivity (S_0^{off}) can then be directly measured and so the molecules in the AIMD trajectories are

prepared to be randomly oriented, in the rotational ground state and sampling the experimental E_i distribution and all the vibrational states accessible at T_n.

In laser-on experiments an optical transition is used to excite molecules from an initial to a target rovibrational state and, since the laser excitation happens after the beam expansion (i.e., after rotational cooling), the molecules maintain the rotational excitation. A large fraction of the molecules is in the desired target state but a variety of other states are still present in the beam. However from the measured laser-on zero-coverage reaction probability (S_0^{on}) is possible to extract the reaction probability ($S_0^{\bar{\nu}}$) for the desired rovibrational state $\bar{\nu}$ once S_0^{off} is known for the same E_i [50]. This can be evaluated as:

$$S_0^{\bar{\nu}} = \frac{S_0^{on} - S_0^{off}}{f_{exc}} + S_0^{v=0}, \tag{2.29}$$

where f_{exc} is the excited fraction, or the fraction of the molecule in the beam excited to the target state, and $S_0^{v=0}$ is the reaction probability of the ground state. $S_0^{v=0}$ can usually be approximated by S_0^{off}, which does result in a small overestimation. Other methods to estimate $S_0^{v=0}$ are available but it has been shown that, for systems like the ones addressed in this Thesis, they all give very similar results [7]. Being able to directly extract $S_0^{\bar{\nu}}$ from the experiments simplifies the simulations because it allows one to prepare all the molecules in the desired $\bar{\nu}$ rovibrational state.

2.4.1 Molecular Beam

The initial conditions imparted to the projectile molecule need to accurately represent the experimental molecular beam that has to be modeled. In the experiments the molecules have a specific collision energy distribution and a specific rovibrational state associated with a defined angular momentum **L**.

First of all the molecular beams simulated are very narrow in translational energy but not monochromatic. In order to describe the distribution of energies (and velocities) $n(E_i)$ of the beam, Michelsen and Auerbach [51] proposed the

expression:

$$n(E_i)dE_i = \frac{1}{N} E_i \exp\left[-4E_s \frac{(\sqrt{E_i} - \sqrt{E_s})^2}{(\Delta E_s)^2} \right] dE_i, \tag{2.30}$$

where the energy spread ΔE_s is defined by:

$$\frac{\Delta E_s}{E_s} \equiv \frac{2\alpha}{v_s}. \tag{2.31}$$

Here the stream velocity v_s and the width of the velocity distributions α can be obtained by fitting time of flight measurements [52]. Once v_s and α are available, the initial collision energy for the molecules in the trajectories is selected by sampling the distribution $n(E_i)$.

In order to prepare the molecule in the desired vibrational state the potential energy V_ν along each vibrational mode needs to be known. The vibrational modes can be obtained using finite differences as the eigenvectors of the mass-weighted Hessian and for each of them a one-dimensional potential is computed by displacing the molecule along the mode itself. This interpolation can be performed just once for each mode before preparing the whole set of molecules. Once the V_ν potentials are available the molecule can be prepared in the desired vibrational state.

In order to prepare a set of molecules in a target vibrational state (e.g., H_2O in ν_1=1, ν_2=0, ν_3=0), one can perform a classical micro-canonical sampling for each mode of each molecule in the set. This is done by running a 1D quasi-classical dynamics simulation along each mode using the energy associated with the state we want to generate and then by randomly selecting the initial velocity ($\boldsymbol{v}_{vib}$) and displacement from the equilibrium positions ($\boldsymbol{\delta q}_{vib}$) from it (i.e., randomly selecting the phase of the vibration). The sum of the displacements and the velocities for all the modes is assigned to the molecule to prepare it in the target vibrational state. It is important to note that, since we sample the initial position classically along the vibrational modes and in the time domain, when we average over many generated molecules prepared in a given vibrational state we obtain

a classical distribution where the molecule has a higher probability to sit close to one of the turning points. Note that applying the shift $\boldsymbol{\delta q}_{vib}$ results in a small change in the inertia of the system and introduces small spurious rotational velocities which are computed and removed. If this correction changes the energy along the normal modes by more than 1 meV, the initial conditions are discarded and generated again from the beginning.

As mentioned before, molecules in the rotational ground state can be initially randomly oriented while, for the rotationally excited molecules, the quantization of the angular momentum $\mathbf{L}$ and the quantization of its projections on a space-fixed axis and on a body-fix axis translate into constraints on the initial orientation effectively aligning the molecule.

Within the rigid rotor approximation, the projection of $\mathbf{L}$ on the reference frame z axis depends only on the choice of the reference frame itself while the projection on the molecular rotational axis depends on the geometry of the molecule. The principal rotational axis of a rigid rotor (here called a, b and c) and the associated moments of inertia (labeled I_A, I_B and I_C from the smallest to the largest) can be obtained from the eigenvectors and the eigenvalues of the inertia tensor $\mathbf{I}$, respectively. Rigid rotors can be divided to four categories: linear, symmetric, spherical and asymmetric according to the moments of inertia. For a linear rotor, as the H_2 molecule, $I_A << I_B = I_C$. Symmetric rotors can be divided to oblate symmetric top (e.g. benzene) for which $I_A = I_B < I_C$ and prolate symmetric top (e.g. methyl-acetate $CH_3C{\equiv}CH$) for which $I_A < I_B = I_C$. Finally spherical top rotors (e.g. CH_4) shows $I_A = I_B = I_C$ and asymmetric top rotors (e.g. HOD) $I_A < I_B < I_C$. In the following paragraphs the procedure to generate a sample of molecules in a rotationally aligned state is described in detail for an oblate symmetric top molecule as the methane isotopologue CHD_3. A few details will be also given on how to proceed for an asymmetric top molecule like partially deuterated water (HOD).

Considering an oblate top molecule like CHD_3, the principal axis (c), associated with the largest moment of inertia I_C, runs through the H atom, the C atom and through the geometrical center of the CD_3 umbrella (Figure 2.1A). The axes

a and b lay in the plane perpendicular to c and are associated with I_A and I_B which are smaller than I_C and of the same magnitude. For CHD_3 a rotational state is defined by the angular momentum $\mathbf{L}$, by its magnitude:

$$\mid \mathbf{L} \mid = \hbar\sqrt{J(J+1)}, \tag{2.32}$$

by its projections on the reference frame z axis:

$$J_z = \hbar M, \tag{2.33}$$

and by its projection on the principal axis c:

$$J_c = \hbar K. \tag{2.34}$$

Here M and K are integers in the range $[-J,+J]$. When the classical analogue of a rotational state is prepared, these projections add constraints to the orientation of the molecules resulting in a certain degree of alignment among the molecules of the sample.

The CHD_3 molecule can be prepared in a given (J, M, K) state according to the following procedure:

- The molecule in its equilibrium geometry is aligned with the principal axis c parallel to the reference frame z which is chosen to be normal to the surface on which the molecule will impinge (Figure 2.1A).
- The rotation in α_1 around the principal axis, which is the first unconstrained degree of freedom, is randomly sampled (Figure 2.1B).
- In order to achieve the projection $\hbar K$ of $\mathbf{L}$ on the principal axis c, the molecule is rotated by:

$$\beta = \cos^{-1}\left(\frac{K}{\sqrt{J(J+1)}}\right). \tag{2.35}$$

Note that the angular momentum $\mathbf{L}$ is still assumed to be aligned with z

(Figure 2.1C).

- The second unconstrained degree of freedom is sampled by randomly fixing the orientation of the principal axis c with respect to the angular momentum $\mathbf{L}$ through the angle α_2 while keeping the projection of $\mathbf{L}$ on c constant (Figure 2.1D).

- The projection $\hbar M$ of the angular momentum $\mathbf{L}$ on the reference frame axis z is then defined, as shown in Figure 2.1E, by rotating both the molecule and the angular momentum by:

$$\phi = \cos^{-1}\left(\frac{M}{\sqrt{J(J+1)}}\right). \tag{2.36}$$

- The last unconstrained degree of freedom is fixed by randomly orienting $\mathbf{L}$ with respect to the reference frame axis z through the rotation α_3 while keeping the projection of $\mathbf{L}$ on z constant. Note that the same random rotation around z is applied to both the angular momentum and the molecule (Figure 2.1F).

- Once the orientation of the molecule and of the angular momentum have been fixed, the rotational component of the velocity $\boldsymbol{v}_{rot}$ can be computed from:

$$\mathbf{L} = \mathbf{I}\,\boldsymbol{\omega}_{rot}, \tag{2.37}$$

$$\boldsymbol{v}_{rot} = \boldsymbol{\omega}_{rot} \times \boldsymbol{q}, \tag{2.38}$$

  where $\mathbf{I}$ is the inertia tensor, $\boldsymbol{\omega}_{rot}$ is the rotational velocity and $\boldsymbol{q}$ is the vector of the coordinates.

Finally, the total velocity $\boldsymbol{v}$ and the position $\boldsymbol{q}$ of each atom of the molecule can be assigned as:

$$\boldsymbol{v} = \boldsymbol{v}_{trans} + \boldsymbol{v}_{rot} + \boldsymbol{v}_{vib}, \tag{2.39}$$

$$\boldsymbol{q} = \mathbf{R}\left(\boldsymbol{q}_0 + \boldsymbol{\delta q}_{vib}\right)_i, \tag{2.40}$$

where $\mathbf{R}$ is the rotational matrix that aligns the molecule as described above, $\boldsymbol{q}_0$ is the equilibrium positions of the atoms with the molecular COM in the origin of the coordinate system and $\boldsymbol{\delta q}_{vib}$ is the sum of the displacements used to impart the vibrational energy. Note that the rotational and the vibrational velocities need to be rotated according to $\mathbf{R}$ as well. When the molecule is prepared in the desired rovibrational state, it can then be translated to its initial position above the metal surface.

The same strategy can be applied to different molecules considering that a different kind of rotor will introduce different constraints on the initial orientation. For an asymmetric rotor as HOD in our approximate representation, a rotational state is characterized by 4 "quantum numbers": (J, M, K_a, K_c). Here J, M, and K_c are the same as observed for CHD_3 and control the magnitude of $\mathbf{L}$, its projection on z and on the principal axis, respectively. The additional K_a number is related to the projection on another molecular axis and adds an extra constraint on the initial orientation, reducing to 2 the number of randomly sampled DOFs (see Chapter 7).

2.4.2 van der Waals Functionals and Residual Energy

When a vdW correlation functional is used the simulation box needs to be big enough to accommodate the large amount of vacuum between the slab and its 1st periodic image ($\approx$ 30 Å) necessary to converge the long range interaction. However, it has been shown for CHD_3 on Ni(111) [7] and on platinum [8] that, to a very good approximation, using a smaller amount of vacuum (e.g., 13 Å instead of a well-converged value of 30 Å) affects the energy of the system only as a small upwards shift of the gas-phase level, due to residual interaction with the slab periodic replica, as sketched in Figure 2.2. The residual energy (E_R) is defined as the difference between the energy of the molecule placed away from the surface, i.e. where it sits at the beginning of the simulations (typically 6 Å), in the cell

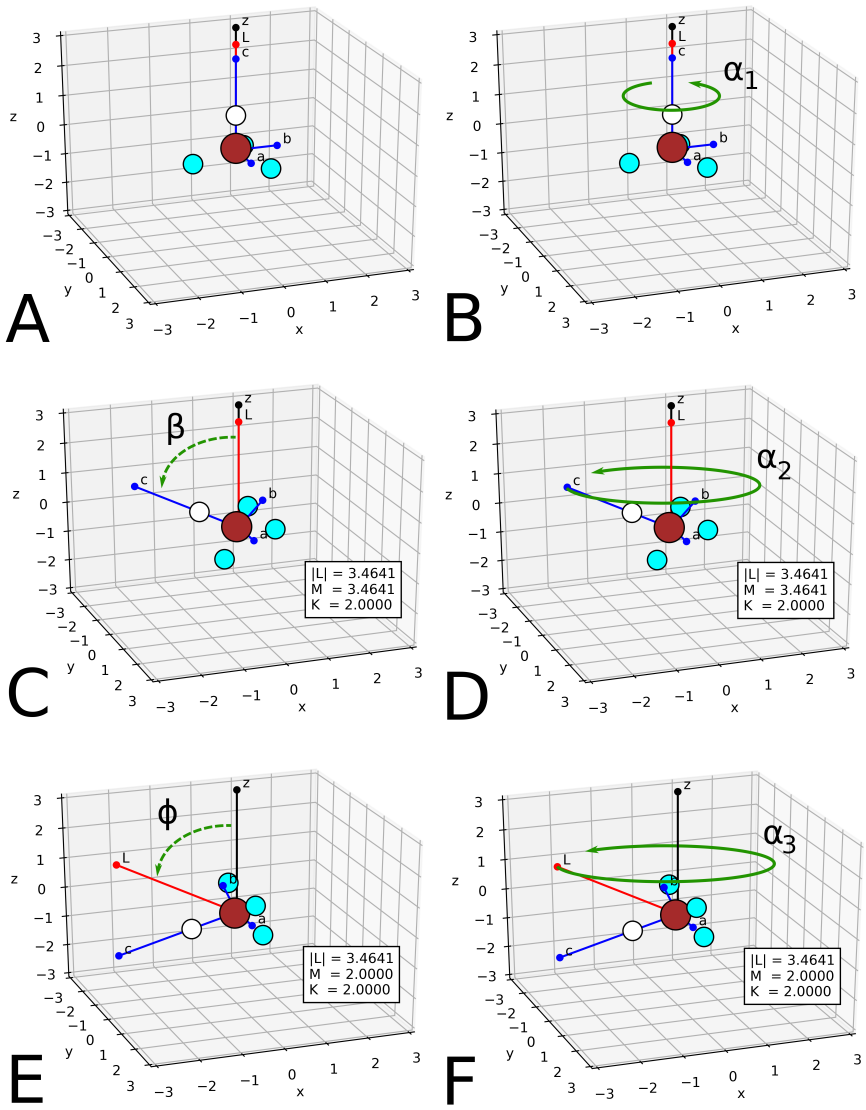

Figure 2.1: Scheme of the rotations needed to prepare the CHD_3 molecule in a generic aligned rotational state ($J = 3$, $M = 2$, $K = 2$). The carbon atom is reported in brown, the hydrogen in white and the deuteriums in light blue. The reference frame axis z is reported in black and the molecular axes a, b and c are reported in blue. The angular momentum $\mathbf{L}$ is indicated in red. Dashed green arrows indicate rotations to obtain the correct projections of $\mathbf{L}$ and full green arrows indicate rotations that are sampled randomly. The values on the axes are reported in Å and $|\mathbf{L}|$ is in atomic units.

with 13 Å and in the one with 30 Å of vacuum:

$$E_R = E^{13\text{Å}}_{Z=6\text{Å}} - E^{30\text{Å}}_{Z=6\text{Å}} \approx \Delta E_b = E_b^{13\text{Å}} - E_b^{30\text{Å}}. \tag{2.41}$$

In order to validate this approximation, E_R has to be the same as the difference in the minimum barrier height (ΔE_b) computed with the two cell sizes ($E_b^{13\text{Å}}$ and $E_b^{30\text{Å}}$, respectively) to within much better than chemical accuracy. In order to correct for the residual interaction in the AIMD simulations the molecules can be assigned an extra translational energy equal to E_R which depends on the system investigated and it is usually on the order of a few of kJ/mol [7, 8, 53]. By imparting this excess energy, the molecules experience an effective barrier (E_b^e) that is approximately equal to the converged barrier height:

$$E_b^e = E_b^{13\text{Å}} - E_R \approx E_b^{30\text{Å}}. \tag{2.42}$$

This implies that the energy barrier converged for the amount of vacuum can be obtained by subtracting E_R from the non-converged barrier. Similarly, the adsorption energies (see Figure 2.2) obtained with the non-converged setup need to be increased by E_R.

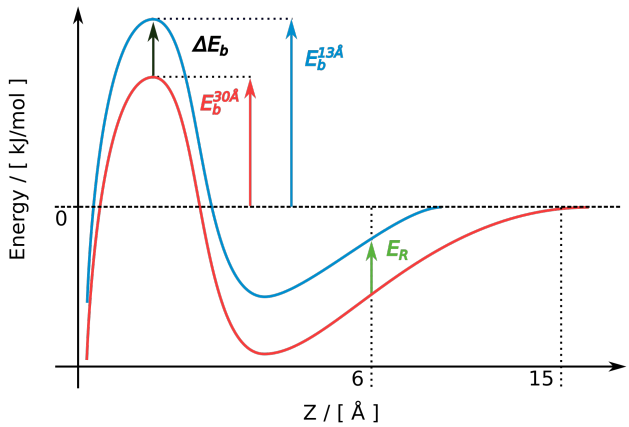

Figure 2.2: Sketch of the barriers considered for a molecule on a metal surface when using a long range functional. The blue and the red curves refer to the 13 Å and to the 30 Å setup, respectively. The barrier heights are shown as arrows in the same color as the related curve. The residual energy (E_R) is reported as a green arrow and the barrier height difference between the two vacuum sizes (ΔE_b) is reported as a black arrow.

2.4.3 Metal Surface Temperature

Since AIMD allows us to treat explicitly all the degrees of freedom, it is important to accurately represent the experimental surface temperature (T_s). Initial velocities and displacements are randomly generated and assigned to the surface atoms according to their vibrational frequencies and sampling a Boltzmann distribution for the desired temperature. This is done by approximating each atom as an independent harmonic oscillator with kinetic energy $K = \frac{1}{2}mv^2$ and potential energy $V = \frac{1}{2}kq^2$.

From the Boltzmann distribution in energy space $f(E)$:

$$f(E) = A\exp(-E/k_bT), \tag{2.43}$$

where k_b is the Boltzmann constant and T is the temperature, we can derive the distributions in the velocity $f(v)$ and in the position $f(q)$ using the expression of K and V and obtaining A as normalization constant:

$$f(v) = \left[\frac{m}{2\pi k_bT}\right]^{\frac{1}{2}} \exp\left(-\frac{mv^2}{2k_bT}\right), \tag{2.44}$$

$$f(q) = \left[\frac{m\omega^2}{2\pi k_b T} \right]^{\frac{1}{2}} \exp\left(- \frac{m\omega^2 q^2}{2k_b T} \right). \tag{2.45}$$

From here it is straightforward to show that $f(v)$ can be rewritten as a Gaussian distribution centered in $\bar{v} = 0$ and with a standard deviation $\sigma_v = \sqrt{\frac{k_b T}{m}}$:

$$f(v \mid \bar{v}, \sigma_v) = \frac{1}{\sqrt{2\pi\sigma_v^2}} \exp\left(- \frac{(v - \bar{v})^2}{2\sigma_v^2} \right). \tag{2.46}$$

Similarly a Gaussian distribution $f(q \mid \bar{q}, \sigma_q)$ centered on $\bar{q} = 0$ and with $\sigma_q = \sqrt{\frac{k_b T}{m\omega^2}}$ can be derived for the positions. Here ω can be taken as the vibrational frequency of a surface atom computed by finite differences.

For each atom a random velocity and position are selected in order to sample these Gaussian distributions for the desired surface temperature T_s. This approximation neglects all kind of coupling and therefore, in order to achieve a sound physical description of the surface at the desired temperature, the slab needs to be equilibrated by performing a standard AIMD propagation for 2 ps. Finally any step among the last ps of equilibration can be chosen as initial condition for the trajectories.

Bibliography

[1] C. Stegelmann, A. Andreasen, and C. T. Campbell, "Degree of Rate Control: How Much the Energies of Intermediates and Transition States Control Rates," *J. Am. Chem. Soc.*, vol. 131, pp. 8077–8082, 2009.

[2] G. J. Kroes, "Six-Dimensional Quantum Dynamics of Dissociative Chemisorption of H_2 on Metal Surfaces," *Prog. Surf. Sci.*, vol. 60, pp. 1–85, 1999.

[3] G. J. Kroes, "Toward a Database of Chemically Accurate Barrier Heights for Reactions of Molecules with Metal Surfaces," *J. Phys. Chem. Lett.*, vol. 6, pp. 4106–4114, 2015.

[4] C. Díaz, E. Pijper, R. A. Olsen, H. F. Busnengo, D. J. Auerbach, and G. J. Kroes, "Chemically Accurate Simulation of a Prototypical Surface Reaction: H_2 Dissociation on Cu(111)," *Science*, vol. 326, pp. 832–834, 2009.

[5] L. Sementa, M. Wijzenbroek, B. J. van Kolck, M. F. Somers, A. Al-Halabi, H. F. Busnengo, R. A. Olsen, G. J. Kroes, M. Rutkowski, C. Thewes, N. F. Kleimeier, and H. Zacharias, "Reactive Scattering of H_2 from Cu(100): Comparison of Dynamics Calculations Based on the Specific Reaction Parameter Approach to Density Functional Theory with Experiment," *J. Chem. Phys.*, vol. 138, p. 044708, 2013.

[6] E. Nour Ghassemi, M. Wijzenbroek, M. F. Somers, and G. J. Kroes, "Chemically Accurate Simulation of Dissociative Chemisorption of D_2 on Pt(111)," *J. Chem. Phys. Lett.*, vol. 683, pp. 329–335, 2017.

[7] F. Nattino, D. Migliorini, G. J. Kroes, E. Dombrowski, E. A. High, D. R. Killelea, and A. L. Utz, "Chemically Accurate Simulation of a Polyatomic Molecule-Metal Surface Reaction," *J. Phys. Chem. Lett.*, vol. 7, pp. 2402–2406, 2016.

[8] D. Migliorini, H. Chadwick, F. Nattino, A. Gutiérrez-González, E. Dombrowski, E. A. High, H. Guo, A. L. Utz, B. Jackson, R. D. Beck, and G. J.

Kroes, "Surface Reaction Barriometry: Methane Dissociation on Flat and Stepped Transition-Metal Surfaces," *J. Phys. Chem. Lett.*, vol. 8, pp. 4177–4182, 2017.

[9] F. Nattino, H. Ueta, H. Chadwick, M. E. van Reijzen, R. D. Beck, B. Jackson, M. C. van Hemert, and G. J. Kroes, "Ab Initio Molecular Dynamics Calculations versus Quantum-State-Resolved Experiments on CHD_3+Pt(111): New Insights into a Prototypical Gas–Surface Reaction," *J. Phys. Chem. Lett.*, vol. 5, pp. 1294–1299, 2014.

[10] A. Groß and A. Dianat, "Hydrogen Dissociation Dynamics on Precovered Pd Surfaces: Langmuir is still Right," *Phys. Rev. Lett.*, vol. 98, p. 206107, 2007.

[11] P. Hohenberg and W. Kohn, "Inhomogeneous Electron Gas," *Phys. Rev.*, vol. 136, pp. B864–B871, 1964.

[12] W. Kohn and L. J. Sham, "Self-Consistent Equations Including Exchange and Correlation Effects," *Phys. Rev. B*, pp. A1133–A1138, 1965.

[13] P. E. Blöchl, "Projector Augmented Wave-Method," *Phys. Rev. B*, vol. 50, pp. 17953–17979, 1994.

[14] G. Kresse and D. Joubert, "From Ultrasoft Pseudopotentials to the Projector Augmented-Wave Method," *Phys. Rev. B*, vol. 59, pp. 1758–1775, 1999.

[15] F. Bloch, "Bemerkung zur Elektronentheorie des Ferromagnetismus und der elektrischen Leitfähigkeit," *Z. Phys.*, vol. 57, pp. 545–555, 1929.

[16] P. A. M. Dirac, "Note on Exchange Phenomena in the Thomas Atom," *Math. Proc. Camb. Philos. Soc.*, vol. 26, pp. 376–385, 1930.

[17] D. M. Ceperley and B. J. Alder, "Ground-State of the Electron-Gas by a Stochastic Method," *Phys. Rev. Lett.*, vol. 45, pp. 566–569, 1980.

[18] J. P. Perdew, K. Burke, and M. Ernzerhof, "Generalized Gradient Approximation Made Simple," *Phys. Rev. Lett.*, vol. 77, pp. 3865–3868, 1996.

[19] J. P. Perdew, K. Burke, and M. Ernzerhof, "Erratum: Generalized Gradient Approximation Made Simple," *Phys. Rev. Lett.*, vol. 78, p. 1396, 1997.

[20] B. Hammer, L. B. Hansen, and J. K. Nørskov, "Improved Adsorption Energetics Within Density-Functional Theory Using Rrevised Perdew-Burke-Ernzerhof Functionals," *Phys. Rev. B*, vol. 59, pp. 7413–7421, 1999.

[21] A. Tkatchenko, "Current Understanding of van der Waals Effects in Realistic Materials," *Adv. Funct. Mater.*, vol. 25, pp. 2054–2061, 2015.

[22] V. G. Ruiz, W. Liu, E. Zojer, M. Scheffler, and A. Tkatchenko, "Density-Functional Theory with Screened van der Waals Interactions for the Modeling of Hybrid Inorganic-Organic Systems," *Phys. Rev. Lett.*, vol. 108, p. 146103, 2012.

[23] F. Furche, "Molecular Tests of the Random Phase Approximation to the Exchange-Correlation Energy Functional," *Phys. Rev. B.*, vol. 64, p. 195120, 2001.

[24] M. Dion, H. Rydberg, E. Schröder, D. C. Langreth, and B. I. Lundqvist, "Van der Waals Density Functional for General Geometries," *Phys. Rev. Lett.*, vol. 92, p. 246401, 2004.

[25] G. Román-Pérez and J. M. Soler, "Efficient Implementation of a van der Waals Density Functional: Application to Double-Wall Carbon Nanotubes," *Phys. Rev. Lett.*, vol. 103, p. 096102, 2009.

[26] K. Berland, V. R. Cooper, K. Lee, E. Schroeder, T. Thonhauser, P. Hyldgaard, and B. I. Lundqvist, "van der Waals Forces in Density Functional Theory: a Review of the vdW-DF Method," *Rep. Prog. Phys.*, vol. 78, p. 066501, 2015.

[27] Y. Y. Chuang, M. L. Radhakrishnan, P. L. Fast, C. J. Cramer, and D. G. Truhlar, "Direct Dynamics for Free Radical Kinetics in Solution: Solvent Effect on the Rate Constant for the Reaction of Methanol with Atomic Hydrogen," *J. Phys. Chem. A*, vol. 103, pp. 4893–4909, 1999.

[28] M. Wijzenbroek and G. J. Kroes, "The Effect of the Exchange-Correlation Functional on H_2 Dissociation on Ru(0001)," *J. Chem. Phys.*, vol. 140, p. 084702, 2014.

[29] P. M. Hundt, B. Jiang, M. E. van Reijzen, H. Guo, and R. D. Beck, "Vibrationally Promoted Dissociation of Water on Ni(111)," *Science*, vol. 344, pp. 504–507, 2014.

[30] F. Nattino, C. Díaz, B. Jackson, and G. J. Kroes, "Effect of Surface Motion on the Rotational Quadrupole Alignment Parameter of D_2 Reacting on Cu(111)," *Phys. Rev. Lett.*, vol. 108, p. 236104, 2012.

[31] P. Nieto, D. Farías, R. Miranda, M. Luppi, E. J. Baerends, M. F. Somers, M. J. T. C. van der Niet, R. A. Olsen, and G. J. Kroes, "Diffractive and Reactive Scattering of H_2 from Ru(0001): Experimental and Theoretical Study," *Phys. Chem. Chem. Phys.*, vol. 13, pp. 8583–8597, 2011.

[32] I. M. N. Groot, H. Ueta, M. J. T. C. van der Niet, A. W. Kleyn, and L. B. F. Juurlink, "Supersonic Molecular Beam Studies of Dissociative Adsorption of H_2 on Ru(0001)," *J. Chem. Phys.*, vol. 127, p. 244701, 2007.

[33] F. Nattino, D. Migliorini, M. Bonfanti, and G. J. Kroes, "Methane Dissociation on Pt(111): Searching for a Specific Reaction Parameter Density Functional," *J. Chem. Phys.*, vol. 144, p. 044702, 2016.

[34] M. Wijzenbroek, D. M. Klein, B. Smits, M. F. Somers, and G. J. Kroes, "Performance of a Non-Local van der Waals Density Functional on the Dissociation of H_2 on Metal Surfaces," *J. Phys. Chem. A*, vol. 119, pp. 12146–12158, 2015.

[35] J. P. Perdew, A. Ruzsinszky, J. M. Tao, V. N. Staroverov, G. E. Scuseria, and G. I. Csonka, "Prescription for the Design and Selection of Density Functional Approximations: More constraint Satisfaction with Fewer Fits," *J. Chem. Phys.*, vol. 123, p. 062201, 2005.

[36] H. Chadwick, A. Gutiérrez-González, and R. D. Beck, "Quantum State Resolved Molecular Beam Reflectivity Measurements: CH_4 Dissociation on Pt(111)," *J. Chem. Phys.*, vol. 145, p. 174707, 2016.

[37] D. A. King and M. G. Wells, "Molecular-Beam Investigation of Adsorption Kinetics on Bulk Metal Targets - Nitrogen on Tungsten," *Surf. Sci.*, vol. 29, pp. 454–482, 1972.

[38] B. Jiang, R. Liu, J. Li, D. Q. Xie, M. H. Yang, and H. Guo, "Mode Selectivity in Methane Dissociative Chemisorption on Ni(111)," *Chem. Sci.*, vol. 4, pp. 3249–3254, 2013.

[39] A. Farjamnia and B. Jackson, "The Dissociative Chemisorption of Water on Ni(111): Mode- and Bond-Selective Chemistry on Metal Surfaces," *J. Chem. Phys.*, vol. 142, p. 234705, 2015.

[40] S. Nave and B. Jackson, "Methane Dissociation on Ni(111): The Role of Lattice Reconstruction," *Phys. Rev. Lett.*, vol. 98, p. 173003, 2007.

[41] M. Blanco-Rey, J. I. Juaristi, R. Díez Muiño, H. F. Busnengo, G. J. Kroes, and M. Alducin, "Electronic Friction Dominates Hydrogen Hot-Atom Relaxation on Pd(100)," *Phys. Rev. Lett.*, vol. 112, p. 103203, 2014.

[42] B. Jackson and S. Nave, "The Dissociative Chemisorption of Methane on Ni(100): Reaction Path Description of Mode-Selective Chemistry," *J. Chem. Phys.*, vol. 135, p. 114701, 2011.

[43] X. G. Wang and E. L. Sibert, "A Nine-Dimensional Perturbative Treatment of the Vibrations of Methane and its Isotopomers," *J. Chem. Phys.*, vol. 111, pp. 4510–4522, 1999.

[44] G. Czako and J. M. Bowman, "Dynamics of the Reaction of Methane with Chlorine Atom on an Accurate Potential Energy Surface," *Science*, vol. 334, pp. 343–346, 2011.

[45] J. R. Manson, "Energy Transfer to Phonons in Atom and Molecule Collisions with Surfaces," in *Handbook of Surface Science* (E. Hasselbrink and B. I. Lundqvist, eds.), vol. 3, pp. 53–93, Elsevier, 2008.

[46] J. R. Manson, "Inelastic-Scattering from Surfaces," *Phys. Rev. B*, vol. 43, pp. 6924–6937, 1991.

[47] J. R. Manson, "Multiphonon Atom-Surface Scattering," *Comput. Phys. Commun.*, vol. 80, pp. 145–167, 1994.

[48] W. L. Hays, *Statistics, 3rd edn.* Holt: Rinehart and Winston, 1981.

[49] K. Shakouri, J. Behler, J. Meyer, and G. J. Kroes, "Accurate Neural Network Description of Surface Phonons in Reactive Gas-Surface Dynamics: N_2 + Ru(0001)," *J. Phys. Chem. Lett.*, vol. 8, pp. 2131–2136, 2017.

[50] L. B. F. Juurlink, D. R. Killelea, and A. L. Utz, "State-Resolved Probes of Methane Dissociation Dynamics," *Progr. Surf. Sci.*, vol. 84, pp. 69–134, 2009.

[51] H. A. Michelsen and D. J. Auerbach, "A Critical Examination of Data on the Dissociative Adsorption and Associative Desorption of Hydrogen at Copper Surfaces," *J. Chem. Phys.*, vol. 94, pp. 7502–7520, 1991.

[52] H. Chadwick, A. Gutiérrez-González, D. Migliorini, R. D. Beck, and G. J. Kroes, "Incident Angle Dependence of CHD_3 Dissociation on the Stepped Pt(211) Surface," *J. Phys. Chem. C*, vol. 122, pp. 19652–19660, 2018.

[53] D. Migliorini, F. Nattino, A. K. Tiwari, and G. J. Kroes, "HOD on Ni(111): Ab Initio Molecular Dynamics Prediction of Molecular Beam Experiments," *J. Chem. Phys.*, vol. 149, p. 244706, 2018.

Chapter 3

Application of van der Waals Functionals to the Calculation of Dissociative Adsorption of N_2 on W(110) for Static and Dynamic Systems

This Chapter is based on:

D. Migliorini, F. Nattino, and G. J. Kroes, *J. Chem. Phys.*, 144, 084702 (2016)
which is reproduced with the permission of AIP publishing.

Abstract

The fundamental understanding of molecule-surface reactions is of great importance to heterogeneous catalysis, motivating many theoretical and experimental studies. Even though much attention has been dedicated to the dissociative chemisorption of N_2 on tungsten surfaces, none of the existing theoretical models has been able to quantitatively reproduce experimental reaction probabilities for the sticking of N_2 on W(110). In this Chapter, the dissociative chemisorption of

N_2 on W(110) has been studied with both static electronic structure and *ab initio* molecular dynamics (AIMD) calculations including the surface temperature effects through surface atom motion. Calculations have been performed using density functional theory (DFT), testing functionals that account for the long range van der Waals (vdW) interactions, which were previously only considered in dynamical calculations within the static surface approximation. The vdW-DF2 functional improves the description of the potential energy surface for N_2 on W(110), returning less deep molecular adsorption wells and a better ratio between the barriers for the indirect dissociation and the desorption, as suggested by previous theoretical work and experimental evidence. Using the vdW-DF2 functional less trapping-mediated dissociation is obtained compared to results obtained with standard semi-local functionals such as PBE and RPBE, improving agreement with experimental data at $E_i = 0.9$ eV. However, at $E_i = 2.287$ eV and off-normal incidence, the vdW-DF2 AIMD underestimates the experimental reaction probabilities, showing that also with the vdW-DF2 functional the N_2 on W(110) interaction is not yet described with quantitative accuracy.

3.1 Introduction

Heterogeneous catalysis plays an important role in many industrial processes [1, 2]. Many experimental and theoretical studies have been performed in order to improve the fundamental understanding of molecular reactions on metal surfaces, since this knowledge can help with the development of more efficient catalysts. Among the industrial processes that make use of heterogeneous catalysis, one of the most important is the Haber-Bosch process that is used to produce ammonia from the reaction of N_2 and H_2 on an iron based catalyst [3]. The dissociation of N_2, catalyzed by the metal surface, is believed to be the rate-determining step of the whole process [3] motivating the interest for this reaction step. The dissociation probability of N_2 on an iron single crystal surface shows a clear dependence on the crystallographic face of the metal on which the reaction occurs [4]. Similarly, tungsten surfaces show a high crystallographic anisotropy

of the nitrogen dissociation probability (S_0): it is known, from molecular beam experiments, that for low collision energies (E_i) the W(100) surface is roughly two orders of magnitude more reactive than the W(110) surface [5]. The observed non-zero reaction probability of N_2 on W(100) for vanishing E_i suggested that, on this surface, non-activated paths for the dissociation exist [6, 7]. For N_2 on W(110) [7, 8] the measured reaction probability is almost zero (i.e., $\approx 10^{-3}$) at low E_i and increases with increasing collision energy, which suggested an activated mechanism for the dissociative chemisorption. The similarity of N_2 on W and the catalytically more relevant Fe surface (the crystallographic anisotropy of the N_2 dissociation) has prompted many studies on N_2 dissociation on W surfaces. Even though much attention has been dedicated to the theoretical study of the dissociative chemisorption of N_2 on tungsten surfaces, none of the existing models has been able to quantitatively reproduce experimental reaction probabilities for the sticking of N_2 to W(110).

Although the experimental S_0 curve shape suggests an activated reaction path, in previous work Alducin *et al.* [9, 10] achieved a qualitative description of the dissociation probability of N_2 on W(110) through molecular dynamics calculations performed on a potential energy surface (PES) that also included non-activated paths for dissociation. Alducin *et al.* [9, 10] and Bocan *et al.* [11] computed the reaction probability on two PESs calculated with DFT at the generalized gradient approximation (GGA) level, using the PW91 [12, 13] functional and the RPBE functional [14], respectively. These dynamical calculations used the ideal static surface approximation. Mixed results have been obtained using these two functionals: using the more repulsive RPBE functional good agreement with experimental results was found for normal incidence ($\Theta_i = 0°$), but the reaction probability at $\Theta_i = 60°$ was underestimated. The PW91 functional returned good agreement with experimental data for $\Theta_i = 60°$ but it failed at describing experiments at normal incidence, with the reaction probability being too high at low E_i. The results showed that the dissociative chemisorption of N_2 on W(110) is very sensitive to the "shape" of the PES, which determines to what extent the minimum energy paths (MEPs) for dissociation are accessible

to the impinging molecules. The results also showed that, in the framework of DFT, the theoretical S_0 strongly depends on the exchange-correlation functional (E_{XC}) chosen for the electronic structure calculations. To explain their results, the authors [15] suggested that the PW91 functional describes the interaction of N_2 with W(110) less accurately close to the surface, where the dissociation occurs. They also suggested that further away from the surface this interaction is described as too repulsive with the RPBE PES, which could explain that this PES underestimates the reactivity at off-normal incidence. Alducin and coworkers arrived at similar conclusions in work on non-reactive scattering of N_2 from W(110), which also suggested that the molecule-surface interaction obtained with the PW91 functional is too corrugated [15].

The importance of modeling surface atom motion for this reaction was demonstrated [15] with AIMD calculations, testing both the RPBE and the PBE [16] functionals. Using the PBE functional (which is similar [16] to the PW91 functional [12, 13] used in Ref. [10]) the reaction probability at normal incidence and $E_i = 0.9$ eV is even larger than for the static surface calculations using PW91. This is because the large amount of energy transferred from the impinging molecules to the surface phonons stabilizes molecules trapped on the surface, thereby enhancing the contribution of a trapping-mediated dissociation mechanism to the reactivity. The RPBE functional gives a better agreement with the experiment for $E_i = 0.9$ eV at normal incidence. The AIMD reaction probabilities computed with PBE and RPBE showed little dependence on E_i, in disagreement with experiments. The authors suggested that the reason of this discrepancy is that both the PBE and the RPBE functionals return too deep molecular adsorption wells. The authors also showed that surface atom motion and energy exchange with the surface cannot be neglected in modeling the dissociation of N_2 on W(110). Especially for the PBE functional, the work showed that inclusion of surface motion may change the reaction probability curve in a qualitative fashion, leading to changes in how the reaction probability depends on incidence energy, and indicating that a verdict on the accuracy of the functional used to describe the interaction should be based on a comparison of accurate

experiments to calculations modeling surface motion accurately.

In order to further improve the theoretical description of N_2 on W(110) Martin-Gondre *et al.* tested different functionals that account for the vdW interaction [17]. The authors performed a static study of some vdW functionals and computed the reaction probability for a few energies with AIMD in the frozen surface approximation (AIMD-FS). Some of the functionals studied improve the static properties of the PES, giving less deep molecular adsorption wells and returning barriers for the desorption and for the dissociation from the molecular adsorption states closer to each other than found with semi-local functionals, in better agreement with experimental evidence [18]. However, the dissociation probabilities calculated with AIMD-FS using the vdW functionals considered did not show better agreement with experiments than the previously used semi-local functionals (i.e., PBE and RPBE).

Two of the most promising functionals that were identified through static calculations are the vdW-DF [19] and the vdW-DF2 [20] functionals. The latter, which has not been tested yet in dynamic simulations, is particularly interesting regarding the depth of the molecular adsorption wells and the balance between desorption and dissociation of N_2 from these wells. On the other hand the vdW-DF2 functional shows high barriers for the direct dissociation, which are located far from the surface, just like the RPBE functional. Therefore the vdW-DF2 functional might provide a good description of the reaction at normal incidence. Moreover the attractive long-range van der Waals interactions might improve the agreement with experiments at off-normal incidence.

Here we have extended the static analysis of the N_2+W(110) PES also considering other molecular adsorption minima [15] than considered in Ref. [17] and testing both the vdW-DF and the vdW-DF2 functionals. We have also performed AIMD calculations for N_2 impinging on the W(110) surface using the vdW-DF2 functional, simultaneously accounting for both the effect of the long range vdW interactions and the effect of surface atom motion on the dissociation probability. Our work is part of a larger effort to construct semi-empirical density functionals for a range of molecule-metal surface systems, with the ultimate aim of construct-

ing a database of chemically accurate reaction barriers for these systems [21].

We found that, even though the vdW-DF2 functional seems to return a PES that is in better agreement with the experimental evidence than the PBE and RPBE functionals, in the sense that barriers of more similar height are found for molecular desorption and dissociative chemisorption starting from the molecular chemisorption well [18], AIMD calculations using this functional still fail at quantitatively reproducing the molecular beam experiments. As for the previously tested semi-local functionals [15], the vdW-DF2 functional returns almost flat reaction probability curves, showing little dependence on incidence energy.

The overall performance of the vdW-DF2 functional in describing the reactivity at normal incidence is similar to that of the PW91 and RPBE functionals, if the experiments of Pfnür *et al.* [8] are taken as the reference. On the other hand, for normal incidence the vdW-DF2 functional yields the best description of the results published by Rettner *et al.* 4 years later [7]. The vdW-DF2 functional also yields the best overall description of the results of Pfnür *et al.* for an incidence angle of 60°. The quality of the description of off-normal incidence by vdW-DF2 might be even better than suggested by the present comparison with the data of Pfnür *et al.*. If the correction factor implied by the comparison of the Rettner *et al.* data to those of Pfnür *et al.* for normal incidence (reaction probabilities diminished by a factor 1.4) was based on improvements of the experiments, and if a similar factor should be applicable for off-normal incidence, the comparison with experiment should be further improved.

This Chapter is organized as follows. Section 3.2 describes the methodology. In Section 3.3 the results are reported and discussed in two Subsections: Section 3.3.1 describes the static study of the PES, including the molecular adsorption states and the barriers involved in the reaction process, and Section 3.3.2 reports and analyzes the AIMD results. Section 3.4 summarizes the results and the main conclusions of this work.

3.2 Method

All the electronic structure calculations have been performed using the Vienna *ab initio* simulation package (VASP) DFT code [22–25]. The basis set employed includes plane waves with a kinetic energy lower than 450 eV. Tungsten is a body centered cubic (bcc) metal and the W(110) surface has been simulated by a 5 layer slab using a 2x2 surface unit cell. The slab is separated from its periodic image by a 14 Å vacuum. The first Brillouin zone has been sampled by a Γ-centered 8x8x1 K-point grid. To facilitate the electronic convergence a Fermi smearing with a width parameter of 0.1 eV has been used. The core electrons have been modeled using the projector augmented wave (PAW) method [25, 26]. For tungsten the 6 valence electrons have been modeled as active while the other electrons have been frozen in the core. We have also tested the PAW implementation which models 6 additional semi-core p electrons as active electrons, but the equilibrium lattice constant for bulk W and the relaxed interlayer distances in the W(110) surface did not considerably change from the 6-active-electrons-PAW results. Furthermore, molecular adsorption energies calculated with vdW-DF2 using the two different PAW implementations differ by less than 26 meV in agreement with tests performed for semi-local functionals [15].

The effect of the size of the supercell has also been carefully tested for the molecular adsorption energy and for one of the barriers involved in the dissociation as found for the 2x2 cell. Increasing the supercell size from 2x2, which we have used, to 3x3 changes the barrier height for the dissociation from the hollow-parallel molecular adsorption site by only 25 meV, and the molecular adsorption energies by less than 40 meV.

In our study we have simulated molecules impinging on the surface at normal and off-normal incidence. In the latter simulations it is possible that the molecule interacts with the surface and subsequently closely interacts with the periodic image of the same part of the surface, in the actual collision. However, it has been shown that the mere distortion of the surface does not significantly affect the reactivity of N_2 on W(110), at least for normal incidence. AIMD simulations

on a frozen surface but with the atoms displaced like in the moving surface calculations [15] have given the same reaction probabilities (within error bars) as dynamics on the ideal frozen surface (computed by Alducin *et al.* [10]), suggesting a small effect on reactivity of the surface distortion induced by periodicity and justifying the use of the smaller 2x2 supercell.

The calculations have been performed using the vdW-DF2 functional developed by Lee *et al.* [20] as efficiently implemented in the VASP code [27, 28]. The vdW-DF functional [19] has been tested too but only in the static calculations.

The equilibrium tungsten lattice constant has been calculated as 3.183 and 3.238 Å with the vdW-DF and vdW-DF2 functionals, respectively, as compared with the experimental low-temperature value of 3.163 Å [29]. Molecular adsorption energies (E_{ads}) and dissociation energies (E_{diss}) have been computed as:

$$E_{ads} = \epsilon_{ads} - \epsilon_{asym}, \tag{3.1}$$

$$E_{diss} = \epsilon_{diss} - \epsilon_{asym}, \tag{3.2}$$

where ϵ_{asym} is the absolute energy of the molecule in its equilibrium geometry placed halfway between two periodic replicas of the slab, ϵ_{ads} is the absolute energy of the molecule in the adsorption configuration and ϵ_{diss} is the absolute energy of the two N atoms in the dissociation configuration. We verified that, in the asymptotic configuration, ϵ_{asym} does not depend on the orientation of the molecule and that, even by doubling the vacuum width, the adsorption energies vary by less than 15 meV. ϵ_{diss} and ϵ_{ads} have been obtained within the static surface approximation, as was done in previous work [15].

The barriers for the direct dissociation ($E_b^{DirDiss}$) have been extracted from pre-computed 2D potential energy surfaces (PESs) in the molecular bond (r) and in the distance of the center of mass from the surface (Z) for different fixed impact sites and orientations. In the process of the indirect dissociation two barriers are involved (as shown in Figure 3.1): the first barrier separates the asymptotic configuration from the molecular adsorption state, while the second barrier sep-

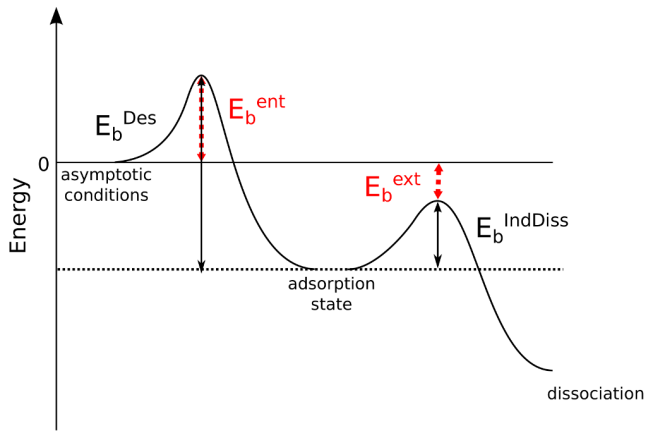

Figure 3.1: Scheme of the barriers considered. The barrier for the desorption (E_b^{Des}) and the barrier for the indirect dissociation ($E_b^{IndDiss}$), represented as thick black lines are referred to the energy of the adsorption state. The entrance channel barrier for the molecular adsorption (E_b^{ent}) and the exit channel barrier for the dissociative chemisorption (E_b^{ext}), represented as red dash lines, are referred to the asymptotic energy.

arates the molecular adsorption state from the dissociative chemisorption state. The barriers for the molecular adsorption (E_b^{ent} or E_b^{Des} as referred to ϵ_{asym} or to ϵ_{ads}, respectively), see Figure 3.1, have been extracted from pre-calculated (r,Z) 2D PESs including the adsorption geometries. The barriers for the indirect dissociation (E_b^{ext} or $E_b^{IndDiss}$ as referred to ϵ_{asym} or to ϵ_{ads}, respectively) have been computed through climbing image nudged elastic band (CI-NEB) calculations. In the CI-NEB calculations, implemented in the VASP-TST package by Henkelman and Jónsson [30, 31], four images have been optimized along the MEP between the reactants and the products. A CI-NEB calculation has been considered converged when the forces acting on all the images become smaller than 20 meV/Å. We tested this threshold by repeating one of the CI-NEB calculations until the forces acting on all the images become smaller than 5 meV/Å and we found the same barrier height within 1 meV. We verified that the barrier geometries obtained with the CI-NEB calculations are real first-order saddle points by computing the vibrational frequencies.

In order to compute the reaction probability we performed AIMD calculations [32–35]. AIMD allows one to model the N_2 + W(110) system while taking

into account not only the six molecular degrees of freedom but also surface atom motion, which is known to considerably affect the dynamics of this system [15]. The AIMD trajectories have been propagated using the Verlet algorithm as implemented in VASP with a 1 fs time-step. With the time-step used the average energy drift of the AIMD trajectories (computed as the difference between the maximum and the minimum value of total free energy in each trajectory) is about 25 meV. Much of the details of our AIMD calculations are similar to those described in Chapter 2 and in Ref. [15].

In order to compare our results with molecular beam experiments [7, 8], which were performed for a surface temperature (T_s) of 800 K, the theoretical 0 K lattice constant has been multiplied with a factor 1.0037 in order to describe the experimental expansion of the bulk at 800 K [36]. For an optimal sampling of the surface initial conditions we equilibrated ten differently initialized W(110) slabs. The initial displacements and velocities of the surface atoms have been generated according to an independent harmonic oscillators model (see Chapter 2). To overcome the harmonic approximation and achieve a proper description of the surface we next performed a 2.5 ps AIMD equilibration of the clean surfaces to impose the appropriate surface temperature. The surface initial conditions for the N_2 + W(110) trajectories have been randomly chosen from the last 1000 configurations assumed by the surfaces in the slab equilibrations, as described in Ref. [15].

In the molecule-surface dynamics the N_2 molecule is initially in the rovibrational ground-state (i.e. $v = 0$, $j = 0$), randomly oriented and placed with its center of mass (COM) 6 Å above the surface where the interaction potential is reasonably close to zero. A molecule has been considered scattered if, after the impact at the surface, the molecule-surface distance becomes larger than 6 Å and the COM velocity is pointing away from the surface. A molecule is considered reacted if the interatomic distance (r) of N_2 becomes larger than 2.0 Å (1.8 times the equilibrium interatomic distance) and if the distance between the two N atoms becomes larger than the distance between the first atom and the closest periodic image of the second atom. The reactive events have been classified as “direct” or

"indirect" depending on whether the molecule performed, respectively, less than four or more than three rebounds on the surface before dissociating [10]. Consistently with previous work [15], one rebound has been counted every time the velocity of the molecule changes from pointing away from the surface to pointing towards the surface. The trajectories have been propagated until one of the described outcomes is reached. However, in a few trajectories (between 6.5% and 4.5% of the total for the lowest E_i at normal and off-normal incidence, respectively, and in even fewer cases at higher E_i) the N_2 molecule remains trapped on the surface for a long time without either desorbing or dissociating. Because of the high computational cost of AIMD, in these cases the propagation has been stopped after 4.2 ps and the corresponding trajectories have been labeled as "unclear". A molecule has been considered trapped on the surface if it performed at least three bounces on the surface. The trapping probability has been defined as the number of trajectories in which the molecule undergoes trapping (regardless of the final outcome) divided by the total number of trajectories.

Each sticking probability value is estimated from 400 NVE trajectories (i.e. constant number of atoms, volume and total energy) performed for the same collision energy (E_i) and incidence angle (Θ_i) while including the N_2 zero-point energy in the calculation (quasi-classical trajectories, QCTs). Assunming energy conservation, for the scattered AIMD trajectories the amount of energy transferred to the surface (E_T) has been computed as:

$$E_T = (K + V)_{initial} - (K + V)_{final}, \tag{3.3}$$

by evaluating the kinetic energy of the molecule (K) and the interaction potential between the two N atoms (V) at the initial and at the final step of the trajectory. A positive value implies that energy is transferred from the molecule to the surface and a negative value that energy is transferred from the surface to the molecule. In Equation 3.3, $K_{initial}$ and K_{final} are computed as the sum of the kinetic energies of the two N atoms in the first and in the last step of the dynamics, respectively. To obtain the potential energy terms we computed a fit of the one-

dimensional interatomic potential for the N_2 molecule and we obtained $V_{initial}$ and V_{final} according to the interatomic N-N distance at the initial and at the final step of the dynamics, respectively. Note that the energy transfer has been evaluated only for scattered molecules, for which our procedure is justified if energy conservation is assumed.

The relative variation of the interlayer distance Δd_{mn} with respect to the corresponding bulk value (d_b) has been defined as:

$$\Delta d_{mn} = \frac{(d_{mn} - d_b)}{d_b} \cdot 100\%, \tag{3.4}$$

where m and n are indexes identifying the two layers considered. The results for $T_s = 0$ K, obtained by optimizing the slab interlayer distances while using the vdW-DF2 functional, show contraction of the first interlayer distance (i.e. $\Delta d_{12} = -3.8\%$) and a slight expansion of the second interlayer distance (i.e. $\Delta d_{23} = 0.10\%$) with respect to the corresponding bulk value (d_b). The same quantities obtained for $T_s = 800$ K, averaging over all the configurations employed for sampling the surface initial conditions, are not considerably different from the corresponding equilibrium values. However, Δd_{23} becomes negative in the dynamics picture. These results are in good agreement with previous theoretical work based on DFT with full-potential linearized augmented plane-waves (DFT-FLAPW) [37] and in reasonable agreement with X-ray diffraction experimental data [38] (Table 3.1).

	vdW-DF2 $T_s = 0$ K (equilibrium)	vdW-DF2 $T_s = 800$ K (dynamics)	DFT FLAPW [37]	X-ray diffraction [38]
Δd_{12}	-4.20 %	-4.10 ± 0.02 %	-4.1 %	-2.7 ± 0.5 %
Δd_{23}	0.10 %	-0.96 ± 0.02 %	-0.4 %	0.0 ± 0.3 %

Table 3.1: Relative interlayer variations with respect to the bulk computed from experiments and with different theoretical methods.

The reaction probabilities are reported with statistical error bars (σ_p) that represent the 68% confidence intervals [39]. For a reaction probability p calculated

from the computation of N trajectories, σ_p is defined as:

$$\sigma_p = \sqrt{p(1-p)/N}. \tag{3.5}$$

The relative interlayer variations (Δd_{mn}) and the mean energy transfer from the molecule to the surface ($\langle E_T \rangle$) are reported with statistical standard errors (i.e., the standard deviation divided by the square root of the number of values used to compute the average).

3.3 Results and Discussion

3.3.1 Static Results

To properly model the dissociation of N_2 on W(110) a density functional that correctly describes the molecule-surface interaction is needed. Therefore we first studied the shape and the features of the PES for molecular nitrogen interacting with an ideal W(110) surface, using the functional considered, through static calculations. The coordinate system employed is represented in Figure 3.2.

There is experimental [18, 40] and theoretical [10, 11, 15, 17] evidence for the existence of molecular adsorption states of N_2 on W(110). The associated configurations are believed to be relevant to the indirect dissociation mechanism in which the molecule remains trapped near the surface before dissociating [10, 15]. The presence of deep molecular adsorption minima leads to a higher probability for the molecule to be trapped close to the surface and, therefore, a higher dissociation probability. As in previous work [15] three molecular adsorption geometries have been found; some details of these geometries are reported in Table 3.2 and a sketch of the molecular adsorption states is represented in Figure 3.3. The molecular adsorption states found are the following: the top-vertical (tpv) state, in which the molecule is perpendicular to the surface and above a top site, the hollow-parallel (hlp) state, in which the molecule is parallel to the surface with the center of mass above the four-fold hollow site (and $\phi = 0°$), and the bridge-hollow-tilted (bht) state, in which one of the two atoms is roughly above a

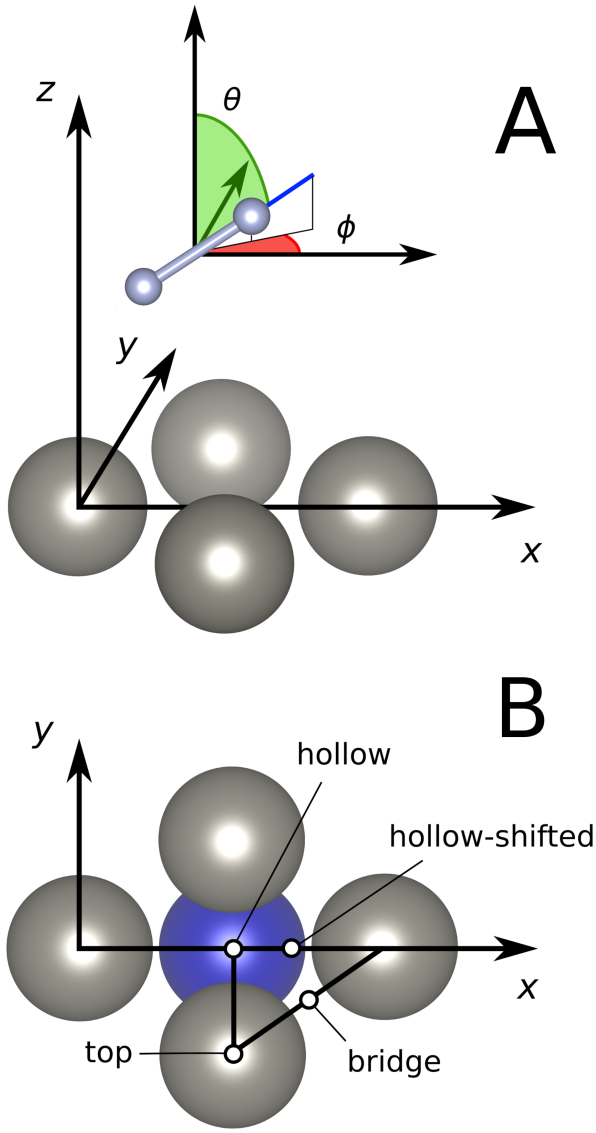

Figure 3.2: Coordinate system (A) and sites on the surface (B). Dark gray, dark blue and light blue are used for first layer W atoms, second layer W atoms and nitrogen respectively. In panel A the orientation angles θ (green) and ϕ (red) are reported for N_2. In panel B the irreducible wedge is indicated.

		θ / [°]	r / [Å]	Z / [Å]
	tpv	0.00	1.137	2.672
PBE	hlp	90.00	1.363	1.378
	bht	74.48	1.307	1.537
	tpv	0.00	1.141	2.694
RPBE	hlp	90.00	1.370	1.391
	bht	74.61	1.316	1.544
	tpv	0.00	1.141	2.707
vdW-DF	hlp	90.00	1.395	1.397
	bht	74.79	1.330	1.560
	tpv	0.00	1.130	2.744
vdW-DF2	hlp	90.00	1.375	1.402
	bht	73.96	1.290	1.598

Table 3.2: Molecular adsorption geometries as obtained with different functionals. Z is the distance between the center of mass (COM) of the molecule and the surface, r is the N-N distance and θ is the polar angle of orientation of the molecule. The tpv, hlp and bht abbreviations stand for top-vertical, hollow-parallel and bridge-hollow-tilted respectively. The PBE and the RPBE data are from Ref. [15].

bridge site and the other one close to a hollow site; in this geometry the molecular axis is neither perpendicular nor parallel to the surface.

The molecular adsorption energies (E_{ads}) for the adsorption states calculated with the vdW-DF2 functional are smaller than both the PBE and the RPBE values, with the exception of the top-vertical state for which E_{ads} is 0.1 eV larger (i.e., more negative) for the vdW-DF2 functional than for the RPBE functional (see Table 3.3). E_{ads} for the bridge-hollow-tilted adsorption is particularly small (i.e., -0.286 eV, vs -0.984 eV for PBE and -0.543 eV for RPBE). Considering that the trapping mediated dissociation represents a large fraction of the reactivity at the lower E_i values investigated for PBE and RPBE and that for this collision energy range the experimental S_0 is overestimated with these functionals, the smaller values of E_{ads} found with the vdW-DF2 functional suggest a lower contribution of the indirect dissociation channel to the reactivity. As is shown in the next Section, this does improve agreement with experimental data. For the vdW-

DF functional the molecular adsorption energies calculated are very similar to the PBE results. Moreover previous static surface AIMD simulations performed by Martin-Gondre *et al.* [17] showed an underestimation of the experimental reaction probability using this functional. Therefore in this work we focus on the more promising vdW-DF2 functional.

Interestingly the tested vdW functionals show generally weaker bonding for the molecular adsorption of N_2, but note that it is not easy to predict and to intuitively explain the behavior of a density functional. Moreover compared to the GGA functionals previously used (PBE and RPBE) both the exchange and the correlation parts have changed. The van der Waals functionals of the DF family (vdW-DF and vdW-DF2) have been designed to reproduce well purely vdW bound systems like rare gas dimers, and they couple a non-local correlation term that accounts for vdW interaction with a GGA exchange functional (i.e., revPBE and rPW86 for the DF and for the DF2 functional respectively [19, 20]). As a result these functionals can be more repulsive at intermediate distances where chemical bonding occurs while they are usually more attractive at long distances where any bonding is due to vdW dispersion (see also Figure 3.4).

	E_{ads} / [eV]		
	tpv	hlp	bht
PBE	-0.621	-1.444	-0.984
RPBE	-0.385	-0.972	-0.543
vdW-DF	-0.661	-1.340	-0.904
vdW-DF2	-0.480	-0.626	-0.286

Table 3.3: Molecular adsorption energies for N_2 on W(110), in eV. The tpv, hlp and bht abbreviations stand for top-vertical, hollow-parallel and bridge-hollow-tilted respectively. The PBE and the RPBE data are from Ref. [15].

If a molecule approaches the surface at normal incidence, it may encounter an energy barrier [15] before reaching a molecular adsorption state. In order to investigate this, we computed two dimensional (r,Z) potential energy cuts setting the remaining degrees of freedom (DOF) equal to the ones characterizing the molecular adsorption geometries. The three elbow plots (Figure 3.3) have

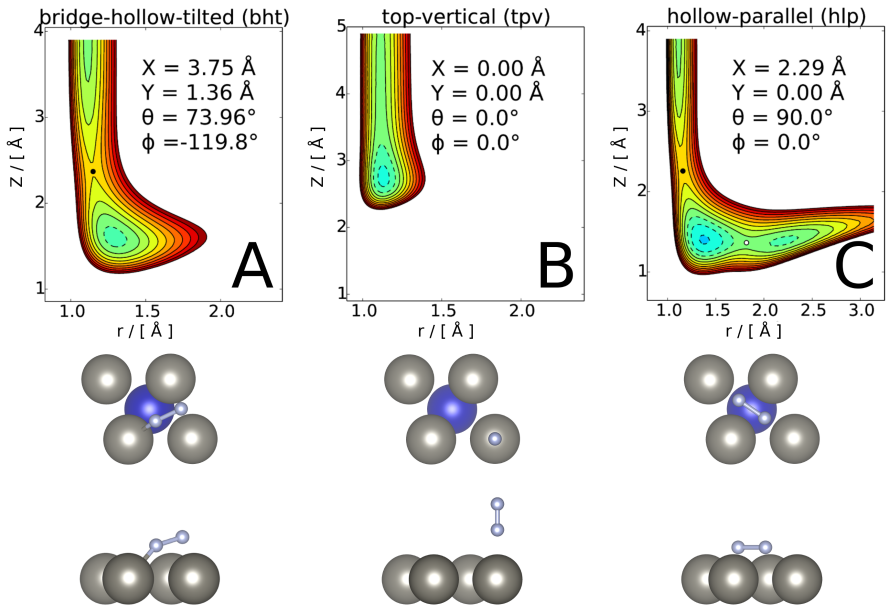

Figure 3.3: 2D (r,Z) cuts of the PES computed for the three molecular adsorption geometries: bridge-hollow-tilted (A), top-vertical (B) and hollow-parallel (C). Contour lines separate 0.2 eV energy intervals, solid lines are used for $E \geq 0$ eV, and dashed lines for $E < 0$ eV. Circles indicate all the (first order) saddle points. The black circles represent the entrance channel barriers for molecular adsorption (E_b^{ent}) and the white circles are 2D saddle-points that are not real first order saddle-points in the 6D space (see text for details). Sketches of the top and of the side views of the geometry are reported below the respective PES. The first layer atoms are shown in gray and the second layer atom is shown in dark blue, the nitrogen atoms are shown in light blue.

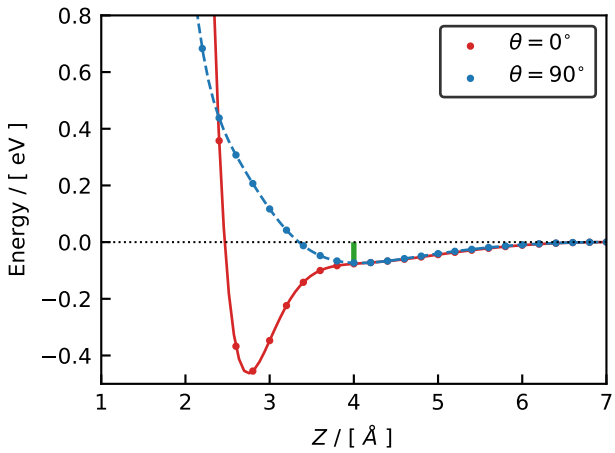

Figure 3.4: 1D cuts of the potential as a function of the distance between the molecule's COM from the surface (Z) above a top site oriented either parallel ($\theta = 90°$, blue) or perpendicular ($\theta = 0°$, red) to the surface. The zero of the energy is the absolute energy of the molecule in the asymptotic configuration at the gas-phase equilibrium intramolecular distance ($r = r_e$). The 75 meV deep vdW well is indicated in green.

been computed interpolating DFT energy values on a fine grid in r and Z. The entrance channel barriers for molecular adsorption E_b^{ent} that are extracted from these 2D cuts are reported in Table 3.4 together with the desorption barriers E_b^{Des}(calculated with respect to the bottom of the adsorption well). The vdW-DF2 barrier heights are intermediate between the PBE and the RPBE values, except for the access to the top-vertical state which is barrierless for the vdW-DF2 functional while small barriers were found for the PBE and the RPBE functionals (0.005 eV and 0.071 eV, respectively). Two saddle points and two local minima have been found in the 2D plot corresponding to the hollow-parallel configuration. The first saddle point (black circle, Figure 3.3) is the E_b^{ent} barrier. We investigated the nature of the second 2D saddle point by means of geometry relaxation and frequency calculations and we found that this is not a first order saddle point (i.e., a stationary point for which all the frequencies are real numbers except for one which is imaginary) in the full 6D space.

The vdW-DF2 functional has been developed to also model long-range attractive van der Waals interactions. To understand the properties of the PES

	E_b^{ent} (E_b^{Des}) / [eV]		
	tpv	hlp	bht
PBE	0.005 (0.626)	0.406 (1.850)	0.387 (1.371)
RPBE	0.071 (0.456)	0.629 (1.601)	0.610 (1.153)
vdW-DF2	- (0.480)	0.465 (1.091)	0.405 (0.691)

Table 3.4: Entrance channel barriers for molecular adsorption (E_b^{ent}) and for the desorption (E_b^{Des}, in brackets), in eV. The tpv, hlp and bht abbreviations stand for top-vertical, hollow-parallel and bridge-hollow-tilted respectively. All the vdW-DF2 values are extracted from the 2D cuts in Figure 3.3, the PBE and the RPBE data are from Ref. [15].

far from the surface, two one-dimensional energy diagrams have been computed (Figure 3.4). The bond length of N_2 has been fixed to the equilibrium value in the gas-phase (i.e., 1.113 Å) and the molecule-surface interaction has been calculated varying the distance of the molecule's COM to the surface. The two potential curves have been computed for the molecule above the top site, one with the molecular axis perpendicular and one with the molecular axis parallel to the surface. For $Z > 4$ Å there is no potential difference between the two molecular orientations. For $Z < 4$ Å a molecule perpendicular to the surface can enter the top-vertical adsorption well without any barrier, as mentioned above. At about 4 Å from the surface an adsorption well (vdW or physisorption well) of about 75 meV depth is observed in the vdW-DF2 results (Figure 3.4). Such a well is not observed with regular GGA functionals like PBE or RPBE and, as is shown in the next Section, it can affect the dynamics by trapping "slow" molecules at about 4 Å from the surface.

In addition to these "straight paths" to access the molecular adsorption wells, a molecule could follow more complicated paths in which the impact site and the molecular orientation change along the path, potentially leading to lower barriers. For instance a molecule could follow a barrierless path to enter the top-vertical adsorption well and then move towards another adsorption state. CI-NEB calculations have been performed to obtain the MEPs and the barriers connecting the top-vertical adsorption state to the bridge-hollow-tilted and the

hollow-parallel configuration. Relative to the asymptotic reference (N_2 far away from the surface at 0 eV) a small (18 meV) barrier has been found for the tpv-to-hlp path (Figure 3.5B) while the tpv-to-bht path is barrierless (Figure 5A). Considering that the minimum initial translation energy of our AIMD trajectories is 0.9 eV, the molecules should in all cases studied have enough energy to overcome the barriers shown in Figure 3.5 and to explore the PES close to the surface without being confined to a specific molecular adsorption minimum.

Previous work [10, 15] showed that PBE overestimates the dissociation probability at $E_i = 0.9$ eV. Moreover, it was found [15] that the molecules that visit at least one of the molecular adsorption states dissociate in the majority of cases. These results would be consistent with the barriers for the dissociative chemisorption being too low compared to the ones for desorption from the molecular chemisorption well. Experimental work [18] suggests that, for the molecule initially in the molecular chemisorption well, barriers for desorption and dissociation of similar height should be expected for N_2 on W(110). In fact, Lin *et al.* [18] studied N_2 on W(110) with different experimental techniques (temperature programmed desorption, Auger spectroscopy and X-ray photoelectron spectroscopy), estimating, for both the dissociation and the desorption, an activation energy of about 0.450 eV, which is reasonably similar to the barrier for the desorption from the top-vertical molecular adsorption state computed using vdW-DF2 (i.e. 0.480 eV).

Indirect dissociation barriers ($E_b^{IndDiss}$) and desorption barriers (E_b^{Des}) have been calculated using the vdW-DF2 functional. The latter have been extracted from the elbow plots in Figure 3.3 and the former have been calculated performing CI-NEB calculations connecting the molecular adsorption state to a dissociated configuration in which the N atoms are above two bridge sites ("hollow-to-bridge" dissociation). The hollow-to-bridge geometry has been chosen as the final configuration of the CI-NEB calculations in order to simulate the dissociation above an hollow site which is known to be involved in the dissociative chemisorption of N_2 on W(110) [10, 15]. Moreover this geometry has been used as the final configuration of CI-NEB calculations on the same system in previous work [17].

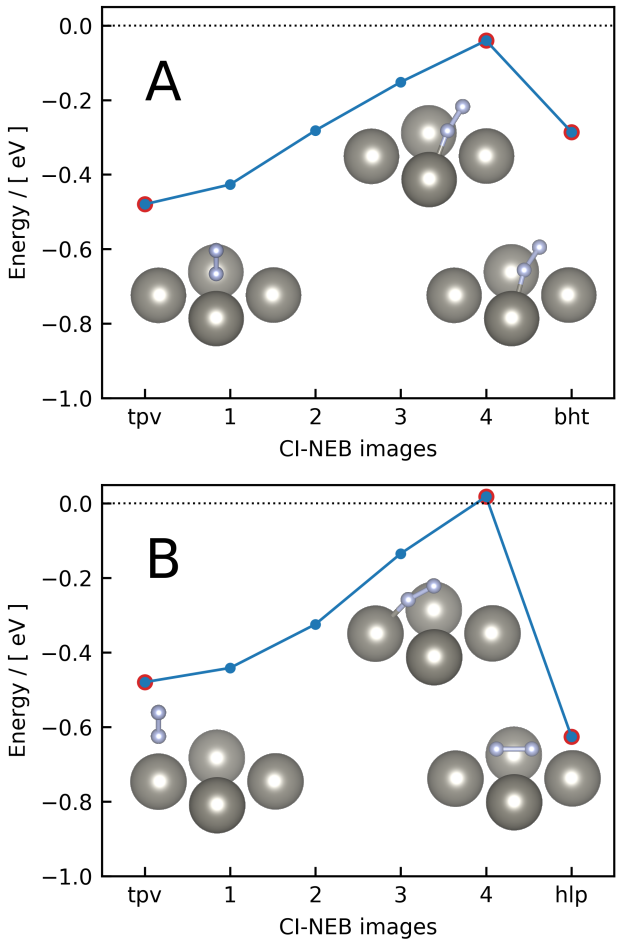

Figure 3.5: Paths connecting two molecular adsorption states as obtained from CI-NEB calculations. The paths connect the top vertical state to either the bridge hollow tilted (A) or to the hollow parallel state (B). The zero of the energy is the absolute energy of the molecule in the asymptotic configuration. The initial, the barrier and the final states are highlighted in red and the respective geometries are sketched as insets in the plots.

The barrier heights, relative to the energy of the adsorption state (as illustrated in Figure 3.1), are reported in Table 3.5A. The $E_b^{IndDiss}$ value for the path connecting the top-vertical molecular adsorption geometry and the hollow-to-bridge dissociation with the vdW-DF2 functional (marked with a dagger† in Table 3.5) is extracted from Figure 2 of Ref. [17]. Note that this value was obtained allowing the relaxation of the two topmost surface layers in the NEB calculation whereas our results have been computed within the frozen surface approximation. With the vdW-DF2 functional it has not been possible to converge the CI-NEB calculation to obtain this barrier within the static surface approximation. Martin-Gondre *et al.* [17] also found problems to obtain the barrier height for the same path within the frozen surface approximation. They managed to properly converge this path and to compute the barrier height only if the two topmost surface layers were allowed to relax. We also report their value in Table 3.5 for this barrier.

The exit channel barriers for the dissociation have also been calculated considering the asymptotic state as the energy zero (E_b^{ext}, reported in Table 3.5B) and, for all the adsorption states and functionals, E_b^{ext} is negative (i.e. below the gas-phase level). The vdW-DF2 functional shows lower desorption barriers than PBE and RPBE [15]; In general the values of $E_b^{IndDiss}$ and E_b^{Des} computed with vdW-DF2 are closer to each other than found with the other functionals, which is consistent with experimental results [18]. The better agreement of vdW-DF2 static results with the experimental findings suggests that, in the molecular dynamics simulation, there might be less indirect reaction, which could result in better agreement with the experimental reaction probability (S_0). As already noted, the vdW-DF2 barrier for the desorption from the top-vertical molecular adsorption state ($E_b^{Des} = 0.480$ eV) is in good agreement with the experimental barrier height suggested by Lin *et al.* (i.e., ≈ 0.450 eV) [18]. However, the vdW-DF2 barrier for the indirect dissociation is somewhat too low ($E_b^{IndDiss} = 0.406$ eV), it should be closer to the desorption barrier height.

Experimentally N_2 is known to adsorb on W(110) in a state which has been labeled γ-N_2 with an estimated adsorption energy of -0.450 eV [40]. This value

	tpv / [eV]		hlp / [eV]		bht / [eV]	
	$E_b^{IndDiss}$	E_b^{Des}	$E_b^{IndDiss}$	E_b^{Des}	$E_b^{IndDiss}$	E_b^{Des}
PBE	0.189	0.626	0.467	1.850	0.498	1.371
RPBE	0.271	0.456	0.442	1.601	0.500	1.153
vdW-DF2	0.406†	0.480	0.182	1.091	0.271	0.691

(A)

	tpv / [eV]		hlp / [eV]		bht / [eV]	
	$E_b^{IndDiss}$	E_b^{ext}	$E_b^{IndDiss}$	E_b^{ext}	$E_b^{IndDiss}$	E_b^{ext}
PBE	0.189	-0.432	0.467	-0.977	0.498	-0.486
RPBE	0.271	-0.114	0.442	-0.550	0.500	-0.043
vdW-DF2	0.406†	-0.170†	0.182	-0.444	0.271	-0.015

(B)

Table 3.5: (A) Barriers (in eV) for the desorption (E_b^{Des}) and for the dissociation ($E_b^{IndDiss}$) as calculated from the bottom of the molecular adsorption wells indicated. (B) Comparison between the dissociation barriers (in eV) calculated with respect to the asymptotic configuration (E_b^{ext}) or with respect of the bottom of the molecular adsorption configuration indicated ($E_b^{IndDiss}$). The tpv, hlp and bht abbreviations stand for top-vertical, hollow-parallel and bridge-hollow-tilted respectively. The PBE and the RPBE data are from Ref. [15]. The $E_b^{IndDiss}$ and E_b^{ext} values for tpv, marked with a dagger (†), are extracted from Figure 2 of Ref. [17]. Note that these values were obtained allowing the relaxation of the two topmost surface layers in the NEB calculation whereas the other results have been computed within the frozen surface approximation, see text for details.

agrees well with the adsorption energy we obtained with vdW-DF2 for the top-vertical adsorption state ($E_{ads} = -0.480$ eV). There is also experimental evidence for another adsorption state of N_2 on W(110) called δ-N_2. Zhang *et al.* [40] reported the presence of this adsorption state generated through electron bombardment of γ-N_2 in electron stimulated desorption (ESD) experiments, and suggested an adsorption geometry with the molecule lying parallel to the surface with the NN bond elongated with respect to N_2 in the gas-phase. The hollow-parallel adsorption state we found is characterized by a molecule placed parallel to the surface with an elongated NN bond. Therefore, it might correspond to the experimentally observed δ-N_2 state. Moreover, the thermal programmed desorption (TPD) spectra before and after the ESD do not significantly differ, suggesting either that the desorption activation energy is similar for γ-N_2 and δ-N_2, or that the adsorbed molecules convert from the δ to the γ state before desorbing. Our findings are consistent with the latter explanation: in fact the hollow-parallel barrier for direct desorption ($E_b^{Des} = 1.091$ eV) is much higher than the barrier to convert the hollow-parallel adsorption state to the top-vertical adsorption state ($E_b = 0.644$ eV). However δ-N_2 has not been found to give rise to atomic N in TPD or ESD experiments, suggesting a large dissociation barrier for the δ-N_2 state, whereas the vdW-DF2 functional shows only a small dissociation barrier for the hollow-parallel state (i.e., $E_b^{IndDiss} = 0.182$ eV).

We have studied the details of the energy landscape that influence the direct dissociation mechanism, which implies dissociation at the first impact on the surface or after a few rebounds. Four additional 2D cuts of the potential (Figure 3.6) have been computed considering four configurations that might be involved in this process. The configurations considered (Figure 3.7) involve the bridge-to-hollow dissociation, the bridge-to-hollow-shifted dissociation, the hollow-to-bridge dissociation, and the top-to-hollow dissociation. The first site specified in the configuration name is the the molecular COM position and the second one is the name of the site to which the two N atoms are pointing (for example, in the bridge-to-hollow configuration the center of mass is above a bridge site and the N atoms point towards two hollow sites). The configurations considered

(Figure 3.7) are representative of all the possible 2D paths that allow the 2 N atoms to end up in two equivalent (local) adsorption minima (hollow, bridge or hollow-shifted) and the corresponding dissociative chemisorption energies (E_{diss}) are reported in Table 3.6. The real absolute atomic adsorption minimum of the infinite system is the one in which the N atoms are infinitely far from each other. Within our supercell, the real absolute energy minimum is the one corresponding to the bridge-to-hollow-shifted dissociation. The atomic adsorption site over the bridge site and the one over the hollow site are not real minima but stationary points with one or two small imaginary frequencies. They have been used as final configurations to simulate the dissociation above the hollow and the bridge sites, respectively, as the associated reaction paths are known to be relevant for this system.

The E_{diss} values are calculated considering the asymptotic energy as the energy zero and Table 3.6 shows that the dissociative chemisorption of N_2 on W(110) is an exothermic process. The most stable dissociative geometry among the ones considered is the bridge-to-hollow-shifted geometry. The bridge-to-hollow and the top-to-hollow dissociation geometries differ in energy by 151 meV because the distances between the two N atoms differ in the dissociated geometries.

2D plots including the dissociation geometries mentioned above have been calculated with the same procedure as used for Figure 3.3. The barriers for the direct dissociation ($E_b^{DirDiss}$), as extracted from the 2D plots in Figure 3.6, are reported in Table 3.7. For the top-to-hollow dissociation we found a very high barrier at $Z = 1.76$ Å. For both the bridge-to-hollow and the hollow-to-bridge dissociation the MEP on the 2D PES shows two local minima and two saddle points. The entrance channel barriers for the direct dissociation ($E_b^{DirDiss}$, represented as black circles in Figure 3.6) are located in the region between 2.0 and 2.5 Å from the surface and the corresponding barrier heights, for vdW-DF2, are larger than for PBE but lower than for RPBE. Compared to RPBE, the vdW-DF2 functional is less repulsive far from the surface ($Z > 2$ Å) where the barriers for the direct dissociation are located. Performing geometry relaxation and frequency calculations we verified that, in both cases, the first minimum along the

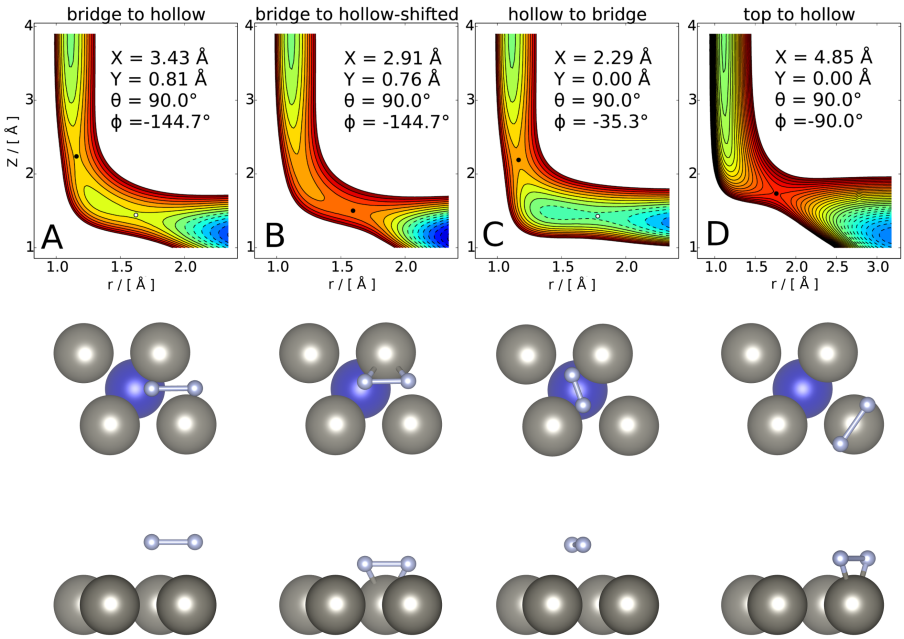

Figure 3.6: 2D (r,Z) cuts of the PES computed for four dissociation geometries: bridge-to-hollow (A), bridge-to-hollow-shifted (B), hollow-to-bridge (C) and top-to-hollow (D). Contour lines separate 0.2 eV energy intervals, solid lines are used for $E \geq 0$ eV and dashed lines for $E < 0$ eV. Circles indicate all the stationary points. The black circles represent the entrance channel barriers for dissociation ($E_b^{DirDiss}$) and the white circles are 2D saddle-points that are not real first order saddle-points in the 6D space (see text for details). The top and the side view sketches of the direct dissociation barrier geometries are reported below the corresponding elbow plots.

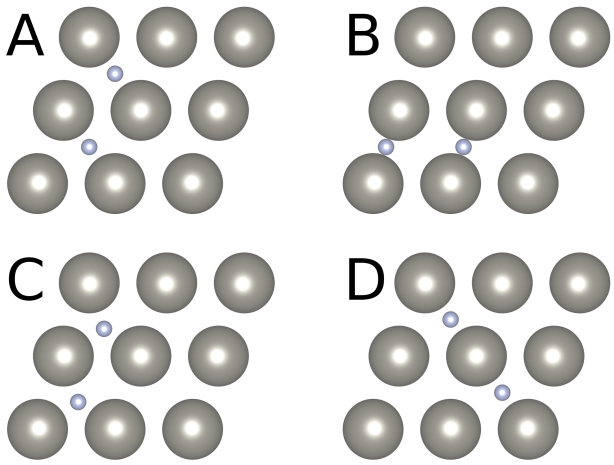

Figure 3.7: Dissociation products considered as a result of a bridge-to-hollow (A), hollow-to-bridge (B), bridge-to-hollow-shifted (C) and top-to-hollow (D) dissociation.

configuration	E_{diss} / [eV]
hollow-to-bridge	-1.273
bridge-to-hollow	-1.848
top-to-hollow	-1.999
bridge-to-hollow-shifted	-2.445

Table 3.6: Dissociation energies (in eV) of the dissociated configurations sketched in Figure 3.7.

MEP (between the two barriers) is not a real minimum in the 6D space for both hollow-to-bridge and bridge-to-hollow dissociation.

3.3.2 AIMD Results

The reaction probability (S_0) has been computed for N_2 on W(110) for two incidence angles ($\Theta_i = 0°$ and $60°$) and four initial collision energies ($E_i = 0.90$, 1.30, 1.70, 2.287 eV). We have compared AIMD results at normal incidence with the results of two molecular beam experiments for N_2 on W(110) performed at $T_s = 800$ K (Figure 3.8). The two experimental data sets, which were obtained by Pfnür *et al.* [8] and Rettner *et al.* [7], show a considerable difference in the reaction

	$E_b^{DirDiss}$ / [eV]			
	hollow to bridge	bridge to hollow	top to hollow	bridge to hollow shifted
PBE	0.543	0.487	-	-
RPBE	0.802	0.726	-	-
vdW-DF2	0.635	0.563	2.612	0.881

Table 3.7: Barriers for the direct dissociation (in eV) extracted from the elbow plots in Figure 3.6. The PBE and the RPBE data are from Ref. [15].

probability (Figure 3.8), in particular at high collision energies: for $E_i = 2.3$ eV the reaction probability obtained by Rettner *et al.* is about 0.1 smaller than the reaction probability obtained by Pfnür *et al.* We found that multiplying the S_0 of Rettner *et al.* by a factor of 1.4 makes the reaction probability curve fall almost on top of the reaction probability curve obtained by Pfnür *et al.* We focused the analysis of our results on the comparison with the Pfnür *et al.* results because their experiments, similarly to previous theoretical work [10, 11, 15], investigated both normal and off-normal incidence. Moreover Rettner *et al.* [7] did not give an explanation about the discrepancies between their sticking probabilities and the earlier results of Pfnür *et al.* [8].

For both incidence angles, the AIMD results are in good agreement with experimental data obtained by Pfnür *et al.* [8] at $E_i = 0.9$ eV but the agreement is less good for higher collision energies. For normal incidence the AIMD fails at reproducing the experimental trend: the experimental S_0 increases monotonically with E_i whereas the computed S_0 seems to show a minimum for E_i between 1.0 and 1.5 eV. For $\Theta_i = 60°$ the results are in good agreement with experiment at $E_i = 0.9$ eV, but at higher energies AIMD gives reaction probabilities that are smaller than the experimental ones. Compared to the data of Rettner *et al.* [7] for $\Theta_i = 0°$ the AIMD results are in quite good agreement with the experiments for $E_i \geq 1.25$ eV (Figure 3.8) while for the lowest collision energy (i.e., $E_i = 0.9$ eV) the AIMD results overestimate the measured reaction probability. Figure 3.8 also shows the upperbounds of the computed reaction probability obtained by

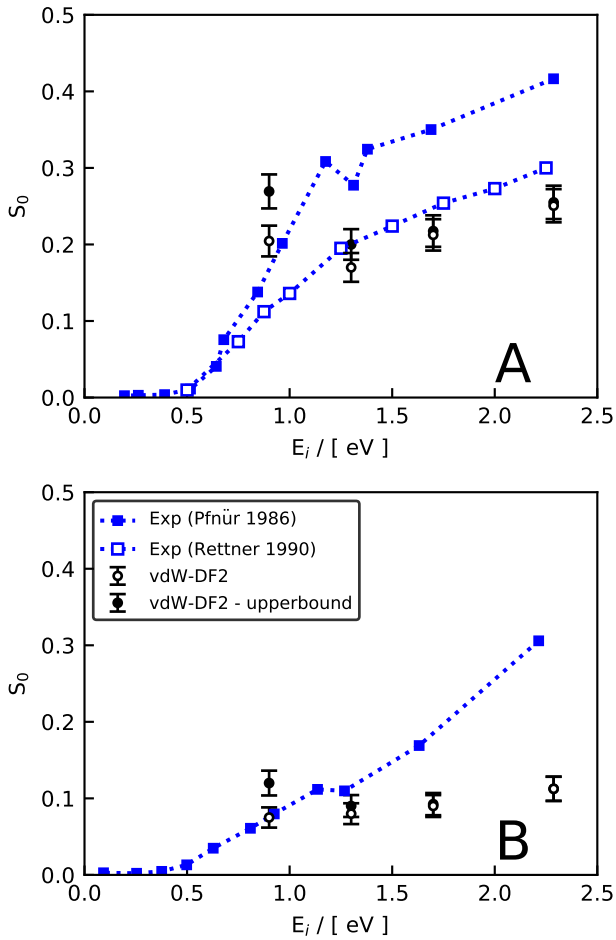

Figure 3.8: Reaction probability as a function of the collision energy E_i for $\Theta_i = 0°$ (panel A) and $\Theta_i = 60°$ (panel B). Comparison between experimental data and AIMD vdW-DF2 results. The dissociation probabilities and their upperbounds are reported as empty and full black symbols, respectively. Experimental data are taken from Ref. [7] (empty blue symbols) and Ref. [8] (full blue symbols).

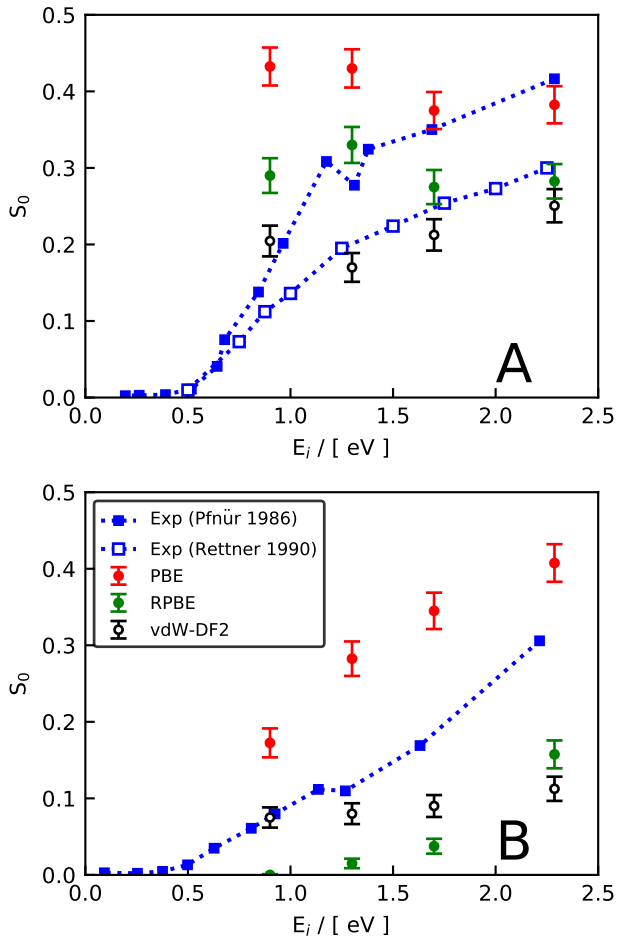

Figure 3.9: Reaction probability as a function of the collision energy E_i for $\Theta_i = 0°$ (panel A) and $\Theta_i = 60°$ (panel B). vdW-DF2 results are reported as black empty circles. PBE and RPBE data (full red and green circles, respectively) for normal incidence are taken from Ref. [15]. Experimental data are taken from Ref. [7] (full blue squares) and Ref. [8] (empty blue squares).

considering all unclear trajectories as reacted. For the lowest E_i investigated the upperbound reaction probabilities are 0.065 and 0.045 larger than the regular ones for $\Theta_i = 0°$ and 60°, respectively. For higher E_i the upperbounds are not considerably different from S_0 and follow a similar trend in the dependence on E_i as the S_0 calculated in the regular way.

In Figure 3.9 vdW-DF2 AIMD results are also compared to previous calculations performed using PBE and RPBE (from Ref. [15]). For all E_i and incidence angles considered, the vdW-DF2 reaction probabilities are lower than the PBE results. Compared to RPBE, vdW-DF2 is less reactive for normal incidence. For $\Theta_i = 60°$, however, vdW-DF2 returns larger reaction probabilities for $E_i = 0.9$ eV but a similar reaction probability for $E_i = 2.3$ eV.

When it comes to the overall performance of the functionals in describing the reactivity at normal incidence as measured by Pfnür *et al.* [8], it is hard to arrive at a verdict. The vdW-DF2 result is closest to experiment at $E_i = 0.95$ eV, the RPBE result at $E_i = 1.3$ eV, and the PW91 result at $E_i = 1.75$ and 2.25 eV. None of the functionals yields a good overall description of the reactivity. However, the vdW-DF2 functional yields the best description of the results published for normal incidence by Rettner *et al.* 4 years later [7]. The vdW-DF2 functional also best describes the results of Pfnür *et al.* for an incidence angle of 60°.

Although we have chosen to emphasize the comparison with the data of Pfnür *et al.*, because they were obtained for both normal and off-normal incidence, it is interesting to speculate about the quality of the two sets of experimental results, and possible consequences for the comparison with the AIMD results. As already noted, the results of Rettner *et al.* for normal incidence compare well with those of Pfnür *et al.* if the latter are divided by a factor 1.4. Unfortunately, Rettner *et al.* did not state whether the difference with the earlier data reflected improvements of the measurements. If that would be the case, and a similar correction factor should be applicable to the data of Pfnür *et al.* for 60°, the agreement of the vdW-DF2 results with the experimental data for this incidence angle should be further improved. New experiments to resolve this and other issues concerning experimental accuracy are clearly desirable, as N_2 + W(110)

has become a benchmark system for surface reaction dynamics. Ideally, in new experiments, the molecular beams used would be well characterized in terms of their velocity distribution and vibrational and rotational temperature of the molecules, as calculations on H_2 + Cu(111) [41] suggest that these might have an important effect on the measured sticking probability.

For the vdW-DF2 functional the indirect dissociation channel is still important at $E_i = 0.9$ eV, whereas at higher energies reactive events via trapping are rare for both $\Theta_i = 0°$ and 60° (Figure 3.10). For $\Theta_i = 0°$ vdW-DF2 indirect reaction probabilities are smaller than for both PBE and RPBE. For $\Theta_i = 60°$ vdW-DF2 indirect reaction probabilities are smaller than for PBE and larger than RPBE at low E_i. Increasing the collision energy, the vdW-DF2 indirect reaction probability decreases, becoming smaller than for both PBE and RPBE. The vdW-DF2 direct reaction probability is always lower than for PBE. As noted before, for $\Theta_i = 60°$ the vdW-DF2 functional reproduces the experimental data of Pfnü*r et al.* [8] well at the lowest E_i simulated but fails for higher energies where the direct dissociation mechanism dominates. One possibility is that this functional overestimates the barriers for direct dissociation returning a too low reaction probability at $E_i = 2.287$ eV.

The molecules that react indirectly at normal incidence spend considerable time bouncing on the surface before dissociating. Even for the direct reaction at the lower E_i values investigated and normal incidence, most of the molecules bounce at least once before the dissociation. This is not the case for $\Theta_i = 60°$ where the direct dissociation occurs mostly as soon as the molecule reaches the surface. Distributions of the COM positions and θ values, evaluated at the time of the dissociation (defined as the time at which the interatomic distance r becomes larger than 2 Å), are reported in Figures 3.11 and 3.12, respectively. Using the vdW-DF2 functional the direct reaction occurs at the hollow and bridge sites, while the indirect reaction occurs mostly at the hollow sites. Using the PBE and the RPBE functionals similar COM distributions are obtained for the direct and the indirect dissociation (not shown). The molecules react only when the axis is almost parallel to the surface ($\theta \approx 90°$) for both the direct and the indirect

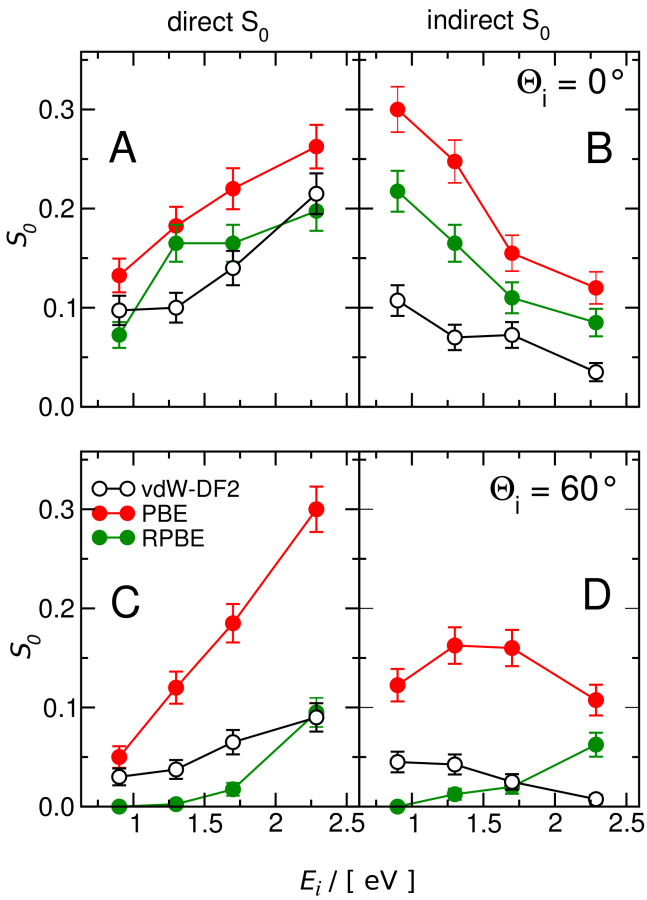

Figure 3.10: Direct (A, C) and indirect (B, D) reaction probability as a function of E_i for $\Theta_i = 0°$ (A, B) and $\Theta_i = 60°$ (C, D). vdW-DF2 results are reported as black empty circles. PBE and RPBE data (full red and green circles, respectively) for normal incidence are taken from Ref. [15].

dissociation mechanisms (Figure 3.12).

The molecular trapping is related to the possibility, for the molecule, to lose its translational kinetic energy by transferring it to other molecular DOFs or to the surface. We evaluated the average amount of energy exchanged with the lattice ($\langle E_T \rangle$) for the scattering trajectories (Table 3.8). For $\Theta_i = 0°$ a large portion of E_i is transferred to the lattice (i.e. 0.26 eV $< \langle E_T \rangle <$ 0.78 eV) whereas for $\Theta_i = 60°$ the energy transferred is smaller by about a factor two. Similar results have been found for PBE and RPBE [15]. Our results are also compared with the energy transfer predicted by the Baule model (E_T^{Baule}), [42] which approximates the molecule-surface impact as a collision between two hard-spheres with masses equal to the N_2 molecule and a target atom, which is typically taken as one of the surface atoms (i.e., a W atom):

$$E_T^{Baule} = E_i \frac{4\mu}{(1+\mu)^2}. \tag{3.6}$$

Here μ is the ratio between the mass of the N_2 molecule and the mass of one W surface atom. If the system considered shows a significant molecular adsorption energy, as for N_2 on W(110), the modified Baule model is generally used to take into account the additional kinetic energy that the projectile gains approaching the surface. In the modified Baule model E_i is substituted by ($E_i + E_{ads}$) where E_{ads} is the adsorption energy (in our case we used the largest adsorption energy, which is the one related to the hollow-parallel configuration, i.e. $E_{ads} =$ 0.626 eV). Table 3.8 reports the energy transfer values computed with the Baule model (Table 3.8A) and the values computed from the average over the AIMD scattered trajectories (Tables 3.8B and 3.8C).

We also compared the energy exchanged by the molecules that scattered after a single impact on the surface ($\langle E_T \rangle_1$) with the Baule model predictions (Figure 3.13), showing that the Baule model considerably overestimates the amount of energy transferred to the surface even considering a single molecule-surface collision.

For PBE and RPBE [15] a large fraction of the molecules undergo molecular

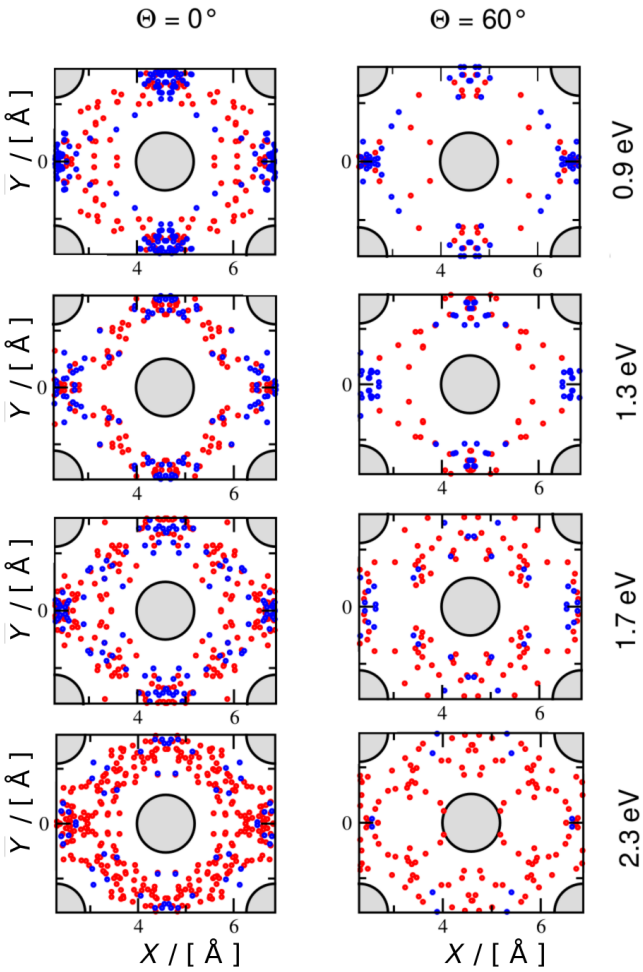

Figure 3.11: XY position of the COM of the reactive molecules at the time of the dissociation (see text for definition). The COM positions have been reported in the minimum wedge and then replicated in the $\sqrt{2}$x$\sqrt{2}$ super-cell using symmetry operations. Direct and indirect events are indicated as red and blue circles respectively. Tungsten first layer atoms in their equilibrium positions are shown as gray circles.

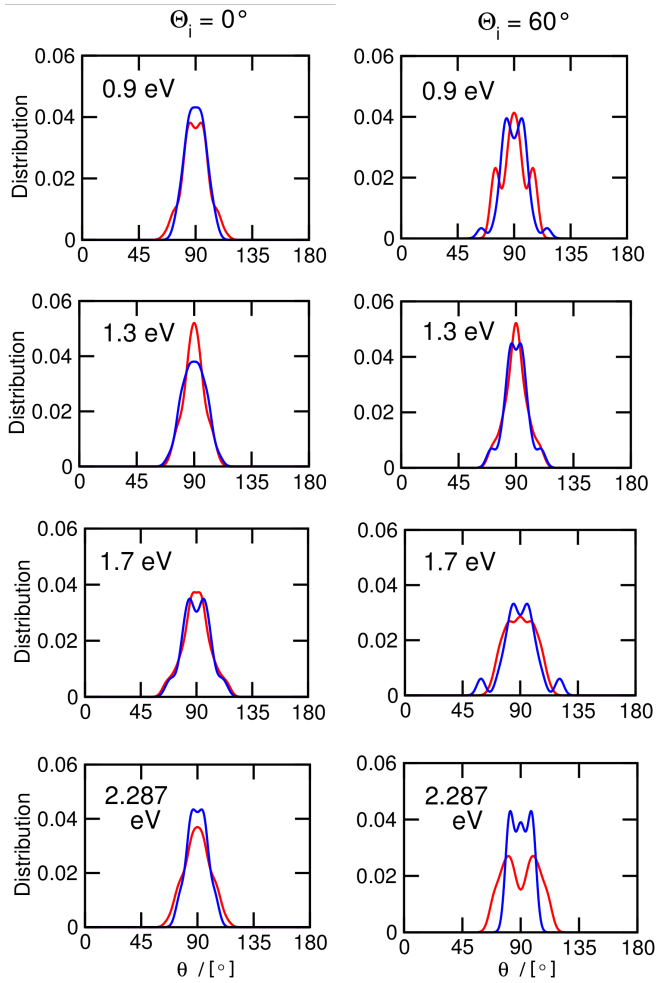

Figure 3.12: Distribution of the angle between the molecular axis and the surface normal (θ) at the time of the reaction (see text for definition) for both the direct and the indirect mechanisms (red and blue lines, respectively). To increase the resolution of the data, for each molecule the two values of θ obtained inverting the N atoms have been reported (i.e., the angles θ and $180° - \theta$ have been reported for each atom). The incidence energy E_i is reported as insets.

E_i / [eV]	Baule / [eV]	Modified Baule / [eV]		
		vdW-DF2	PBE	RPBE
0.900	0.413	0.700	1.075	0.859
1.300	0.596	0.884	1.259	1.042
1.700	0.780	1.067	1.443	1.226
2.287	1.049	1.336	1.712	1.495

(A)

$\Theta_i = 0°$

	$\langle E_T \rangle$ / [eV]		
E_i / [eV]	vdW-DF2	PBE	RPBE
0.900	0.257 ± 0.001	0.214 ± 0.012	0.210 ± 0.011
1.300	0.396 ± 0.002	0.348 ± 0.016	0.335 ± 0.014
1.700	0.546 ± 0.002	0.483 ± 0.022	0.450 ± 0.019
2.287	0.779 ± 0.001	0.654 ± 0.022	0.623 ± 0.022

(B)

$\Theta_i = 60°$

	$\langle E_T \rangle$ / [eV]		
E_i / [eV]	vdW-DF2	PBE	RPBE
0.900	0.104 ± 0.001	0.071 ± 0.008	0.002 ± 0.002
1.300	0.183 ± 0.001	0.225 ± 0.016	0.005 ± 0.006
1.700	0.280 ± 0.001	0.414 ± 0.022	0.011 ± 0.011
2.287	0.388 ± 0.001	0.546 ± 0.028	0.019 ± 0.019

(C)

Table 3.8: (A) Energy transfer to the surface according to the Baule model and the modified Baule model (see text for details) for the E_i considered. (B, C) The mean energy transfer $\langle E_T \rangle$ computed averaging over the scattered trajectories for all the functionals and collision energies is reported for $\Theta_i = 0°$ and $\Theta_i = 60°$. PBE and RPBE data are taken from Ref. [15].

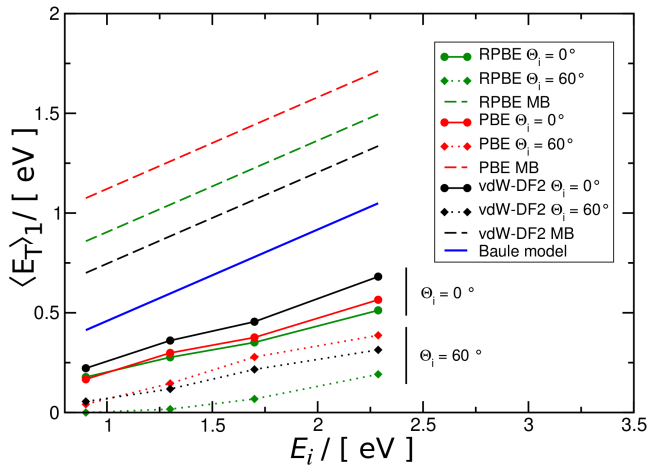

Figure 3.13: Comparison between the mean energy transfer to the surface calculated from the molecules that do not perform any rebounds on the surface ($\langle E_T \rangle_1$) and the energy transfer predicted by the modified Baule model. Data are reported for the functionals considered (in red, green, and black, for PBE, RPBE and vdW-DF2, respectively) for $\Theta_i = 0°$ (solid lines), $\Theta_i = 60°$ (dotted lines) and for the modified Baule model (dashed lines). The standard Baule model is reported as a thick blue line. PBE and RPBE data are taken from Ref. [15].

trapping (between 15 and 40%, depending on E_i and Θ_i) as also reported in Figure 3.14. Most of the trapped molecules end up dissociating. For vdW-DF2 we found that the fraction of the trajectories that involve molecular trapping (between 0.05 and 0.2) is significantly lower than for the other functionals at $\Theta_i = 0°$ (Figure 3.14). For $\Theta_i = 60°$ the fraction of trapped molecules found with vdW-DF2 is smaller than for PBE and monotonically decreases with increasing collision energy (Figure 3.14). For normal incidence, on average $\approx 60\%$ of the trapped molecules dissociate (Figure 3.15). As found for PBE and RPBE [15], for normal incidence the fraction of trapped molecules that dissociate is independent of the collision energy. For $\Theta_i = 60°$ it is not possible to identify a clear trend because the statistics are poor due to the low number of trapped trajectories at this incidence angle (Figure 3.15).

Some trajectories are still trapped on the surface at the end of the propagation time (i.e., 4200 fs) without a clear outcome (reaction or scattering). 80% of the reactive events occur before a propagation time $t' = 1600$ fs (roughly 40%

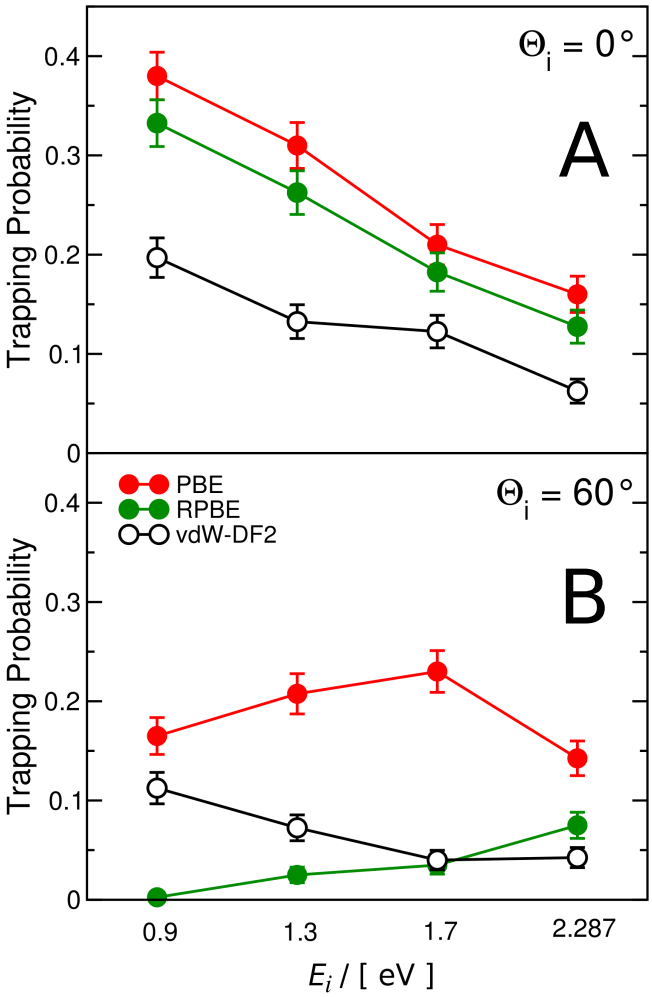

Figure 3.14: Comparison between the trapping probabilities computed with the PBE, RPBE and vdW-DF2 functional (reported as full red, full green and empty black circles respectively) for both $\Theta_i = 0°$ (panel A) and $\Theta_i = 60°$ (panel B).

of our maximum propagation time) and all the molecules that dissociate after that time go through the indirect dissociation channel. If we assume the ratio between the molecule scattered and dissociated after t' to be constant in time, we can extrapolate dissociation probabilities for larger propagation times assigning an outcome to the unclear trajectories. The two S_0 points associated with the highest number of unclear trajectories are at $E_i = 0.9$ eV for both $\Theta_i = 0°$ and $60°$ and they show a reaction/desorption ratio after t' of 1.25 and 0.56, respectively. If an outcome is assigned to the unclear trajectories according to this extrapolation the computed S_0 values would increase by 0.036 for $E_i = 0.9$ eV and $\Theta_i = 0°$ and by 0.016 for $E_i = 0.9$ eV and $\Theta_i = 60°$. The main conclusions of our work would not change on the basis of these estimates, and the small increase of the reaction probability due to this extrapolation shows that the upperbounds to the reaction probabilities reported in Figure 3.8 are probably somewhat too large.

The long range van der Waals interaction (Figure 3.4) directly affects the dynamics through the introduction of a shallow molecular adsorption (physisorption) well. Note that this physisorption well is not present if traditional functionals like PBE and RPBE are employed, as regular GGA functionals fail to describe long-range dispersion interactions. A molecule can be trapped either in one of the molecular adsorption (chemisorption) minima previously described (at $Z \approx 3$ Å from the surface) or in the vdW well (at Z between 3.5 and 5 Å from the surface). To illustrate the two kinds of adsorption we have chosen two representative trajectories (Figure 3.16). In Figure 3.16D the kinetic energy along the surface normal is plotted as a function of time for a molecule trapped in the vdW well (reported in red) and for a molecule trapped close to the surface (reported in green). We observe trapping in the vdW well only following the molecule-surface collision: it is only through the impact with the surface that the high collision energy can be transferred from the Z degree of freedom to other molecular or surface DOFs, allowing for the trapping in the shallow vdW well. Due to the low corrugation of the potential and the large distance from the surface, energy exchange between the molecular and the molecule-surface DOFs is expected to be slow. Therefore the dissociation of a molecule trapped in the vdW well might

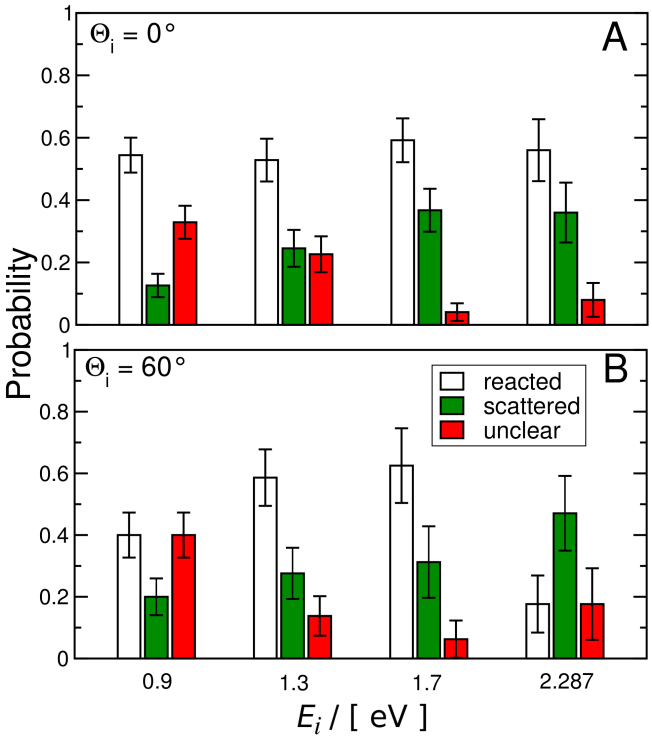

Figure 3.15: The white, green and red bars represent the probabilities for a trapped molecule to dissociate, to scatter or to remain trapped (unclear outcome), respectively. The results reported are for $\Theta_i = 0°$ (panel A) and $\Theta_i = 60°$ (panel B).

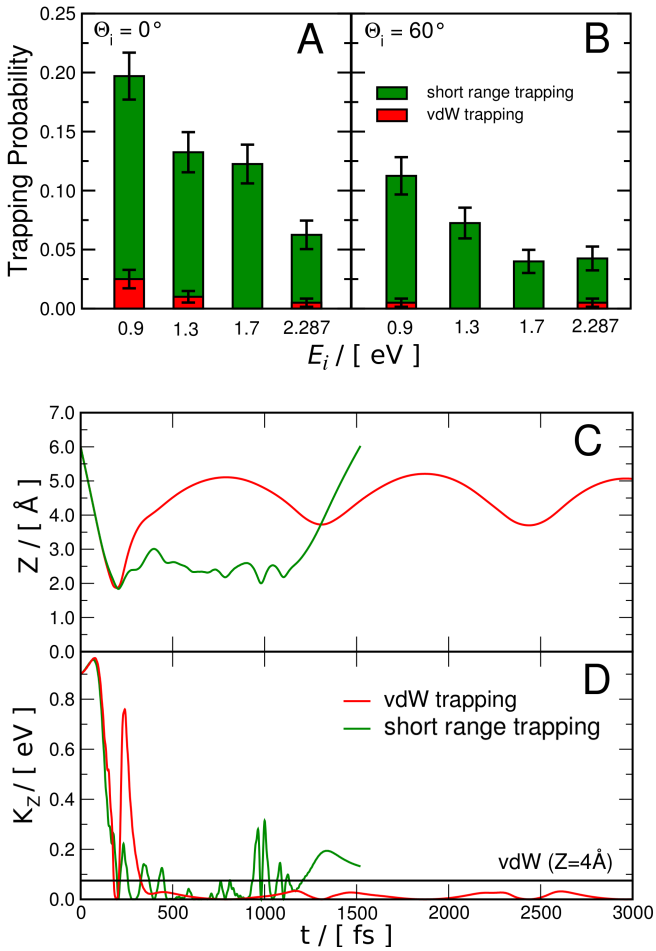

Figure 3.16: (A, B) Probability of short range and vdW trapping for the collision energies and angles studied. (C, D) Comparison between two trajectories undergoing short-range (green) and vdW (red) trapping; the distance from the surface (Z) and the kinetic energy along Z (K_Z) are plotted as a function of time. In panel (D), the interaction potential calculated at $Z = 4$ Å is plotted as a horizontal black line.

occur on a time scale that is too large compared to that which can be afforded with the AIMD method. However, using the vdW-DF2 functional, the trapping in the vdW well is quite rare at the collision energies investigated: for $\Theta_i = 0°$ at the lowest E_i we found that only 3% of the trajectories undergo trapping in the vdW well, and this value decreases to zero for higher collision energies and angles (Figure 3.16A). Therefore, assigning an outcome to these trajectories would not considerably change the conclusions of this work.

3.4 Summary and Conclusions

In this work, we have studied the static properties of the PES and we have computed the sticking probability for N_2 on W(110) employing AIMD. In the study of the PES the electronic structure calculations have been performed using functionals that include long range van der Waals interactions, as already tested on this system by Martin-Gondre *et al.* [17] with static and dynamic calculations, but only within the ideal and frozen surface approximation. We extended the static study with the vdW-DF and the vdW-DF2 functionals by considering more molecular adsorption configurations and we performed AIMD calculations, testing the vdW-DF2 functional, accounting for surface atom motion effects and long range interactions.

Using the vdW-DF2 functional, the PES shows improvements compared to PESs obtained with standard GGA functionals like PBE and RPBE [15]. The molecular adsorption wells are less deep and the barriers for the indirect dissociation and for the desorption from these molecular adsorption states are more similar to each other than with PBE and RPBE, in better agreement with experimental evidence [18]. Using the vdW-DF2 functional, the AIMD simulations show a lower trapping-mediated reaction probability than found for PBE and RPBE [15], resulting in a reasonable agreement with the molecular beam experiments of Pfnür *et al.* [8] at $E_i = 0.9$ eV.

However, AIMD underestimates the reaction probability measured by Pfnür *et al.* at the higher E_i values investigated, where the trapping-mediated dissociation

mechanism is negligible, resulting in a dissociation probability curve that does not depend on E_i, as previously found with semi-local functionals modeling surface atom motion [15]. This seems to suggest that the vdW-DF2 functional is still too repulsive in the area of the PES far from the surface in spite of the attractive vdW interaction modeled, and that the barriers for direct dissociation computed with the vdW-DF2 functional might still be too high.

When it comes to the overall performance of the functionals used with AIMD in describing the experiments of Pfnür *et al.* [8], the vdW-DF2, PBE, and RPBE functionals are of similar quality in describing the reaction probabilities measured at normal incidence, with none of the functionals performing very well. On the other hand, the vdW-DF2 functional performs best in describing the normal incidence data measured four years later by Rettner *et al.* The vdW-DF2 functional is also best at describing the reaction probabilities measured by Pfnür *et al.* [8] for off-normal incidence. We suggest that new experiments be performed to determine whether the difference between the normal incidence results of Pfnür *et al.* and Rettner *et al.* reflected improvements in the measurement techniques made over the four year time span that elapsed between the two publications. In surface science the N_2 + W(110) system has become a benchmark system for the accuracy of dynamical methods and density functionals at describing reactivity on metal surfaces. Unfortunately, in the study of this system we are arriving at a point where further progress is becoming hampered by the absence of well characterized and accurate molecular beam experiments, and by the presence of unexplained differences between the two experiments that are available for normal incidence.

Bibliography

[1] A. Nilsson, L. G. M. Pettersson, and J. K. Nørskov, *Chemical Bonding at Surfaces and Interfaces*. Amsterdam: Elsevier, 2008.

[2] G. A. Somorjai and Y. M. Li, "Impact of Surface Chemistry," *Proc. Natl. Acad. Sci. U. S. A.*, vol. 108, pp. 917–924, 2011.

[3] G. Ertl, "Surface Science and Catalysis-Studies on the Mechanism of Ammonia Synthesis: The P. H. Emmett Award Address," *Catal. Rev.*, vol. 21, pp. 201–223, 1980.

[4] F. Bozso, G. Ertl, M. Grunze, and M. Weiss, "Interaction of Nitrogen with Iron Surfaces," *J. Catal.*, vol. 49, pp. 18–41, 1977.

[5] S. P. Singh-Boparai, M. Bowker, and D. A. King, "Crystallographic Anisotropy in Chemisorption: Nitrogen on Tungsten Single-Crystal Planes," *Surf. Sci.*, vol. 53, pp. 55–73, 1975.

[6] C. T. Rettner, H. Stein, and E. K. Schweizer, "Effect of Collision Energy and Incidence Angle on the Precursor-Mediated Dissociative Chemisorption of N_2 on W(100)," *J. Chem. Phys.*, vol. 89, pp. 3337–3341, 1988.

[7] C. T. Rettner, E. K. Schweizer, and H. Stein, "Dynamics of the Chemisorption of N_2 on W(100): Precursor-Mediated and Activated Dissociation," *J. Chem. Phys.*, vol. 93, pp. 1442–1454, 1990.

[8] H. E. Pfnür, C. T. Rettner, J. Lee, R. J. Madix, and D. J. Auerbach, "Dynamics of the Activated Dissociative Chemisorption of N_2 on W(110): A Molecular Beam Study," *J. Chem. Phys.*, vol. 85, pp. 7452–7466, 1986.

[9] M. Alducin, R. Díez Muiño, H. F. Busnengo, and A. Salin, "Why N_2 Molecules with Thermal Energy Abundantly Dissociate on W(100) and Not on W(110)," *Phys. Rev. Lett.*, vol. 97, p. 056102, 2006.

[10] M. Alducin, R. Díez Muiño, H. F. Busnengo, and A. Salin, "Low Sticking Probability in the Nonactivated Dissociation of N_2 Molecules on W(110)," *J. Chem. Phys.*, vol. 125, p. 144705, 2006.

[11] G. A. Bocan, R. Díez Muiño, M. Alducin, H. F. Busnengo, and A. Salin, "The Role of Exchange-Correlation Functionals in the Potential Energy Surface and Dynamics of N_2 Dissociation on W Surfaces," *J. Chem. Phys.*, vol. 128, p. 154704, 2008.

[12] J. P. Perdew, J. A. Chevary, S. H. Vosko, K. A. Jackson, M. R. Pederson, D. J. Singh, and C. Fiolhais, "Atoms, Molecules, Solids, and Surfaces: Applications of the Generalized Gradient Approximation for Exchange and Correlation," *Phys. Rev. B*, vol. 46, pp. 6671–6687, 1992.

[13] J. P. Perdew, J. A. Chevary, S. H. Vosko, K. A. Jackson, M. R. Pederson, D. J. Singh, and C. Fiolhais, "Erratum: Atoms, Molecules, Solids, and Surfaces: Applications of the Generalized Gradient Approximation for Exchange and Correlation," *Phys. Rev. B*, vol. 48, p. 4978, 1993.

[14] B. Hammer, L. B. Hansen, and J. K. Nørskov, "Improved Adsorption Energetics Within Density-Functional Theory Using Rrevised Perdew-Burke-Ernzerhof Functionals," *Phys. Rev. B*, vol. 59, pp. 7413–7421, 1999.

[15] F. Nattino, F. Costanzo, and G. J. Kroes, "N_2 Dissociation on W(110): An Ab Initio Molecular Dynamics Study on the Effect of Phonons," *J. Chem. Phys.*, vol. 142, p. 104702, 2015.

[16] J. P. Perdew, K. Burke, and M. Ernzerhof, "Generalized Gradient Approximation Made Simple," *Phys. Rev. Lett.*, vol. 77, pp. 3865–3868, 1996.

[17] L. Martin-Gondre, J. I. Juaristi, M. Blanco-Rey, R. Díez Muiño, and M. Alducin, "Influence of the van der Waals Interaction in the Dissociation Dynamics of N_2 on W(110) from First Principles," *J. Chem. Phys.*, vol. 142, p. 074704, 2015.

[18] J. C. Lin, N. Shamir, Y. B. Zhao, and R. Gomer, "Adsorption, Desorption and Dissociation of N_2 on W(110)," *Surf. Sci.*, vol. 231, pp. 333–343, 1990.

[19] M. Dion, H. Rydberg, E. Schröder, D. C. Langreth, and B. I. Lundqvist, "Van der Waals Density Functional for General Geometries," *Phys. Rev. Lett.*, vol. 92, p. 246401, 2004.

[20] K. Lee, É. D. Murray, L. Z. Kong, B. I. Lundqvist, and D. C. Langreth, "Higher-Accuracy van der Waals density functional," *Phys. Rev. B*, vol. 82, p. 081101, 2010.

[21] G. J. Kroes, "Toward a Database of Chemically Accurate Barrier Heights for Reactions of Molecules with Metal Surfaces," *J. Phys. Chem. Lett.*, vol. 6, pp. 4106–4114, 2015.

[22] G. Kresse and J. Hafner, "Ab Initio Molecular Dynamics for Liquid Metals," *Phys. Rev. B*, vol. 47, pp. 558–561, 1993.

[23] G. Kresse and J. Furthmüller, "Efficiency of Ab-Initio Total Energy Calculations for Metals and Semiconductors Using a Plane-Wave Basis Set," *Comput. Mater. Sci*, vol. 6, pp. 15–50, 1996.

[24] G. Kresse and J. Furthmüller, "Efficient Iterative Schemes for Ab Initio Total-Energy Calculations Using a Plane-Wave Basis Set," *Phys. Rev. B*, vol. 54, pp. 11169–11186, 1996.

[25] G. Kresse and D. Joubert, "From Ultrasoft Pseudopotentials to the Projector Augmented-Wave Method," *Phys. Rev. B*, vol. 59, pp. 1758–1775, 1999.

[26] P. E. Blöchl, "Projector Augmented Wave-Method," *Phys. Rev. B*, vol. 50, pp. 17953–17979, 1994.

[27] G. Román-Pérez and J. M. Soler, "Efficient Implementation of a van der Waals Density Functional: Application to Double-Wall Carbon Nanotubes," *Phys. Rev. Lett.*, vol. 103, p. 096102, 2009.

[28] J. Klimeš, D. R. Bowler, and A. Michaelides, "Chemical Accuracy for the van der Waals Density Functional," *J. Phys. Condens. Matter*, vol. 22, p. 022201, 2010.

[29] J. S. Shah and M. E. Straumanis, "Thermal Expansion of Tungsten at Low Temperatures," *J. Appl. Phys.*, vol. 42, pp. 3288–3289, 1971.

[30] G. Henkelman, B. P. Uberuaga, and H. Jónsson, "A Climbing Image Nudged Elastic Band Method for Finding Saddle Points and Minimum Energy Paths," *J. Chem. Phys.*, vol. 113, pp. 9901–9904, 2000.

[31] G. Henkelman and H. Jónsson, "Improved Tangent Estimate in the Nudged Elastic Band Method for Finding Minimum Energy Paths and Saddle Points," *J. Chem. Phys.*, vol. 113, pp. 9978–9985, 2000.

[32] A. De Vita, I. Štich, M. J. Gillan, M. C. Payne, and L. J. Clarke, "Dynamics of Dissociative Chemisorption: Cl_2/Si(111)-(2×1)," *Phys. Rev. Lett.*, vol. 71, pp. 1276–1279, 1993.

[33] I. Štich, M. C. Payne, A. De Vita, M. J. Gillan, and L. J. Clarke, "Chemically Driven Molecular Decomposition at Semiconductor Surfaces," *Chem. Phys. Lett.*, vol. 212, pp. 617–623, 1993.

[34] I. Štich, A. De Vita, M. C. Payne, M. J. Gillan, and L. J. Clarke, "Surface Dissociation from First Principles: Dynamics and Chemistry," *Phys. Rev. B*, vol. 49, pp. 8076–8085, 1994.

[35] A. Groß and A. Dianat, "Hydrogen Dissociation Dynamics on Precovered Pd Surfaces: Langmuir is still Right," *Phys. Rev. Lett.*, vol. 98, p. 206107, 2007.

[36] L. S. Dubrovinsky and S. K. Saxena, "Thermal Expansion of Periclase (MgO) and Tungsten (W) to Melting Temperatures," *Phys. Chem. Miner.*, vol. 24, pp. 547–550, 1997.

[37] X. Qian and W. Hübner, "First-Principles Calculation of Structural and Magnetic Properties for Fe Monolayers and Bilayers on W(110)," *Phys. Rev. B*, vol. 60, pp. 16192–16197, 1999.

[38] H. L. Meyerheim, D. Sander, R. Popescu, P. Steadman, S. Ferrer, and J. Kirschner, "Interlayer Relaxation of W(110) Studied by Surface X-Ray Diffraction," *Surf. Sci.*, vol. 475, pp. 103–108, 2001.

[39] W. L. Hays, *Statistics, 3rd edn.* Holt: Rinehart and Winston, 1981.

[40] Q. J. Zhang, J. C. Lin, N. Shamir, and R. Gomer, "Electron-Stimulated Desorption and Conversion of N_2 Adsorbed on a Tungsten (110) Plane," *Surf. Sci.*, vol. 231, pp. 344–355, 1990.

[41] C. Díaz, E. Pijper, R. A. Olsen, H. F. Busnengo, D. J. Auerbach, and G. J. Kroes, "Chemically Accurate Simulation of a Prototypical Surface Reaction: H_2 Dissociation on Cu(111)," *Science*, vol. 326, pp. 832–834, 2009.

[42] B. Baule, "Theoretische Behandlung der Erscheinungen in verdünnten Gasen," *Ann. Phys.*, vol. 349, pp. 145–176, 1914.

Chapter 4

Surface Reaction Barriometry: Methane Dissociation on Flat and Stepped Transition Metal Surfaces

This Chapter is based on:

D. Migliorini[1], H. Chadwick[1], F. Nattino, A. Gutiérrez-González, E. Dombrowski, E. A. High, H. Guo, A. L. Utz, B. Jackson, R. D. Beck, and G. J. Kroes, *J. Chem. Phys. Lett.*, 8, 4177 (2017); (E) *J. Chem. Phys. Lett.*, 10, 661 (2019)

https://pubs.acs.org/doi/abs/10.1021/acs.jpclett.7b01905

(E) https://pubs.acs.org/doi/abs/10.1021/acs.jpclett.9b00186

which are reproduced with the permission of ACS Publications[2].

[1]These authors contributed equally to the paper.

[2]further permissions related to the material excerpted should be directed to the ACS.

Abstract

Accurately simulating heterogeneously catalyzed reactions requires reliable barriers for molecules reacting at defects on metal surfaces, such as steps. However, first principles methods capable of computing these barriers to chemical accuracy have yet to be demonstrated. In this Chapter we show that state-resolved molecular beam experiments combined with *ab initio* molecular dynamics using specific reaction parameter density functional theory (SRP-DFT) can determine the molecule-metal surface interaction with the required reliability. Crucially, SRP-DFT exhibits transferability: the functional devised for methane reacting on a flat (111) face of Pt (and Ni) also describes its reaction on stepped Pt(211) with chemical accuracy. Our approach can help bridge the materials gap between fundamental surface science studies on regular surfaces and heterogeneous catalysis in which defected surfaces are important.

4.1 Introduction

Heterogeneous catalysis plays a key role in the production of most chemicals, and quantitatively accurate predictions of the rates and pathways of elementary steps can guide catalyst design and optimization. With the theoretical toolbox now available, it is possible to predict trends in transition-metal catalysis, and identify which materials should constitute good catalysts for making particular chemicals [1]. However, theory still struggles to compute reaction rates reliably, with errors in the rate of ammonia production over Ru still being approximately 1-2 orders of magnitude [2].

Several factors complicate the calculation of rates of heterogeneously catalyzed processes [3]. These processes typically consist of sequences of elementary surface reactions, as illustrated by the Haber-Bosch production of NH_3 in work that contributed to G. Ertl winning the 2007 Nobel Prize in chemistry [4]. Typically, only one or a few reactions are "rate-controlling", so one can focus on these reactions [5]. However, the exponential dependence of reaction rate on activa-

tion energy places severe demands on the accuracy of reaction barrier heights calculated for the associated rate-controlling transition states [3, 6]. These barrier heights cannot be measured directly, and are best determined through a close comparison of molecular beam experiments and dynamics calculations reproducing the reaction probabilities measured therein [7]. On the theory side, first principles methods capable of computing the electronic energies of these states with chemical accuracy (1 kcal/mol) have yet to be demonstrated, and efforts to develop databases of reaction barriers for surface reactions are in their infancy [7]: Presently chemically accurate barriers are available only for four systems, in which a molecule reacts with a flat, low index metal surface [7–10].

While a semi-empirical density functional theory (DFT) approach [10, 11] for computing barriers on flat surfaces has been demonstrated, it has long been known [12] that catalyzed reactions proceed mainly over sites usually called "defects", such as kinks and steps [13–16]. Simulations of catalyzed reactions often attempt to take this into account by computing the energies of the relevant states for model "defected surfaces" using standard density functionals [6, 17, 18]. Here, by defected surface we mean a surface containing line defects (such as steps or edges) or point defects (such as kinks or corners), even though such a surface might be a regular crystal surface definable through Miller indices. Unfortunately, such simulations cannot yet be expected to capture the important effects of point and extended surface defects and of multifaceted surfaces [3]. Furthermore, standard density functionals (i.e., the classes of non-empirical functionals based on constraints and semi-empirical functionals fitted to a range of chemical and/or material properties [3]) only yield semi-quantitative results for barrier heights of surface reactions on metals [7].

Here, we test the accuracy of a joint theoretical-experimental approach (which we call reaction barriometry) that uses results from a flat, low index metal surface to obtain the minimum barrier for a molecule (CHD_3) reacting on a stepped Pt(211) surface. We apply a surface science approach to derive a semi-empirical functional that accurately describes a reaction on a flat metal surface (CHD_3 + Pt(111)), and then rely on the transferability of that functional to describe

the reaction on the defected surface (Pt(211), note that (211) surfaces of fcc metals consist of 3-atom wide (111) terraces and (100) steps). For catalysis by Pt-particles, the molecule-surface reaction we address is the rate-limiting step of the steam-reforming process [19], which is widely used for industrial hydrogen production. Microkinetic simulations of steam reforming on Ni (the commercial catalyst) and Pt often use the (211) surface to simulate step site reactivity [6, 18]. Dissociation of methane on transition metal surfaces is also of fundamental interest, as a benchmark system exhibiting several interesting dynamical features [20–22], including selective bond breaking of partially deuterated methane [23].

This Chapter is organized as follows. The method used to perform and analyze the calculations is reported in Section 4.2, the main results and their implications for heterogeneous catalysis are then discussed in Section 4.3 and the conclusions are summarized in Section 4.4.

4.2 Method

Our approach for determining barriers for molecules reacting at defected surfaces can be summarized in five steps (extensively discussed in Chapter 2 and Refs. [10, 24]): (i) Perform conventional ("laser-off") molecular beam experiments on the molecule (here: CHD_3) reacting on a flat surface (here: Pt(111), top view in Figure 4.1A) to determine the reaction probability as a function of average incident kinetic energy, $\langle E_i \rangle$. In these experiments, the $\langle E_i \rangle$, the nozzle temperature T_n, and the surface temperature T_s should be taken such that the applicability of classical mechanics is ensured. Next, (ii) fit a candidate specific reaction parameter (SRP) functional to the measured reaction probabilities (S_0) using *ab initio* molecular dynamics (AIMD) calculations. Subsequently (iii) measure the initial state-resolved reaction probabilities (here: for $CHD_3(\nu_1 = 1)$), and (iv) validate the candidate SRP functional by showing that AIMD calculations using this functional also reproduce the initial state-resolved experiments. The new finding presented here is that, in the final step (v), the SRP density functional derived for the molecule interacting with the flat surface can be used to derive

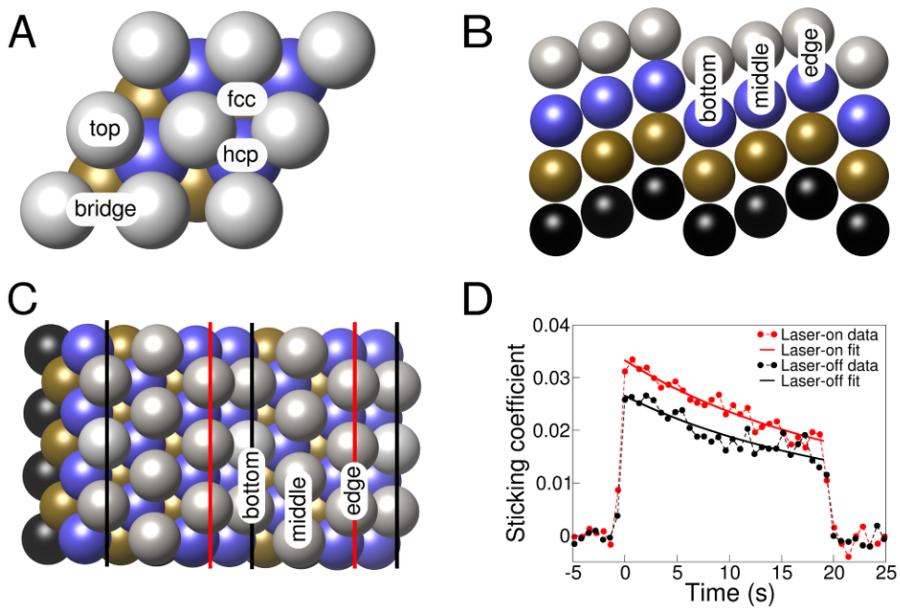

Figure 4.1: Views of the (111) and the (211) faces of fcc metals (like Ni and Pt), and experimental Kings and Well trace. (A) Top view of the (111) face. (B and C) Side and top views of the (211) face. (D) Kings and Wells trace of a measurement on CHD_3 + Pt(111) at $\langle E_i \rangle = 82$ kJ/mol.

the barrier height for the molecule reacting on the defected (stepped) surface, as we will show here for CHD_3 + Pt(211) (top and side views in Figures 4.1B and 4.1C). The underlying assumption, which has been argued before [10, 11], is this: if an SRP functional provides chemically accurate predictions of S_0 for measurements made near the energy threshold and for multiple combinations of $\langle E_i \rangle$ and vibrational excitation (laser-off or $\nu_1 = 1$ reaction), it will also provide a chemically accurate description of the height of the minimum barrier, and accurately describe its geometry. All experiments and calculations reported here were done for normal incidence. As the dissociation of methane on transition metal surfaces like Ni(111) [25] and Pt(111) [26] typically follows normal energy scaling, this samples the initial conditions which have the most significant effect on the reactivity.

In modeling the reaction of methane with transition metal surfaces we compute reaction probabilities with AIMD, which allows modeling of the effects of

surface atom vibrations and T_s, as required [27]. The calculations use the *ab initio* total energy and AIMD program VASP [28, 29]. The SRP functional derived previously [10] for CHD_3 + Ni(111) is:

$$E_{XC}^{SRP} = x \cdot E_X^{RPBE} + (1 - x) \cdot E_X^{PBE} + E_C^{\text{vdW-DF}}. \tag{4.1}$$

In Equation 4.1 (for detailed justification see Refs. [10, 24] and Chapter 2), E_X^{RPBE} and E_X^{PBE} are the exchange parts of the RPBE [30] and PBE [31] functionals, and $E_C^{\text{vdW-DF}}$ is a correlation functional that provides an approximate description of the attractive van der Waals interaction [32]. Adjusting the fit parameter x allows one to reproduce reactivity [10], while the use of well-constrained exchange and correlation functionals ensures the functional's robustness for other system properties, e.g. crystal lattice structure. As before [10], molecular beam reflectivity experiments [33] are used to determine CHD_3 sticking coefficients, with typical data shown in Figure 4.1D. Laser preparation of the incident CHD_3 in a specific rovibrationally excited quantum state ($\nu_1 = 1$, $J = 2$, $K = 1$) yields state-resolved reaction probabilities of $CHD_3(\nu_1 = 1)$. For further methodological details, see Chapter 2 and the SI of Ref. [24].

4.3 Results and Discussion

4.3.1 Theory-Experiment Comparison

To enable us to make an important point regarding the transferability of our approach, reaction probabilities computed and measured earlier for CHD_3 + Ni(111) are presented in Figure 4.2A.

For CHD_3 + Ni(111), the value of x (0.32) was fitted with AIMD calculations modeling laser-off experiments with $\langle E_i \rangle = 112$ and 121 kJ/mol ($T_n = 600$ and 650 K). Using that x value, AIMD calculations predicted S_0 for $CHD_3(\nu_1 = 1)$ with chemical accuracy, confirming the quality of the SRP functional (Figure 4.2A). For $\langle E_i \rangle > 130$ kJ/mol calculations slightly overestimated laser-off reactivity. This was attributed to quasi-classical mechanics overestimating the reac-

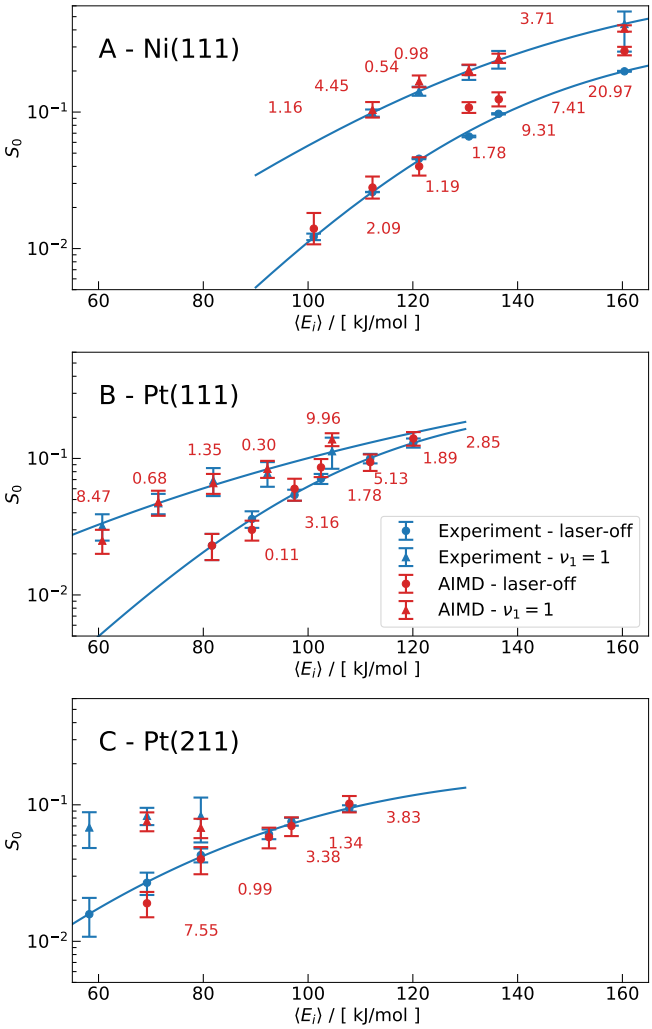

Figure 4.2: Comparison of theory with experiments for CHD_3 + Ni(111), Pt(111), and Pt(211): Reaction probabilities as a function of $\langle E_i \rangle$. (A) Reaction probabilities calculated with AIMD and measured in molecular beam experiments for CHD_3 + Ni(111). Blue symbols and lines: experimental results and fits to experiment. Red symbols: AIMD results. Circles are for laser-off conditions and triangles for $\nu_1 = 1$ CHD_3. Numbers show the distance of the computed reaction probability to the fitted experimental curve along the incidence energy axis, in kJ/mol. Results reported in Panel A are reproduced from Ref. [10]. (B and C) Same as Panel A, but results from this Chapter for CHD_3 + Pt(111) and Pt(211).

tivity of excited CD vibrational states, which become increasingly populated at higher T_n ($\geq$ 700 K). Under these conditions AIMD calculations overestimate the fraction of CHD_3 molecules dissociating via CD bond cleavage [10]. Here, new experiments and AIMD calculations are performed for CHD_3 + Pt(111). In the fitting of x in Equation 4.1 we could take a shortcut as the value of $x = 0.32$ derived for CHD_3 + Ni(111) also provided excellent agreement between experiment and theory for CHD_3 + Pt(111) (Figure 4.2B). For laser-off reaction chemical accuracy is obtained over the entire range of $\langle E_i \rangle$: on average the distance between the computed reaction probabilities and the fitted experimental curve along the energy axis is less than 4.2 kJ/mol ($\approx$ 1 kcal/mol). The minimum barrier height to reaction, calculated with the surface frozen in its relaxed 0 K configuration, on Pt(111) (E_b = 79 kJ/mol, Table 4.1) is considerably lower than on Ni(111) (98 kJ/mol, Table 4.1). Therefore, laser-off experiments with $\langle E_i \rangle \leq 120$ kJ/mol ($T_n \leq 650$ K) sample the full reactivity range of interest on Pt(111), and the complications associated with excited CD vibrational states at higher T_n seen for Ni(111) are avoided. The AIMD results also show chemical accuracy for $CHD_3(\nu_1 = 1)$ + Pt(111), a result that is not achieved using the PBE functional [34] despite the transition state being similar to the SRP functional, as shown in Table 4.1 and discussed in Chapter 6. We attribute the observation of larger individual deviations to statistical fluctuations in the calculated reaction probabilities, and we note that in two of the three cases, computed probabilities are compared to an extrapolated ($\nu_1 = 1$) experimental curve. The comparison of the AIMD results to the molecular beam data also meets a statistical accuracy test (see Table S1 and the SI of Ref. [24]).

The good agreement observed here for CHD_3 + Pt(111) using an SRP functional developed for CHD_3 + Ni(111) suggests that SRP functionals are transferable among chemically related systems (here: systems in which the same molecule reacts on the same low index surface of group 10 metals). We take this as additional proof of the sound physical basis of the SRP-DFT approach. We now proceed to CHD_3 reacting on the stepped Pt(211) surface. Again, the agreement between theory and experiment is excellent (Figure 4.2C). The theory using

metal surface	E_b / [kJ/mol]	r_b / [Å]	Z_b / [Å]	θ_{CH} / [∘]
Ni(111)	97.9 (104.2)	1.61 (1.60)	2.18 (2.12)	136 (133)
Pt(111)	78.7 (77.8)	1.56 (1.50)	2.28 (2.25)	133 (134)
Pt(211)	53.9 (46.0)	1.53 (1.48)	2.27 (2.24)	133 (134)

Table 4.1: Computed barrier heights E_b, the CH distance of the dissociating bond r_b, the distance of the C atom to the surface Z_b, and the angle the dissociating bond makes with the surface normal (θ_{CH}) in the minimum barrier geometry for the SRP functional. PBE results (from Ref. [35] for Ni(111), Ref. [36] for Pt(111), and from this work for Pt(211)) are shown in brackets for comparison.

$x = 0.32$, describes the measured laser-off reactivity with chemical accuracy. Not enough data were available to make a fit of the experimental data for $\nu_1 = 1$ reaction, but the theoretical reaction probabilities agree with the experimental values within error bars. Again, the comparison of the AIMD results to the molecular beam data also meets our statistical accuracy test (Table S1 in the SI of Ref. [24]). Note that we were not able to compare experiment with AIMD calculations at the lowest $\langle E_i \rangle$ for which experimental results were available. For this condition, large calculated trapping probabilities precluded an accurate comparison of the AIMD results with the experiments (see Figure 4.3). However, this does not invalidate our comparison since the average trapping time on the surface has been estimated using Frenkel's formula [37] to be about 43 ps. In this long trapping time the molecule has time to explore the surface and to react on higher order defects (such as kinks) that might be present on the experimental surface possibly reducing the difference between experiments and theory (more details are reported in Chapter 5). Furthermore, at higher $\langle E_i \rangle$ where the trapping probability is negligible, the agreement with the experiments is excellent. The E_b value extracted for CH_4 + Pt(211) (54 kJ/mol, Table 4.1) is much lower than for Pt(111) (79 kJ/mol).

The AIMD calculations also yield insights into reaction dynamics. Figure 4.4 shows that even vibrationally pre-excited CHD_3 reacts preferentially at the steps (near the under-coordinated Pt atoms labeled "edge" in Figures 4.1B and 4.1C). This prediction can be tested with reflection absorption infrared spectroscopy

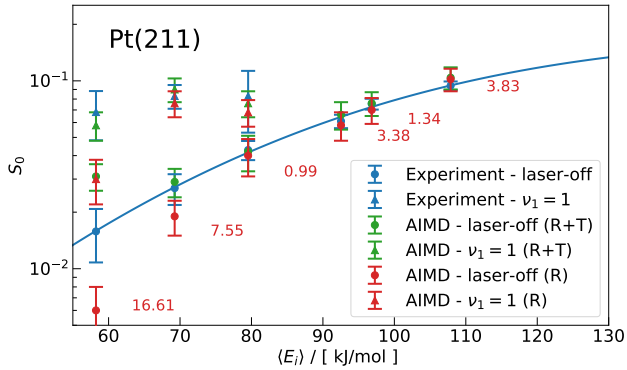

Figure 4.3: Experimental and AIMD results (blue and red, respectively) for CHD_3 on Pt(211). The AIMD results computed considering the trapped trajectories as reacted (R+T) are reported in green. The distance from the AIMD results to the experimental fit (in kJ/mol) is reported in red.

[38]. While approaching the surface at normal incidence, the reactive molecules hardly change their projection on the surface (Figure 4.4). This result simplifies high-dimensional quantum dynamics calculations, because the dimensionality can be reduced using the "sudden" approximation to the molecule's motion along the surface. This amounts to averaging over calculations performed for fixed projections of the molecule on the surface [39–41]. Finally, calculations on CHD_3 + Pt(111) using the reaction path Hamiltonian (RPH) method [39] reveal how the molecular physisorption well affects reactivity. As discussed in the SI of Ref. [24], according to RPH calculations the use of the SRP functional yields a larger promoting effect on the reaction of pre-exciting the CH- and CD-stretch vibrations than the use of the PBE functional (see Figure S2 and the SI of Ref. [24]). Model calculations attribute this to the molecule's acceleration in the physisorption well, which leads to increased energy transfer from these vibrations to motion along the reaction path (see Figure S3 in the SI of Ref. [24]).

Our results point to the following promising approach to simulating heterogeneously catalyzed processes where elementary dissociative chemisorption reactions are rate controlling. First, perform AIMD calculations and molecular beam measurements of dissociative chemisorption on a low index face of the cat-

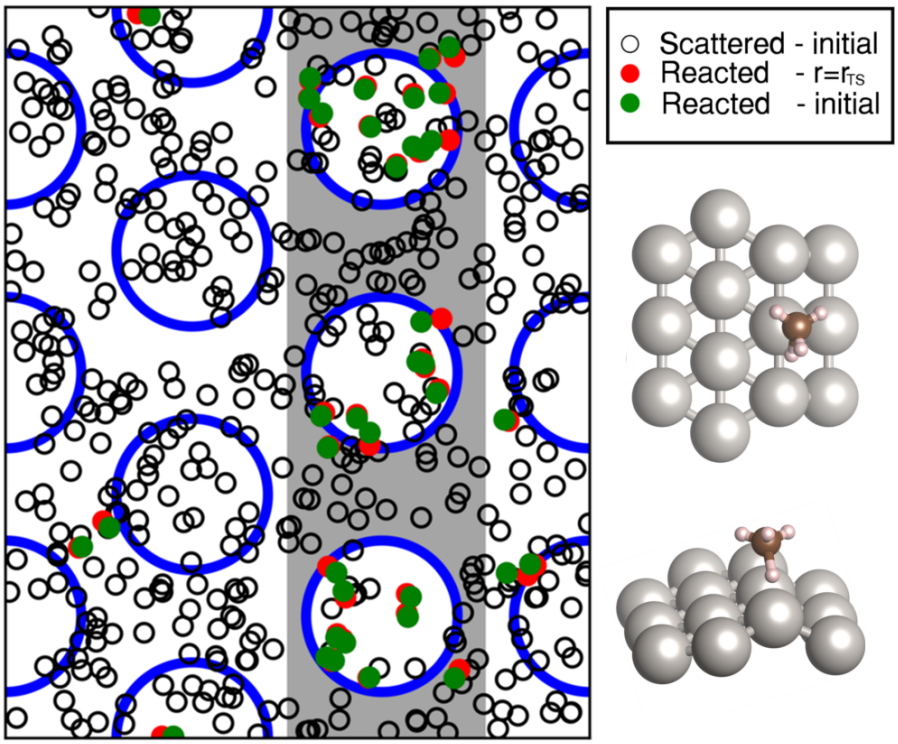

Figure 4.4: Points of impact of $CHD_3(\nu_1 = 1)$ molecules that react on Pt(211) for $\langle E_i \rangle = 69$ kJ/mol, at time zero (green circles) and at the time of reaction (red circles), and initial points of impact of the molecules that scatter (white circles). The blue circles denote the top layer Pt atoms and the grey zone consists of the step edge atoms where the molecules react predominantly. The top and side views of the minimum barrier geometry, which is located on a step edge atom, are reported as insets.

alyst metal to derive an SRP functional. Next, exploit the transferability of the SRP functional demonstrated here (between Pt(111) and Pt(211)) to simulate the overall reaction proceeding on multifaceted catalyst particles on which point and extended surface defects are also present. The SRP functional is then used to also compute barriers (or activation energies) at these defects, and at other low index facets (the transferability of SRP functionals among low index faces of metals was already demonstrated for H_2 + Cu(111) and Cu(100) [8]). Such an approach can help bridge the materials gap between surface science (which deals with smooth surfaces) and catalysis (with reactions typically proceeding over nanoparticles exhibiting defects) [42, 43]. The present research describes a test-case of transferability in which a single σ-bond is broken, for which the transition state typically occurs over a surface atom, and surface defects promote the reaction by decreasing the coordination of the surface atoms [44]. While the transferability is here demonstrated for only one example, arguments based on the dependence of the molecular adsorption energy on the co-ordination of the metal atom adsorbed to, experiments, and transition-state scaling relations suggest that the demonstrated transferability should hold more generally for σ-bond breaking (more details are reported in the next Section).

An additional structural requirement (high coordination of the transition state [44]) needs to be met for defect sites at which double or triple π-bonds are broken. Further investigations will therefore have to test whether the transferability found here for σ-bond breakage also holds when double and triple π-bonds are broken, as we believe. This belief can be supported on the basis of transition-state scaling relations also holding for the breaking of double and triple bonds (more details are reported in the next Section). Future investigation might also test whether our approach can be extended to deal with direct support effects on the catalysis (i.e., other than the effect that the support may alter the size distribution and the shape of the supported nanonparticles), and the presence of dopant atoms and additives [3]. Finally, on the basis of accurate quantum Monte-Carlo calculations on H_2 + Cu(111) [45] we anticipate that it will soon be possible to fit accurate SRP functionals to reliable QMC calculations on molecules reacting on surfaces.

This will put SRP-DFT on a first principles basis, and will yield a method that is easier to apply than the combined experimental/theoretical approach presented.

4.3.2 Implications for Simulating Heterogeneous Catalysis

The transferability of SRP functionals shown here for dissociative chemisorption of a molecule on a low-index, flat surface to a stepped surface points to a promising approach for accurately simulating rates of heterogeneously catalyzed reactions over metal nanoparticles. In this approach, one would use the finding that usually only a few states (transition states, or states describing adsorbed reactants, adsorbed reaction intermediates, or adsorbed products) exhibit a large degree of rate control [5]. Only for these states should it be necessary to determine the molecule-metal surface interaction energy accurately [5]. Of these states, accurate calculations of the transition states should be most important, as molecular adsorption energies are reasonably accessible through experiments using single crystal adsorption calorimetry and thermal desorption spectroscopy [46, 47]. It should be possible to fit a semi-empirical functional with an expression similar to that of Equation 4.1 to a molecule or reaction intermediate adsorbed on a low index metal surface either using existing experimental information, or in a procedure involving a new adsorption experiment. We argue that the transferability observed in the present work for transition states then suggests that the semi-empirical functional determined in this fashion should also accurately predict adsorption at surface defects, such as steps, edges, kinks and corners. Strong supporting evidence comes from recent work by Sautet and co-workers which showed that adsorption energies of OH and OOH on Pt [48] and other transition metal [49] surfaces depends linearly on the generalized coordination number of the surface atom these species adsorb to, and the finding that, based on these relations, theory is able to correctly predict that specific stepped Pt surfaces are more active for oxygen reduction than the Pt(111) surface [50].

The reaction studied in the present work is an important representative of a class of structure sensitive reactions in which the bond broken is a single σ-type bond (e.g., a CH or single CC bond) [44]. In the transition state of such reactions,

the dissociating molecule usually sits on top of a surface atom [44] (a "top site" if the reaction occurs on a low index surface). Usually, the reaction barrier is lowered over surface atoms of lower coordination number [44] (surrounded by fewer nearest neighbour metal atoms), for instance over surface atoms at the top edge of a step, as observed here for CHD_3 + Pt(211). The implication of our present work and earlier work on transferability among metal facets [8] is that one can use an SRP functional developed for the reaction on a low index surface to accurately compute barrier heights for the molecule's dissociation over surface atoms occurring in other low index facets and at surface line and point defects with lower coordination numbers of surface atoms. The derived barrier heights can then be used in kinetics simulations of the overall heterogeneously catalyzed reaction as it occurs over a metal nanoparticle exhibiting specific facets, line defects, and point defects. We argue that the rates calculated in this manner should be more accurate than rates calculated on the basis of standard density functionals (non-empirical functionals based on constraints, or conventional semi-empirical functions fitted to a range of chemical properties and/or materials properties [3]).

The above argument that rates over defected surfaces computed from SRP functionals accurately describe transition state energies on flat surfaces also has a basis in the recent work of Sautet and co-workers, and the so-called transition state scaling relationships. As noted above, it is already possible with standard functionals to predict which Pt crystal surface (with atoms located at defects possessing specific generalized coordination numbers) is most active for a specific reaction (oxygen reduction [50]). The adsorption energies of involved reactant molecules depend linearly on the generalized coordination number [48]. In turn, transition state energies usually scale linearly with the adsorption energies of reactants (the transition state scaling relationship) [1, 51]. The above suggests that transition state energies should scale linearly with generalized coordination numbers, and that if the off-set of the linear relationship is accurately determined (by determining the transition state energy for the flat surface) it should be possible to accurately determine the transition state energy for other generalized coordination numbers (on stepped surfaces) accurately as well.

Another class of structure-sensitive reactions, in which a double or triple π-bond breaks in the molecule, may present a greater challenge to transferability. Examples of such reactions are CO and N_2 bond breaking, where an additional requirement of the transition state (additional to presenting surface atoms with lower coordination number) is that the reaction site is able to coordinate many surface atoms to the dissociating molecule, to facilitate the breaking of a strong double or triple bond [44]. A well-known example concerns ammonia production over Ru particles, in which the rate limiting step is N_2 bond breaking. Nørskov and co-workers have established that this reaction is accelerated by so-called B5-sites, in which the dissociation molecule is co-ordinated by 5 surface atoms [17]. Incidentally, such B5 sites are also present at the Pt(211) steps, and, more generally, at surfaces where hcp(0001) terraces or fcc(111) terraces are connected by (100)-type steps (see Ref. [52] and Figure 1 therein). Our present results show that on Pt(211) methane reacts at the step edge sites that are part of these B5 sites. The additional requirement of providing a higher coordination to the dissociating molecule might be perceived to present a greater challenge to the transferability of SRP functionals. However, we emphasize that the difference between the two broad classes of structure sensitive reactions is gradual. In the case we have looked at, the SRP functional is able to accurately describe the effect of changing the coordination number of the surface atom above which dissociation occurs. In the case of double or triple bond breaking, the SRP functional should additionally be able to describe the effect of the coordination to additional surface atoms for transferability to hold. While the accuracy with which this can be done has yet to be established, we argue that a similar approach to that taken here for CHD_3 + Pt(111) and Pt(211) and based on an SRP functional for the flat surface should be better than simply taking a constraint-based or conventional semi-empirical functional to obtain reaction barrier heights on facets and at surface defect reaction sites. In this respect, it is encouraging that the transition scaling relations accurately describe the relation between the transition state energies of N_2, CO, and NO on fcc(211) surfaces and the adsorption energies of these molecules at the upper terrace hcp sites [53].

Finally, the question might arise whether the approach we advocate would be sensible if, for example, simple bond breaking of a reactant molecule dominates the reaction at steps, while the breaking of this bond is preceded by reaction with another reactant on the terraces. A practical example is the initiation of Fischer-Tropsch synthesis over $\approx$ 4.6 nm Co nanoparticles, which expose 15% undercoordinated sites, which are mostly step edges of A- and B-type capable of direct CO-dissociation [54]. For this example, Westrate *et al.* [54] concluded that one can reasonably assume that direct CO dissociation at the undercoordinated sites is the primary mechanism for the initiation of the Fischer-Tropsch reaction, even though the reaction on the facets might proceed through a mechanism in which CO is hydrogenated prior to CO bond breaking. Therefore, the development of an SRP functional for dissociative chemisorption of the CO molecule on a terrace and its application to the reaction of the same molecule at steps might help to accurately describe an overall catalyzed reaction if this reaction is dominated by the steps, even though the rate limiting step, and indeed the mechanism of the catalyzed reaction, could be different on the flat surfaces making up the facets. Here, by the overall catalyzed process we mean the initiation of a Fischer-Tropsch synthesis reaction, and not necessarily the complete Fischer-Tropsch reaction making higher hydrocarbons. Note that one can determine whether line defects (such as steps) or point defects (such as kinks) dominate the rate of a catalyzed process over catalyst particles by determining the degree of structure reactivity parameter α, which describes the dependence of the rate on the catalyst particle diameter d [55]. For example, $\alpha = 1$ describes a process where the rate is dominated by line defects, and this value was found to accurately describe the rate of steam reforming over supported Pt nanoparticles [19].

The above finding of $\alpha = 1$ for steam reforming over Pt nanoparticles is only one reason that steam reforming over Pt nanoparticles should constitute an ideal test case for our SRP density functional for methane interacting with Pt particles. Wei and Iglesia also found that steam reforming rates over Pt particles were exclusively limited by the first CH bond cleavage [19]. Additionally, they found that steam reforming over supported Pt nanoparticles proceeds over

essentially uncovered catalyst particles, and that support effects are indirect (they are described fully by how the support affects the shape of the catalyst particles).

Our approach is useful for getting accurate transition states for elementary dissociation reactions of molecules that are stable in the gas-phase, and therefore useful for simulating heterogeneous catalysis if such reactions play an important role in the mechanism of the catalyzed reaction. Examples of such reactions are dissociative chemisorption of methane in steam reforming [18, 19], of water in the water gas shift reaction [56], of N_2 in ammonia production [17, 57], and of CO in many realizations of the Fischer-Tropsch process [58]. It is less useful if the rate limiting step is, for instance, the hydrogenation of an already adsorbed reaction intermediate, as is the case for the overall Fischer-Tropsch synthesis reaction over supported Fe nanoparticles [59]. Catalyzed reactions with complex reaction mechanisms (such as hydrogenation of olefins on supported Pd catalysts involving sub-surface hydrogen [60]) certainly exist for which the present approach will be of little help. Nevertheless, our new approach is likely to provide valuable input for catalyzed reactions in which the overall rate is dominated by simple dissociation reactions of stable molecules.

4.4 Summary and Conclusions

We have demonstrated a joint theoretical-experimental approach (which we call reaction barriometry) that uses results from a reaction on a flat, low index metal surface to obtain a chemically accurate barrier for the same reaction on a stepped surface of the metal. We have applied a surface science approach to derive a semi-empirical functional that accurately describes the dissociation of CHD_3 on Pt(111), and then have shown the transferability of this functional to describe its dissociation on the stepped Pt(211) surface. Our approach can help bridge the materials gap between fundamental surface science studies on regular surfaces and real-life heterogeneous catalysis where reactions often proceed over defected metal nanoparticles.

Bibliography

[1] A. J. Medford, A. Vojvodic, J. S. Hummelshøj, J. Voss, F. Abild-Pedersen, F. Studt, T. Bligaard, A. Nilsson, and J. K. Nørskov, "From the Sabatier Principle to a Predictive Theory of Transition-Metal Heterogeneous Catalysis," *J. Catal.*, vol. 328, pp. 36–42, 2015.

[2] A. J. Medford, J. Wellendorff, A. Vojvodic, F. Studt, F. Abild-Pedersen, K. W. Jacobsen, T. Bligaard, and J. K. Nørskov, "Assessing the Reliability of Calculated Catalytic Ammonia Synthesis Rates," *Science*, vol. 345, pp. 197–200, 2014.

[3] M. K. Sabbe, M. F. Reyniers, and K. Reuter, "First-Principles Kinetic Modeling in Heterogeneous Catalysis: an Industrial Perspective on Best-Practice, Gaps and Needs," *Catal. Sci. Technol.*, vol. 2, pp. 2010–2024, 2012.

[4] G. Ertl, "Primary Steps in Catalytic Synthesis of Ammonia," *J. Vac. Sci. Technol. A*, vol. 1, pp. 1247–1253, 1983.

[5] C. Stegelmann, A. Andreasen, and C. T. Campbell, "Degree of Rate Control: How Much the Energies of Intermediates and Transition States Control Rates," *J. Am. Chem. Soc.*, vol. 131, pp. 8077–8082, 2009.

[6] C. A. Wolcott, A. J. Medford, F. Studt, and C. T. Campbell, "Degree of Rate Control Approach to Computational Catalyst Screening," *J. Catal.*, vol. 330, pp. 197–207, 2015.

[7] G. J. Kroes, "Toward a Database of Chemically Accurate Barrier Heights for Reactions of Molecules with Metal Surfaces," *J. Phys. Chem. Lett.*, vol. 6, pp. 4106–4114, 2015.

[8] L. Sementa, M. Wijzenbroek, B. J. van Kolck, M. F. Somers, A. Al-Halabi, H. F. Busnengo, R. A. Olsen, G. J. Kroes, M. Rutkowski, C. Thewes, N. F. Kleimeier, and H. Zacharias, "Reactive Scattering of H_2 from Cu(100): Comparison of Dynamics Calculations Based on the Specific Reaction Parameter

Approach to Density Functional Theory with Experiment," *J. Chem. Phys.*, vol. 138, p. 044708, 2013.

[9] E. Nour Ghassemi, M. Wijzenbroek, M. F. Somers, and G. J. Kroes, "Chemically Accurate Simulation of Dissociative Chemisorption of D_2 on Pt(111)," *J. Chem. Phys. Lett.*, vol. 683, pp. 329–335, 2017.

[10] F. Nattino, D. Migliorini, G. J. Kroes, E. Dombrowski, E. A. High, D. R. Killelea, and A. L. Utz, "Chemically Accurate Simulation of a Polyatomic Molecule-Metal Surface Reaction," *J. Phys. Chem. Lett.*, vol. 7, pp. 2402–2406, 2016.

[11] C. Díaz, E. Pijper, R. A. Olsen, H. F. Busnengo, D. J. Auerbach, and G. J. Kroes, "Chemically Accurate Simulation of a Prototypical Surface Reaction: H_2 Dissociation on Cu(111)," *Science*, vol. 326, pp. 832–834, 2009.

[12] H. S. Taylor, "A Theory of the Catalytic Surface," *Proc. R. Soc. Lond. A*, vol. 108, pp. 105–111, 1925.

[13] T. Zambelli, J. Wintterlin, J. Trost, and G. Ertl, "Identification of the "Active Sites" of a Surface-Catalyzed Reaction," *Science*, vol. 273, pp. 1688–1690, 1996.

[14] B. Hammer, "Bond Activation at Monatomic Steps: NO Dissociation at Corrugated Ru(0001)," *Phys. Rev. Lett.*, vol. 83, pp. 3681–3684, 1999.

[15] A. T. Gee, B. E. Hayden, C. Mormiche, A. W. Kleyn, and B. Riedmüller, "The Dynamics of the Dissociative Adsorption of Methane on Pt(533)," *J. Chem. Phys.*, vol. 118, pp. 3334–3341, 2003.

[16] F. Abild-Pedersen, O. Lytken, J. Engbæk, G. Nielsen, I. Chorkendorff, and J. K. Nørskov, "Methane Activation on Ni(111): Effects of Poisons and Step Defects," *Surf. Sci.*, vol. 590, pp. 127–137, 2005.

[17] K. Honkala, A. Hellman, I. N. Remediakis, A. Logadottir, A. Carlsson, S. Dahl, C. H. Christensen, and J. K. Nørskov, "Ammonia Synthesis from First-Principles Calculations," *Science*, vol. 307, pp. 555–558, 2005.

[18] Y. Xu, A. C. Lausche, S. G. Wang, T. S. Khan, F. Abild-Pedersen, F. Studt, J. K. Nørskov, and T. Bligaard, "In Silico Search for Novel Methane Steam Reforming Catalysts," *New J. Phys.*, vol. 15, p. 125021, 2013.

[19] J. M. Wei and E. Iglesia, "Mechanism and Site Requirements for Activation and Chemical Conversion of Methane on Supported Pt Clusters and Turnover Rate Comparisons among Noble Metals," *J. Phys. Chem. B*, vol. 108, pp. 4094–4103, 2004.

[20] R. R. Smith, D. R. Killelea, D. F. DelSesto, and A. L. Utz, "Preference for Vibrational over Translational Energy in a Gas-Surface Reaction," *Science*, vol. 304, pp. 992–995, 2004.

[21] R. D. Beck, P. Maroni, D. C. Papageorgopoulos, T. T. Dang, M. P. Schmid, and T. R. Rizzo, "Vibrational Mode-Specific Reaction of Methane on a Nickel Surface," *Science*, vol. 302, pp. 98–100, 2003.

[22] B. L. Yoder, R. Bisson, and R. D. Beck, "Steric Effects in the Chemisorption of Vibrationally Excited Methane on Ni(100)," *Science*, vol. 329, pp. 553–556, 2010.

[23] D. R. Killelea, V. L. Campbell, N. S. Shuman, and A. L. Utz, "Bond-Selective Control of a Heterogeneously Catalyzed Reaction," *Science*, vol. 319, pp. 790–793, 2008.

[24] D. Migliorini, H. Chadwick, F. Nattino, A. Gutiérrez-González, E. Dombrowski, E. A. High, H. Guo, A. L. Utz, B. Jackson, R. D. Beck, and G. J. Kroes, "Surface Reaction Barriometry: Methane Dissociation on Flat and Stepped Transition-Metal Surfaces," *J. Phys. Chem. Lett.*, vol. 8, pp. 4177–4182, 2017.

[25] M. B. Lee, Q. Y. Yang, and S. T. Ceyer, "Dynamics of the Activated Dissociative Chemisorption of CH_4 and Implication for the Pressure Gap in Catalysis: A Molecular-Beam High-Resolution Electron Energy Loss Study," *J. Chem. Phys.*, vol. 87, pp. 2724–2741, 1987.

[26] A. C. Luntz and D. S. Bethune, "Activation of Methane Dissociation on a Pt(111) Surface," *J. Chem. Phys.*, vol. 90, pp. 1274–1280, 1989.

[27] S. Nave and B. Jackson, "Methane Dissociation on Ni(111): The Role of Lattice Reconstruction," *Phys. Rev. Lett.*, vol. 98, p. 173003, 2007.

[28] G. Kresse and J. Furthmüller, "Efficient Iterative Schemes for Ab Initio Total-Energy Calculations Using a Plane-Wave Basis Set," *Phys. Rev. B*, vol. 54, pp. 11169–11186, 1996.

[29] G. Kresse and D. Joubert, "From Ultrasoft Pseudopotentials to the Projector Augmented-Wave Method," *Phys. Rev. B*, vol. 59, pp. 1758–1775, 1999.

[30] B. Hammer, L. B. Hansen, and J. K. Nørskov, "Improved Adsorption Energetics Within Density-Functional Theory Using Rrevised Perdew-Burke-Ernzerhof Functionals," *Phys. Rev. B*, vol. 59, pp. 7413–7421, 1999.

[31] J. P. Perdew, K. Burke, and M. Ernzerhof, "Generalized Gradient Approximation Made Simple," *Phys. Rev. Lett.*, vol. 77, pp. 3865–3868, 1996.

[32] M. Dion, H. Rydberg, E. Schröder, D. C. Langreth, and B. I. Lundqvist, "Van der Waals Density Functional for General Geometries," *Phys. Rev. Lett.*, vol. 92, p. 246401, 2004.

[33] D. A. King and M. G. Wells, "Reaction Mechanism in Chemisorption Kinetics: Nitrogen on the {100} Plane of Tungsten," *Proc. R. Soc. Lond. A*, vol. 339, pp. 245–269, 1974.

[34] F. Nattino, H. Ueta, H. Chadwick, M. E. van Reijzen, R. D. Beck, B. Jackson, M. C. van Hemert, and G. J. Kroes, "Ab Initio Molecular Dynamics Calculations versus Quantum-State-Resolved Experiments on CHD_3+Pt(111): New Insights into a Prototypical Gas–Surface Reaction," *J. Phys. Chem. Lett.*, vol. 5, pp. 1294–1299, 2014.

[35] S. Nave, A. K. Tiwari, and B. Jackson, "Dissociative Chemisorption of Methane on Ni and Pt Surfaces: Mode-Specific Chemistry and the Effects of Lattice Motion," *J. Phys. Chem. A*, vol. 118, pp. 9615–9631, 2014.

[36] F. Nattino, D. Migliorini, M. Bonfanti, and G. J. Kroes, "Methane Dissociation on Pt(111): Searching for a Specific Reaction Parameter Density Functional," *J. Chem. Phys.*, vol. 144, p. 044702, 2016.

[37] J. Frenkel, "Theorie Der Adsorption Und Verwandter Erscheinungen," *Z. Phys.*, vol. 26, pp. 117–138, 1924.

[38] L. Chen, H. Ueta, R. Bisson, and R. D. Beck, "Quantum State-Resolved Gas/Surface Reaction Dynamics Probed by Reflection Absorption Infrared Spectroscopy," *Rev. Sci. Instrum.*, vol. 84, p. 053902, 2013.

[39] B. Jackson and S. Nave, "The Dissociative Chemisorption of Methane on Ni(100): Reaction Path Description of Mode-Selective Chemistry," *J. Chem. Phys.*, vol. 135, p. 114701, 2011.

[40] B. Jiang, R. Liu, J. Li, D. Q. Xie, M. H. Yang, and H. Guo, "Mode Selectivity in Methane Dissociative Chemisorption on Ni(111)," *Chem. Sci.*, vol. 4, pp. 3249–3254, 2013.

[41] X. J. Shen, Z. J. Zhang, and D. H. Zhang, "Communication: Methane Dissociation on Ni(111) Surface: Importance of Azimuth and Surface Impact Site," *J. Chem. Phys.*, vol. 144, p. 101101, 2016.

[42] G. A. Somorjai, R. L. York, D. Butcher, and J. Y. Park, "The evolution of Model Catalytic Systems; Studies of Structure, Bonding and Dynamics from Single Crystal Metal Surfaces to Nanoparticles, and from Low Pressure ($<10^{-3}$ Torr) to High Pressure ($>10^{-3}$ Torr) to Liquid Interfaces," *Phys. Chem. Chem. Phys.*, vol. 9, pp. 3500–3513, 2007.

[43] H. J. Freund, H. Kuhlenbeck, J. Libuda, G. Rupprechter, M. Bäumer, and H. Hamann, "Bridging the Pressure and Materials Gaps between Catalysis and Surface Science: Clean and Modified Oxide Surfaces," *Top. Catal.*, vol. 15, pp. 201–209, 2001.

[44] R. A. van Santen, "Complementary Structure Sensitive and Insensitive Catalytic Relationships," *Acc. Chem. Res.*, vol. 42, pp. 57–66, 2009.

[45] K. Doblhoff-Dier, J. Meyer, P. E. Hoggan, and G. J. Kroes, "Quantum Monte Carlo Calculations on a Benchmark Molecule–Metal Surface Reaction: H_2+Cu(111)," *J. Chem. Theory Comput.*, vol. 13, pp. 3208–3219, 2017.

[46] T. L. Silbaugh and C. T. Campbell, "Energies of Formation Reactions Measured for Adsorbates on Late Transition Metal Surfaces," *J. Phys. Chem. C*, vol. 120, pp. 25161–25172, 2016.

[47] J. Wellendorff, T. L. Silbaugh, D. Garcia-Pintos, J. K. Nørskov, T. Bligaard, F. Studt, and C. T. Campbell, "A Benchmark Database for Adsorption Bond Energies to Transition Metal Surfaces and Comparison to Selected DFT Functionals," *Surf. Sci.*, vol. 640, pp. 36–44, 2015.

[48] F. Calle-Vallejo, J. Tymoczko, V. Colic, Q. H. Vu, M. D. Pohl, K. Morgenstern, D. Loffreda, P. Sautet, W. Schuhmann, and A. S. Bandarenka, "Finding Optimal Surface Sites on Heterogeneous Catalysts by Counting Nearest Neighbors," *Science*, vol. 350, pp. 185–189, 2015.

[49] F. Calle-Vallejo, D. Loffreda, M. T. M. Koper, and P. Sautet, "Introducing Structural Sensitivity into Adsorption-Energy Scaling Relations by Means of Coordination Numbers," *Nat. Chem.*, vol. 7, pp. 403–410, 2015.

[50] F. Calle-Vallejo, M. D. Pohl, D. Reinisch, D. Loffreda, P. Sautet, and A. S. Bandarenka, "Why Conclusions from Platinum Model Surfaces Do Not Necessarily Lead to Enhanced Nanoparticle Catalysts for the Oxygen Reduction Reaction," *Chem. Sci.*, vol. 8, pp. 2283–2289, 2017.

[51] A. A. Latimer, A. R. Kulkarni, H. Aljama, J. H. Montoya, J. S. Yoo, C. Tsai, F. Abild-Pedersen, F. Studt, and J. K. Nørskov, "Understanding Trends in C–H Bond Activation in Heterogeneous Catalysis," *Nat. Mater.*, vol. 16, pp. 225–229, 2017.

[52] K. Reuter, C. P. Plaisance, H. Oberhofer, and M. Andersen, "Perspective: On the Active Site Model in Computational Catalyst Screening," *J. Chem. Phys.*, vol. 146, p. 040901, 2017.

[53] P. N. Plessow and F. Abild-Pedersen, "Examining the Linearity of Transition State Scaling Relations," *J. Phys. Chem. C*, vol. 119, pp. 10448–10453, 2015.

[54] C. J. Weststrate, P. van Helden, and J. W. Niemantsverdriet, "Reflections on the Fischer-Tropsch Synthesis: Mechanistic Issues from a Surface Science Perspective," *Catal. Today*, vol. 275, pp. 100–110, 2016.

[55] J. K. Nørskov, T. Bligaard, B. Hvolbæk, F. Abild-Pedersen, I. Chorkendorff, and C. H. Christensen, "The Nature of the Active Site in Heterogeneous Metal Catalysis," *Chem. Soc. Rev.*, vol. 37, pp. 2163–2171, 2008.

[56] J. Nakamura, J. M. Campbell, and C. T. Campbell, "Kinetics and Mechanism of the Water-Gas Shift Reaction Catalysed by the Clean and Cs-Promoted Cu(110) Surface: a Comparison with Cu(111)," *J. Chem. Soc. Faraday Trans.*, vol. 86, pp. 2725–2734, 1990.

[57] C. T. Campbell, "Future Directions and Industrial Perspectives Micro- and Macro-Kinetics: Their Relationship in Heterogeneous Catalysis," *Top. Catal.*, vol. 1, pp. 353–366, 1994.

[58] R. A. van Santen, A. J. Markvoort, I. A. W. Filot, M. M. Ghouri, and E. J. M. Hensen, "Mechanism and Microkinetics of the Fischer–Tropsch Reaction," *Phys. Chem. Chem. Phys.*, vol. 15, pp. 17038–17063, 2013.

[59] T. J. Okeson, K. Keyvanloo, J. S. Lawson, M. D. Argyle, and W. C. Hecker, "On the Kinetics And Mechanism of Fischer-Tropsch Synthesis on a Highly Active Iron Catalyst Supported on Silica-Stabilized Alumina," *Catal. Today*, vol. 261, pp. 67–74, 2016.

[60] H. J. Freund, N. Nilius, T. Risse, and S. Schauermann, "A Fresh Look at an Old Nano-Technology: Catalysis," *Phys. Chem. Chem. Phys.*, vol. 16, pp. 8148–8167, 2014.

Chapter 5

Methane on a Stepped Surface: Dynamical Insights on the Dissociation of CHD_3 on Pt(111) and Pt(211)

This Chapter is based on:

D. Migliorini, H. Chadwick, and G. J. Kroes *J. Chem. Phys.*, 149, 094701 (2018)

which is reproduced with the permission of AIP publishing.

Abstract

The simulation of the dissociation of molecules on metal surfaces is a cornerstone for the understanding of heterogeneously catalyzed processes. However, due to high computational demand, the accurate dynamical simulation of the dissociative chemisorption of polyatomic molecules has been limited mostly to flat low-index metal surfaces. The study of surfaces that feature "defected" sites, such as steps, is crucial to improve the understanding of the overall catalytic process due to the high reactivity of under-coordinated sites for this kind of reaction. In this work we have extensively analyzed more than 10000 AIMD tra-

jectories where a CHD_3 molecule is impinging either on the flat Pt(111) or on the stepped Pt(211) surface for different initial rovibrational states and collision energies. The results have been compared in order to get insights into the effect of the step on the dissociation of methane. We have found that, despite a large difference in the activation barrier and consequently in reactivity, the geometry of the lowest transition states is very similar on the two surfaces and this results in a similar dissociation dynamics. Furthermore, the trapping observed on the Pt(211) surface can be explained with energy transfer to parallel translational motion induced by the geometry of the slab and by a larger energy transfer to phonons for the stepped Pt(211) surface.

5.1 Introduction

The dissociative chemisorption of methane on a transition metal surface has been employed, both theoretically [1–10] and experimentally [11–14], as a model system to understand one of the most important steps in steam reforming [15], a fundamental industrial process which is currently one of the most common ways to produce molecular hydrogen. The CH bond cleavage on a Ni or Pt based catalyst is believed to be one of the rate determining steps [15] of the overall process in the high temperature regime. Due to the large complexity of molecule-surface reactions and to the necessity of treating accurately both the molecule and the metal slab, these systems have always been challenging for appropriate dynamical simulations [16–21]. The large number of degrees of freedom (DOFs) makes density functional theory (DFT) at the generalized gradient approximation (GGA) or meta-GGA level the go-to method for these systems and excludes any higher level of theory, at least for dynamical simulations [22]. Unfortunately, standard GGA and meta-GGA functionals are known for their poor accuracy in the calculation of activation barriers (E_b) [22] for molecule-surface systems; this has encouraged, in the last few decades, the pursuit of semi-empirical functionals [3, 5, 23–25] able to compute activation barriers with errors as small as 1 kcal/mol ($\approx$ 4.2 kJ/mol), so-called chemical accuracy.

One of the viable semi-empirical methods to develop an accurate density functional is a variation of the specific reaction parameter (SRP) approach originally proposed by Truhlar and coworkers [26]. In our implementation for molecules on metals this approach consists of mixing two GGA functionals through a mixing parameter so that the SRP functional is able to reproduce the experimental zero-coverage reaction probability (S_0) with chemical accuracy. This has been applied successfully to different catalytically relevant systems where a molecule dissociates on a low-index flat metal surface [3, 5, 23–25]. Recently, chemical accuracy has been achieved for CHD_3 on Ni(111) [5] using the SRP32-vdW functional obtained by mixing the RPBE [27] and the PBE [28, 29] exchange functionals (E_X^{RPBE} and E_X^{PBE}, respectively) with a mixing parameter $x = 0.32$ and using the correlation functional developed by Dion *et al.* [30, 31] ($E_C^{\text{vdW-DF}}$) that also models van der Waal interactions. The exchange correlation part of the SRP32-vdW functional ($E_{XC}^{\text{SRP32-vdW}}$) reads as:

$$E_{XC}^{\text{SRP32-vdW}} = 0.32 \cdot E_X^{RPBE} + (1 - 0.32) \cdot E_X^{PBE} + E_C^{\text{vdW-DF}}. \tag{5.1}$$

The SRP32-vdW functional has been successfully transferred from CHD_3 dissociation on Ni(111) to Pt(111) and, more importantly, it was able to achieve chemical accuracy also on the stepped Pt(211) surface, as shown in Chapter 4 and in Ref. [3]. The transferability of the SRP functional from the flat Pt(111) to the stepped Pt(211) surface suggests that an SRP functional developed for a relatively simple system, such as the flat (111) surface, can be used to obtain accurate reaction barriers on different defected sites of the same metal (see Chapter 4, Ref. [3] and references therein). The study of a stepped transition metal surface such as Pt(211) is highly relevant for heterogeneous catalysis since it is known that under-coordinated sites usually show enhanced reactivity for processes like the dissociative chemisorption of methane [32–36]. Moreover the dissociation of methane on Pt(211) has been previously used to model the overall catalytic process through microkinetic simulations [1, 2].

In this Chapter we report the analysis of 12500 *ab initio* molecular dynamics

(AIMD) trajectories of CHD_3 impinging on Pt(111) and Pt(211) in order to study and compare the dynamical features of the dissociation on the two surfaces, focusing on the differences introduced by the presence of the step. The Chapter is organized as follows: the method used to setup, propagate and analyze the trajectories is reported in Section 5.2, the results are presented and discussed in Section 5.3 and the main conclusions are summarized in Section 5.4.

5.2 Method

Most of the results discussed in this Chapter have been obtained by analyzing AIMD trajectories of CHD_3 impinging on the Pt(111) and on the Pt(211) surfaces. These simulations have been used to compute the zero-coverage reaction probability (S_0) which has been compared to molecular beam experiments to define and test the SRP32-vdW functional for said systems [3]. The computational details have been recently published [3] and therefore, they will only be summarized in this Section.

The electronic structure calculations have been performed on a DFT level using the Vienna *ab initio* simulation package (VASP) [37–40] version 5.3.5. The first Brillouin zone has been sampled with a 4x4x1 Γ-centered K-point grid and the basis set includes plane waves with kinetic energy up to 350 eV. The core electrons have been represented through projector augmented-wave (PAW) pseudopotentials [41, 42]. The Pt(111) surface has been represented using a 5 layer (3x3) supercell slab, consistent with previous work [3, 6]. The stepped Pt(211) surface has been modelled using a 4 layer (1x3) supercell. For both surfaces, the slab is separated from its first periodic replica by 13 Å of vacuum. A 0.1 eV Fermi smearing has been used to facilitate the SCF convergence. The setup used for these calculations has been extensively tested and the results of the tests are available in the Supporting Information of Ref. [3].

The AIMD trajectories have been setup in order to reproduce the molecular beam experiments performed by Beck and co-workers [3] including the surface temperature (T_s) of 500 K and 650 K for Pt(111) and Pt(211) respectively, and

modelling the initial kinetic energy and rovibrational population of the methane molecules. Note that, even though the simulations have been performed at different temperatures for the two surfaces, previous work suggests that the temperature dependence of the reactivity on Pt is small [6, 43]. Quasi-classical trajectories (i.e., classical trajectories where the vibrational zero-point energy is imparted to the molecule) have been propagated with a 0.4 fs time-step until dissociation or scattering was observed. A molecule has been considered reacted if a bond was stretched over 3.0 Å and it has been considered scattered if, after the impact, it reached a certain distance above the surface (i.e., 6.0 Å or 6.5 Å for Pt(111) and Pt(211), respectively) while the center of mass (COM) velocity was pointing away from the surface. For the reactive trajectories the time of the dissociation (t_{diss}) has been defined as the first time step at which the dissociating bond is as elongated as in the minimum energy transition state ±0.04 Å. In this work the molecules that did not reach an outcome within the first 2 ps of propagation have been considered trapped.

The transition state (TS) geometries presented have been computed using the dimer method included in the VASP transition state tools package (VTST) [44–47]. Frequency analysis calculations have been performed to confirm that all the TSs reported in this work are true 1st order saddle points (i.e., one and only one imaginary frequency is present) except where stated differently. The analysis has been carried out on 7000 trajectories for Pt(111) and on 5500 trajectories for Pt(211) for an initial average incident energy ($\langle E_i \rangle$) ranging between 60.7 and 120.1 kJ/mol for Pt(111) and between 58.2 and 107.9 kJ/mol for Pt(211). Several dynamics-relevant features have been investigated and the results have been binned and smeared using a sum of Gaussian curves such that, for a sample of N data, the final distribution $\mathcal{F}(\alpha)$ of the observable α is represented as:

$$\mathcal{F}(\alpha) = \sum_{i}^{Nbins} \sum_{j}^{Ndata} \frac{1}{\sqrt{2\pi\sigma_G^2}} \cdot exp\left(- \frac{(bin_0 + i \cdot binsize - data(j))^2}{2\sigma_G^2} \right), \quad (5.2)$$

where the indices i and j run over the bins and the data respectively, bin_0 is the first value of α considered for the binning procedure and σ_G is the standard

deviation of the Gaussian used (i.e., the broadening). The final distribution is the sum of Gaussians centered on the data values for each element of the dataset. Since we are comparing datasets of different sizes the area of the final distributions is always normalized to 1. In this Chapter the distributions reported in the same plot always have the same broadening and all the distribution parameters are reported in the Supplementary Material (SM) of Ref. [48].

Using a broadening can improve the quality and the readability of the results but can cause small tails at the edge of the distribution that might assume unphysical values. However this does not affect the interpretation of the results. In order to calculate the distributions all the available trajectories have been used. This means that the distribution takes into account results for different CHD_3 vibrational states and average collision energies (see Ref. [3]) unless explicitly stated. For some of the observables α, the average value is reported together with the standard deviation σ and standard error σ_M:

$$\sigma = \sqrt{\frac{\sum_{i=1}^{N}(\alpha_i - \langle\alpha\rangle)^2}{N-1}}, \tag{5.3}$$

$$\sigma_M = \frac{\sigma}{\sqrt{N}}. \tag{5.4}$$

Here, N is the sample size and $\langle\alpha\rangle$ is the sample average.

5.3 Results and Discussion

Platinum is an fcc metal and its (111) surface shows the well-known hexagonal lattice structure. The Pt(211) surface is composed of 3 atom wide (111)-like terraces and (100)-like steps. In order to analyze the dynamics on the Pt(211) surface three non-equivalent sites have been defined: edge (on the step edge), middle (the row of atoms in the middle of the terrace) and bottom (the row of atoms on the low end of the step). Moreover some of the analysis is referenced to facets instead of sites considering the step (i.e., the (100) facet) and the terrace (i.e., the (111) facet). The side and top views of the surfaces are shown in Figure

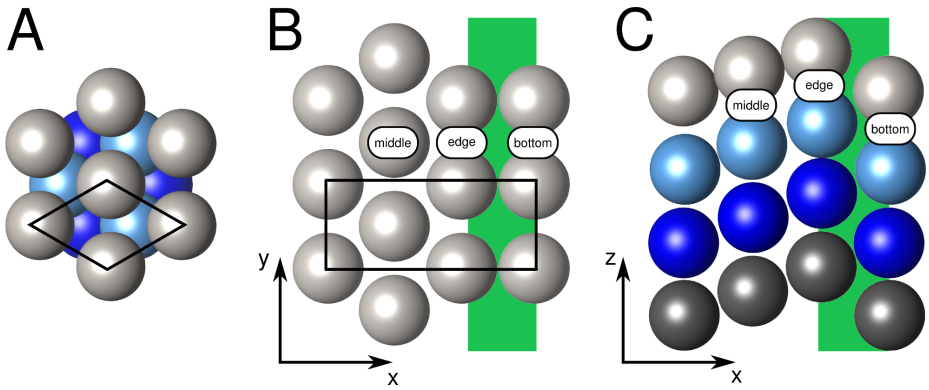

Figure 5.1: (A) top view of the Pt(111) surface. (B) top view of the first layer of the Pt(211) surface. (C) side view of the Pt(211) surface. For both the surfaces, the atoms are reported in their equilibrium position. The unit cell is marked in black and different layers are reported in different colors. For the Pt(211) surface, the three rows of atoms in the unit cell are called edge, middle, and bottom according to their position: edge is on top of the step edge, middle is in the middle of the terrace, and bottom is on the low side of the step. The (100) step is shaded in green while the remainder of the surface is the (111) terrace.

5.1 where the atoms are reported in their equilibrium positions and the step facet is highlighted in green for the Pt(211) surface. The impact (reaction) site is defined as the nearest site (i.e., bottom, middle or edge) in the xy plane at the closest approach (reaction) time. Molecules that hit the surface or dissociate at an x coordinate between the edge and the bottom site (green shaded area in Figure 5.1) are considered step facet events. It has been shown in previous work [3] and in Chapter 4 that the reactivity on the stepped surface happens almost completely through the dissociation on top of the step edge atom. Therefore the analysis of reacted trajectories has been carried out by looking at the different behavior of molecules impacting on the different surface sites (i.e., edge, middle and bottom atoms). For non-reactive trajectories the differences in the dynamics upon impacting on the (111)-like terrace facet or on the (100)-like step facet have also been considered.

On the Pt(211) surface trapping has been observed and the average trapping time has been estimated to be about 40 ps [3] (i.e., 43 ps), which is too short to be detected experimentally and too long to be simulated with an expensive method

like AIMD. For the previously published work [3], reported also in Chapter 4, the trapped trajectories have been propagated for 1 ps (or 2 ps in a few test cases). To ensure a fair analysis, in this work all the trapped trajectories have been propagated up to 2 ps. Out of the 69 trajectories that were considered trapped after 1 ps, 35 were scattered upon further propagation. However this does not necessarily affect the main conclusions of earlier work since a large number of trapped trajectories are still present even after 2 ps of propagation, especially at low incidence energy. This also suggests that, in order to be considered trapped (i.e., characterized by some average trapping time), the molecules need some time to equilibrate with the surface.

To understand the dynamics of the CHD_3 on the different surfaces, the number of bounces has been counted for all the trajectories, where a bounce is defined as two sign-changes of the COM velocity along the direction perpendicular to the macroscopic surface. As observed for other metal surfaces, the CHD_3 dissociative chemisorption is usually a "sudden" process: on both platinum surfaces the molecules react on the first impact and without bouncing. This is also true for almost all the scattered trajectories on Pt(111) (only 5 out of more than 6500 perform one and only one bounce) and for most of the scattered trajectories on Pt(211). On Pt(211) we observe a few trajectories bouncing either one or two times before scattering. The trapped trajectories bounce between one and four times during the propagation (see Figure 5.2).

5.3.1 Transition States

Several transition states have been located on the stepped Pt(211) surface by performing calculations using the dimer method [44–47]. All the TSs presented are real 1st order saddle points as confirmed by a normal mode analysis unless stated differently. The energy (i.e. the barrier height, E_b), the length of the dissociating CH bond (r_b) and the θ, β and γ angles have been determined. θ is the angle between the dissociating bond and the surface normal (i.e., z) and β is the angle between the umbrella axis ($\vec{a}$) and the surface normal, where $\vec{a}$ is defined as the vector going from the geometric center of the (non-reacting)

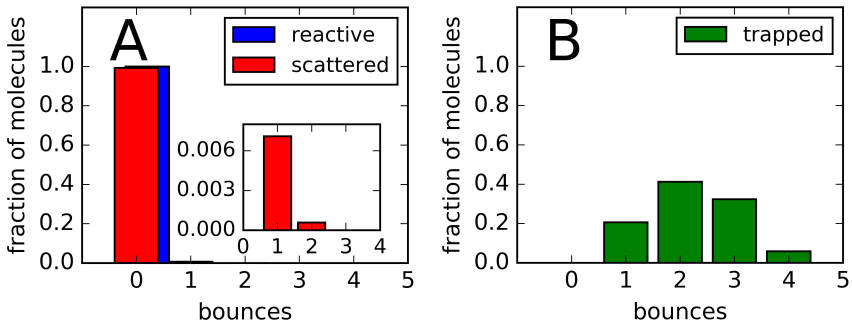

Figure 5.2: Number of bounces for the molecules impinging on the Pt(211) surface. (A) fraction of scattered and reacted trajectories in red and blue, respectively. The inset in panel A is a magnification for the few trajectories that bounce before scattering. (B) results for the trapped trajectories on Pt(211).

umbrella hydrogens to the carbon atom (Figure 5.3). γ is the angle between the dissociating CH bond and the $\vec{a}$ axis. The γ angle describes the internal geometry of the TS, while β and θ describe the geometry of the molecule with respect to the macroscopic surface normal. All the results, and the minimum energy TS for the flat Pt(111) surface, are reported in Table 5.1 including all the TS geometries (also represented in Figure 5.4) and the studied angles (also shown in Figure 5.3). The angle α (sketched in Figure 5.3 and reported in Table 5.1) describes the orientation of the dissociating bond in the xy plane for the Pt(211) surface and it will be discussed later in this Chapter.

For Pt(211), four TSs have been found on top of a step edge atom, with a different orientation of the dissociating CH bond. These have been labeled according to the positions of the carbon and of the dissociating hydrogen:
Edge2Edge-Bridge (Edge2Edge-B) dissociating parallel to the step edge (Figure 5.4B), Edge2Middle-Hollow (Edge2Mid-H) dissociating on a hollow site toward the middle row of the terrace (Figures 5.4C and 5.4D), and Edge2Bottom-Bridge (Edge2Bot-B) dissociating toward a bridge site on the (100) step site (Figure 5.4E). Note that the two TSs depicted in Figures 5.4C and 5.4D are related by a hindered rotation about the umbrella axis. Three TSs have been found on the middle terrace atom dissociating toward different bridge sites, and

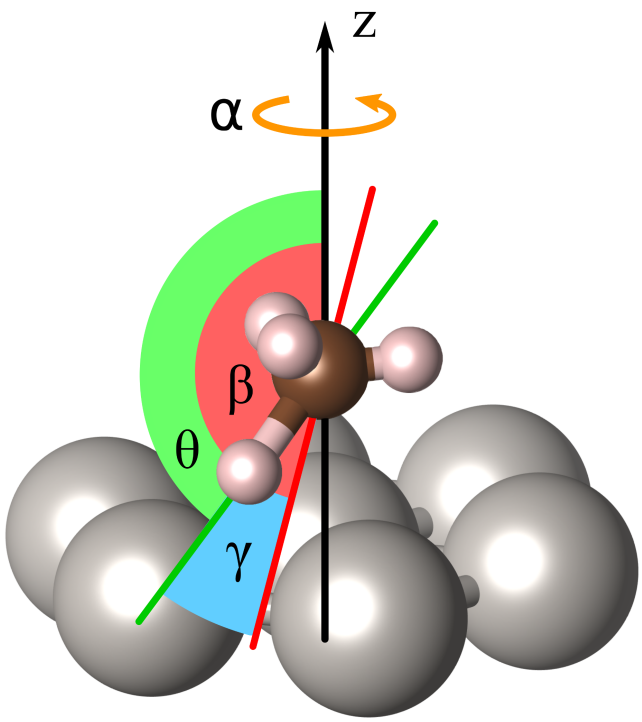

Figure 5.3: Sketch of the angles studied: θ (green shade) is the angle between the CH bond (green line) and the z axis, β (red) is the angle between the umbrella axis $\vec{a}$ (red line) and the z axis (i.e., the macroscopic surface normal), and γ (blue) is the angle between the CH bond and the umbrella axis $\vec{a}$. The angle α (orange) represents the orientation of the dissociating bond in the xy plane.

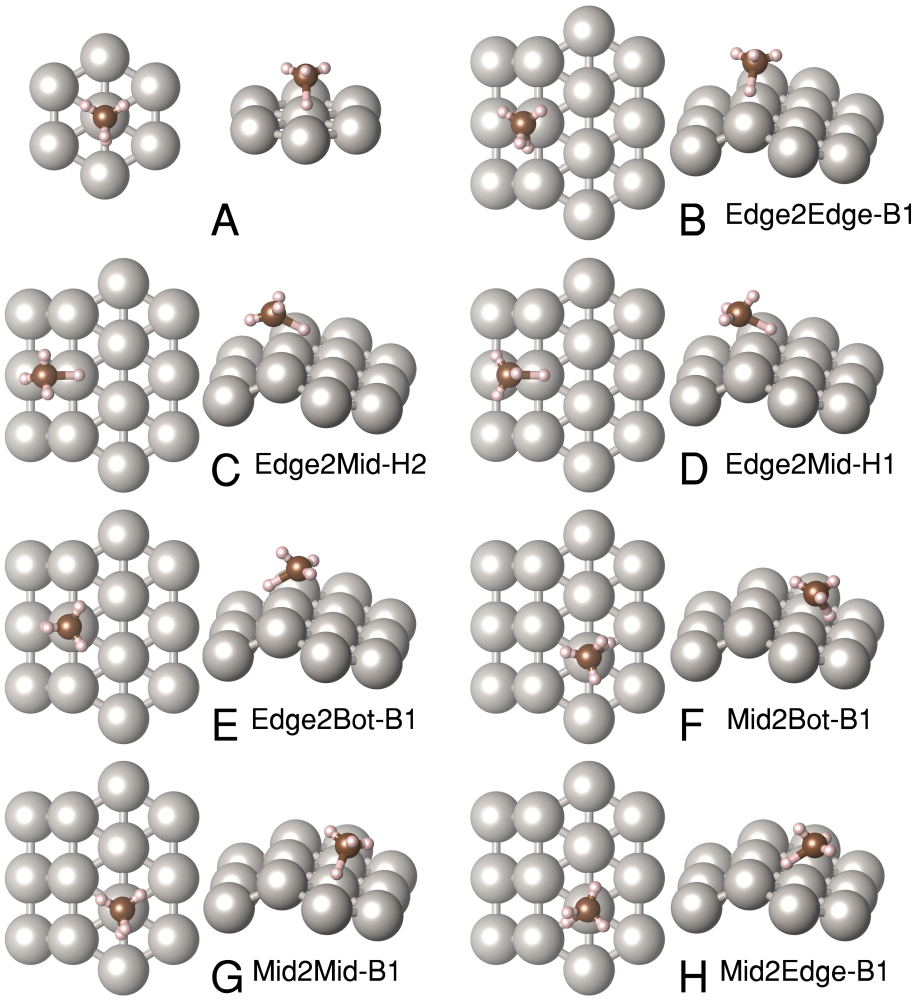

Figure 5.4: Depiction of the transition state geometries found in side and top views. TS A is the one found for Pt(111) and reported in Chapter 4 and Ref. [3]. TSs B to H have been found on Pt(211) and are also labeled with the names reported in Table 5.1.

Surface	L	Name	θ [∘]	β [∘]	γ [∘]	α [∘]	r_b [Å]	E_b [kJ/mol]
Pt(111)	A	...	133.4	168.3	34.8	...	1.55	78.6
Pt(211)	B	Edge2Edge-B1	132.9	166.0	33.1	85.0	1.53	53.9
Pt(211)	C	Edge2Mid-H2	115.6	145.6	30.0	181.3	1.60	57.1
Pt(211)	D	Edge2Mid-H1	113.7	145.9	32.2	179.4	1.62	57.7 *
Pt(211)	E	Edge2Bot-B1	122.9	156.8	33.9	0.5	1.65	65.1 *
Pt(211)	F	Mid2Bot-B1	145.8	171.8	35.0	226.3	1.55	97.9
Pt(211)	G	Mid2Mid-B1	130.2	158.5	34.9	72.1	1.57	98.0
Pt(211)	H	Mid2Edge-B1	119.0	151.7	33.4	25.3	1.56	96.4

Table 5.1: Comparison of the TSs found on the two platinum surfaces. For each, the following properties are reported: the surface on which it has been found, the label (L) as in Figure 5.4, the name of the TS, the θ, β, γ and α angles, the length of the dissociating bond (r_b) in Å, and the energy barrier (E_b) in kJ/mol. Note that if the energy barrier is followed by a star (*), the TS reported still has a second imaginary frequency (i.e., it is not a real 1st order saddle-point).

they have been labeled as Middle2Bottom-Bridge (Mid2Bot-B), Middle2Middle-Bridge (Mid2Mid-B), and Middle2Edge-Bridge (Mid2Edge-B) according to which site they are dissociating toward (Figures 5.4F-5.4H, respectively). The numbers, either 1 or 2, at the end of a TS name identify the eclipsed or the staggered orientation of the umbrella relative to the dissociating CH bond, respectively. Note that the TSs depicted in Figures 5.4D and 5.4E still have a second small imaginary frequency (i.e., they are not real 1st order saddle points; see Table 5.1).

There is a clear difference in the E_b between dissociation on the step edge atom and on the terrace middle atom (i.e., $\approx$ 39 kJ/mol on average), regardless of the molecular orientation: the TSs centered on the step edge atom have very similar energies and the same is true for the TSs centered on the terrace middle atom. The step edge site is more reactive than the flat Pt(111) surface, while terrace middle sites show barriers even larger than on the ideal flat surface (78.6 kJ/mol, Table 5.1). Despite this large range of E_b , the TSs are geometrically similar: all of them have a dissociating bond length between 1.53 and 1.65 Å and an angle γ between the dissociating bond and $\vec{a}$ between 30° and 35°. As expected

β and θ show more variability because they depend on the molecular geometry as well as on the surface orientation with respect to the reference frame (z axis). β and θ can be compared for the TS on Pt(111) and the lowest energy TS on Pt(211) (i.e., Edge2Edge-B1) and both angles have the same values within less than 2.5°.

5.3.2 Energy Transfer to Parallel Motion

In Figure 5.5, the COM lateral displacement (δ_{COM}) has been reported for all the trajectories, where δ_{COM} has been computed as the difference between the COM xy position at the initial and at the reaction step (for dissociative events) or at the step of 1st closest approach (for scattered and trapped trajectories). For the flat surface, the reactive events happen in a "sudden" fashion where the molecule does not change its position in the xy plane significantly, as they show $\langle\delta_{COM}\rangle$ smaller than 0.09 Å (Figure 5.5A). The same is true for the molecules reacting on the step edge of Pt(211) (Figure 5.5B).

Scattered and trapped molecules on Pt(211) show a significantly larger $\langle\delta_{COM}\rangle$ that can go up to 0.25 Å for molecules trapped after impacting on the step facet (all the data are reported in the SM of Ref. [48]). This is due to the fact that, even though all molecules start with a COM velocity aligned with the z axis, the topology of the surface can induce energy transfer from the translational motion in the z direction to the motion along the surface (energy transfer to parallel motion). In order to study this phenomenon, the distance travelled in the xy plane has been computed (for each individual trajectory) as:

$$d_{xy} = \sum_{t=1}^{T} \sqrt{(x_t - x_{t-1})^2 + (y_t - y_{t-1})^2}, \tag{5.5}$$

$$d_{\alpha=x,y} = \sum_{t=1}^{T} \left|(\alpha_t - \alpha_{t-1})\right|, \tag{5.6}$$

Here, d_{xy} is the distance travelled in the xy plane, d_α is the distance travelled in the α direction (i.e., $\alpha = x, y$), and t is the time step. T is the total number

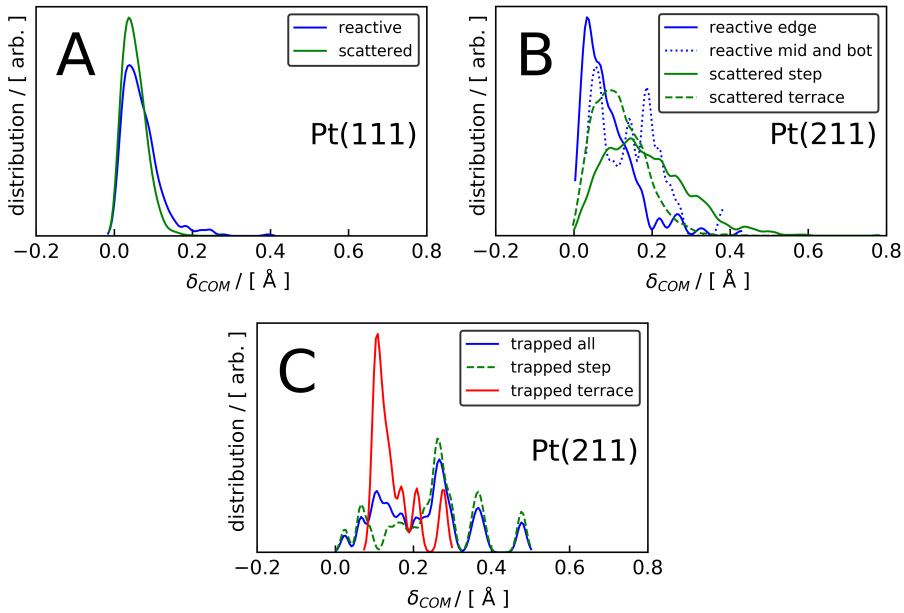

Figure 5.5: (A) δ_{COM} computed for the reactive (blue) and scattered (green) trajectories on Pt(111). (B) δ_{COM} computed for the reactive (blue) and scattered (green) trajectories on Pt(211), the solid lines describe step edge atom reaction and step facet scattering, the dotted line describes bottom and middle atom reactions, and the dashed line describes terrace facet scattering. (C) δ_{COM} computed on Pt(211) for all the trapped trajectories (blue) and for the trapped trajectories impacting first on the step (green) or on a terrace (red).

of time steps. Note that d_{xy} and d_α are dependent on the time step (0.4 fs) and on the total propagation time (i.e., the number of time steps T). On Pt(211), x and y are perpendicular and parallel to the step edge, respectively. If we consider d_{xy}, reported in Figure 5.6, it is noticeable how the molecules scattered from the step can travel significantly further than the ones scattered from the flat surface (Figures 5.6A and 5.6B). On average, we observe $\langle d_{xy} \rangle = 0.8$ Å on Pt(111) and $\langle d_{xy} \rangle = 2.8$ Å on Pt(211), but on the stepped surface, scattered molecules have been observed to travel up to 30 Å.

If we look at the trajectories trapped on the Pt(211) surface (Figure 5.6C), we can see that the molecules can travel considerable distances in our simulations (i.e., up to almost 50 Å) especially in the direction perpendicular to the step edge

(i.e., along x). Note that for these trajectories the propagation has been stopped after 2 ps and the longer we would propagate them the further they would travel. This is due to the large velocity the trapped molecules have in the xy plane. The distribution of the average velocity in xy upon trapping ($\langle v_{xy} \rangle^{trap}$) is reported in Figure 5.6D. $\langle v_{xy} \rangle^{trap}$ has been computed as:

$$\langle v_{xy} \rangle^{trap} = \sum_{t=1}^{N^{trap}} \frac{\sqrt{v_{x(t)}^2 + v_{y(t)}^2}}{N^{trap}}, \tag{5.7}$$

$\langle v_{xy} \rangle^{trap}$ is averaged over the total of N^{trap} time steps. Here t ranges from the first impact with the surface to the last step of the propagation (i.e., when the molecule is considered trapped). The velocity distribution is centered on $\langle v_{xy} \rangle^{trap} = 0.014$ Å/fs which means that during the estimated trapping time of 43 ps, those molecules can travel, on average, as far as 593 Å and this goes up to 642 Å if we consider only the molecules trapped after impinging on the step. This suggests that the trapped molecules have enough time to explore a large portion of the surface, increasing their chance of finding a favorable orientation to react or even a higher order defect with a lower dissociation barrier, such as kinks.

The importance of the energy transfer from motion normal to the surface to motion parallel to the surface can be quantified by calculating the amount of kinetic energy that molecules have in the xy plane after the impact with the surface (K_{xy}). To ensure a fair comparison, K_{xy} has been calculated at the end of the trajectory for scattered molecules and at the first outer turning point for trapped molecules. In Figure 5.7, K_{xy} is reported for scattered and trapped molecules on Pt(211) distinguishing between molecules which impact on the step facet and on the terrace facet. As expected, both trapped and scattered molecules show large values of K_{xy}. Moreover, the step site is more efficient than the terrace in promoting energy transfer to the parallel motion, probably because it makes a larger angle with the normal to the macroscopic surface.

In Figure 5.8, K_{xy} is reported as a function of the initial average collision en-

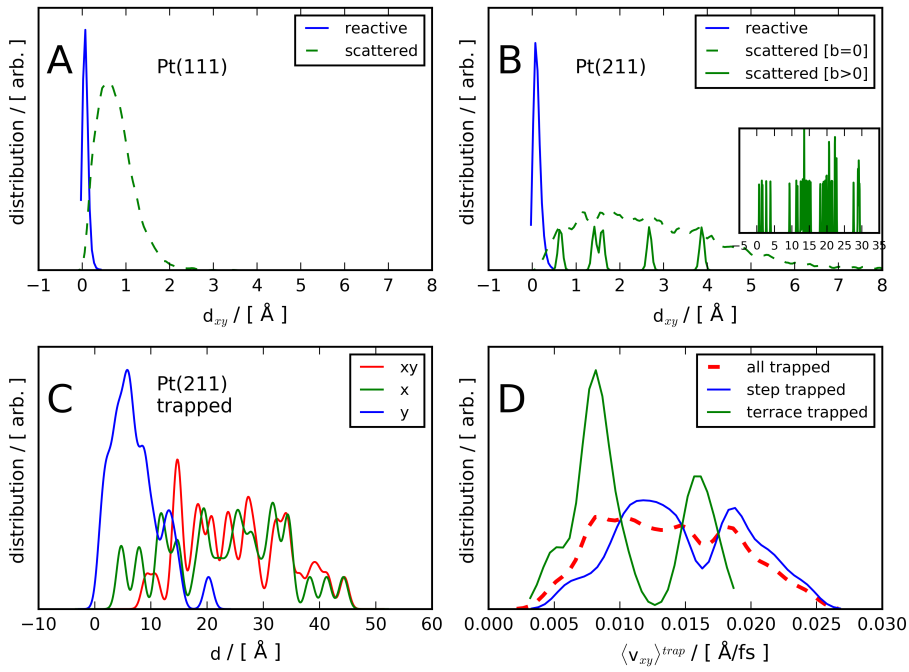

Figure 5.6: (A, B) distributions of the distance travelled by the molecules in the xy plane (d_{xy}) for reactive and scattered trajectories on the Pt(111) and Pt(211) surfaces, respectively. In panels A and B, the blue solid lines represent reactive trajectories (the distributions have been multiplied by 0.2 for a better comparison) and the green lines represent scattered trajectories without bouncing ($b = 0$, dashed green) and with bouncing ($b > 0$, solid green) on the surface. (C) distance travelled (d) by the molecules trapped on the Pt(211) surface. The distance travelled in the x direction, in the y direction, and the total distance travelled in the xy plane are reported in green, blue, and red, respectively. (D) distribution of average COM velocity in the xy plane for the trapped trajectories $\langle v_{xy} \rangle^{trap}$ for molecules that have the first impact on the terrace (green solid line), on the step (blue solid line), and for all the trapped molecules (red dashed line).

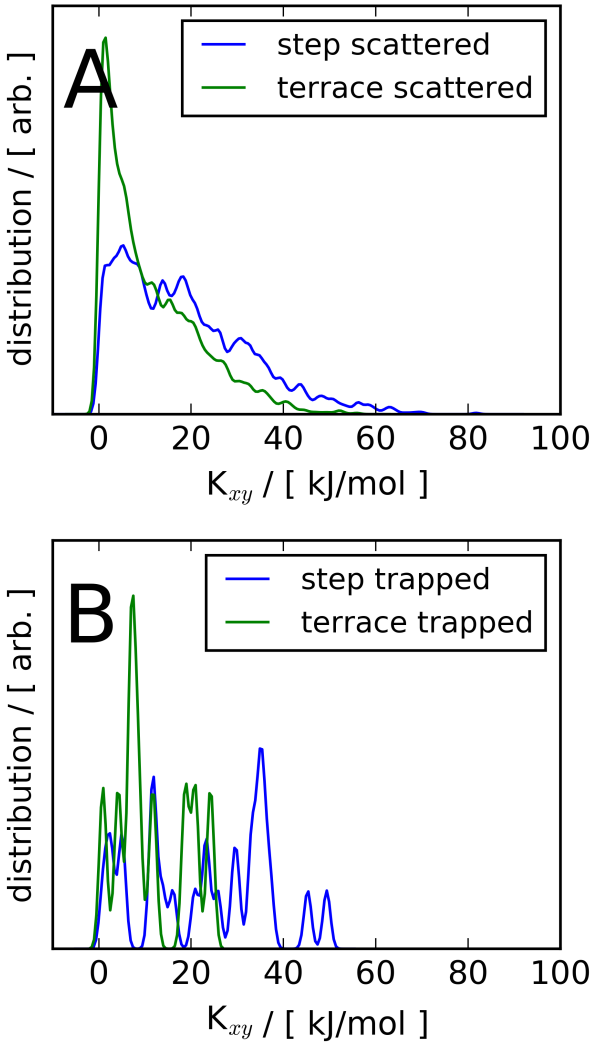

Figure 5.7: (A) distribution of kinetic energy in the xy plane (K_{xy}) after the impact with the Pt(211) surface for scattered molecules. (B) same of panel A but for trapped molecules. Results for molecules that impacted on the step and on the terrace are reported in blue and green, respectively.

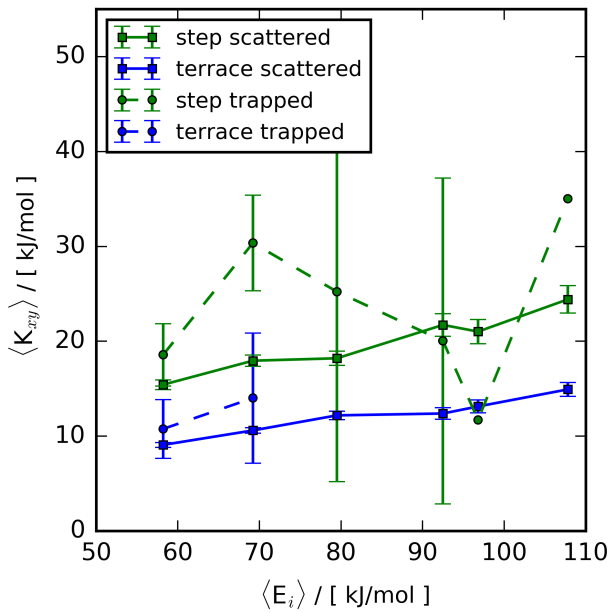

Figure 5.8: Average kinetic energy in the xy plane (K_{xy}) as a function of the average initial kinetic energy ($\langle E_i \rangle$) after the impact with the Pt(211) surface. Results for scattered molecules are reported as squares and solid lines and results for trapped molecules as circles and dashed lines. Green data represent molecules impacting on the step and blue data represent molecules impacting on the terrace. Two points are reported without error bars because the sample size for those data sets is 1. The lines are drawn to guide the eye.

ergy of the molecules ($\langle E_i \rangle$). The energy transfer to parallel translational motion increases with $\langle E_i \rangle$ and confirms that the step induces more energy transfer to the parallel motion than the terrace. The values of $\langle K_{xy} \rangle$ for the trapped trajectories show large error bars due to the small sample size, but the results suggest that the trapped molecules show a larger energy transfer to the parallel motion than the scattered ones at low $\langle E_i \rangle$ (Figure 5.8). In turn, this suggests that, especially at low $\langle E_i \rangle$, energy transfer to parallel motion at the step contributes to the trapping.

Out of a total of 34 trapped trajectories, 25 of them impacted on the step while only 9 on the terrace. If we weight these results according to the step:terrace area ratio (i.e., 1:1.8), we find that the trapping probability is 5 times larger if

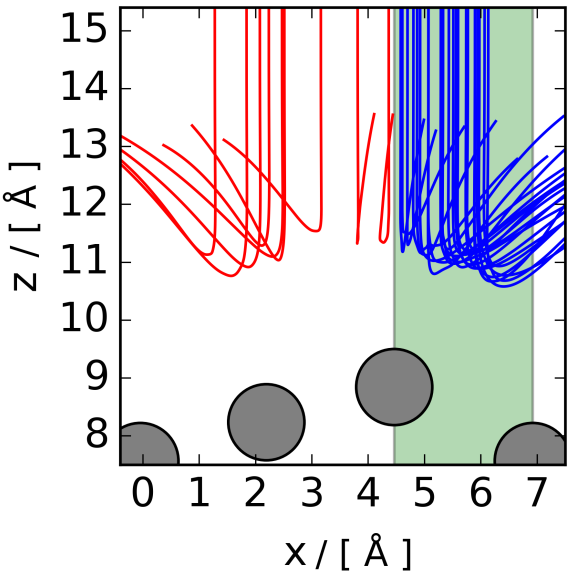

Figure 5.9: xz projection of the first part of the trapped trajectories. The first layer atoms 0 K positions are reported as gray circles and the step is highlighted in green. The trajectories are reported in blue if the first impact is on the step and in red if it is on the terrace.

the molecule impacts on the step than on the terrace. The xz projection of the first part of the trapped trajectories is reported in Figure 5.9. In Figure 5.10 the distribution of the average velocity in x for the trapped molecules ($\langle v_x \rangle^{trap}$) is reported. Again, these results suggest that one of the main reasons for the trapping we observe on Pt(211) is the geometry of the surface: the molecules that hit the step start travelling in the positive x direction. Most of the molecules impacting on the terrace travel in the negative x direction.

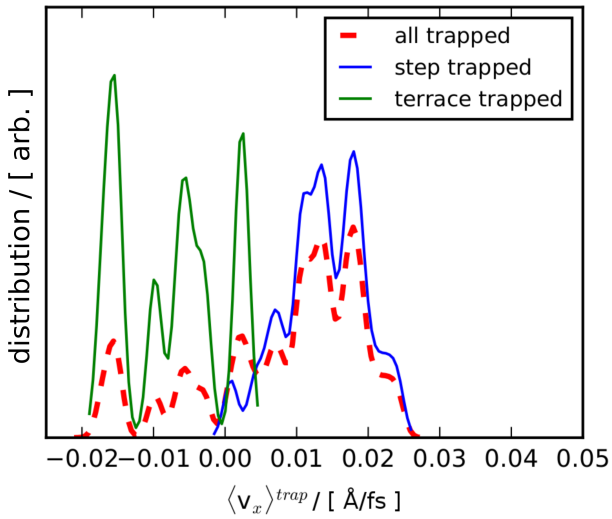

Figure 5.10: Distribution of the average velocity along x during trapping $\langle v_x \rangle^{trap}$ for all the trapped molecules (red line), the trapped molecules that have the first impact on the step (blue line), and the ones that have the first impact on the terrace (green line).

5.3.3 Energy Transfer to Surface Phonons

The energy transfer from the molecules to the surface phonons (E_T) is reported in Figure 5.11. All the scattered molecules transfer roughly the same amount of energy to the phonons independently from the Pt surface on which they impact; on average, molecules that hit the Pt(111) and the Pt(211) surface show $\langle E_T \rangle = 15.5 \pm 0.2$ and 13.9 ± 0.2 kJ/mol, respectively. Note that Pt(111) shows a somewhat larger $\langle E_T \rangle$, but the AIMD trajectories have been performed over a larger range of $\langle E_i \rangle$. This can be seen in Figure 5.11B where E_T is reported as a function of the incident energy: the linear regression for the two sets of data shows the same slope (i.e., 0.165) and very similar intercepts (i.e., 0.914 kJ/mol and 1.400 kJ/mol for Pt(111) and Pt(211), respectively). Note that the difference of 0.486 kJ/mol in the intercept is smaller than the average error for both surfaces (i.e., 0.527 kJ/mol and 0.514 kJ/mol for Pt(111) and Pt(211), respectively). The small number of trapped trajectories reduces the statistical significance of their analysis. However the results suggest that, especially at

low $\langle E_i \rangle$, some trajectories can undergo a larger energy transfer to the surface phonons (i.e., $\langle E_T \rangle = 23.2 \pm 1.9$ kJ/mol) which would increase the probability of being trapped. This suggests that energy transfer to the phonons contributes to the trapping on Pt(211).

The E_T has been calculated approximately from the molecular kinetic (K) and potential (V) energy. The initial configuration (i) is always the first step of the dynamics. For the scattered molecule, the final configuration (f) is taken from the last step of the dynamics, while for the trapped molecule, we considered the E_T upon first impact with the surface, and therefore, the final configuration is taken from the first outer turning point configuration. This means that, in the initial and in the final configurations, the molecules might not be at the same distance from the slab. Therefore the energy transfer has been estimated using Equation 5.8, which includes a correction for the interaction energy (I). I has been computed using Equation 5.9 and subtracting the absolute energy of the isolated CHD_3 and of the bare slab from the energy of the system containing both the molecule and the metal surface:

$$E_T = -\big[\big(K_f + V_f + I_f\big) - \big(K_i + V_i + I_i\big)\big], \tag{5.8}$$

$$I = V_{slab+CHD_3} - V_{slab} - V_{CHD_3}. \tag{5.9}$$

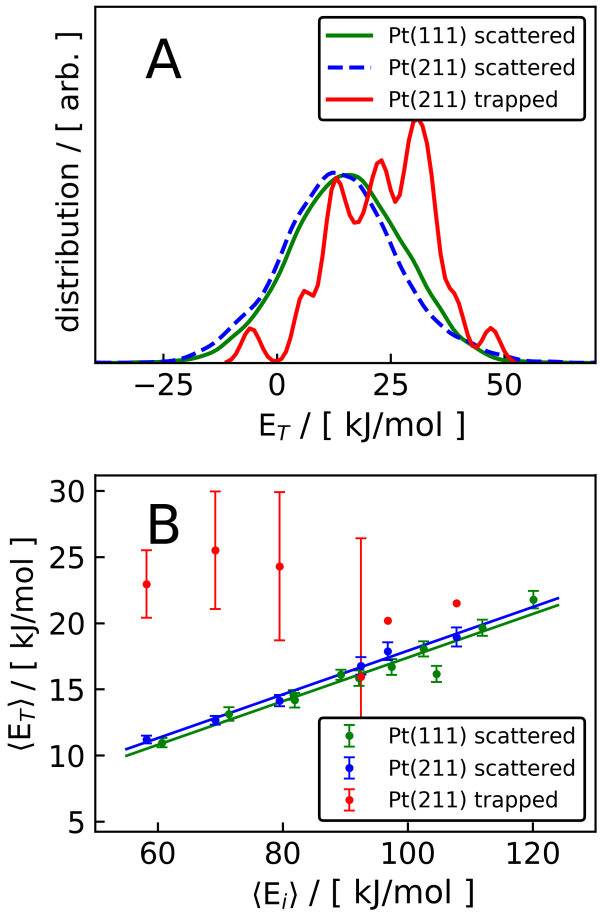

Figure 5.11: (A) energy transfer to the surface (E_T). Results are reported for scattered molecules on the flat Pt(111) (green line), on the stepped Pt(211) (blue line), and for trapped molecules (after the first impact on the Pt(211)) (red line). (B) average energy transfer to the surface versus average incident energy ($\langle E_i \rangle$). Results are reported for scattered molecules on the flat Pt(111) (green), on the stepped Pt(211) (blue), and for trapped molecules (after the first impact on the Pt(211)) (red). The lines are linear regressions of the data. Note that error bars are not shown for samples containing only one trapped trajectory.

5.3.4 Reaction Site and Dissociation Geometry

On Pt(211), the vast majority of the reactive events happen on the step edge. The reaction site has been studied by measuring the distance in the xy plane from the center of mass of the molecule to the closest atom in the first layer and reporting the distributions for all the trajectories simulated. The results are reported in Figure 5.12A for Pt(111) and in Figure 5.12B for Pt(211) for the reacted molecules at $t = 0$ and at the time of the dissociation ($t = t_{diss}$). For both surfaces, the reaction happens preferentially close to top sites (i.e., atoms in the first layer), but for the stepped surface, a considerable number of molecules dissociate further than 1 Å away from the closest Pt atom.

The effect of the orientation of the molecules on the reaction has been analyzed by monitoring the β (Figure 5.13), the θ (Figure 5.14), and the γ (Figure 5.15) angles throughout the dynamics and investigating their dependence on $\langle E_i \rangle$ (Figure 5.16). These three angles describe the orientation of the umbrella axis (β) and of the dissociating bond (θ) with respect to the surface normal and the angle between the dissociating bond and the umbrella axis (γ) (see Figure 5.3). The angles have been computed at the start of the trajectories ($t = 0$) and at the time of the dissociation ($t = t_{diss}$) for the reactive trajectories. For both θ and β, the initial distribution considering all the molecules simulated is a sine distribution proving the accurate random sampling of the initial conditions.

Comparing the Pt(111) results to the Pt(211) results, one can see that the dissociation dynamics on the two surfaces are qualitatively very similar: the two known key aspects of the dissociation of CHD_3 on Pt and Ni are the pre-orientation of the dissociating bond [4, 5] and the umbrella reorientation [4]. The distributions of θ reported in Figure 5.14 show that only bonds initially pointing toward the surface (i.e., close to the TS value of $\theta \approx 133°$) can dissociate and that the angular acceptance range for the dissociation on the Pt(211) surface is broader as the final θ distributions are less localized and exhibit larger σ values (see Figure 5.14 and Table 5.2).

The results for β (see Figure 5.13) confirm the important role of the umbrella

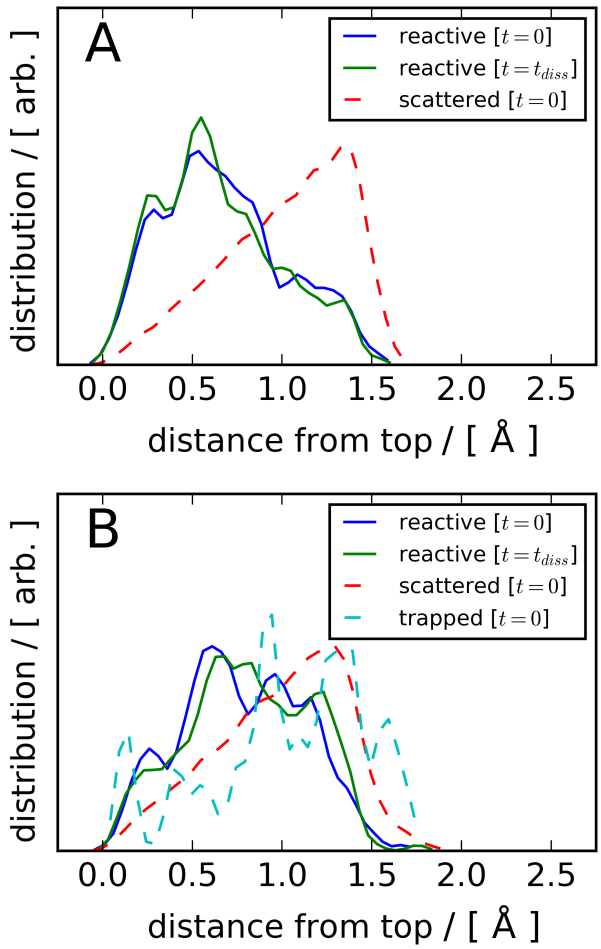

Figure 5.12: Distance from the closest top site in xy. (A, B) results for the Pt(111) surface and for the Pt(211) surface, respectively. Results for reactive trajectories are reported in blue and green for the initial position and the position at the dissociation time, respectively. Results for scattered and trapped trajectories are reported in red and cyan, respectively.

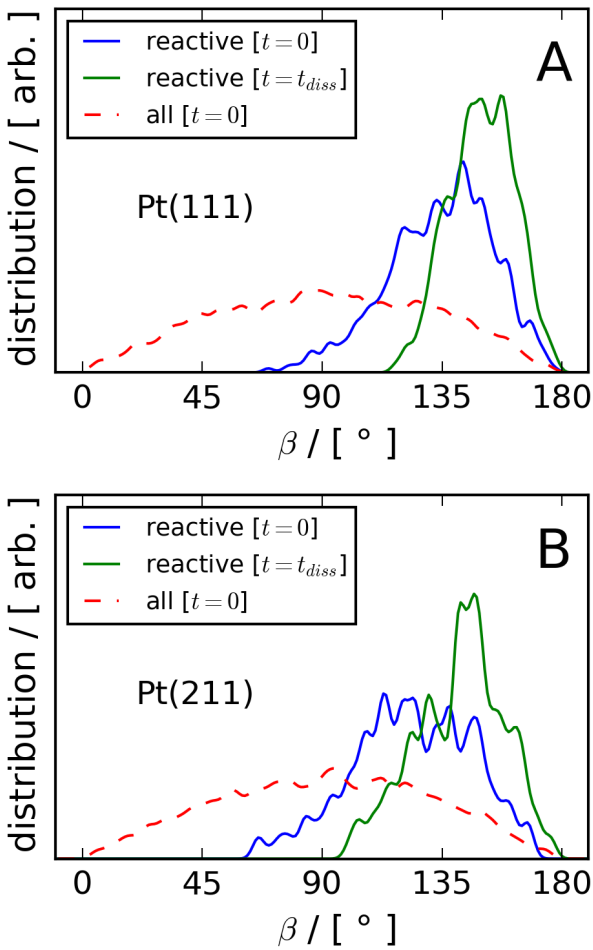

Figure 5.13: (A) β distributions for CHD_3 on Pt(111). Results for the reactive trajectories are reported in blue and green for the initial and the dissociation step, respectively. Results for the first time step of all the trajectories are reported in red. (B) the same as panel A but for Pt(211).

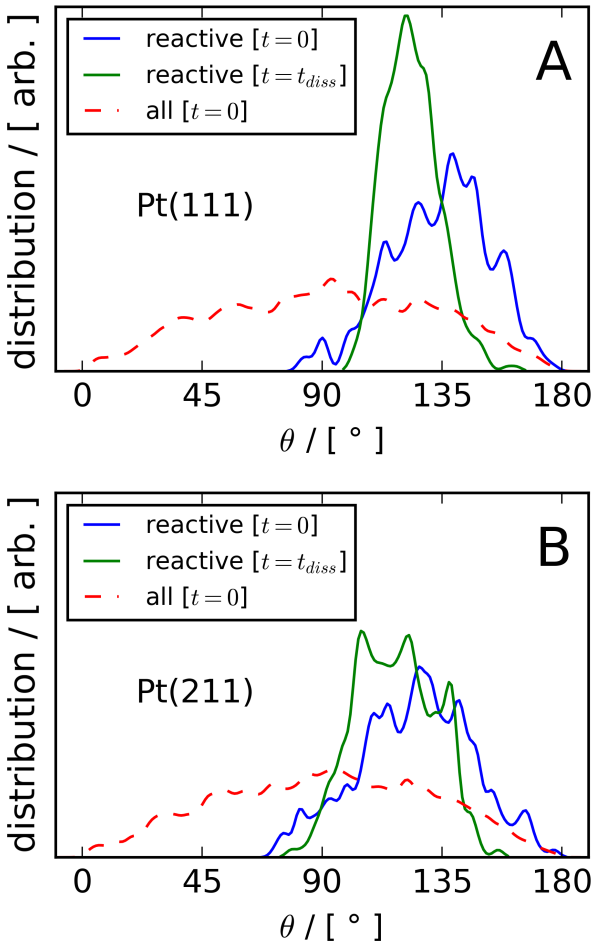

Figure 5.14: The same as Figure 5.13 but for θ.

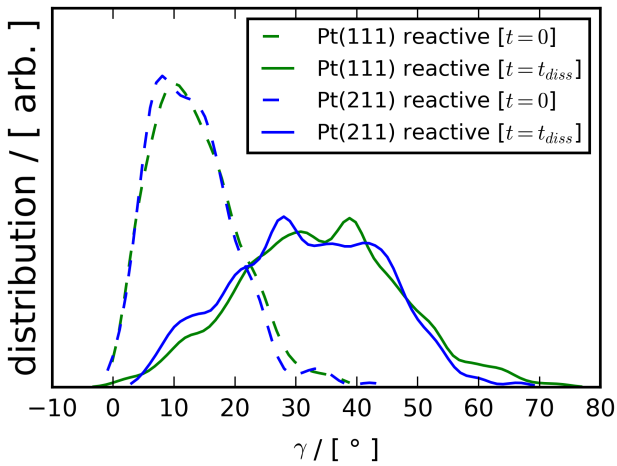

Figure 5.15: γ distributions for $t = 0$ and for the dissociation step as dashed and solid lines, respectively. Green lines are for Pt(111) results, and blue lines are for Pt(211) results.

	β / [∘]		θ / [∘]		γ [∘]	
Surface	$\langle\beta\rangle \pm \sigma_M$	σ	$\langle\theta\rangle \pm \sigma_M$	σ	$\langle\gamma\rangle \pm \sigma_M$	σ
Pt(111)	149.9 ± 0.6	12.1	123.6 ± 0.5	10.2	33.8 ± 0.6	13.0
Pt(211)	141.2 ± 1.1	16.7	117.3 ± 1.0	15.0	31.9 ± 0.8	12.2

Table 5.2: Average value, standard deviation (σ), and standard error (σ_M) for β, θ, and γ at the time of the dissociation as reported in Figures 5.13, 5.14 and 5.15, respectively.

reorientation [4] for CHD_3 on Pt(111) and extend this confirmation to the reaction on the stepped Pt(211) surface as well. In order to react, the molecule not only needs to approach the surface with the CH bond pre-oriented toward the surface, but in the meantime the umbrella has to swing upwards increasing the value of β. In previous work [4] , Füchsel *et al.* studied the dissociation of CHD_3 on Pt(111) and, for $\langle E_i \rangle$ between 49 and 84 kJ/mol, they observed that the centers of the distributions of θ do not shift during the reaction. Extending the range of initial average kinetic energy, we do observe a dependence of θ and of γ on $\langle E_i \rangle$ at the time of the reaction (see Figure 5.16) that can be explained by considering that, since the hydrogen (or deuterium) atom is oriented toward the surface,

the dissociating bond bends away from the surface upon impacting on the slab proportionally to the COM velocity, and this results in a decrease of θ and in an increase of γ (since β does not depend on $\langle E_i \rangle$).

Figure 5.16 also shows that, at the moment of the dissociation, β and θ (Figures 5.16A and 5.16B) are smaller for Pt(211) than for Pt(111), while γ is very similar (Figure 5.16C). This suggests that at the moment of the reaction the internal molecular geometry is the same on the two surfaces. However the molecules react, on average, more parallel to the macroscopic surface for the stepped Pt(211). This can be explained by looking at the θ angle of the TSs on the two surfaces. All the TSs on Pt(111) show $\theta \approx 133°$ (see Table III in Ref. [49]) which is the same value of the lowest E_b TS on Pt(211) (Edge2Edge-B1 in Figure 5.4 and Table 5.1). However, the TSs perpendicular to the step edge on Pt(211) (i.e., C, D, and E in Table 5.1) show values of θ about 10°–19° smaller and this effectively broadens the angular acceptance range for the dissociation on the stepped surface. The TSs C, D, and E dissociate in the direction perpendicular to the step edge and, even though they show larger E_b, they play a big role in the dissociative process. In Figure 5.17, the distribution of the angle α is plotted at $t = 0$ and the moment of the dissociation for molecules reacting on the step edge atom. α is defined as the counter-clockwise angle between x and the projection of the dissociating bond on the xy plane. Therefore, $\alpha = 0°$ corresponds to a dissociation in the x direction and $\alpha = 90°$ corresponds to the y direction (i.e., perpendicular and parallel to the step edge, respectively). Even though the minimum energy barrier TS occurs at $\alpha \approx 90°$ (and, equivalently, at $\alpha \approx 270°$), most of the reactions on the step edge atom happen for $\alpha \approx 180°$. This can be partially explained taking into account that the orientation of the molecules is sampled as $\sin(\theta)$ which makes $\theta \approx 114°$ (i.e., the ideal value for $\alpha = 180°$) oversampled with respect to $\theta \approx 133°$ (i.e., the ideal value for $\alpha = 90°$) (see Table 5.1).

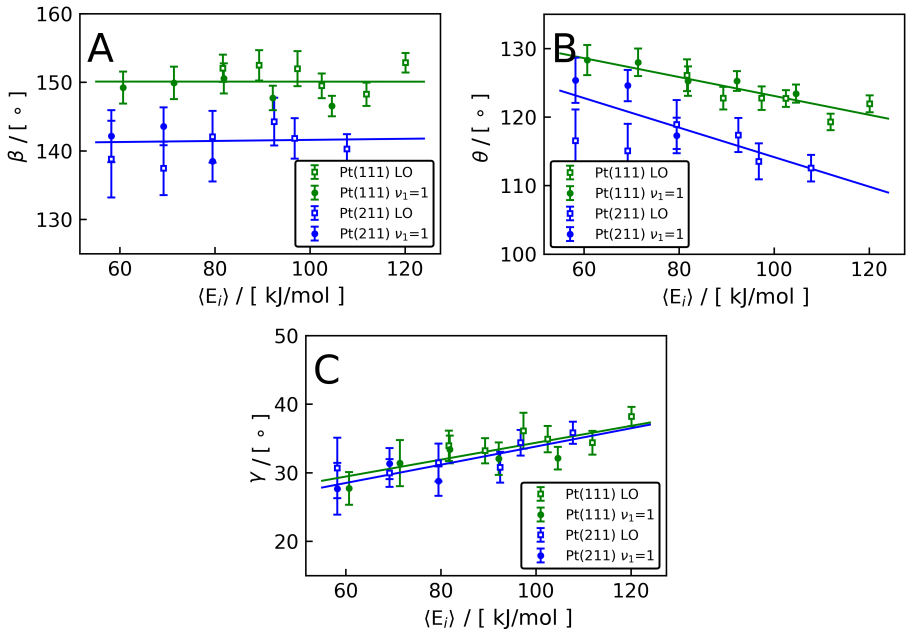

Figure 5.16: Dependence of β, θ and γ on $\langle E_i \rangle$ the moment of the dissociation. Results for the Pt(111) and for the Pt(211) are reported in green and blue, respectively. Open squares represent laser-off (LO) calculations, and filled circles represent $\nu_1 = 1$ calculations. The linear regressions reported are computed considering both LO and $\nu_1 = 1$ trajectories.

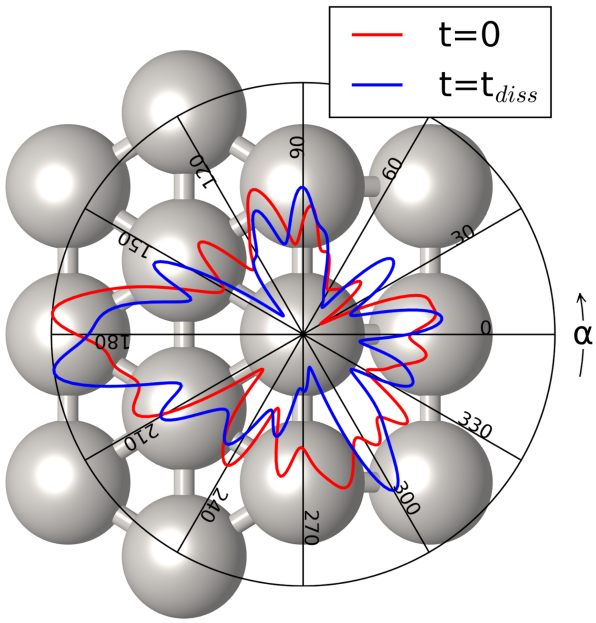

Figure 5.17: Distribution of α at $t = 0$ and at the time of the dissociation (t_{diss}) (in red and blue, respectively) for molecules that reacted on the step edge atom. The value of α is reported in black and it increases counter-clockwise. The plot is superimposed on the Pt(211) 1st layer top view. The closer the distribution is to the external black circle, the more the value of α is represented.

5.4 Summary and Conclusions

In this Chapter, we have analyzed a total of 12500 trajectories where CHD_3 is impinging either on the flat Pt(111) or on the stepped Pt(211) surface. Moreover several different TSs have been found on the Pt(211) surface. The TSs found all have a very similar molecular geometry and the ones located on a step edge atom of the Pt(211) surface show a significantly lower energy barrier. The ones on the terrace middle atom have larger barrier heights, even larger than for the flat Pt(111) surface. On both surfaces, the dissociation has been shown to proceed through a very similar mechanism where the dissociative CH bond needs to be pre-oriented toward the surface and the methyl umbrella rotates upwards to promote the reaction. However the stepped Pt(211) has a broader angular acceptance range for the dissociative chemisorption and the molecules react on average more parallel to the surface. The stepped Pt(211) surface can trap molecules due to a larger energy transfer to phonons and to corrugation-promoted energy transfer to parallel translational motion. The large velocity in the direction parallel to the surface of the trapped trajectories suggests that they can travel long distances, on average more than 600 Å for step impacts with trapping times > 1 ps, while bouncing on the surface. This implies that, in experiments, the trapped molecule has time to explore the surface, and therefore, it has an increased probability of reacting by finding the most favorable geometry or even a higher order defect, such as a kink.

Bibliography

[1] C. A. Wolcott, A. J. Medford, F. Studt, and C. T. Campbell, "Degree of Rate Control Approach to Computational Catalyst Screening," *J. Catal.*, vol. 330, pp. 197–207, 2015.

[2] Y. Xu, A. C. Lausche, S. G. Wang, T. S. Khan, F. Abild-Pedersen, F. Studt, J. K. Nørskov, and T. Bligaard, "In Silico Search for Novel Methane Steam Reforming Catalysts," *New J. Phys.*, vol. 15, p. 125021, 2013.

[3] D. Migliorini, H. Chadwick, F. Nattino, A. Gutiérrez-González, E. Dombrowski, E. A. High, H. Guo, A. L. Utz, B. Jackson, R. D. Beck, and G. J. Kroes, "Surface Reaction Barriometry: Methane Dissociation on Flat and Stepped Transition-Metal Surfaces," *J. Phys. Chem. Lett.*, vol. 8, pp. 4177–4182, 2017.

[4] G. Füchsel, P. S. Thomas, J. den Uyl, Y. Öztürk, F. Nattino, H. D. Meyer, and G. J. Kroes, "Rotational Effects on the Dissociation Dynamics of CHD_3 on Pt(111)," *Phys. Chem. Chem. Phys.*, vol. 18, pp. 8174–8185, 2016.

[5] F. Nattino, D. Migliorini, G. J. Kroes, E. Dombrowski, E. A. High, D. R. Killelea, and A. L. Utz, "Chemically Accurate Simulation of a Polyatomic Molecule-Metal Surface Reaction," *J. Phys. Chem. Lett.*, vol. 7, pp. 2402–2406, 2016.

[6] F. Nattino, D. Migliorini, M. Bonfanti, and G. J. Kroes, "Methane Dissociation on Pt(111): Searching for a Specific Reaction Parameter Density Functional," *J. Chem. Phys.*, vol. 144, p. 044702, 2016.

[7] H. Guo and B. Jackson, "Mode- and Bond-Selective Chemistry on Metal Surfaces: The Dissociative Chemisorption of CHD_3 on Ni(111)," *J. Phys. Chem. C*, vol. 119, pp. 14769–14779, 2015.

[8] S. Nave and B. Jackson, "Methane Dissociation on Ni(111): The Role of Lattice Reconstruction," *Phys. Rev. Lett.*, vol. 98, p. 173003, 2007.

[9] A. K. Tiwari, S. Nave, and B. Jackson, "The Temperature Dependence of Methane Dissociation on Ni(111) and Pt(111): Mixed Quantum-Classical Studies of the Lattice Response," *J. Chem. Phys.*, vol. 132, p. 134702, 2010.

[10] X. J. Shen, Z. J. Zhang, and D. H. Zhang, "Communication: Methane Dissociation on Ni(111) Surface: Importance of Azimuth and Surface Impact Site," *J. Chem. Phys.*, vol. 144, p. 101101, 2016.

[11] R. R. Smith, D. R. Killelea, D. F. DelSesto, and A. L. Utz, "Preference for Vibrational over Translational Energy in a Gas-Surface Reaction," *Science*, vol. 304, pp. 992–995, 2004.

[12] D. R. Killelea, V. L. Campbell, N. S. Shuman, and A. L. Utz, "Bond-Selective Control of a Heterogeneously Catalyzed Reaction," *Science*, vol. 319, pp. 790–793, 2008.

[13] R. D. Beck, P. Maroni, D. C. Papageorgopoulos, T. T. Dang, M. P. Schmid, and T. R. Rizzo, "Vibrational Mode-Specific Reaction of Methane on a Nickel Surface," *Science*, vol. 302, pp. 98–100, 2003.

[14] B. L. Yoder, R. Bisson, and R. D. Beck, "Steric Effects in the Chemisorption of Vibrationally Excited Methane on Ni(100)," *Science*, vol. 329, pp. 553–556, 2010.

[15] J. M. Wei and E. Iglesia, "Mechanism and Site Requirements for Activation and Chemical Conversion of Methane on Supported Pt Clusters and Turnover Rate Comparisons among Noble Metals," *J. Phys. Chem. B*, vol. 108, pp. 4094–4103, 2004.

[16] B. Jiang, R. Liu, J. Li, D. Q. Xie, M. H. Yang, and H. Guo, "Mode Selectivity in Methane Dissociative Chemisorption on Ni(111)," *Chem. Sci.*, vol. 4, pp. 3249–3254, 2013.

[17] X. J. Shen, J. Chen, Z. J. Zhang, K. J. Shao, and D. H. Zhang, "Methane Dissociation on Ni(111): A Fifteen-Dimensional Potential Energy Surface Using Neural Network Method," *J. Chem. Phys.*, vol. 143, p. 144701, 2015.

[18] P. M. Hundt, B. Jiang, M. E. van Reijzen, H. Guo, and R. D. Beck, "Vibrationally Promoted Dissociation of Water on Ni(111)," *Science*, vol. 344, pp. 504–507, 2014.

[19] S. Nave and B. Jackson, "Vibrational Mode-Selective Chemistry: Methane Dissociation on Ni(100)," *Phys. Rev. B*, vol. 81, p. 233408, 2010.

[20] B. Jackson and S. Nave, "The Dissociative Chemisorption of Methane on Ni(111): The Effects of Molecular Vibration and Lattice Motion," *J. Chem. Phys.*, vol. 138, p. 174705, 2013.

[21] A. Farjamnia and B. Jackson, "The Dissociative Chemisorption of Water on Ni(111): Mode- and Bond-Selective Chemistry on Metal Surfaces," *J. Chem. Phys.*, vol. 142, p. 234705, 2015.

[22] G. J. Kroes, "Toward a Database of Chemically Accurate Barrier Heights for Reactions of Molecules with Metal Surfaces," *J. Phys. Chem. Lett.*, vol. 6, pp. 4106–4114, 2015.

[23] C. Díaz, E. Pijper, R. A. Olsen, H. F. Busnengo, D. J. Auerbach, and G. J. Kroes, "Chemically Accurate Simulation of a Prototypical Surface Reaction: H_2 Dissociation on Cu(111)," *Science*, vol. 326, pp. 832–834, 2009.

[24] L. Sementa, M. Wijzenbroek, B. J. van Kolck, M. F. Somers, A. Al-Halabi, H. F. Busnengo, R. A. Olsen, G. J. Kroes, M. Rutkowski, C. Thewes, N. F. Kleimeier, and H. Zacharias, "Reactive Scattering of H_2 from Cu(100): Comparison of Dynamics Calculations Based on the Specific Reaction Parameter Approach to Density Functional Theory with Experiment," *J. Chem. Phys.*, vol. 138, p. 044708, 2013.

[25] E. Nour Ghassemi, M. Wijzenbroek, M. F. Somers, and G. J. Kroes, "Chemically Accurate Simulation of Dissociative Chemisorption of D_2 on Pt(111)," *J. Chem. Phys. Lett.*, vol. 683, pp. 329–335, 2017.

[26] Y. Y. Chuang, M. L. Radhakrishnan, P. L. Fast, C. J. Cramer, and D. G. Truhlar, "Direct Dynamics for Free Radical Kinetics in Solution: Solvent

Effect on the Rate Constant for the Reaction of Methanol with Atomic Hydrogen," *J. Phys. Chem. A*, vol. 103, pp. 4893–4909, 1999.

[27] B. Hammer, L. B. Hansen, and J. K. Nørskov, "Improved Adsorption Energetics Within Density-Functional Theory Using Rrevised Perdew-Burke-Ernzerhof Functionals," *Phys. Rev. B*, vol. 59, pp. 7413–7421, 1999.

[28] J. P. Perdew, K. Burke, and M. Ernzerhof, "Generalized Gradient Approximation Made Simple," *Phys. Rev. Lett.*, vol. 77, pp. 3865–3868, 1996.

[29] J. P. Perdew, K. Burke, and M. Ernzerhof, "Erratum: Generalized Gradient Approximation Made Simple," *Phys. Rev. Lett.*, vol. 78, p. 1396, 1997.

[30] G. Román-Pérez and J. M. Soler, "Efficient Implementation of a van der Waals Density Functional: Application to Double-Wall Carbon Nanotubes," *Phys. Rev. Lett.*, vol. 103, p. 096102, 2009.

[31] M. Dion, H. Rydberg, E. Schröder, D. C. Langreth, and B. I. Lundqvist, "Van der Waals Density Functional for General Geometries," *Phys. Rev. Lett.*, vol. 92, p. 246401, 2004.

[32] H. S. Taylor, "A Theory of the Catalytic Surface," *Proc. R. Soc. Lond. A*, vol. 108, pp. 105–111, 1925.

[33] T. Zambelli, J. Wintterlin, J. Trost, and G. Ertl, "Identification of the "Active Sites" of a Surface-Catalyzed Reaction," *Science*, vol. 273, pp. 1688–1690, 1996.

[34] B. Hammer, "Bond Activation at Monatomic Steps: NO Dissociation at Corrugated Ru(0001)," *Phys. Rev. Lett.*, vol. 83, pp. 3681–3684, 1999.

[35] A. T. Gee, B. E. Hayden, C. Mormiche, A. W. Kleyn, and B. Riedmüller, "The Dynamics of the Dissociative Adsorption of Methane on Pt(533)," *J. Chem. Phys.*, vol. 118, pp. 3334–3341, 2003.

[36] F. Abild-Pedersen, O. Lytken, J. Engbæk, G. Nielsen, I. Chorkendorff, and J. K. Nørskov, "Methane Activation on Ni(111): Effects of Poisons and Step Defects," *Surf. Sci.*, vol. 590, pp. 127–137, 2005.

[37] G. Kresse and J. Hafner, "Ab Initio Molecular-Dynamics Simulation of the Liquid-Metal-Amorphous-Semiconductor Transition in Germanium," *Phys. Rev. B*, vol. 49, pp. 14251–14269, 1994.

[38] G. Kresse and J. Furthmüller, "Efficient Iterative Schemes for Ab Initio Total-Energy Calculations Using a Plane-Wave Basis Set," *Phys. Rev. B*, vol. 54, pp. 11169–11186, 1996.

[39] G. Kresse and J. Furthmüller, "Efficiency of Ab-Initio Total Energy Calculations for Metals and Semiconductors Using a Plane-Wave Basis Set," *Comput. Mater. Sci*, vol. 6, pp. 15–50, 1996.

[40] G. Kresse and J. Hafner, "Ab Initio Molecular Dynamics for Liquid Metals," *Phys. Rev. B*, vol. 47, pp. 558–561, 1993.

[41] P. E. Blöchl, "Projector Augmented Wave-Method," *Phys. Rev. B*, vol. 50, pp. 17953–17979, 1994.

[42] G. Kresse and D. Joubert, "From Ultrasoft Pseudopotentials to the Projector Augmented-Wave Method," *Phys. Rev. B*, vol. 59, pp. 1758–1775, 1999.

[43] H. Chadwick, A. Gutiérrez-González, and R. D. Beck, "Quantum State Resolved Molecular Beam Reflectivity Measurements: CH_4 Dissociation on Pt(111)," *J. Chem. Phys.*, vol. 145, p. 174707, 2016.

[44] P. H. Xiao, D. Sheppard, J. Rogal, and G. Henkelman, "Solid-State Dimer Method for Calculating Solid-Solid Phase Transitions," *J. Chem. Phys.*, vol. 140, p. 174104, 2014.

[45] J. Kästner and P. Sherwood, "Superlinearly Converging Dimer Method for Transition State Search," *J. Chem. Phys.*, vol. 128, p. 014106, 2008.

[46] A. Heyden, A. T. Bell, and F. J. Keil, "Efficient Methods for Finding Transition States in Chemical Reactions: Comparison of Improved Dimer Method and Partitioned Rational Function Optimization Method," *J. Chem. Phys.*, vol. 123, p. 224101, 2005.

[47] G. Henkelman and H. Jónsson, "A Dimer Method for Finding Saddle Points on High Dimensional Potential Surfaces Using Only First Derivatives," *J. Chem. Phys.*, vol. 111, pp. 7010–7022, 1999.

[48] D. Migliorini, H. Chadwick, and G. J. Kroes, "Methane on a Stepped Surface: Dynamical Insights on the Dissociation of CHD_3 on Pt(111) and Pt(211)," *J. Chem. Phys.*, vol. 149, p. 094701, 2018.

[49] S. Nave, A. K. Tiwari, and B. Jackson, "Methane Dissociation and Adsorption on Ni(111), Pt(111), Ni(100), Pt(100), and Pt(110)-(1×2): Energetic Study," *J. Chem. Phys.*, vol. 132, p. 054705, 2010.

Chapter 6

CHD_3 Dissociation on Pt(111): A Comparison of the Reaction Dynamics Based on the PBE Functional and on a Specific Reaction Parameter Functional

This Chapter is based on:

H. Chadwick[1], D. Migliorini[1] and G. J. Kroes *J. Chem. Phys.*, 149, 044701 (2018)

which is reproduced with the permission of AIP publishing.

Abstract

We present a comparison of *ab initio* molecular dynamics calculations for CHD_3 dissociation on Pt(111) using the Perdew, Burke and Ernzerhof (PBE) functional

[1]These authors contributed equally to the paper.

and a specific reaction parameter (SRP) functional. Despite the two functionals predicting approximately the same activation barrier for the reaction, the calculations using the PBE functional consistently overestimate the experimentally determined dissociation probability, whereas the SRP functional reproduces the experimental values within chemical accuracy (4.2 kJ/mol). In this Chapter we present evidence that suggests that this difference in reactivity can at least in part be attributed to the presence of a van der Waals well in the potential of the SRP functional, which is absent from the PBE description. This leads to the CHD_3 molecules being accelerated and spending less time near the surface for the trajectories run with the SRP functional, as well as more energy being transferred to the surface atoms. We suggest that both these factors reduce the reactivity observed in the SRP calculations compared to the PBE calculations.

6.1 Introduction

The dissociation of methane on a transition metal catalyst is one of the rate controlling steps in the steam reforming reaction [1], used for the commercial production of hydrogen. Developing an accurate predictive understanding of this industrially important reaction is of potentially great value and could provide a method of improving the catalyst rather than relying on trial and error. Quantum-state resolved reactivity measurements [2–5] have shown that the dissociation of methane is mode-specific, i.e., the initial dissociation probability, or sticking coefficient, depends not only on the total energy of the methane but also how the energy is distributed among the degrees of freedom of the molecule [6–9]. Additionally, in partially deuterated methanes, the CH bond can be selectively broken by adding a quantum of C-H stretch vibration to the molecule [6, 10, 11]. The reaction has also been shown to be stereospecific [12, 13] and site-selective [14]. The above observations mean that the dissociative chemisorption of methane on transition metal surfaces cannot be accurately described using statistical theories [15]. Several groups [16–22] have used dynamical methods to describe the dissociation of methane on transition metal surfaces, all of which rely on den-

sity functional theory (DFT) to calculate the molecule surface interaction in the system.

For interactions at the gas-surface interface, generalized gradient approximation (GGA) exchange-correlation functionals are typically used. Even for reactions in the gas-phase, these functionals have a mean unsigned error of 3.8 kcal/mol (15.9 kJ/mol) [23], well above the 1 kcal/mol (4.2 kJ/mol) limit which is considered to define chemical accuracy. This value has not been determined for gas-surface reactions, but using DFT with the most common GGA functionals fails to predict the activation barrier (E_b) for dissociation within chemical accuracy [24]. An alternative, semi-empirical method is to mix two GGA functionals, one which overestimates E_b and one which underestimates the reaction barrier, to create a specific reaction parameter (SRP) functional [25, 26]. For gas-surface reactions, Perdew, Burke and Ernzerhof (PBE) [27, 28] and Perdew Wang 91 (PW91) [29] typically underestimate E_b and Revised PBE (RPBE) [30] tends to overestimate E_b [26, 31–37]. Combining these to make an SRP functional can produce chemically accurate results for gas-surface reactions, as was first demonstrated by mixing the PW91 [29] and RPBE [30] functionals for H_2 on Cu(111) [26, 38] and Cu(100) [31]. More details on the SRP-DFT approach are reported and discussed in Chapter 2. We have also demonstrated that an SRP exchange correlation functional can be used to reproduce the experimental sticking coefficients for CHD_3 on Ni(111) for both molecules prepared with a quantum of C-H stretch vibration and those without vibrational excitation [22]. The same SRP functional, which uses the RPBE [30] and PBE [28] for exchange and van der Waals for correlation [39], was also shown to give chemically accurate results for the sticking coefficients for CHD_3 dissociation on Pt(111) and Pt(211) (see Chapter 4 and Ref. [40]), demonstrating the transferability of the SRP functional among systems in which methane reacts with group 10 transition metals of the periodic table, and from a flat to a stepped transition metal surface. In recent work, the same SRP functional has been shown to accurately describe site-specific reactivity by reproducing the sticking coefficients for the dissociation of CH_4 on the step sites of Pt(211) [14].

For the dissociation of methane on Pt(111), the PBE and SRP functionals both predict the same E_b for the reaction, within 1 kJ/mol. Despite this, and as we will show, the PBE functional considerably overestimates the experimentally determined sticking coefficients for CHD_3 on Pt(111), whereas the SRP functional reproduces the measurements within chemical accuracy. The inclusion of the van der Waals correlation in the SRP functional reproduces the physisorption well which is present in the system [41] but is absent from the PBE description as discussed in more detail in Section 6.3. Previous work by Jackson and co-workers using their reaction path Hamiltonian model presented in the supplementary material of Ref. [40] has suggested that the coupling of translational motion along the minimum energy path (MEP) to vibrational motion is larger with the SRP functional than the PBE functional due to the presence of the van der Waals well. The effect of this may be to remove energy from motion along the MEP and convert it to motion away from the MEP, reducing the observed reactivity with the SRP functional. Similar arguments have also been presented to explain why vibrational energy can promote the dissociation of methane on transition metal surfaces more than the same amount of translational energy, i.e., the vibrational efficacy can be more than 1 [7, 42–46]. The vibrationally excited molecules stay closer to the MEP than the molecules with only translational energy, meaning they sample parts of the potential energy surface (PES) with a lower E_b. This can lead to an increase in reactivity which is more than would be anticipated by the amount of vibrational energy added [7].

Another effect of including the van der Waals correlation could be to change the energetic corrugation of the PES, i.e., how the shape of the PES changes with motion parallel to the plane of the surface. A recent study [36] compared several density functionals for the dissociation of H_2 on Ru(0001) and found that those which included van der Waals correlation better reproduced the dependence of experimentally determined sticking coefficients on incident translational energy than functionals which did not include van der Waals correlation. As the gradient of the sticking coefficient curve reflects the distribution of activation barrier heights present on the surface, this was attributed to functionals that in-

cluded van der Waals correlation providing a better description of the energetic corrugation than functionals without van der Waals correlation.

In this Chapter, we will present a detailed comparison of the results from *ab initio* molecular dynamics (AIMD) calculations performed using the SRP and PBE functionals to further investigate why they predict such different reactivity for the dissociation of CHD_3 on Pt(111). The rest of the Chapter is organized as follows. In Section 6.2, we give an overview of the theoretical methods used in the current work, before presenting the results and discussion in Section 6.3. Section 6.4 presents a summary of the key points.

6.2 Method

The theoretical methods employed in the current work have been described in detail in Chapter 2 and in previous work [37, 40] and only the most relevant aspects will be presented here. In brief, we ran between 500 and 1000 quasi-classical trajectories per incidence condition for CHD_3 colliding with Pt(111) for a range of incident energies, using the Vienna *ab initio* simulation package (VASP) version 5.3.5. [47–50] The first Brillouin zone has been sampled using a 4x4x1 Γ-centered K-point grid, and the cut off energy for the plane wave basis set was 350 eV. Projector augmented wave pseudopotentials [51, 52] have been used to represent the core electrons. For the SRP calculations, the same pseudopotentials have been used consistently throughout the calculations, whereas for the PBE calculations, a different Pt pseudopotential was used for equilibrating the surface and in the AIMD trajectory calculations. As discussed in more detail in the supplementary material of Ref. [53], the maximum error this introduces in the E_b for the reaction calculated using the PBE functional is 0.4 kJ/mol, which is not large enough to change the results of the PBE trajectories presented here. The Pt(111) surface has been modeled using a 5 layer (3x3) supercell slab [37, 40] with each slab separated from its first periodic replica by 13 Å of vacuum. A 0.1 eV Fermi smearing has been used to facilitate the convergence. Extensive tests of the parameters used in the calculations have been performed, the results of

which can be found in the supplementary material of Ref. [40].

The PBE [28] and the SRP functional developed in Ref. [22] have been used in the DFT calculations. The SRP exchange-correlation functional (E_{XC}^{SRP}) is defined as:

$$E_{XC}^{SRP} = x \cdot E_X^{RPBE} + (1-x) \cdot E_X^{PBE} + E_C^{\text{vdW-DF}}, \tag{6.1}$$

where E_X^{PBE} and E_X^{RPBE} are, respectively, the PBE and RPBE exchange functionals, and $E_C^{\text{vdW-DF}}$ is the van der Waals correlation functional [39]. Chapter 4 and previous work [40] has shown that $x = 0.32$ produces chemically accurate results for the dissociation of CHD_3 on Pt(111), and we will use this value of x here. We will refer to this SRP functional as SRP32-vdW.

The initial conditions used for the trajectory calculations were sampled to replicate the molecular beam scattering experiments of Beck and co-workers presented in Ref. [40]. For the "laser-off" trajectories, the vibrational populations of the molecules were sampled using a Boltzmann distribution at the nozzle temperature used to create the molecular beam expansion, whereas for the $\nu_1 = 1$ calculations, all the molecules were prepared with a single quantum of CH stretch vibration. The translational energies of the molecules in each case were sampled from the experimental time of flight distribution, and the positions and velocities of the surface atoms from dynamics calculations run to equilibrate the bare slab at a surface temperature of 500 K. More details about the sampling of the molecular initial conditions can be found in the supplementary material of Refs. [22] and [40].

At the start of the trajectory, the CHD_3 is positioned 6 Å above the surface with x and y chosen to randomly sample all the positions on the Pt(111) slab. The trajectories were propagated with a time step of 0.4 fs using the velocity-Verlet algorithm until the CHD_3 either dissociated on the Pt(111) surface or scattered back into the gas-phase. The molecule was considered to have reacted if one of the bonds in the molecule was greater than 3 Å, whereas if the center of mass (COM) of the molecule was 6 Å away from the surface with the COM velocity

directed away from the surface, it was considered to have been scattered [40]. All the trajectories were found to either react or scatter within the maximum 1 ps timeframe that the trajectory was propagated for; we observed that no molecules remained trapped on the surface.

The sticking coefficients (S_0), were calculated from the AIMD calculations using:

$$S_0 = N_{react}/N_{tot}, \tag{6.2}$$

where N_{react} is the number of trajectories that dissociate and N_{tot} is the total number of trajectories. The statistical error bars were found as:

$$\sigma_p = \sqrt{\frac{S_0(1 - S_0)}{N_{tot}}}, \tag{6.3}$$

and represent 68% confidence limits.

6.3 Results and Discussion

The sticking coefficients calculated from the AIMD trajectories using the PBE functional (green) are compared with those obtained experimentally [40] (red) in Figure 6.1, for molecules under laser-off conditions (Panel A) and those prepared with a single quantum of the C-H stretch (Panel B). The calculated S_0 are seen to systematically overestimate the values that have been measured both with and without laser excitation. To quantify the extent to which the PBE functional overestimates S_0, the experimental data were fit to an S-shape curve using:

$$S_0(E_i) = \frac{A}{2}\left(1 + \mathrm{erf}\left(\frac{E_i - E_0}{W}\right)\right), \tag{6.4}$$

where A is the value of S_0 at infinitely high translational energy, E_i is the incident energy, E_0 is the average activation barrier height for the dissociation, and W is the width of curve. The energy shift between the fit to the experimental data

Functional	E_b / [kJ/mol]	E_b^c / [kJ/mol]
SRP32-vdW	78.6	66.5
PBE	78.0	66.1
RPBE [37]	112.8	100.9

Table 6.1: The activation barriers (E_b) and zero point energy corrected activation barriers (E_b^c) for the dissociation of CHD_3 on Pt(111) calculated using the SRP32-vdW, PBE, and RPBE density functionals.

and the S_0 determined using the PBE functional could then be found, with the values (in kJ/mol) also presented in Figure 6.1. The shift of the two highest energy laser-off and $\nu_1 = 1$ points have not been included in this average, as the energy shift has to be determined by extrapolating the fit to the experimental data outside the energy range where sticking coefficients were measured. The average energy shift between the two sets of data is 13.1 kJ/mol. This is over a factor of 3 higher than the 4.2 kJ/mol (1 kcal/mol) which is typically considered to define chemical accuracy.

In Figure 6.2, the S_0 calculated from AIMD trajectories using the PBE functional (green) are compared with those obtained using the SRP32-vdW functional [40] (blue). The results using the PBE functional are larger than those obtained using the SRP32-vdW functional. Using the same analysis as described above, the average energy shift between the PBE and the SRP32-vdW functional is 13.9 kJ/mol, where the highest two energy PBE points have not been included in the average as the energy shifts have to be determined by extrapolating the SRP32-vdW fit outside the E_i range where values of S_0 have been determined. This result might suggest that the PBE functional would give an activation barrier which is approximately 14 kJ/mol lower in energy than the SRP32-vdW functional. However, as shown in Table 6.1, the values of the E_b obtained from the PBE and SRP32-vdW functionals are almost the same (differing by no more than 1 kJ/mol) both with and without zero point energy corrections.

Whilst the activation barriers for the dissociation calculated with the SRP32-vdW and PBE functionals are similar, an important difference between the two functionals is that the SRP32-vdW description includes a van der Waals well,

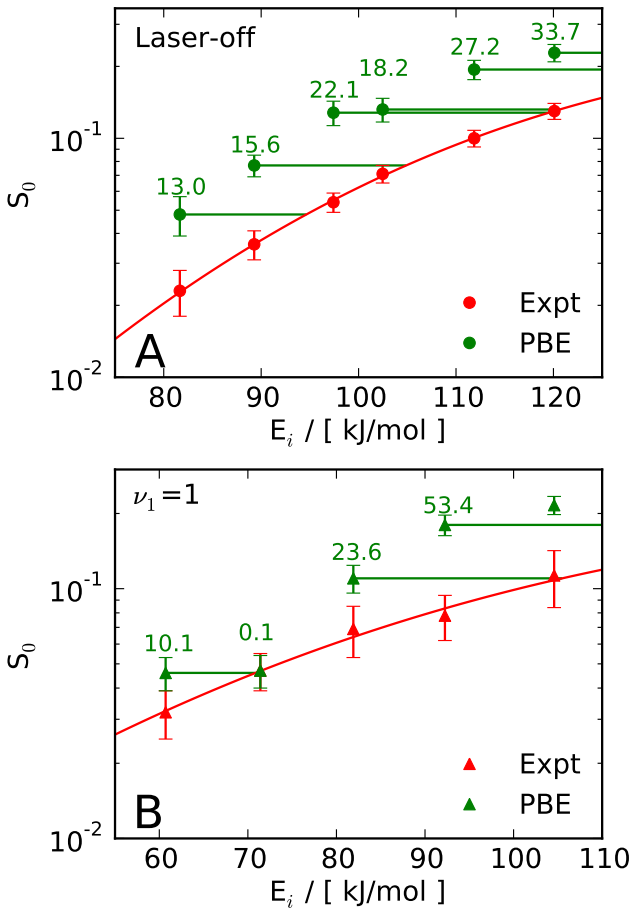

Figure 6.1: Comparison of the experimentally measured sticking coefficients [40] (red) with those calculated using the PBE functional (green) for CHD_3 dissociation on Pt(111) under laser-off conditions (A) and for molecules prepared with a single quantum of C–H stretch vibration (B). The numbers in the plots are the energy shift in kJ/mol between S_0 calculated with the PBE functional and the fit to the experimental data.

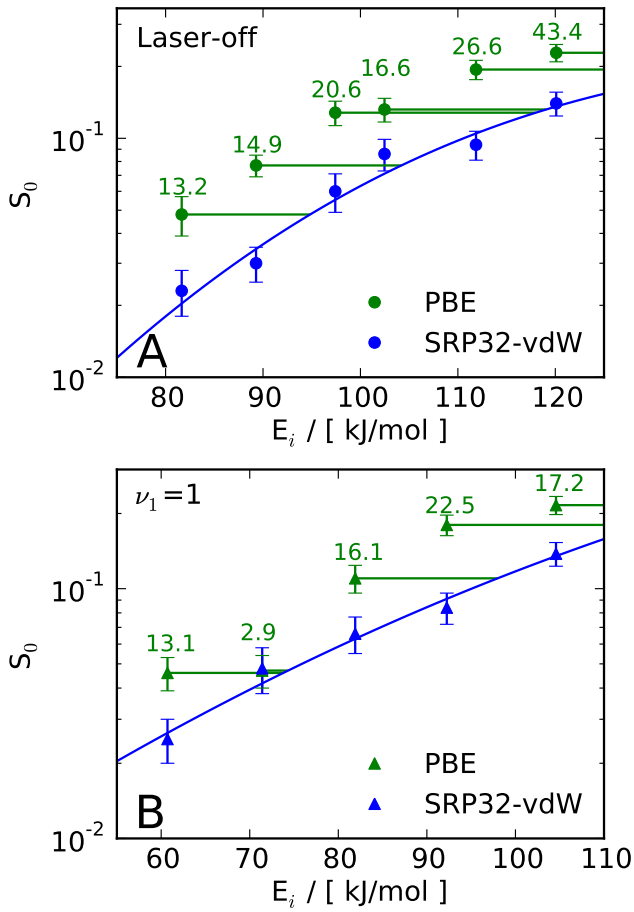

Figure 6.2: Comparison of the sticking coefficients calculated using the PBE functional (green) and the SRP32-vdW functional [40] (blue) for CHD_3 dissociation on Pt(111) under laser-off conditions (A) and for molecules prepared with a single quantum of C-H stretch vibration (B). The numbers in the plots are the energy shift in kJ/mol between S_0 calculated with the PBE functional and the fit to the SRP32-vdW data.

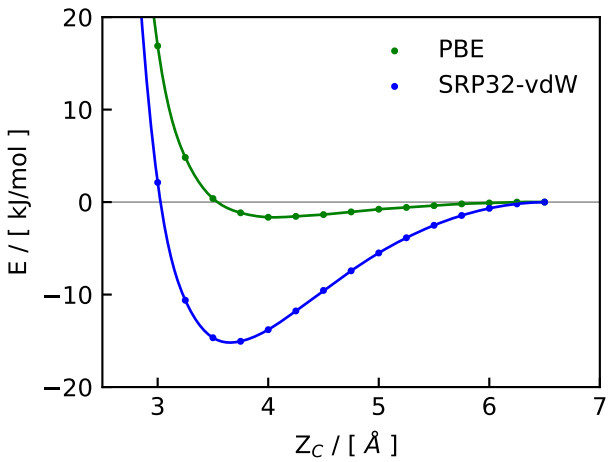

Figure 6.3: One dimensional cuts through the SRP32-vdW (blue) and PBE (green) PESs showing the difference in the van der Waals well obtained with the two functionals. The energy is reported as a function of the distance between the carbon atom and the surface (Z_C) for the molecule with three hydrogen atoms pointing toward the slab.

whereas the PBE does not, as shown by the one dimensional cuts through the PESs in Figure 6.3. As the SRP32-vdW functional predicts the experimental S_0 within chemical accuracy unlike the PBE functional, we compared the dynamics obtained using the two functionals to determine to what extent the differences in the reactivity can be attributed to the presence of the van der Waals well in the SRP32-vdW description or to other topological features of the PES. Specifically we have investigated the effect of surface motion on the effective activation barrier height, how closely the trajectories that dissociate follow the minimum energy path, how significant the acceleration of the SRP32-vdW trajectories due to the van der Waals well on the approach to the surface is, and the extent to which energy is transferred from the molecules to the surface for the two functionals. Each of these will be addressed in turn in the following Sections.

6.3.1 Surface Motion and Effective Barriers

The activation barriers presented in Table 6.1 were calculated for a frozen 0 K surface, whereas the AIMD calculations were run at a surface temperature of 500

K. Previous studies [19, 54–58] have shown that the molecule surface distance at the transition state (TS) and the effective activation barrier height depend on the motion of the closest surface atom out of the plane of the surface making S_0 dependent on surface temperature. The distance in z between the COM of the TS and the surface plane as a function of Q is presented in Figure 6.4A for the PBE functional (green) and the SRP32-vdW functional (blue). Positive values of Q correspond to the surface atom closest to the methane being above the plane, negative Q to it being below the plane, and 0 to the atom being in the plane of the surface. The change in height of the TS with surface atom motion is similar for both functionals, with the mechanical coupling [19, 59] $\alpha = dZ_b/dQ$ being 0.80 for the PBE functional and $\alpha = 0.82$ for the SRP32-vdW functional, in reasonable agreement with previous results [59, 60]. In the Equation for α, Z_b defines the distance from the COM of the TS to the macroscopic surface. The barrier height as a function of the out of plane surface atom displacement under the dissociating CHD_3 is presented in Figure 6.4B for the PBE functional (green) and the SRP32-vdW functional (blue). For both functionals, the barrier height increases as the surface atom moves into the bulk and decreases as it moves above the plane. This effect is larger for the PBE functional, where the electronic coupling [19, 59] $\beta = -dE_b/dQ$ is equal to 90.2 (kJ/mol)/Å. For the SRP32-vdW functional, $\beta = 77.8$ (kJ/mol)/Å. The same surface atom displacement therefore leads to a larger decrease in E_b for the PBE functional than for the SRP32-vdW functional.

The distribution of Q for each functional has been calculated by analyzing 1 ps of bare slab dynamics for ten different initial slabs, and the two distributions are presented in Figure 6.4C for the PBE (green) and SRP32-vdW (blue) functionals. These have been obtained using Gaussian binning with a 0.01 Å bin size and a 0.05 Å broadening parameter. Both the distributions are centered close to 0 Å, but the distribution for the SRP32-vdW functional is slightly broader and with a tail to larger positive values of Q. From the activation barriers and the distribution of Q presented in Figures 6.4B and 6.4C, the average activation

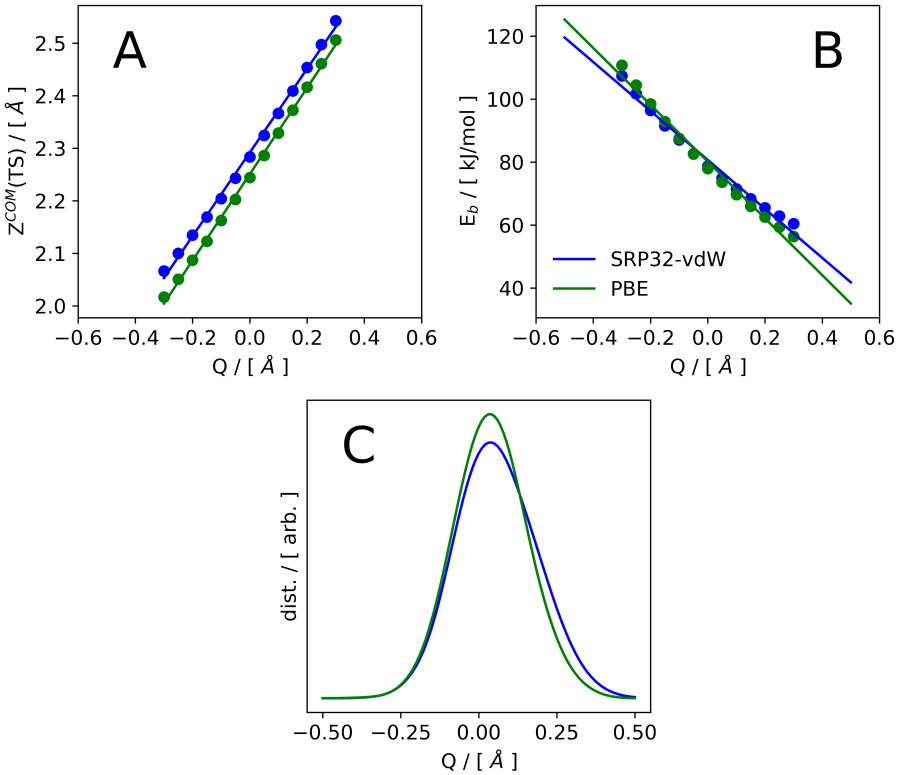

Figure 6.4: (A) the variation of the distance of the molecule's center of mass of the transition state to the surface plane as a function of the displacement of the surface atom (mechanical coupling) from the Pt(111) surface for PBE (green) and SRP32-vdW (blue) functionals. The straight lines are fits to the data. (B) the variation in the activation barrier height as a function of the displacement of the surface atom (the electronic coupling) from the Pt(111) surface for the PBE (green) and SRP32-vdW (blue) functionals. The straight lines are fits to the data. (C) The distribution of the surface atom displacements averaged over the AIMD slabs at a surface temperature of 500 K for the PBE (green) and SRP32-vdW (blue) functionals.

barrier experienced by the CHD_3 in the calculations has been determined using:

$$\langle E_b(Q)\rangle = \frac{\sum_{i=0}^{i_{max}} P(Q_i)E_b(Q_i)\Delta Q_i}{\sum_{i=0}^{i_{max}} P(Q_i)\Delta Q_i}, \tag{6.5}$$

$$Q_i = Q_{i=0} + i \cdot \Delta Q_i, \tag{6.6}$$

where $P(Q_i)$ is the probability of finding the surface atom displaced by Q_i, $E_b(Q_i)$ is the value of the barrier for the displacement Q_i , and $i = 0$ and i_{max} correspond to values of Q_i for which $P(Q_i)$ is negligible. The effective barriers calculated in this way are 76.6 kJ/mol and 76.2 kJ/mol for the PBE and SRP32-vdW functionals, respectively, so that the difference between these barriers does not account for the energy shift between the two curves presented in Figure 6.2.

6.3.2 Motion Across the Potential Energy Surface and the Minimum Energy Path

Whilst the activation barriers for methane dissociation determined with the SRP32-vdW and PBE functionals are similar, dissociation does not necessarily occur via the lowest energy transition state, and so other differences in the SRP32-vdW and PBE potentials could be responsible for the differences in reactivity predicted using the two functionals. Two-dimensional cuts through the PESs for the SRP32-vdW functional (Panel A) and PBE functional (Panel B) are presented in Figure 6.5. These were calculated holding the internal coordinates of the molecule fixed in the TS geometry given in Table 6.2 for dissociation above a top site on the surface. In each plot, the MEP is shown as a white dotted line and the TS as a black square. The coordinate perpendicular to the MEP at the TS (χ) is reported as a dashed black line. As shown in Figure S1 and Table SIII in the supplementary material of Ref. [53], the curvature of the MEP for the SRP32-vdW PES is slightly larger than that for the PBE functional as the turn in the MEP toward the TS for the SRP32-vdW functional is tighter.

Figure S2 of the supplementary material of Ref. [53] presents one dimensional cuts through the PES perpendicular to the MEP at the TS (along χ) for the

	r^{TS} / [Å]	Z_C^{TS} / [Å]	θ / [∘]	β / [∘]	γ / [∘]
SRP32-vdW	1.55	2.29	133	168	35
PBE	1.51	2.24	132	169	37

Table 6.2: The dissociating bond length (r^{TS}), height of the carbon atom above the surface (Z_C^{TS}), angle between the dissociating bond and the surface normal (θ), angle between the umbrella axis and surface normal (β), and the angle between the umbrella axis and dissociating bond (γ) at the transition state for the SRP32-vdW functional (top row) and PBE functional (bottom row).

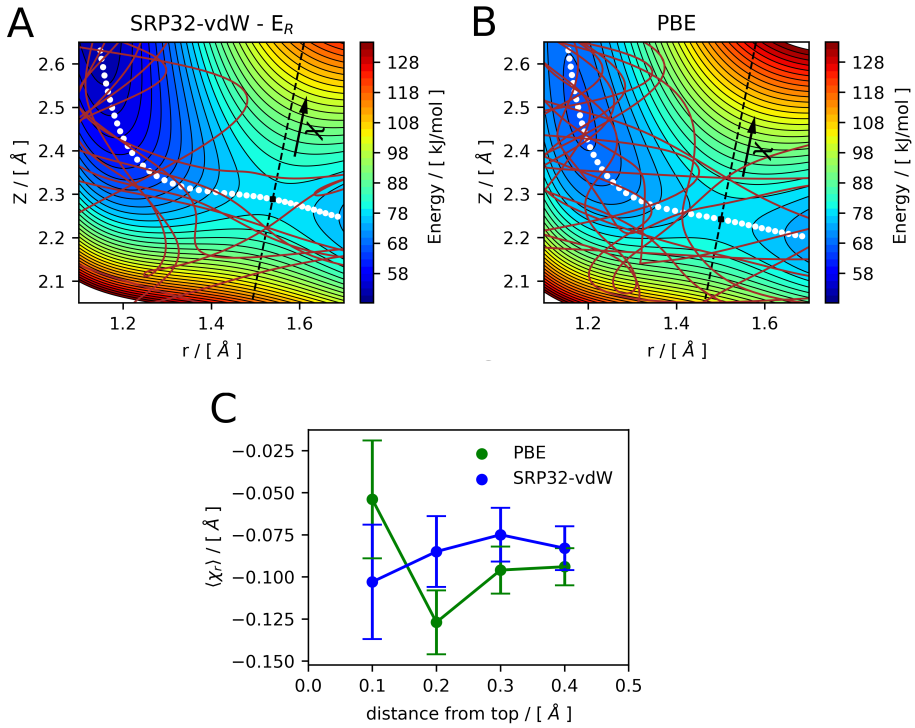

Figure 6.5: Two-dimensional cuts through the SRP32-vdW (A) and PBE (B) potential energy surfaces showing the transition state (black square), minimum energy path (white dotted line), and the vector perpendicular to the minimum energy path (χ, black dashed line). Trajectories that start within 0.1 Å of a top site are also shown (brown lines). All molecular coordinates except Z and r have been fixed at the TS values. (C) The average distance between the transition state and where the reacted trajectories cross the vector perpendicular to the minimum energy path calculated using Equation 6.7 for different distances from a top site for the PBE (green) and SRP32-vdW (blue) trajectories.

SRP32-vdW (blue) and PBE (green) functionals. The curves have been shifted down by E_b for each functional so that the TS energy is at 0 kJ/mol. The saddle point in the SRP32-vdW PES is slightly wider than that for the PBE PES, but not by much. As shown by the averaged properties of the reacted trajectories presented in Table SIV of the supplementary material of Ref. [53], the geometries of the trajectories that react are similar for the two functionals. From this, we can conclude that the width of the saddle point at the TS is similar for the PBE and SRP32-vdW functionals, and small differences probably do not contribute to the different reactivity of the two functionals. There is also no evidence of significantly different energetic corrugation of the two PESs, as the average distances between the COM and the nearest top sites while the molecules dissociate (δ_{Top}) are similar (see Table SIV of the supplementary material of Ref. [53]). To quantify the extent to which the PBE and SRP32-vdW trajectories follow the MEP across the PES, χ_r was calculated as the distance from the TS in r and Z when the trajectory crosses the χ coordinate:

$$\chi_r = \sqrt{(Z_C - Z_C^{TS})^2 + (r - r^{TS})^2}, \tag{6.7}$$

where Z_C is the height of the carbon above the surface, r the dissociating bond length, and the quantities with a TS superscript are the corresponding transition state values. The angle between the dissociating bond and surface normal, θ, has not been included in this analysis as the values at the transition state are very similar for both functionals, as shown in Table 6.2. Additionally, there is no significant difference in the distributions of θ for the trajectories that react, which are given in Table SIV of the supplementary material of Ref. [53]. $\langle \chi_r \rangle$ has been calculated for trajectories that begin within 0.1 Å, 0.2 Å, 0.3 Å and 0.4 Å of a top site in the xy plane. The results are presented in Figure 6.5C for the PBE (green) and SRP32-vdW (blue) trajectories and the distributions of χ_r in Figure S3 of the supplementary material of Ref. [53]. Additionally, the paths of the reactive trajectories that start within 0.1 Å of a top site for each functional are shown as brown lines in Figures 6.5A and 6.5B. Whilst the analysis at 0.1 Å suggests

that the SRP32-vdW trajectories follow the MEP less, the opposite trend is seen considering the trajectories that start further away from the top site. In this analysis, we therefore see no firm evidence of the "bobsled effect" [61–63], where it would be expected that the SRP32-vdW trajectories which are accelerated by the van der Waals well and therefore move faster, as shown in Figure 6.6 would go further up the repulsive wall of the PES and might be expected to cross χ at more negative values of χ_r. The motion up the repulsive wall would also lead to an oscillation (a vibration) in the motion with respect to the MEP, and we find no evidence of increased vibrational excitation of the scattered SRP32-vdW trajectories compared to the PBE trajectories, as shown in Table SV of the supplementary material of Ref. [53] (δE_{vib}).

This is in contrast to an earlier suggestion presented in the supplementary material of Ref. [40], where larger coupling constants were found between motion along the MEP to vibration for the SRP32-vdW functional than for the PBE functional using the Reaction Path Hamiltonian model, which was attributed to the presence of the van der Waals well. However, the results from the AIMD trajectories presented here suggest that the presence of the van der Waals well may not lead to increased energy transfer from translation to vibrations for the SRP32-vdW functional compared to the PBE functional.

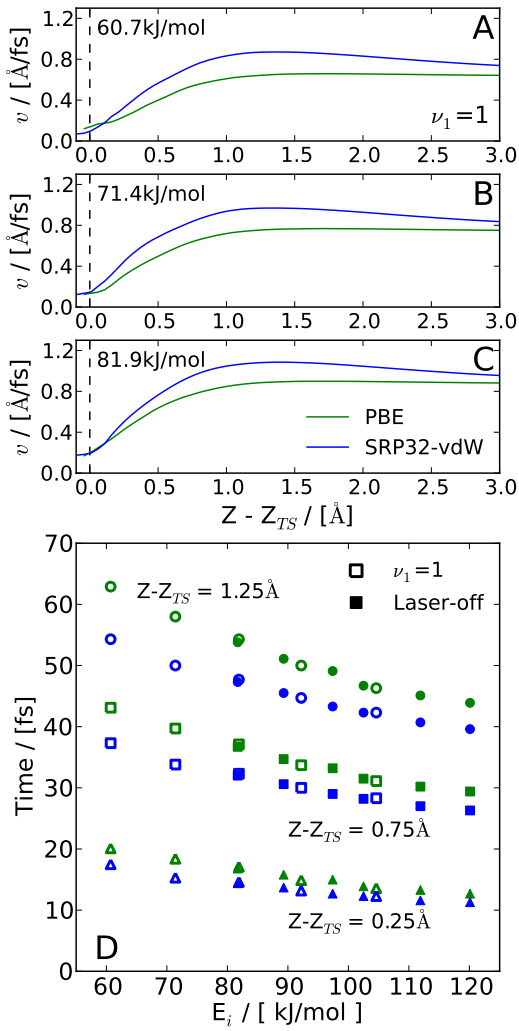

Figure 6.6: The average velocity of the PBE (green) and SRP32-vdW (blue) trajectories that react as they approach the surface at an incident energy of 60.7 kJ/mol (A), 71.4 kJ/mol (B), and 81.9 kJ/mol (C) with a quantum of initial C-H stretch excitation. The dashed vertical line shows the position of the transition state. (D) The average time it takes for the scattered trajectories to travel a distance ΔZ of 1.25 Å (circles), 0.75 Å (squares), and 0.25 Å (triangles) along Z to Z_{TS} for the PBE trajectories (green) and the SRP32-vdW trajectories (blue). The open symbols show the times for the trajectories prepared with a quantum of the C-H stretch and the filled symbols show the laser-off trajectories.

6.3.3 Molecule-Surface Interaction Times

Although the van der Waals well accelerates the SRP32-vdW trajectories, the molecules arrive at the TS (black dashed line in Figure 6.6) with a similar velocity for both functionals. However, as the SRP32-vdW trajectories are accelerated, the time they take to travel over a certain distance to the TS is less than that for the PBE trajectories (green), as shown in Figure 6.6D. The TS for the SRP32-vdW functional is also 0.05 Å further from the surface than for the PBE functional. All this means that the interaction time with the surface is shorter and the molecules have less time to distort toward the TS geometry, given in Table 6.2, in the SRP32-vdW calculations. The TS also has a longer bond length (r) for the SRP32-vdW functional. The TS being later in r for the SRP32-vdW functional and the CHD_3 having less time to distort to the TS geometry will likely contribute to the sticking coefficient observed in the SRP32-vdW calculations being lower than in the PBE calculations, although it is not easy to quantify by how much.

6.3.4 Energy Transfer to the Surface

The analysis of the scattered trajectories shows that the energy transfer to the surface is between 1 kJ/mol and 3 kJ/mol larger for the SRP32-vdW calculations than for the PBE calculations. This difference can be explained qualitatively using the modified Baule model. The initial Baule model estimates the energy transfer (E_T^{Baule}) to the surface treating the molecule as a hard sphere colliding with a single surface atom. [64] For an incident energy E_i, E_T^{Baule} is given by:

$$E_T^{Baule} = \frac{4\mu E_i}{(1+\mu)^2}, \tag{6.8}$$

where μ is the mass ratio between the mass of CHD_3 and an effective surface mass M_S , often taken as the mass of a single Pt atom. The Modified Baule (M. Baule) model takes into account the additional kinetic energy the methane gains while travelling toward the surface due to the interaction with the surface. For

an incident energy E_i:

$$E_T^{M.Baule} = \frac{4\mu(E_i + E_{ads})}{(1+\mu)^2}, \tag{6.9}$$

where E_{ads} is the molecular adsorption energy. The results for the Baule model (black) and for the Modified Baule model for the SRP32-vdW (blue) and PBE (green) functionals are compared with the energy transfer calculated from the AIMD trajectories (blue and green open symbols for SRP32-vdW and PBE, respectively) in Figure 6.7. The solid lines are straight line fits to the data. For the Modified Baule model, ΔE_T reads:

$$\Delta E_T = \frac{4\mu(E_{ads}^{SRP} - E_{ads}^{PBE})}{(1+\mu)^2}, \tag{6.10}$$

where E_{ads}^{SRP} and E_{ads}^{PBE} are the largest molecular adsorption energies computed with the two functionals and are equal to 21.9 kJ/mol and 1.5 kJ/mol, respectively. This is deeper than that shown in Figure 6.3 for the SRP32-vdW functional as the value here includes the residual energy correction of 4.0 kJ/mol, as discussed in Chapter 2 and in the supplementary material of Ref. [40]. Using Equation 6.10 gives a value of 6.6 kJ/mol, qualitatively reproducing the difference in energy transfer to the surface for the PBE and SRP32-vdW trajectories. This suggests that the difference in energy transfer can be attributed to the difference in E_{ads}.

We note that the actual amount of energy transferred to the surface in the reactive collisions may well be higher than that for scattered trajectories. Previous research has shown that CHD_3 reacts close to surface atoms, while scattered CHD_3 also samples surface sites away from the top sites (for the positions of the surface atoms, see Figure 2 of Ref. [21]). For the former trajectories, the approximation that the effective surface mass in the Baule model is equal to the mass of the surface atom will therefore be better than for in the scattered trajectories. In the latter, the effective surface mass that one should use to calculate the mass ratio may be a factor of 2 to 3 higher for molecules scattering off bridge and hollow

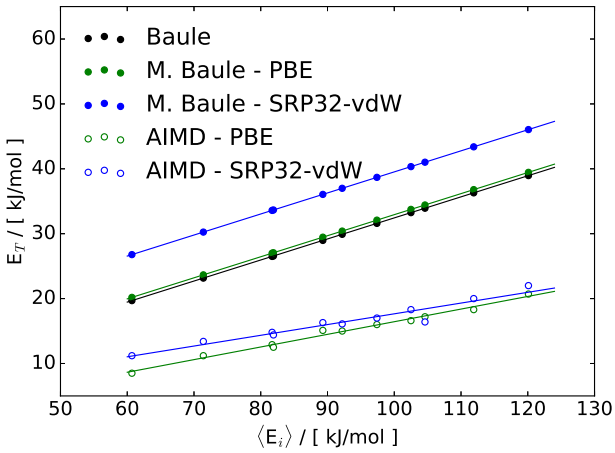

Figure 6.7: Comparison of the energy transferred to the surface in the AIMD trajectories using the PBE functional (open green symbols) and the SRP32-vdW functional (open blue symbols) with that predicted by the Baule model (black filled symbols) and the Modified Baule model (filled green and blue symbols for PBE and SRP32-vdW, respectively). The lines are fits to the data.

sites. If the Modified Baule model with M_S equal to the mass of a surface atom is applicable to the reactive collision, the difference in energy transfer between PBE and SRP32-vdW (6.6 kJ/mol) accounts for approximately half the energy shift between the associated sticking curves (13.9 kJ/mol).

6.4 Summary and Conclusions

The SRP32-vdW and PBE functionals both predict the same activation barrier for the dissociation of CHD_3 on Pt(111), but AIMD trajectory calculations using the PBE functional give a significantly higher sticking coefficient than calculations using the SRP32-vdW functional. The PBE results are also larger than the values determined experimentally, which the SRP32-vdW functional reproduces within chemical accuracy. We suggest that the reasons that the two functionals predict such different reactivity are related to the presence of van der Waals correlation in the SRP32-vdW functional, which is absent from the PBE functional. The resultant van der Waals well accelerates the CHD_3 trajectories toward the surface

in the case that the SRP32-vdW functional is used, meaning that the molecule has less time to distort toward the transition state geometry. It also leads to more energy being transferred from the molecule to the surface, resulting in a lower reactivity. However, we do not find any evidence that the van der Waals well leads to more efficient translational to vibrational energy transfer in the SRP32-vdW trajectories compared to the PBE trajectories, or that the SRP32-vdW potential energy surface is more energetically corrugated than the PBE potential energy surface. Whilst both these factors could lead to a decrease in the reactivity of the SRP32-vdW trajectories compared to the PBE trajectories, neither appears to make a considerable contribution to the difference in reactivity that we observe.

Bibliography

[1] I. Chorkendorff and J. W. Niemantsverdriet, *Concepts of Modern Catalysis and Kinetics.* Weinheim: Wiley-VCH, 2003.

[2] H. Chadwick, A. Gutiérrez-González, and R. D. Beck, "Quantum State Resolved Molecular Beam Reflectivity Measurements: CH_4 Dissociation on Pt(111)," *J. Chem. Phys.*, vol. 145, p. 174707, 2016.

[3] H. Chadwick and R. D. Beck, "Quantum State–Resolved Studies of Chemisorption Reactions," *Annu. Rev. Phys. Chem.*, vol. 68, pp. 39–61, 2017.

[4] R. D. Beck and A. L. Utz, *Dynamics of Gas-Surface Interactions: Atomic-level Understanding of Scattering Processes at Surfaces.* Berlin: Springer, 2013.

[5] L. B. F. Juurlink, D. R. Killelea, and A. L. Utz, "State-Resolved Probes of Methane Dissociation Dynamics," *Progr. Surf. Sci.*, vol. 84, pp. 69–134, 2009.

[6] P. M. Hundt, H. Ueta, M. E. van Reijzen, B. Jiang, H. Guo, and R. D. Beck, "Bond-Selective and Mode-Specific Dissociation of CH_3D and CH_2D_2 on Pt(111)," *J. Phys. Chem. A*, vol. 119, pp. 12442–12448, 2015.

[7] R. R. Smith, D. R. Killelea, D. F. DelSesto, and A. L. Utz, "Preference for Vibrational over Translational Energy in a Gas-Surface Reaction," *Science*, vol. 304, pp. 992–995, 2004.

[8] R. D. Beck, P. Maroni, D. C. Papageorgopoulos, T. T. Dang, M. P. Schmid, and T. R. Rizzo, "Vibrational Mode-Specific Reaction of Methane on a Nickel Surface," *Science*, vol. 302, pp. 98–100, 2003.

[9] P. M. Hundt, M. E. van Reijzen, H. Ueta, and R. D. Beck, "Vibrational Activation of Methane Chemisorption: The Role of Symmetry," *J. Phys. Chem. Lett.*, vol. 5, pp. 1963–1967, 2014.

[10] D. R. Killelea, V. L. Campbell, N. S. Shuman, and A. L. Utz, "Bond-Selective Control of a Heterogeneously Catalyzed Reaction," *Science*, vol. 319, pp. 790–793, 2008.

[11] L. Chen, H. Ueta, R. Bisson, and R. D. Beck, "Vibrationally Bond-Selected Chemisorption of Methane Isotopologues on Pt(111) Studied by Reflection Absorption Infrared Spectroscopy," *Faraday Discuss.*, vol. 157, pp. 285–295, 2012.

[12] B. L. Yoder, R. Bisson, and R. D. Beck, "Steric Effects in the Chemisorption of Vibrationally Excited Methane on Ni(100)," *Science*, vol. 329, pp. 553–556, 2010.

[13] B. L. Yoder, R. Bisson, P. M. Hundt, and R. D. Beck, "Alignment Dependent Chemisorption of Vibrationally Excited $CH_4(\nu_3)$ on Ni(100), Ni(110), and Ni(111)," *J. Chem. Phys.*, vol. 135, p. 224703, 2011.

[14] H. Chadwick, H. Guo, A. Gutiérrez-González, J. P. Menzel, B. Jackson, and R. D. Beck, "Methane Dissociation on the Steps and Terraces of Pt(211) Resolved by Quantum State and Impact Site," *J. Chem. Phys.*, vol. 148, p. 014701, 2018.

[15] S. B. Donald and I. Harrison, "Dynamically Biased RRKM Model of Activated Gas-Surface Reactivity: Vibrational Efficacy and Rotation as a Spectator in the Dissociative Chemisorption of CH_4 on Pt(111)," *Phys. Chem. Chem. Phys.*, vol. 14, pp. 1784–1795, 2012.

[16] A. Lozano, X. J. Shen, R. Moiraghi, W. Dong, and H. F. Busnengo, "Cutting a Chemical Bond With Demon's Scissors: Mode- and Bond-Selective Reactivity of Methane on Metal Surfaces," *Surf. Sci.*, vol. 640, pp. 25–35, 2015.

[17] B. Jiang, M. H. Yang, D. Q. Xie, and H. Guo, "Quantum Dynamics of Polyatomic Dissociative Chemisorption on Transition Metal Surfaces: Mode

Specificity and Bond Selectivity," *Chem. Soc. Rev.*, vol. 45, pp. 3621–3640, 2016.

[18] H. Guo and B. Jiang, "The Sudden Vector Projection Model for Reactivity: Mode Specificity and Bond Selectivity Made Simple," *Acc. Chem. Res.*, vol. 47, pp. 3679–3685, 2014.

[19] S. Nave, A. K. Tiwari, and B. Jackson, "Dissociative Chemisorption of Methane on Ni and Pt Surfaces: Mode-Specific Chemistry and the Effects of Lattice Motion," *J. Phys. Chem. A*, vol. 118, pp. 9615–9631, 2014.

[20] H. Guo and B. Jackson, "Mode- and Bond-Selective Chemistry on Metal Surfaces: The Dissociative Chemisorption of CHD_3 on Ni(111)," *J. Phys. Chem. C*, vol. 119, pp. 14769–14779, 2015.

[21] F. Nattino, H. Ueta, H. Chadwick, M. E. van Reijzen, R. D. Beck, B. Jackson, M. C. van Hemert, and G. J. Kroes, "Ab Initio Molecular Dynamics Calculations versus Quantum-State-Resolved Experiments on CHD_3+Pt(111): New Insights into a Prototypical Gas–Surface Reaction," *J. Phys. Chem. Lett.*, vol. 5, pp. 1294–1299, 2014.

[22] F. Nattino, D. Migliorini, G. J. Kroes, E. Dombrowski, E. A. High, D. R. Killelea, and A. L. Utz, "Chemically Accurate Simulation of a Polyatomic Molecule-Metal Surface Reaction," *J. Phys. Chem. Lett.*, vol. 7, pp. 2402–2406, 2016.

[23] R. Peverati and D. G. Truhlar, "Quest for a Universal Density Functional: The Accuracy of Density Functionals Across a Broad Spectrum of Databases in Chemistry and Physics," *Philos. Trans. Royal Soc. A*, vol. 372, p. 20120476, 2014.

[24] Golibrzuch, K. and Bartels, N. and Auerbach, D. J. and Wodtke, A. M., "The dynamics of molecular interactions and chemical reactions at metal surfaces: Testing the foundations of theory," *Annu. Rev. Phys. Chem.*, vol. 66, pp. 399–425, 2015.

[25] G. J. Kroes, "Towards Chemically Accurate Simulation of Molecule–Surface Reactions," *Phys. Chem. Chem. Phys.*, vol. 14, pp. 14966–14981, 2012.

[26] C. Díaz, E. Pijper, R. A. Olsen, H. F. Busnengo, D. J. Auerbach, and G. J. Kroes, "Chemically Accurate Simulation of a Prototypical Surface Reaction: H_2 Dissociation on Cu(111)," *Science*, vol. 326, pp. 832–834, 2009.

[27] J. P. Perdew, K. Burke, and M. Ernzerhof, "Generalized Gradient Approximation Made Simple," *Phys. Rev. Lett.*, vol. 77, pp. 3865–3868, 1996.

[28] J. P. Perdew, K. Burke, and M. Ernzerhof, "Erratum: Generalized Gradient Approximation Made Simple," *Phys. Rev. Lett.*, vol. 78, p. 1396, 1997.

[29] J. P. Perdew, J. A. Chevary, S. H. Vosko, K. A. Jackson, M. R. Pederson, D. J. Singh, and C. Fiolhais, "Atoms, Molecules, Solids, and Surfaces: Applications of the Generalized Gradient Approximation for Exchange and Correlation," *Phys. Rev. B*, vol. 46, pp. 6671–6687, 1992.

[30] B. Hammer, L. B. Hansen, and J. K. Nørskov, "Improved Adsorption Energetics Within Density-Functional Theory Using Rrevised Perdew-Burke-Ernzerhof Functionals," *Phys. Rev. B*, vol. 59, pp. 7413–7421, 1999.

[31] L. Sementa, M. Wijzenbroek, B. J. van Kolck, M. F. Somers, A. Al-Halabi, H. F. Busnengo, R. A. Olsen, G. J. Kroes, M. Rutkowski, C. Thewes, N. F. Kleimeier, and H. Zacharias, "Reactive Scattering of H_2 from Cu(100): Comparison of Dynamics Calculations Based on the Specific Reaction Parameter Approach to Density Functional Theory with Experiment," *J. Chem. Phys.*, vol. 138, p. 044708, 2013.

[32] P. M. Hundt, B. Jiang, M. E. van Reijzen, H. Guo, and R. D. Beck, "Vibrationally Promoted Dissociation of Water on Ni(111)," *Science*, vol. 344, pp. 504–507, 2014.

[33] F. Nattino, C. Díaz, B. Jackson, and G. J. Kroes, "Effect of Surface Motion on the Rotational Quadrupole Alignment Parameter of D_2 Reacting on Cu(111)," *Phys. Rev. Lett.*, vol. 108, p. 236104, 2012.

[34] P. Nieto, D. Farías, R. Miranda, M. Luppi, E. J. Baerends, M. F. Somers, M. J. T. C. van der Niet, R. A. Olsen, and G. J. Kroes, "Diffractive and Reactive Scattering of H_2 from Ru(0001): Experimental and Theoretical Study," *Phys. Chem. Chem. Phys.*, vol. 13, pp. 8583–8597, 2011.

[35] I. M. N. Groot, H. Ueta, M. J. T. C. van der Niet, A. W. Kleyn, and L. B. F. Juurlink, "Supersonic Molecular Beam Studies of Dissociative Adsorption of H_2 on Ru(0001)," *J. Chem. Phys.*, vol. 127, p. 244701, 2007.

[36] M. Wijzenbroek and G. J. Kroes, "The Effect of the Exchange-Correlation Functional on H_2 Dissociation on Ru(0001)," *J. Chem. Phys.*, vol. 140, p. 084702, 2014.

[37] F. Nattino, D. Migliorini, M. Bonfanti, and G. J. Kroes, "Methane Dissociation on Pt(111): Searching for a Specific Reaction Parameter Density Functional," *J. Chem. Phys.*, vol. 144, p. 044702, 2016.

[38] C. Díaz, R. A. Olsen, D. J. Auerbach, and G. J. Kroes, "Six-Dimensional Dynamics Study of Reactive and Non Reactive Scattering of H_2 from Cu(111) Using a Chemically Accurate Potential Energy Surface," *Phys. Chem. Chem. Phys.*, vol. 12, pp. 6499–6519, 2010.

[39] M. Dion, H. Rydberg, E. Schröder, D. C. Langreth, and B. I. Lundqvist, "Van der Waals Density Functional for General Geometries," *Phys. Rev. Lett.*, vol. 92, p. 246401, 2004.

[40] D. Migliorini, H. Chadwick, F. Nattino, A. Gutiérrez-González, E. Dombrowski, E. A. High, H. Guo, A. L. Utz, B. Jackson, R. D. Beck, and G. J. Kroes, "Surface Reaction Barriometry: Methane Dissociation on Flat and Stepped Transition-Metal Surfaces," *J. Phys. Chem. Lett.*, vol. 8, pp. 4177–4182, 2017.

[41] Y. Matsumoto, Y. A. Gruzdkov, K. Watanabe, and K. Sawabe, "Laser-Induced Photochemistry of Methane on Pt(111): Excitation Mechanism and Dissociation Dynamics," *J. Chem. Phys.*, vol. 105, pp. 4775–4788, 1996.

[42] C. Díaz and R. A. Olsen, "A Note on the Vibrational Efficacy in Molecule-Surface Reactions," *J. Chem. Phys.*, vol. 130, p. 094706, 2009.

[43] P. M. Holmblad, J. Wambach, and I. Chorkendorff, "Molecular Beam Study of Dissociative Sticking of Methane on Ni(100)," *J. Chem. Phys.*, vol. 102, pp. 8255–8263, 1995.

[44] C. T. Rettner, H. E. Pfnür, and D. J. Auerbach, "On the Role of Vibrational Energy in the Activated Dissociative Chemisorption of Methane on Tungsten and Rhodium," *J. Chem. Phys.*, vol. 84, pp. 4163–4167, 1986.

[45] J. H. Larsen, P. M. Holmblad, and I. Chorkendorff, "Dissociative Sticking of CH_4 on Ru(0001)," *J. Chem. Phys.*, vol. 110, pp. 2637–2642, 1999.

[46] A. C. Luntz, "CH_4 Dissociation on Ni(100): Comparison of a Direct Dynamical Model to Molecular Beam Experiments," *J. Chem. Phys.*, vol. 102, pp. 8264–8269, 1995.

[47] G. Kresse and J. Hafner, "Ab Initio Molecular Dynamics for Liquid Metals," *Phys. Rev. B*, vol. 47, pp. 558–561, 1993.

[48] G. Kresse and J. Hafner, "Ab Initio Molecular-Dynamics Simulation of the Liquid-Metal-Amorphous-Semiconductor Transition in Germanium," *Phys. Rev. B*, vol. 49, pp. 14251–14269, 1994.

[49] G. Kresse and J. Furthmüller, "Efficient Iterative Schemes for Ab Initio Total-Energy Calculations Using a Plane-Wave Basis Set," *Phys. Rev. B*, vol. 54, pp. 11169–11186, 1996.

[50] G. Kresse and J. Furthmüller, "Efficiency of Ab-Initio Total Energy Calculations for Metals and Semiconductors Using a Plane-Wave Basis Set," *Comput. Mater. Sci*, vol. 6, pp. 15–50, 1996.

[51] G. Kresse and D. Joubert, "From Ultrasoft Pseudopotentials to the Projector Augmented-Wave Method," *Phys. Rev. B*, vol. 59, pp. 1758–1775, 1999.

[52] P. E. Blöchl, "Projector Augmented Wave-Method," *Phys. Rev. B*, vol. 50, pp. 17953–17979, 1994.

[53] H. Chadwick, D. Migliorini, and G. J. Kroes, "CHD_3 Dissociation on Pt(111): A Comparison of the Reaction Dynamics Based on the PBE Functional and on a Specific Reaction Parameter Functional," *J. Chem. Phys.*, vol. 149, p. 044701, 2018.

[54] V. L. Campbell, N. Chen, H. Guo, B. Jackson, and A. L. Utz, "Substrate Vibrations as Promoters of Chemical Reactivity on Metal Surfaces," *J. Phys. Chem. A*, vol. 119, pp. 12434–12441, 2015.

[55] A. K. Tiwari, S. Nave, and B. Jackson, "The Temperature Dependence of Methane Dissociation on Ni(111) and Pt(111): Mixed Quantum-Classical Studies of the Lattice Response," *J. Chem. Phys.*, vol. 132, p. 134702, 2010.

[56] H. Guo, A. Farjamnia, and B. Jackson, "Effects of Lattice Motion on Dissociative Chemisorption: Toward a Rigorous Comparison of Theory with Molecular Beam Experiments," *J. Phys. Chem. Lett.*, vol. 7, pp. 4576–4584, 2016.

[57] R. Moiraghi, A. Lozano, and H. F. Busnengo, "Theoretical Study of the Dissociative Adsorption of Methane on Ir(111): The Role of Steps and Surface Distortions at High Temperatures," *J. Phys. Chem. C*, vol. 120, pp. 3946–3954, 2016.

[58] X. J. Shen, Z. J. Zhang, and D. H. Zhang, "CH_4 Dissociation on Ni(111): A Quantum Dynamics Study of Lattice Thermal Motion," *Phys. Chem. Chem. Phys.*, vol. 17, pp. 25499–25504, 2015.

[59] S. Nave, A. K. Tiwari, and B. Jackson, "Methane Dissociation and Adsorption on Ni(111), Pt(111), Ni(100), Pt(100), and Pt(110)-(1×2): Energetic Study," *J. Chem. Phys.*, vol. 132, p. 054705, 2010.

[60] S. Nave and B. Jackson, "Methane Dissociation on Ni(111) and Pt(111): Energetic and Dynamical Studies," *J. Chem. Phys.*, vol. 130, p. 054701, 2009.

[61] E. A. McCullough and R. E. Wyatt, "Quantum Dynamics of the Collinear (H, H_2) Reaction," *J. Chem. Phys.*, vol. 51, pp. 1253–1254, 1969.

[62] R. A. Marcus, "On Analytical Mechanics of Chemical Reactions. Quantum Mechanics of Linear Collisions," *J. Chem. Phys.*, vol. 45, pp. 4493–4499, 1966.

[63] R. D. Levine, *Molecular Reaction Dynamics.* Cambridge: Cambridge University Press, 2005.

[64] B. Baule, "Theoretische Behandlung der Erscheinungen in verdünnten Gasen," *Ann. Phys.*, vol. 349, pp. 145–176, 1914.

Chapter 7

HOD on Ni(111): *Ab Initio* Molecular Dynamics Prediction of Molecular Beam Experiments

This Chapter is based on:

D. Migliorini, F. Nattino, A. K. Tiwari and G. J. Kroes, *J. Chem. Phys.*, 149, 244706 (2018)

which is reproduced with the permission of AIP publishing.

Abstract

The dissociation of water on a transition-metal catalyst is a fundamental step in relevant industrial processes such as the water-gas shift reaction and steam reforming. Although many theoretical studies have been performed, quantitative agreement between theoretical simulations and molecular beam experiments has not yet been achieved. In this Chapter we present a predictive *ab initio* molecular dynamics study on the dissociation of mono-deuterated water (HOD) on Ni(111). The analysis of the trajectories gives useful insight into the full-dimensional dynamics of the process and suggests that rotational steering plays a key role in the

dissociation. The computed reaction probability suggests that, in combination with accurate molecular beam experiments, the specific reaction parameter density functional developed for CHD_3 on Ni(111) (SRP32-vdW) represents a good starting point for developing a semi-empirical functional able to achieve chemical accuracy for HOD on Ni(111).

7.1 Introduction

The interaction between molecules and metal surfaces has been extensively studied due to its great relevance to both fundamental research and practical applications. Among the many heterogeneously catalyzed processes steam reforming is particularly important because it is commonly used to produce molecular hydrogen. One of the most relevant steps of this process is the so-called water-gas shift (WGS) [1, 2] reaction where H_2O deprotonates on a transition-metal based catalyst in presence of CO to give ultimately molecular hydrogen and carbon dioxide.

Due to the high complexity of the real catalytic conditions, the dissociative chemisorption of H_2O that gives OH and H chemisorbed on the surface has been subject of many theoretical studies that have been carried out using low-index transition metals surfaces as a model for the catalyst (with particular focus on Ni and Cu) and employing density functional theory (DFT) at the generalized-gradient approximation (GGA) level to obtain the electronic structure [3–26].

It has been shown that the dissociative chemisorption of water (as well as the overall WGS reaction) does not only depend on the energy of the transition state (TS) but also on molecular adsorption states [5, 27–29]. Moreover a good understanding of the process has been achieved performing classical and quantum dynamical simulations gradually including more and more degrees of freedom (DOFs) and details in the potential energy surface (PES) [3, 4, 7–11, 15, 17–24, 26, 30].

The dissociation of water on metal surfaces is a late barrier process [3, 4, 15] which is greatly promoted by vibrational energy in the molecule [3, 4, 20,

21], and it exhibits large mode [9, 10] and bond [19] specificity in agreement with Polanyi's rule [31]. This is also in agreement with results of the sudden vector projection (SVP) model [5, 6] which predicts large couplings between the vibrational modes of the reactant and the reaction coordinate at the transition state [5]. The dynamical simulations uncovered the key role that the topology of the PES plays in the dissociative chemisorption: on Ni(111) the top site has the lowest barrier but the tight entrance channel drives the reaction to different sites which, despite the higher barrier, have a broader entrance channel and thereby a more accessible transition state [22]. Moreover, dynamical simulations have shown that including only high-symmetry sites is not enough to achieve a proper description of the total reactivity [23], which also strongly depends on the azimuthal angle (ϕ) [7, 24, 25]. Therefore full [8, 15] (or high) [23, 24] dimensional calculations are crucial to properly simulate and understand this reaction.

The dissociation of water on transition metal surfaces is similar in many aspects to the well-studied dissociative chemisorption of methane. For both molecules, at high incidence energies we observe direct dissociation with a late barrier, the height of which also depends on the displacement(s) of the surface atom(s) above which the reaction happens [3, 5, 26, 32, 33]. State-selected molecular beam experiments have been performed on both methane [34, 35] and water [3]. Using *ab initio* molecular dynamics (AIMD) paired with a semi-empirical density functional, it has been possible to reproduce the experiments with chemical accuracy (i.e., ≈ 4.2 kJ/mol) for methane (specifically the CHD_3 isotopologue) on Ni(111) [35], Pt(111) [34] and Pt(211) [34]. The quantum dynamical and classical calculations for water, on the other hand, only achieved qualitative or, at best, semi-quantitative agreement [3] with experiments. This can be attributed to two main reasons: the reduced dimensionality of the dynamics calculations or otherwise the approximations in the PES and uncertainty in the barrier height due to the standard GGA density functional used.

A previous attempt to develop an accurate semi-empirical specific reaction parameter (SRP) functional for water (D_2O) on Ni(111) was not succesful [11]. The authors argued that the discrepancy between theory and experiments might

be due to the GGA exchange-correlation functional used (which included either PW91 [36] or RPBE [37] exchange, but the correlation functional did not model the attractive van der Waals interaction) and to the approximate treatment of surface effects through the lattice relaxed sudden (LRS) model [38].

We hope to improve on the first attempt of deriving an SRP functional for water interacting with Ni(111) in two ways. Firstly, it has been shown that the description of the molecule-surface interaction for methane + Pt(111) can be improved [34, 35, 39] by using a correlation functional that models the van der Waals contribution (i.e., the vdW-DF correlation developed by Dion *et al.* [40] which has been employed in this study).

Secondly, using AIMD avoids uncertainties that come with the use of the more approximate LRS model, in that it allows one to explicitly treat all the DOFs of the system, including surface phonons, and hence to correctly represent the dynamics without the necessity of computing a high dimensional PES. Moreover it has been shown in previous work [12] that non-adiabatic effects (such as electron-hole pair excitation) are small for water on Ni(111) and they do not qualitatively affect the dynamics. AIMD can then be used to obtain an SRP functional by fitting the functional to reproduce molecular beam sticking results (for more details see Chapter 2 and Refs. [35] and [34]). It has been shown that the SRP approach to dissociative chemisorption on transition metal surfaces can overcome the inaccuracy of standard GGA functionals and provide a semi-empirical functional that is able to return chemically accurate barrier heights that are expected to be correct to within 1 kcal/mol [34, 35, 41–44]. The systems for which this has been shown include H_2 on Cu(111) [41], H_2 on Cu(100) [42], D_2 on Pt(111) [43], CHD_3 on Ni(111) [35] and CHD_3 on Pt(111) [34] and Pt(211) [34].

In order to successfully develop an SRP functional, the sticking data considered should be in the range of applicability of the dynamical model. For AIMD, this means that the total energy in the molecules has to be above the minimum energy barrier so that quantum effects can be neglected, that the molecular beams have to be well-characterized so that an accurate sampling of the initial conditions can be done in the simulations, and that the sticking probability (S_0)

has to be larger than 1% in order to obtain a good statistical sampling with a reasonable number of trajectories (see Chapter 2). Unfortunately, to the best of our knowledge, such experimental results are not available yet for water. Note that once the SRP functional has been developed it can be used with DFT calculations and coupled with a neural network approach [45–47] to develop a high dimensional chemically accurate PES, which can be used to investigate low collision energies for which AIMD is not suitable while also modelling the surface phonons.

Here we present a predictive AIMD study of HOD impinging on Ni(111) in order to get insight on the full dimensional dynamical process including surface motion explicitly. We hope that our results will encourage new experiments for conditions at which AIMD is applicable so as to enable a comparison with the present predictive results and improvements of the functional used here.

This Chapter is organized as follows: the method used to setup, perform and analyze the AIMD simulations is described in Section 7.2 and the results are discussed in Section 7.3. The main conclusions are then summarized in Section 7.4.

7.2 Method

7.2.1 Electronic Structure Method

The calculations presented in this Chapter have been performed using version 5.3.5 of the Vienna *ab initio* simulation package (VASP) [48–51] and the computational setup has been transferred from recent work on the dissociation of CHD_3 on Ni(111) [35] and successively tested for HOD on Ni(111). The convergence tests reported in the Supplementary Material (SM) of Ref. [52] show that the setup is accurate enough for the purpose of this work. A 4x4x1 Γ-centered K-point grid has been used to sample the first Brillouin zone and plane waves with a kinetic energy up to 350 eV have been included. The core electrons have been described employing projector augmented-wave (PAW) [53, 54] pseudopotentials

and the SCF convergence has been facilitated by a 0.1 eV Fermi smearing. Due to the ferromagnetic nature of nickel all the calculations performed are spin-polarized. The Ni(111) surface has been simulated using a 3x3 unit cell slab with 4 layers which is separated from its first periodic replica by 13 Å of vacuum. The optimized 0 K lattice constant $a = 3.556$ Å agrees within 1.2% with the low-temperature experimental value $a = 3.513$ Å [55]. The calculations have been performed using the SRP32-vdW functional developed for CHD_3 + Ni(111) [35] with the exchange correlation functional (E_{XC}) defined as:

$$E_{XC}^{SRP} = 0.32 \cdot E_X^{RPBE} + (1 - 0.32) \cdot E_X^{PBE} + E_C^{\text{vdW-DF}}. \tag{7.1}$$

Here E_X^{RPBE} and E_X^{PBE} are the exchange parts of the widely-used RPBE [37] and PBE [56, 57] functionals and $E_C^{\text{vdW-DF}}$ is the long-range correlation functional developed by Dion *et al.* [40, 58], which also models the attractive van der Waals interaction. More details on how the SRP32-vdW functional has been obtained for methane on Ni(111) can be found in Ref. [35] and in its supporting information.

The transition states have been located using the dimer method provided in the VASP transition state tool (VTST) package [59–62] and frequency analysis has confirmed that they are real 1st order saddle-points (i.e., one and only one imaginary frequency was found).

Note that with the used setup, when the molecule is placed 6.5 Å away from the slab and from its first periodic replica (i.e., so-called gas-phase geometry) there is still a 1.2 kJ/mol difference between the energy of the system with the molecule lying in a plane parallel to the surface or perpendicular to the surface. This could be due to the presence of a dipole in the cell, which is not corrected for in the calculation, or to a non-converged vacuum space (discussed more extensively later in this Section). However this small energy error does not affect much the predictive value of our results and, in this Chapter, all the relative energies will be reported with respect to the “planar gas-phase configuration” in which the molecule is parallel to the surface.

7.2.2 Dynamics Calculations

The AIMD calculations have been performed keeping the number of particles, the volume of the cell and the total energy constant (NVE simulations) and exploiting the quasi-classical trajectory (QCT) approach, which consists in imparting zero-point energy to the vibrational modes of the molecule.

A known problem of QCT is artificial intramolecular vibrational energy redistribution (artificial IVR) which consists of a quantum mechanically forbidden energy transfer among coupled vibrational modes. This problem has been circumvented for methane by focusing on the CHD_3 isotopologue [34, 35, 39]. The ν_1 vibrational mode, localized on the CH stretch, is weakly coupled to the CD modes due to the large frequency difference. Therefore if vibrational energy is imparted to the ν_1 mode of CHD_3, the artificial IVR is slow enough to ensure the applicability of AIMD [63, 64]. For the same reason, in this Chapter the isotopologue of choice is HOD rather than H_2O.

HOD has 3 vibrational modes: a stretching mode mostly localized on the OH bond (ν_{OH}), a second stretching mode mostly localized on the OD bond (ν_{OD}) and a bending mode (ν_{bend}). Due to the localized nature of ν_{OH} and its frequency difference from the other modes (see Table 7.1 and Figure S1 in the SM of Ref. [52]) we expect the artificial IVR to be negligible on the simulation timescale.

The AIMD simulations have been performed for plausible experimental conditions where molecular beams are characterized by the nozzle temperature (T_n), the stream velocity (v_s) and the width parameter (α) which determine the rovibrational state distributions of the molecules and the average collision energy ($\langle E_i \rangle$). Since to the best of our knowledge there is no suitable experimental data for HOD molecular beams available, we have used parameters measured for H_2 seeded CHD_3 beams (See Table 7.2). Specifically, the beam parameters for $T_n = 450$ K have been measured by Beck and coworkers [34] and for all the other sets by Utz and coworkers [35]. Our choice is justified by the fact that, the two molecules having the same mass, the velocity and the broadening of the beams

Isotopologue	Mode	SRP32-vdW / [cm^{-1}]	Exp. / [cm^{-1}]
H_2O	ν_{asym}	3752.0	3755.8
	ν_{sym}	3639.5	3657.1
	ν_{bend}	1603.8	1594.8
D_2O	ν_{asym}	2747.6	2787.7
	ν_{sym}	2620.7	2668.1
	ν_{bend}	1173.8	1178.4
HOD	ν_{OH}	3697.9	3707.5
	ν_{OD}	2682.2	2782.0
	ν_{bend}	1405.9	1402.2

Table 7.1: Vibrational modes for the different water isotopologues. ν_{asym} and ν_{sym} are the antisymmetric and the symmetric stretch, respectively, and ν_{bend} is the bend mode. For HOD ν_{OH} and ν_{OD} are the vibrational modes localized on the OH and on the OD stretch, respectively. The harmonic frequencies computed with the setup used in the calculations (SRP32-vdW) are reported together with the experimental values of the fundamental frequencies. The experimental data are taken from Ref. [65].

are expected to be similar making the CHD_3 beam parameters a sound guess to predict HOD experimental conditions. Note that the small differences in $\langle E_i \rangle$ between CHD_3 and HOD reported in Table 7.2 are due to the rounding of the mass used (i.e., 19.061 amu for CHD_3 [34, 35] and 19 amu for HOD).

The AIMD simulations have been carried out for two different types of initial conditions: laser-off and $\nu_{OH} = 1$. For laser-off molecules the vibrational state distribution is determined only by T_n and so, in each set of trajectories, it is chosen to sample a Boltzmann distribution at said temperature. Since complete rotational cooling is assumed, all the molecules are simulated in the rotational ground state, which translates into a random initial orientation.

Instead of using the beam parameters taken from the suggested CHD_3 experiments, for a predictive work one could in principle simulate the reactivity for specific energies and initial vibrational states and at a later stage, when the experiments are available, average the results according to the experimental beam parameters. However this would at present not be applicable to the laser-off conditions we want to simulate, for which a distribution of vibrational states is

T_n	v_s	α	$\langle E_i \rangle^w$	$\langle E_i \rangle^m$
[K]	[m/s]	[m/s]	[kJ/mol]	[kJ/mol]
450	3026	246	89.0	89.3†
600	3418	168	111.9	112.3*
650	3548	192	120.8	121.2*
700	3683	205	130.3	130.7*
750	3761	217	135.9	136.4*
900	4070	275	159.9	160.4*

Table 7.2: Molecular beam parameters used to sample the molecular initial conditions in the AIMD simulations. The Table reports the nozzle temperature (T_n), the stream velocity (v_s), the velocity width (α) and the average kinetic energy for the water (HOD) beams ($\langle E_i \rangle^w$). The Table also reports the average kinetic energy originally measured for methane (CHD_3) beams ($\langle E_i \rangle^m$) in the works from which the beam parameters have been taken. Energies marked with a dagger (†) have been taken from Ref. [34] and energies marked with a star (*) have been taken from Ref. [35].

observed in the beams due to the nozzle temperature. Furthermore, it would require calculations on a fine incidence energy grid for the initial-state resolved reactivity for both laser-off conditions and for $\nu_{OH} = 1$ HOD. The way we prepare the calculations (by performing Monte-Carlo averaging over the initial velocity and initial state population at once for each suggested experiment) is currently the only computationally feasible way of performing predictions with AIMD for molecular beam experiments on reaction of polyatomic molecules.

In order to simulate the effect of laser excitation on S_0, the molecules have been prepared in $\nu_{OH} = 1$, hence putting one quantum of energy in the OH stretching mode. HOD can be approximated as an asymmetric rotor for which the three moments of inertia are different. The principal axis of the molecule (c), associated with the largest moment of inertia, lies normal to the molecular plane while the other two rotational axes (a and b) lie in the plane. A general rotational state (J, M, K_a, K_c) is characterized by the quantization of the magnitude of the angular momentum ($|\mathbf{L}|$), by its projections (J_z) on the reference frame axis z, chosen normal to the surface, and by its projections on the molecular axis a

and c (J_a and J_c , respectively), as:

$$|\mathbf{L}| = \hbar\sqrt{J \cdot (J+1)}, \tag{7.2}$$

$$J_z = \hbar M, \tag{7.3}$$

$$J_a = \hbar K_a, \tag{7.4}$$

$$J_c = \hbar K_c. \tag{7.5}$$

Therefore, in order to prepare the initial molecular orientation for a generic (J, M, K_a, K_c) state, once the projections reported in Equations 7.2–7.5 have been fixed, only two angles are undetermined and need to be randomly sampled: the orientation of the axis a relative to $\mathbf{L}$ and the projection of $\mathbf{L}$ on the xy plane. This affects the initial orientation of the rotationally excited molecules (more details are reported in the SM of Ref. [52]).

Experimentally it is possible to excite the HOD molecule to the $\nu_{OH} = 1$ state by going from ($v = 0$, $J = 1$, $K_a = 0$, $K_c = 1$) to ($v = 1$, $J = 2$, $K_a = 0$, $K_c = 2$) [66] through an R-branch transition. This transition was chosen due to its high dipole moment and the likely population of the initial state in the molecular beam expansion. In principle this transition would only populate all accessible M states (i.e., $M = -1$, 0, 1) and $K_c = \pm 2$. However, as seen for methane [67], the alignment of M should be lost due to hyperfine coupling since the laser excitation normally takes place relatively far from the surface. Moreover, for $K_a = 0$, the molecular orientation is independent of the sign of K_c (see Figure 7.1). Therefore in our simulations, each set of $\nu_{OH} = 1$ molecules contains 500 trajectories in the ($J = 2$, $K_a = 0$, $K_c = 2$) rotational state where the 5 experimentally populated M states (i.e., $M = -2$, -1, 0, 1, 2) have been sampled with 100 trajectories each.

The trajectories have been propagated with a 0.4 fs time step until the molecule was either dissociated or scattered. A molecule is considered reacted if one of the bonds stays longer than 2.0 Å for 100 fs or if it gets longer than 3.0 Å, and it is considered scattered if it is 6.0 Å away from the surface with the COM

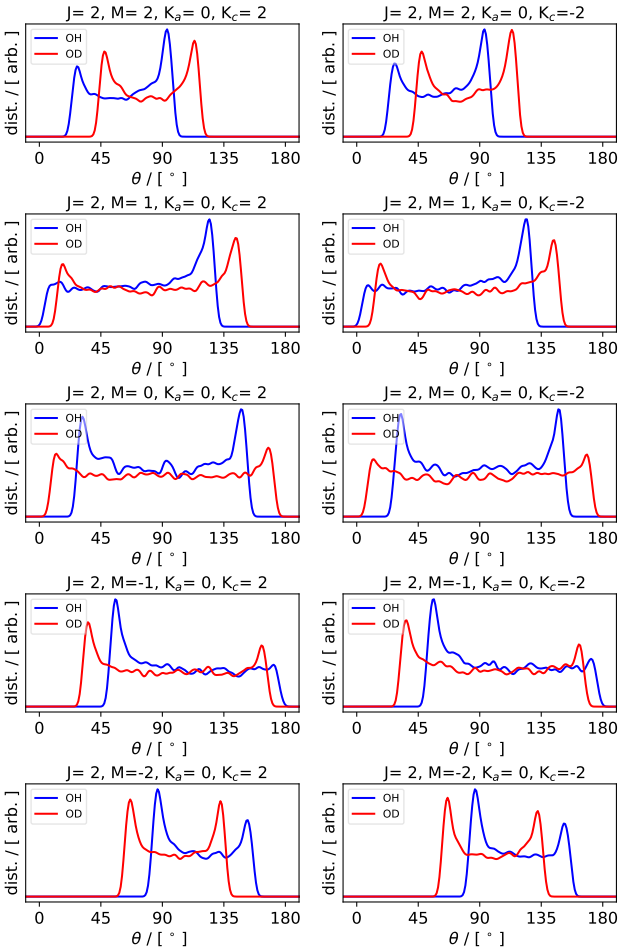

Figure 7.1: Distribution of the initial angle θ between the bond and the z axis for the OH (blue) and the OD (red) bond computed over 5000 initial orientations for each rotational state. Plots on the same line refer to rotational states that only differ in the sign of K_c.

velocity pointing away from the slab. The trajectories that did not reach one of these outcomes within the first ps of propagation have been considered trapped.

For each $\langle E_i \rangle$, the zero-coverage reaction probability has been computed as:

$$S_0 = N_{react}/N_{tot}, \tag{7.6}$$

where N_{tot} and N_{react} are the number of simulated and of reacted trajectories, respectively. Reaction probabilities are reported with the statistical error:

$$\sigma_p = \sqrt{\frac{S_0(1 - S_0)}{N_{tot}}}, \tag{7.7}$$

with error bars representing a 68% confidence interval.

The 13 Å of vacuum between the slab replicas is not enough to converge the long range interaction due to the vdW correlation employed. However, this affects the potential only as a small energy shift (residual energy, E_R) if compared to a setup with 30 Å of vacuum. E_R can be compensated, as successfully done in previous work for CHD_3 [34, 35] and discussed in Chapter 2, by adding an extra normal translational energy to the molecule at the beginning of the trajectory . An additional energy "kick" of 2.4 kJ/mol has been added to the molecules for all sets excluding the laser-off calculations for the three largest $\langle E_i \rangle$. For those sets the energy kick was slightly smaller (i.e., as small as 1.6 kJ/mol). However, since there are no experimental data to directly compare with and since this difference is so small, this collision energy offset does not affect much the qualitative results and predictive purpose of this work.

The Ni(111) slab was prepared and used in previous work [35] at a surface temperature $T_s = 550$ K. The procedure used to optimize, equilibrate and sample the initial positions and velocities of the surface atoms is therefore the same as in Ref. [35].

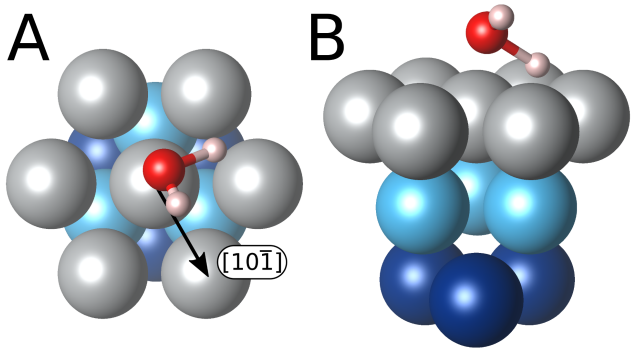

Figure 7.2: Panels A and B depict the top and the side view of the fcc transition state, respectively. The surface atoms are depicted in gray, light and dark blue for the 1st, the 2nd and the 3rd layers respectively. The arrow in Panel A indicates the [10$\bar{1}$] direction.

7.3 Results and Discussion

Two TSs have been located on the surface, both have a very similar geometry but the dissociating H is pointed towards either the fcc or the hcp site, respectively (see Figure 7.2). The energy barrier (E_b) is 67.0 kJ/mol for the hcp dissociation and 66.5 kJ/mol for the fcc dissociation. The barriers obtained are similar to that found in previous work using the PW91 functional (i.e., 64.6 kJ/mol) [3]. Note that, even though the barrier heights obtained with PW91 and with SRP32-vdW are similar, the two functionals are different, especially in the correlation part. Therefore the topology of the potential might be very different possibly resulting in a different dynamics and reactivity, similarly to what was observed for CHD_3 on Pt(111) [68].

Four angles have been used to characterize the molecular geometry: θ_d, θ_s, ϕ and γ (sketched in Figure 7.3). The angles θ_s and θ_d are measured between the z axis and the spectator bond and the dissociative bond, respectively. The angle γ is measured between the two bonds and the azimuthal angle ϕ describes the projection of the dissociative bond on the surface plane. ϕ is zero if the bond is pointing in the [10$\bar{1}$] direction (shown in Figure 7.2) and increases counterclockwise. The geometry is almost identical for the two TSs identified, which have the dissociating bond elongated (r = 1.54 Å) and pointing towards the surface

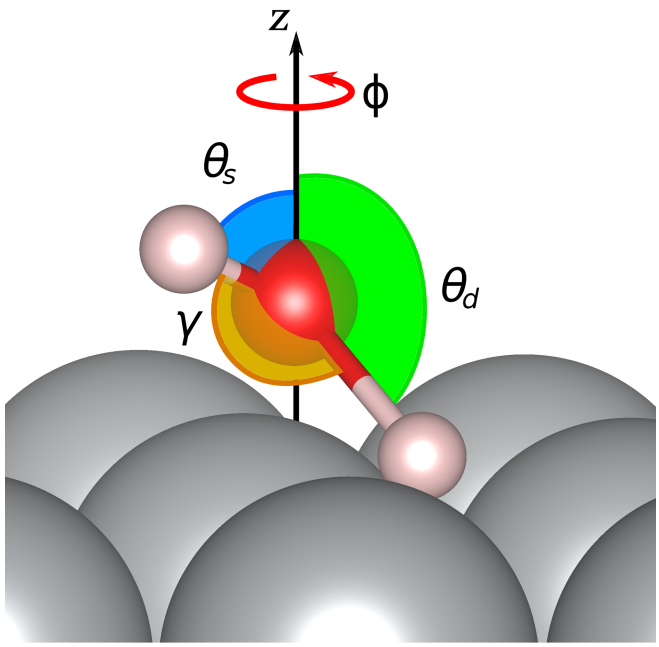

Figure 7.3: Sketch of the angles studied. The angle between the bond and the surface normal z is reported in green for the dissociative bond (θ_d) and in blue for the spectator bond (θ_s). The molecular bond angle (γ), reported in orange, is measured between the two bonds and the azimuthal angle (ϕ) refers to the xy projection of the dissociative bond on the surface. This angle has been taken with respect to the $[10\bar{1}]$ direction indicated in Figure 7.2.

with $\theta_d = 123°$ while the spectator bond points away from it with $\theta_s = 62°$. The angle γ between the two bonds is 103°, very close to the SRP32-vdW gas-phase value of 104.6°.

S_0 has been computed for $\langle E_i \rangle$ ranging between 89 and 160 kJ/mol (see Table 7.2) and the results are reported in Figure 7.4A. The reaction is strongly promoted by vibrational energy which, according to previous work [3, 4], helps to overcome the late barrier for the dissociative chemisorption. Previous work shows that, due to the large vibrational efficacy, under specific conditions there may be a large contribution of the thermally excited states to the laser-off reactivity [4]. However this is not true at the large $\langle E_i \rangle$ that we investigate here and the zero-coverage reaction probability for the laser-off beams (S_0^{LO}) falls within error bars from the ground state results ($S_0^{v=0}$) as shown in Figure S2 in the SM of Ref. [52].

Trapping has been observed especially at the lower $\langle E_i \rangle$ investigated where some molecules did not reach a definite outcome in the first ps of propagation. The dissociative chemisorption of HOD is a direct process and only 1 out of the 825 reactive trajectories simulated does not involve a molecule reacting on the first impact with the surface. However this does not exclude the possibility that the trapped molecules at lower $\langle E_i \rangle$ may react at longer propagation times. For this reason, in Figure 7.4 we also indicate the sum of the trapping and the reaction probability for $\langle E_i \rangle$ at which trapping was observed as an upper bound to the reactivity.

The fraction of OH cleavage (Figure 7.4B) shows that almost all the $\nu_{OH} = 1$ molecules react through the dissociation of the vibrationally excited OH bond confirming the bond-specificity of the reaction [4]. It has been shown in previous work [4] that in the laser-off experiments molecules show a preference for the OH dissociation over the OD dissociation and the branching ratio approaches the statistical value of 0.5 for larger $\langle E_i \rangle$. At the large $\langle E_i \rangle$ investigated, we observe that the branching ratio for the laser-off molecules is always close to 0.5.

The computed S_0 are reported in Figure 7.5 together with the molecular beam results for D_2O on Ni(111) measured by Beck and coworkers [3], which have been obtained for laser-off conditions and for molecules excited with one or two quanta in the antisymmetric stretch ($\nu_{asym} = 1, 2$, respectively). Even if the experiments have been performed for a different isotopologue and for low $\langle E_i \rangle$, which give too small S_0 to be simulated with AIMD, comparing the results can give us an indication on how accurate the SRP32-vdW functional must be for this system. Extrapolating by eye Beck and coworkers' experimental reaction probabilities to higher $\langle E_i \rangle$ suggests that our AIMD results might overestimate the experimental datasets. This is expected since the HOD ground state should be more reactive than that of D_2O due to the zero-point energy (ZPE) difference [4] and the HOD vibrational state $\nu_{OH} = 1$ should be more coupled with the reaction coordinate hence more efficient in promoting the reaction than the D_2O antisymmetric stretch $\nu_{asym} = 1$ state [5]. Even taking into account the different isotopologue, Figure 7.5 suggests that the SRP32-vdW density functional might

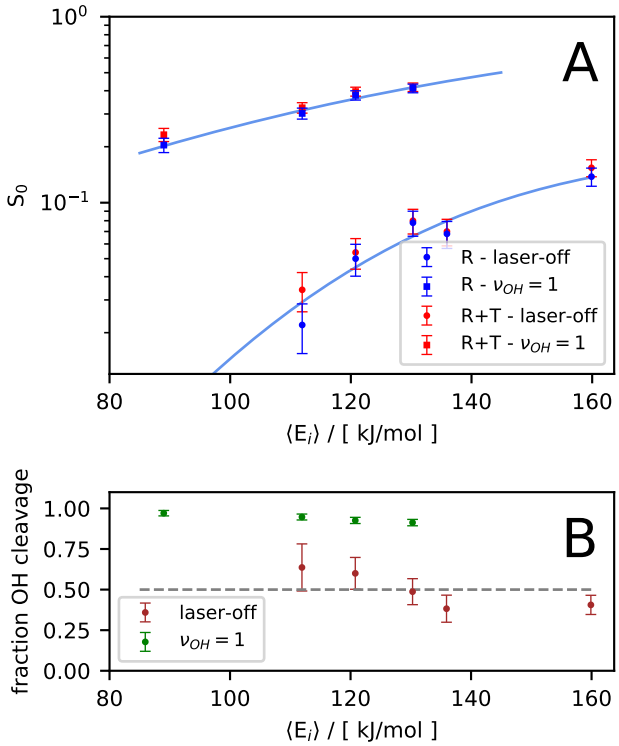

Figure 7.4: (A) computed S_0 for laser-off and $\nu_{OH} = 1$ simulations (blue circles and squares, respectively). The results reported in red represent the sum of the reaction probability and the trapping probability. The ERF fits of the results are reported as light blue lines. (B) fraction of OH cleavage for laser-off (brown) and $\nu_{OH} = 1$ (green) simulations.

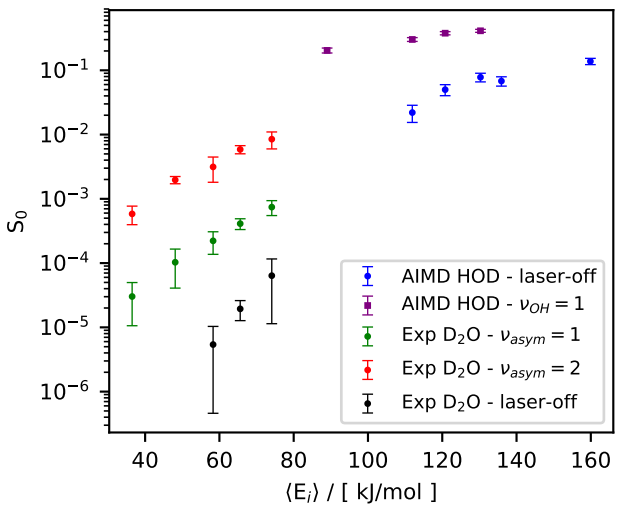

Figure 7.5: AIMD sticking probabilities computed for HOD on Ni(111) (blue and purple) compared with results of molecular beam experiments performed for D_2O on Ni(111) by Beck and coworkers (green, red and black). Experimental data are taken from Ref. [3].

still be somewhat too attractive to accurately reproduce the dissociation barrier for this system, but experimental results for HOD and for higher $\langle E_i \rangle$ are needed to confirm this.

Having said that, the results suggest that the SRP32-vdW density functional might be a good starting point to develop an SRP functional able to describe the dissociation of water on nickel with chemical accuracy. On the basis of extrapolation by eye we suspect that at the high $\langle E_i \rangle$ of our predictions, the SRP32-vdW functional would overestimate reaction. With the RPBE mixing coefficient now set at 0.32 there is plenty of scope for solving this problem by mixing in more repulsive RPBE exchange (and therefore less PBE exchange) in the exchange functional. However, molecular beam experiments performed under conditions where AIMD is applicable are needed to properly test the accuracy of the functional used.

Figure 7.6A shows a top view of the unit cell reporting the initial ($t = 0$) and final ($t = t_{diss}$) center of mass (COM) position for the reacted molecules and Figure 7.6B shows the distributions of the distances between the COM and

the closest top site at $t = 0$ and $t = t_{diss}$ for the reacted molecules. Here the dissociation time (t_{diss}) is defined as the time step when the dissociating bond is as long as in the TS geometry. The molecule has been observed to react far from the top site as also found in other calculations [23] even though the minimum barrier site is close to the top site. An interesting difference with earlier work by Guo and coworkers [23], who performed QCT calculations for D_2O on a rigid-surface 9D PES, is that they observe that most of the molecules react at a distance from the top site somewhere around 0.8-0.9 Å while, in our simulations, we observe the distribution peaking around 1.2 Å. This difference could be due to a different corrugation of the PES due to the different density functionals used or to the lattice motion which is taken explicitly into account in our simulations (see Figure 7.6 and Figure 5 in Ref. [23]).

Figure 7.6 seems to suggest there is no evidence of translational steering (i.e., a change in the xy projection of the COM position of the molecule during its flight to the surface and due to the forces exerted by the surface) because the initial distribution and the distribution at the time of reaction are very similar for the reactive molecules. However looking at the average lateral drift of the COM ($\langle \delta_{COM} \rangle$, see Figure 7.7) we observe that a small translational steering is indeed present in agreement with earlier work [23]. δ_{COM} has been computed as the distance between the xy position of the COM at the beginning and at the time of the impact with the surface, which is defined as the dissociation time for reactive trajectories and as the time at which the first sign change occurs in the z component of the COM velocity for the scattered molecules. Figure 7.7 shows that the translational steering is more significant for reactive trajectories in laser-off beams than for scattered molecules and for $\nu_{OH} = 1$ reactive trajectories. In agreement with what was observed in previous work [23] the amount of translational steering decreases for larger $\langle E_i \rangle$ (Figure 7.7). This trend has not been observed for laser-off reaction for which the number of events is small and the statistics is poor.

The motion in the four angles θ_d, θ_s, ϕ and γ (sketched in Figure 7.3) has been studied throughout the dynamics for both laser-off and $\nu_{OH} = 1$ conditions. Only

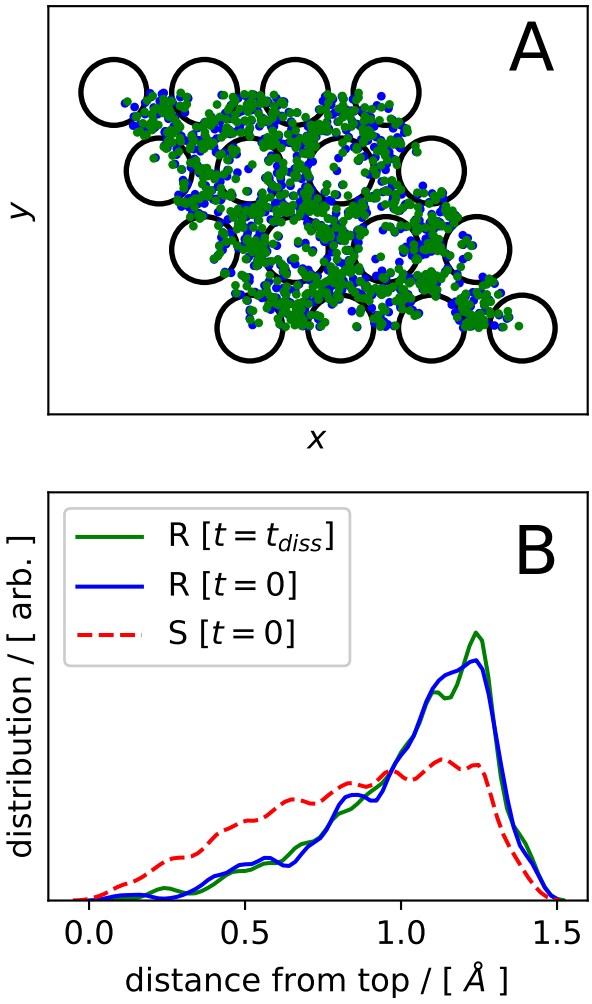

Figure 7.6: in Panel A depicts the slab 1st layer with the Ni atoms, reported as black circles, in their ideal positions and the initial ($t = 0$, blue) and final ($t = t_{diss}$, green) xy projection of the reacted molecules COM. Panel B reports the distributions of the distance of the COM from the closest top site for reacted molecules (R) at $t = 0$ (blue) and $t = t_{diss}$, (green) and for scattered molecules (S) at $t = 0$ (red).

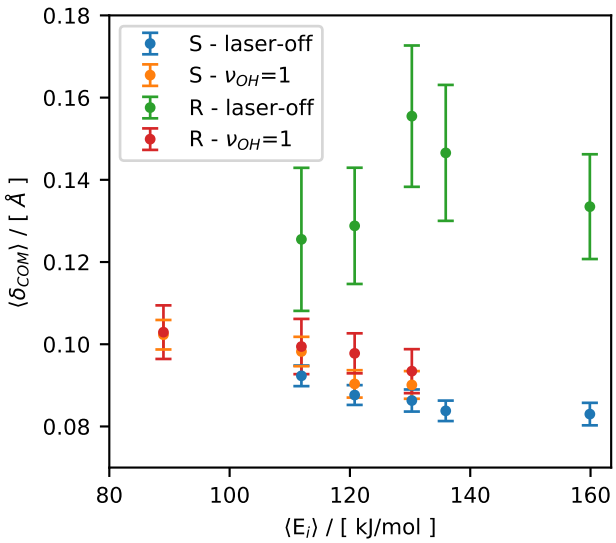

Figure 7.7: Average distance in xy between the COM at the beginning and the end of the trajectories ($\langle\delta_{COM}\rangle$) as a function of $\langle E_i\rangle$. The results are reported in different colors for scattered (S) and reacted (R) molecules for both laser-off and $\nu_{OH} = 1$ initial conditions.

laser-off results are reported and discussed here (Figure 7.8) because $\nu_{OH} = 1$ trajectories show the same trends (see Figure S3 in the SM of Ref. [52]). At the beginning of the simulations, the molecules sample all the accessible value of θ. The reactive molecules are also randomly oriented initially (blue curves, Panels A and B). During the reactive trajectories the molecules undergo large rotational steering, where the forces exerted by the surface reorient the molecule so that the observed values of θ_d and θ_s cluster around the value of the TS at the time of the dissociation ($t = t_{diss}$, green). Note that the rotational steering in the dissociative bond was already predicted earlier [30] for a different isotopologue of water (D_2O) reacting with Ni(111). This is significantly different from what is observed for CHD_3 which, in order to react, needs to be pre-oriented with the dissociating bond pointing towards the surface while not much rotational steering is observed [34, 35, 69]. The initial distribution of γ, reported in Figure 7.8C, reflects the classical constant-energy sampling of the bending mode of the

molecule, with the turning points of the oscillator being more populated than the equilibrium position. At the dissociation time $t = t_{diss}$ the distribution of γ peaks near the TS value.

To investigate the movement in ϕ throughout the dynamics, the difference between the initial and the final value of the angle ($\Delta\phi$) is reported in Figure 7.9. Note that ϕ is associated with the projection of the dissociative bond on the xy plane so a large jump in the value of ϕ can be associated with a small movement of the bond if the H is pointing upwards or downwards along z and this complicates the interpretation of the results. Therefore to have a qualitative insight into the ϕ motion, only the molecules for which θ_d remains between 30° and 160° throughout the whole trajectory have been considered. The results reported in Figure 7.9 show that the majority of the molecules have little or no change in ϕ. However the large extent of the distributions shows that, for some molecules, $\Delta\phi$ can be very large.

In Figure 7.10 the correlation between θ_s and θ_d has been studied to investigate whether there is a set of initial configurations and orientations that promotes the dissociative chemisorption. Panels A and C report the values at $t = 0$ for the scattered and the reactive trajectories and Panel E reports the same for the reactive trajectories at $t = t_{diss}$. Panels B, D and F report heat-maps for the same quantities where the results have been binned into $5° \times 5°$ cells and darker shades of red represent higher concentrations of results. Figure 7.10 clearly shows that there is no correlation between θ_s and θ_d at $t = 0$ as the results for both the scattered (Panels A and B) and the reactive (Panels C and D) trajectories at $t = 0$ sample all the accessible values. This underlines once more the importance of the rotational steering, as all the reactive molecules show clustered values of (θ_s, θ_d) at $t = t_{diss}$ (Panels E and F).

As described in the previous sections, in order to simulate the HOD molecules in the $\nu_{OH} = 1$ state we prepared them in the ($J = 2$, $K_a = 0$, $K_c = 2$) rotational state and we sampled all the accessible M states (i.e., $M = -2, -1, 0, 1, 2$). The initial rotational state translates into a preferential orientation of the molecules. The initial distributions of θ for the H atom (θ_H) are reported in Figure 7.11 for

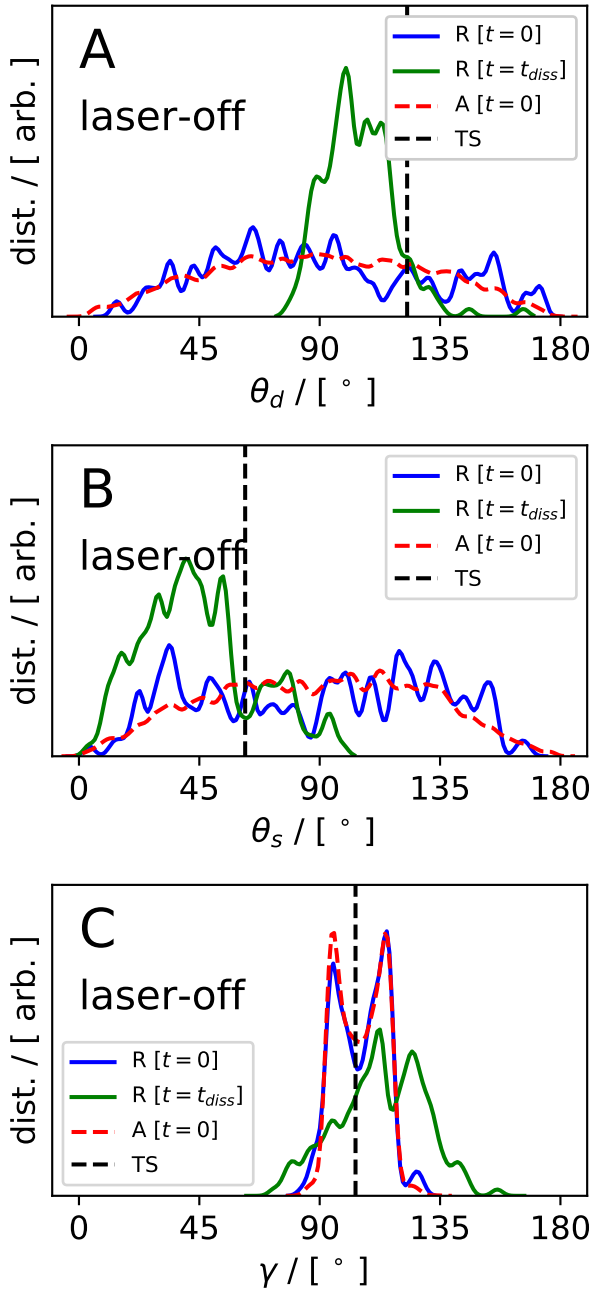

Figure 7.8: Angular distributions for θ_d (Panel A), θ_s (Panel B) and γ (Panels C) for laser-off trajectories. Results for $\nu_{OH} = 1$ are reported in Figure S3 in the SM of Ref. [52]. The distributions are reported in blue and green for the reactive trajectories at $t = 0$ and $t = t_{diss}$, respectively. Red dashed lines represent all the trajectories (reacted and scattered) at $t = 0$ and black dashed lines report the TS values.

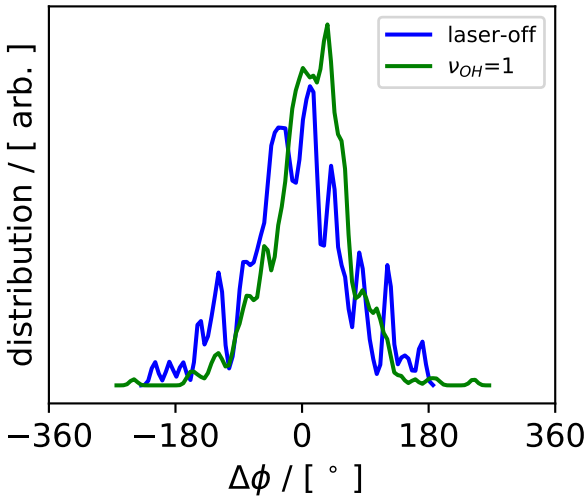

Figure 7.9: Distribution of the difference $\Delta\phi$ between the initial and the final value of ϕ for the molecule for which θ_d remains in the range [30°, 160°] throughout the whole propagation. Results for laser-off and $\nu_{OH} = 1$ are reported in blue and green, respectively.

the simulated rotational state considering the different values of M. Even though negative values of M are associated with molecules that are generally more likely to have the H atom pointing towards the surface, this does not even result in a larger S_0 for those states (Figure 7.11G) as the most reactive states are associated with positive M values. This result suggests that aligning the molecules of the beam to have a bond pointing towards the surface may not increase the reactivity for HOD as it does for CHD_3 [70]. It rather suggests the opposite is true. However in light of the strong rotational steering observed this might be an artifact due to the poor statistics. Note that previous work on D_2O on Ni(111) [30] did suggest an orientational dependence on the reactivity, where molecules aligned in $M = J$ are significantly more reactive than in $M = 0$. Further research would be required in this sense to investigate the effect of pre-orientation on the reactivity.

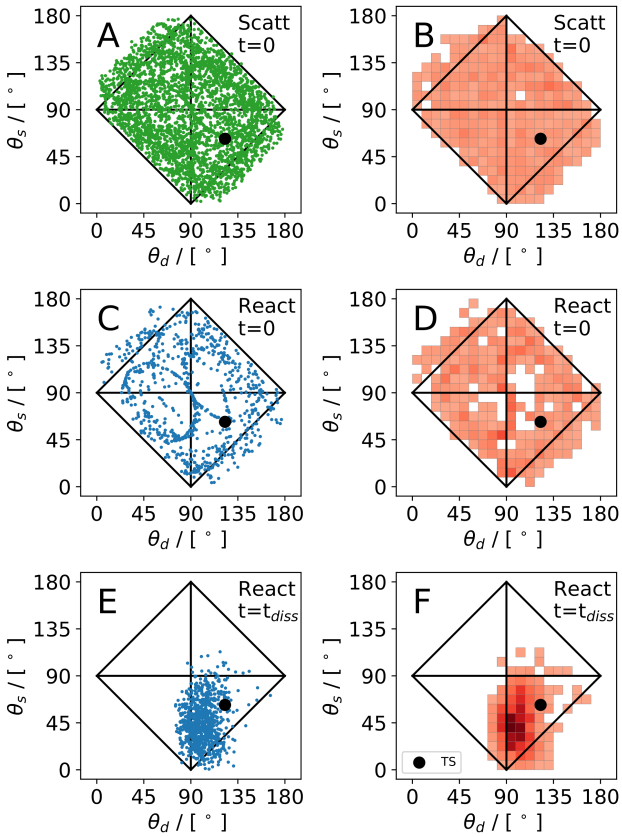

Figure 7.10: Correlation between θ_s and θ_d for the scattered and reactive trajectories (in green and blue, respectively, for Panels A, C and E). Results for the reactive trajectories have been reported for $t = 0$ (Panels C and D) and for $t = t_{diss}$ (Panels E and F). Panels B, D and F report heat-maps that depict the density of the results: a darker shade of red corresponds to a higher density. In all the Panels the black circle represents the TS values and the black lines have been drawn to guide the eye.

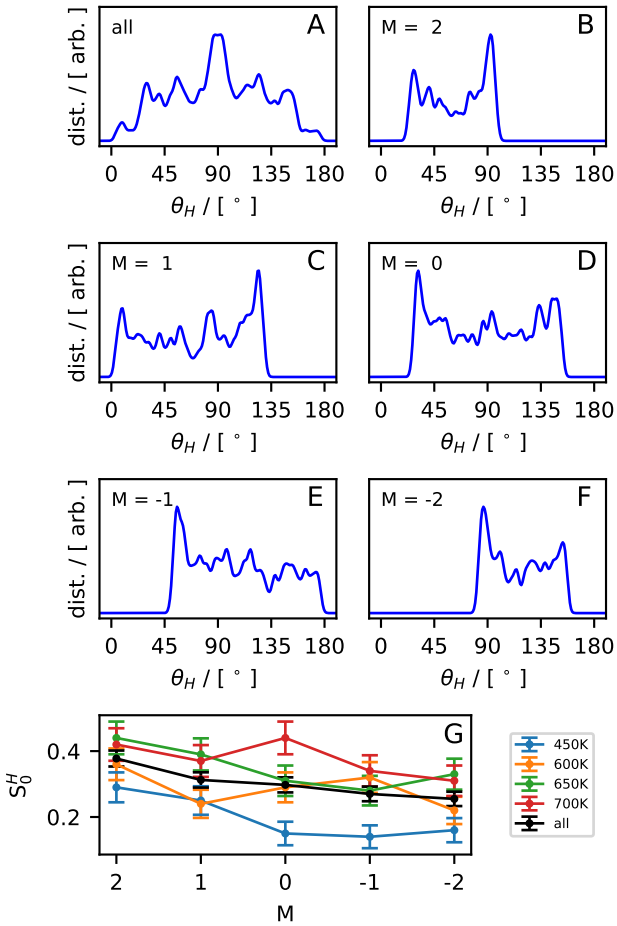

Figure 7.11: In Panel A the distributions of the initial values of θ_H (i.e., the angle between the OH bond and the surface normal) is reported for ($J = 2$, $K_a = 0$, $K_c = 2$). Panels B to F report the same observables for the different values of M simulated and reported as insets. Panels G reports the reactions probability for the OH cleavage for different nozzle temperatures and as a function of M.

7.4 Summary and Conclusions

In this Chapter we presented AIMD simulations of molecular beam experiments for the dissociation of HOD on Ni(111). The simulations confirmed previously known features of the dissociative chemisorption of water on metal surfaces such as the strong bond and mode-selectivity. Evidence for some translational steering has been found, in particular for laser-off reactive molecules. Substantial rotational steering has been observed as the molecules can react regardless of the initial orientation and large changes in the value of θ towards the TS value are observed on the way to the surface for both bonds. For most of the analyzed molecules the value of the azimuthal angle ϕ does not significantly change. We have shown that full dimensional and accurate AIMD simulations of molecular beam experiments are possible and computationally affordable for HOD on a metal surface. Moreover the SRP32-vdW functional is a good starting point to develop a specific reaction parameter functional for the system studied. Therefore we hope that our work will encourage new experiments performed under conditions in which AIMD is applicable, so that an SRP functional can be developed in order to improve the accuracy of the available theoretical results for this fundamental heterogeneously-catalyzed process. As predicted, reaction probabilities $> 1\%$ should be measurable for the incidence energies sampled in this Chapter, which can be achieved using beams of HOD seeded with H_2.

Bibliography

[1] C. Ratnasamy and J. P. Wagner, "Water Gas Shift Catalysis," *Catal. Rev.*, vol. 51, pp. 325–440, 2009.

[2] P. A. Thiel and T. E. Madey, "The Interaction of Water with Solid Surfaces: Fundamental Aspects," *Surf. Sci. Rep.*, vol. 7, pp. 211–385, 1987.

[3] P. M. Hundt, B. Jiang, M. E. van Reijzen, H. Guo, and R. D. Beck, "Vibrationally Promoted Dissociation of Water on Ni(111)," *Science*, vol. 344, pp. 504–507, 2014.

[4] A. Farjamnia and B. Jackson, "The Dissociative Chemisorption of Water on Ni(111): Mode- and Bond-Selective Chemistry on Metal Surfaces," *J. Chem. Phys.*, vol. 142, p. 234705, 2015.

[5] B. Jiang and H. Guo, "Prediction of Mode Specificity, Bond Selectivity, Normal Scaling, and Surface Lattice Effects in Water Dissociative Chemisorption on Several Metal Surfaces Using the Sudden Vector Projection Model," *J. Phys. Chem. C*, vol. 118, pp. 26851–26858, 2014.

[6] H. Guo and B. Jiang, "The Sudden Vector Projection Model for Reactivity: Mode Specificity and Bond Selectivity Made Simple," *Acc. Chem. Res.*, vol. 47, pp. 3679–3685, 2014.

[7] T. H. Liu, Z. J. Zhang, B. N. Fu, X. M. Yang, and D. H. Zhang, "Mode Specificity for the Dissociative Chemisorption of H_2O on Cu(111): A Quantum Dynamics Study on an Accurately Fitted Potential Energy Surface," *Phys. Chem. Chem. Phys.*, vol. 18, pp. 8537–8544, 2016.

[8] T. H. Liu, J. Chen, Z. J. Zhang, X. M. Shen, B. N. Fu, and D. H. Zhang, "Water Dissociating on Rigid Ni(100): A Quantum Dynamics Study on a Full-Dimensional Potential Energy Surface," *J. Chem. Phys.*, vol. 148, p. 144705, 2018.

[9] T. H. Liu, B. N. Fu, and D. H. Zhang, "An Approximate Full-Dimensional Quantum Dynamics Study of the Mode Specificity in the Dissociative Chemisorption of D_2O on Rigid Cu(111)," *Phys. Chem. Chem. Phys.*, vol. 19, pp. 11960–11967, 2017.

[10] H. Seenivasan, B. Jackson, and A. K. Tiwari, "Water Dissociation on Ni(100), Ni(110), and Ni(111) Surfaces: Reaction Path Approach to Mode Selectivity," *J. Chem. Phys.*, vol. 146, p. 074705, 2017.

[11] B. Jiang and H. Guo, "Towards an Accurate Specific Reaction Parameter Density Functional for Water Dissociation on Ni(111): RPBE versus PW91," *Phys. Chem. Chem. Phys.*, vol. 18, pp. 21817–21824, 2016.

[12] B. Jiang, M. Alducin, and H. Guo, "Electron-Hole Pair Effects in Polyatomic Dissociative Chemisorption: Water on Ni(111)," *J. Phys. Chem. Lett.*, vol. 7, pp. 327–331, 2016.

[13] S. Ghosh, H. Seenivasan, and A. K. Tiwari, "Water Adsorption and Dissociation on Copper/Nickel Bimetallic Surface Alloys: Effect of Surface Temperature on Reactivity," *J. Phys. Chem. C*, vol. 121, pp. 16351–16365, 2017.

[14] D. Ray, S. Ghosh, and A. K. Tiwari, "Controlling Heterogeneous Catalysis of Water Dissociation Using Cu–Ni Bimetallic Alloy Surfaces: A Quantum Dynamics Study," *J. Phys. Chem. A*, vol. 122, pp. 5698–5709, 2018.

[15] Z. J. Zhang, T. H. Liu, B. N. Fu, X. M. Yang, and D. H. Zhang, "First-Principles Quantum Dynamical Theory for the Dissociative Chemisorption of H_2O on Rigid Cu(111)," *Nat. Commun.*, vol. 7, p. 11953, 2016.

[16] H. Seenivasan and A. K. Tiwari, "Water Adsorption and Dissociation on Ni(110): How is it Different from its Close Packed Counterparts?," *J. Chem. Phys.*, vol. 140, p. 174704, 2014.

[17] A. Mondal, H. Seenivasan, and A. K. Tiwari, "Water Dissociation on Cu(111): Effects of Molecular Orientation, Rotation, and Vibration On Reactivity," *J. Chem. Phys.*, vol. 137, p. 094708, 2012.

[18] B. Jiang, J. Li, D. Q. Xie, and H. Guo, "Effects of Reactant Internal Excitation and Orientation on Dissociative Chemisorption of H_2O on Cu(111): Quasi-Seven-Dimensional Quantum Dynamics on a Refined Potential Energy Surface," *J. Chem. Phys.*, vol. 138, p. 044704, 2013.

[19] T. H. Liu, Z. J. Zhang, J. Chen, B. N. Fu, and D. H. Zhang, "Mode Specificity of the Dissociative Chemisorption of HOD on Rigid Cu(111): an Approximate Full-Dimensional Quantum Dynamics Study," *Phys. Chem. Chem. Phys.*, vol. 18, pp. 26358–26364, 2016.

[20] B. Jiang, X. F. Ren, D. Q. Xie, and H. Guo, "Enhancing Dissociative Chemisorption of H_2O on Cu(111) via Vibrational Excitation," *Proc. Natl. Acad. Sci. U. S. A.*, vol. 109, pp. 10224–10227, 2012.

[21] B. Jiang, D. Q. Xie, and H. Guo, "Vibrationally Mediated Bond Selective Dissociative Chemisorption of HOD on Cu(111)," *Chem. Sci.*, vol. 4, pp. 503–508, 2013.

[22] B. Jiang and H. Guo, "Dynamics of Water Dissociative Chemisorption on Ni(111): Effects of Impact Sites and Incident Angles," *Phys. Rev. Lett.*, vol. 114, p. 166101, 2015.

[23] B. Jiang and H. Guo, "Quantum and Classical Dynamics of Water Dissociation on Ni(111): A Test of the Site-Averaging Model in Dissociative Chemisorption of Polyatomic Molecules," *J. Chem. Phys.*, vol. 143, p. 164705, 2015.

[24] B. Jiang, H. W. Song, M. H. Yang, and H. Guo, "Quantum Dynamics of Water Dissociative Chemisorption on Rigid Ni(111): An Approximate Nine-Dimensional Treatment," *J. Chem. Phys.*, vol. 144, p. 164706, 2016.

[25] T. H. Liu, Z. J. Zhang, B. N. Fu, X. M. Yang, and D. H. Zhang, "A Seven-Dimensional Quantum Dynamics Study of the Dissociative Chemisorption of H_2O on Cu(111): Effects of Azimuthal Angles and Azimuthal Angle-Averaging," *Chem. Sci.*, vol. 7, pp. 1840–1845, 2016.

[26] H. Seenivasan and A. K. Tiwari, "Water Dissociation on Ni(100) and Ni(111): Effect of Surface Temperature on Reactivity," *J. Chem. Phys.*, vol. 139, p. 174707, 2013.

[27] M. Pozzo, G. Carlini, R. Rosei, and D. Alfè, "Comparative Study of Water Dissociation on Rh(111) and Ni(111) Studied with First Principles Calculations," *J. Chem. Phys.*, vol. 126, p. 164706, 2007.

[28] R. C. Catapan, A. A. M. Oliveira, Y. Chen, and D. G. Vlachos, "DFT Study of the Water–Gas Shift Reaction and Coke Formation on Ni(111) and Ni(211) Surfaces," *J. Phys. Chem. C*, vol. 116, pp. 20281–20291, 2012.

[29] A. Mohsenzadeh, K. Bolton, and T. Richards, "DFT Study of the Adsorption and Dissociation of Water on Ni(111), Ni(110) and Ni(100) Surfaces," *Surf. Sci.*, vol. 627, pp. 1–10, 2014.

[30] B. Jiang, "Rotational and Steric Effects in Water Dissociative Chemisorption on Ni(111)," *Chem. Sci.*, vol. 8, pp. 6662–6669, 2017.

[31] J. C. Polanyi, "Some Concepts in Reaction Dynamics," *Science*, vol. 236, pp. 680–690, 1987.

[32] S. Nave, A. K. Tiwari, and B. Jackson, "Methane Dissociation and Adsorption on Ni(111), Pt(111), Ni(100), Pt(100), and Pt(110)-(1×2): Energetic Study," *J. Chem. Phys.*, vol. 132, p. 054705, 2010.

[33] S. Nave and B. Jackson, "Methane Dissociation on Ni(111) and Pt(111): Energetic and Dynamical Studies," *J. Chem. Phys.*, vol. 130, p. 054701, 2009.

[34] D. Migliorini, H. Chadwick, F. Nattino, A. Gutiérrez-González, E. Dombrowski, E. A. High, H. Guo, A. L. Utz, B. Jackson, R. D. Beck, and G. J. Kroes, "Surface Reaction Barriometry: Methane Dissociation on Flat and Stepped Transition-Metal Surfaces," *J. Phys. Chem. Lett.*, vol. 8, pp. 4177–4182, 2017.

[35] F. Nattino, D. Migliorini, G. J. Kroes, E. Dombrowski, E. A. High, D. R. Killelea, and A. L. Utz, "Chemically Accurate Simulation of a Polyatomic Molecule-Metal Surface Reaction," *J. Phys. Chem. Lett.*, vol. 7, pp. 2402–2406, 2016.

[36] J. P. Perdew and Y. Wang, "Accurate and Simple Analytic Representation of the Electron-Gas Correlation Energy," *Phys. Rev. B*, vol. 45, pp. 13244–13249, 1992.

[37] B. Hammer, L. B. Hansen, and J. K. Nørskov, "Improved Adsorption Energetics Within Density-Functional Theory Using Rrevised Perdew-Burke-Ernzerhof Functionals," *Phys. Rev. B*, vol. 59, pp. 7413–7421, 1999.

[38] A. K. Tiwari, S. Nave, and B. Jackson, "The Temperature Dependence of Methane Dissociation on Ni(111) and Pt(111): Mixed Quantum-Classical Studies of the Lattice Response," *J. Chem. Phys.*, vol. 132, p. 134702, 2010.

[39] F. Nattino, D. Migliorini, M. Bonfanti, and G. J. Kroes, "Methane Dissociation on Pt(111): Searching for a Specific Reaction Parameter Density Functional," *J. Chem. Phys.*, vol. 144, p. 044702, 2016.

[40] M. Dion, H. Rydberg, E. Schröder, D. C. Langreth, and B. I. Lundqvist, "Van der Waals Density Functional for General Geometries," *Phys. Rev. Lett.*, vol. 92, p. 246401, 2004.

[41] C. Díaz, E. Pijper, R. A. Olsen, H. F. Busnengo, D. J. Auerbach, and G. J. Kroes, "Chemically Accurate Simulation of a Prototypical Surface Reaction: H_2 Dissociation on Cu(111)," *Science*, vol. 326, pp. 832–834, 2009.

[42] L. Sementa, M. Wijzenbroek, B. J. van Kolck, M. F. Somers, A. Al-Halabi, H. F. Busnengo, R. A. Olsen, G. J. Kroes, M. Rutkowski, C. Thewes, N. F. Kleimeier, and H. Zacharias, "Reactive Scattering of H_2 from Cu(100): Comparison of Dynamics Calculations Based on the Specific Reaction Parameter Approach to Density Functional Theory with Experiment," *J. Chem. Phys.*, vol. 138, p. 044708, 2013.

[43] E. Nour Ghassemi, M. Wijzenbroek, M. F. Somers, and G. J. Kroes, "Chemically Accurate Simulation of Dissociative Chemisorption of D_2 on Pt(111)," *J. Chem. Phys. Lett.*, vol. 683, pp. 329–335, 2017.

[44] G. J. Kroes, "Towards Chemically Accurate Simulation of Molecule–Surface Reactions," *Phys. Chem. Chem. Phys.*, vol. 14, pp. 14966–14981, 2012.

[45] K. Shakouri, J. Behler, J. Meyer, and G. J. Kroes, "Accurate Neural Network Description of Surface Phonons in Reactive Gas-Surface Dynamics: N_2 + Ru(0001)," *J. Phys. Chem. Lett.*, vol. 8, pp. 2131–2136, 2017.

[46] B. Kolb, X. Luo, X. Y. Zhou, B. Jiang, and H. Guo, "High-Dimensional Atomistic Neural Network Potentials for Molecule–Surface Interactions: HCl Scattering from Au(111)," *J. Phys. Chem. Lett.*, vol. 8, pp. 666–672, 2017.

[47] Q. H. Liu, X. Y. Zhou, L. S. Zhou, Y. L. Zhang, X. Luo, H. Guo, and B. Jiang, "Constructing High-Dimensional Neural Network Potential Energy Surfaces for Gas–Surface Scattering and Reactions," *J. Phys. Chem. C*, vol. 122, pp. 1761–1769, 2018.

[48] G. Kresse and J. Hafner, "Ab Initio Molecular-Dynamics Simulation of the Liquid-Metal-Amorphous-Semiconductor Transition in Germanium," *Phys. Rev. B*, vol. 49, pp. 14251–14269, 1994.

[49] G. Kresse and J. Furthmüller, "Efficient Iterative Schemes for Ab Initio Total-Energy Calculations Using a Plane-Wave Basis Set," *Phys. Rev. B*, vol. 54, pp. 11169–11186, 1996.

[50] G. Kresse and J. Furthmüller, "Efficiency of Ab-Initio Total Energy Calculations for Metals and Semiconductors Using a Plane-Wave Basis Set," *Comput. Mater. Sci*, vol. 6, pp. 15–50, 1996.

[51] G. Kresse and J. Hafner, "Ab Initio Molecular Dynamics for Liquid Metals," *Phys. Rev. B*, vol. 47, pp. 558–561, 1993.

[52] D. Migliorini, F. Nattino, A. K. Tiwari, and G. J. Kroes, "HOD on Ni(111): Ab Initio Molecular Dynamics Prediction of Molecular Beam Experiments," *J. Chem. Phys.*, vol. 149, p. 244706, 2018.

[53] P. E. Blöchl, "Projector Augmented Wave-Method," *Phys. Rev. B*, vol. 50, pp. 17953–17979, 1994.

[54] G. Kresse and D. Joubert, "From Ultrasoft Pseudopotentials to the Projector Augmented-Wave Method," *Phys. Rev. B*, vol. 59, pp. 1758–1775, 1999.

[55] M. Kresch, O. Delaire, R. Stevens, J. Y. Y. Lin, and B. Fultz, "Neutron Scattering Measurements of Phonons in Nickel at Elevated Temperatures," *Phys. Rev. B*, vol. 75, p. 104301, 2007.

[56] J. P. Perdew, K. Burke, and M. Ernzerhof, "Generalized Gradient Approximation Made Simple," *Phys. Rev. Lett.*, vol. 77, pp. 3865–3868, 1996.

[57] J. P. Perdew, K. Burke, and M. Ernzerhof, "Erratum: Generalized Gradient Approximation Made Simple," *Phys. Rev. Lett.*, vol. 78, p. 1396, 1997.

[58] G. Román-Pérez and J. M. Soler, "Efficient Implementation of a van der Waals Density Functional: Application to Double-Wall Carbon Nanotubes," *Phys. Rev. Lett.*, vol. 103, p. 096102, 2009.

[59] P. H. Xiao, D. Sheppard, J. Rogal, and G. Henkelman, "Solid-State Dimer Method for Calculating Solid-Solid Phase Transitions," *J. Chem. Phys.*, vol. 140, p. 174104, 2014.

[60] J. Kästner and P. Sherwood, "Superlinearly Converging Dimer Method for Transition State Search," *J. Chem. Phys.*, vol. 128, p. 014106, 2008.

[61] A. Heyden, A. T. Bell, and F. J. Keil, "Efficient Methods for Finding Transition States in Chemical Reactions: Comparison of Improved Dimer Method and Partitioned Rational Function Optimization Method," *J. Chem. Phys.*, vol. 123, p. 224101, 2005.

[62] G. Henkelman and H. Jónsson, "A Dimer Method for Finding Saddle Points on High Dimensional Potential Surfaces Using Only First Derivatives," *J. Chem. Phys.*, vol. 111, pp. 7010–7022, 1999.

[63] G. Czako and J. M. Bowman, "Dynamics of the Reaction of Methane with Chlorine Atom on an Accurate Potential Energy Surface," *Science*, vol. 334, pp. 343–346, 2011.

[64] F. Nattino, H. Ueta, H. Chadwick, M. E. van Reijzen, R. D. Beck, B. Jackson, M. C. van Hemert, and G. J. Kroes, "Ab Initio Molecular Dynamics Calculations versus Quantum-State-Resolved Experiments on CHD_3+Pt(111): New Insights into a Prototypical Gas–Surface Reaction," *J. Phys. Chem. Lett.*, vol. 5, pp. 1294–1299, 2014.

[65] G. Herzberg, *Molecular Spectra and Molecular Structure Volume II: Infrared and Raman Spectra of Polyatomic Molecules.* Krieger Publishing Company, 1991.

[66] L. S. Rothman, I. E. Gordon, Y. Babikov, A. Barbe, D. C. Benner, P. F. Bernath, M. Birk, L. Bizzocchi, V. Boudon, L. R. Brown, A. Campargue, K. Chance, E. A. Cohen, L. H. Coudert, V. M. Devi, B. J. Drouin, A. Fayt, J. M. Flaud, R. R. Gamache, J. J. Harrison, J. M. Hartmann, C. Hill, J. T. Hodges, D. Jacquemart, A. Jolly, J. Lamouroux, R. J. Le Roy, G. Li, D. A. Long, O. M. Lyulin, C. J. Mackie, S. T. Massie, S. Mikhailenko, H. S. P. Müller, O. V. Naumenko, A. V. Nikitin, J. Orphal, V. Perevalov, A. Perrin, E. R. Polovtseva, C. Richard, M. A. H. Smith, E. Starikova, K. Sung, S. Tashkun, J. Tennyson, G. C. Toon, V. G. Tyuterev, and G. Wagner, "The HITRAN2012 Molecular Spectroscopic Database," *J. Quant. Spectrosc. Radiat. Transf.*, vol. 130, pp. 4–50, 2013.

[67] W. R. Simpson, T. P. Rakitzis, S. A. Kandel, A. J. Orr-Ewing, and R. N. Zare, "Reaction of Cl with Vibrationally Excited CH_4 and CHD_3: State-to-State Differential Cross Sections and Steric Effects for the HCl Product," *J. Chem. Phys.*, vol. 103, pp. 7313–7335, 1995.

[68] H. Chadwick, D. Migliorini, and G. J. Kroes, "CHD_3 Dissociation on Pt(111): A Comparison of the Reaction Dynamics Based on the PBE Functional and on a Specific Reaction Parameter Functional," *J. Chem. Phys.*, vol. 149, p. 044701, 2018.

[69] G. Füchsel, P. S. Thomas, J. den Uyl, Y. Öztürk, F. Nattino, H. D. Meyer, and G. J. Kroes, "Rotational Effects on the Dissociation Dynamics of CHD_3 on Pt(111)," *Phys. Chem. Chem. Phys.*, vol. 18, pp. 8174–8185, 2016.

[70] B. L. Yoder, R. Bisson, and R. D. Beck, "Steric Effects in the Chemisorption of Vibrationally Excited Methane on Ni(100)," *Science*, vol. 329, pp. 553–556, 2010.

Samenvatting

Chemische reacties spelen een fundamentele rol in vele aspecten van ons leven en, zowel in de natuur als in industriële processen, kunnen zij versneld en gecontroleerd worden door katalysatoren. Een katalysator is een substantie die de energie barrière voor de chemische conversie verlaagt door te zorgen voor een ander mechanisme voor de reactie. Verder wordt de katalysator niet geconsumeerd tijdens het proces en kan die gebruikt worden voor vele katalytische cycli. Onder de vele klassen van katalysatoren zijn metaal oppervlakken zeer relevant vanwege hun industriële toepassingen. Processen zoals de stoomreforming en de water-gas-verschuivingsreactie voor de productie van moleculaire waterstof en de Haber-Bosch synthese van ammoniak worden uitgevoerd op industriële schaal door gebruik te maken van op overgangsmetaal gebaseerde katalysatoren.

Momenteel is het ontwerpen van experimenten die heterogeen gekatalyseerde processen in zijn geheel onderzoeken uiterst uitdagend en tegelijkertijd zijn de computationele kosten te hoog om zulke systemen te benaderen met theoretische simulaties. Door de jaren heen is het begrip van deze fundamentele processen verbeterd dankzij een oppervlakte wetenschap aanpak. Dit bestaat uit het opbreken van een heterogeen gekatalyseerd proces in fundamentele reactie stappen en aanpakken van de meest belangrijke van deze (oftewel degene die de snelheid van het gehele proces bepalen) door gebruik te maken van een model systeem waarbij een enkel molecuul reageert op een schoon en ideaal monokristallijn metaal oppervlak.

Ondanks de fundamentele rol van oppervlakte wetenschap, moeten vele uitdagin-

gen nog aangegaan worden voordat een compleet begrip van heterogeen gekatalyseerde processen bereikt wordt. Een van de hoofdproblemen is dat de industriële condities aanzienlijk anders zijn vergeleken met degene waaronder oppervlakte wetenschap experimenten gehouden worden. Ten eerste refereert de zogenaamde "drukkloof" naar het feit dat doorgaans industriële processen uitgevoerd worden bij hoge temperatuur en druk, terwijl oppervlakte wetenschap experimenten meestal uitgevoerd worden in ultrahoog vacuüm. Ten tweede zijn industriële katalysatoren onregelmatig en overgangsmetaal gebaseerde deeltjes van verschillende groottes verspreid op een ondersteuning, terwijl oppervlakte wetenschap zich richt op ideale monokristallijn overgangsmetaal oppervlakken. Dit verschil is bekend als de "materiaal kloof".

Een van de meest efficiënte strategieën om heterogeen gekatalyseerde processen te begrijpen, is door experimenten en nauwkeurige theoretische simulaties te vergelijken. Helaas maakt de grote hoeveelheid aan vrijheidsgraden betrokken bij dit soort reacties het onmogeljik om volledig-dimensionale dynamische simulaties uit te voeren met een zeer nauwkeurige methode zoals kwantumdynamica. Verder steunt het grootste deel van oppervlakte wetenschap studies op dichtheidsfunctionaaltheorie (DFT) om de elektronische energie en de krachten die werken op de ionen te berekenen. Helaas vereist de DFT methode de keuze van een benaderende uitwisselings-correlatiefunctionaal (E_{UC}) om de elektronische energie te berekenen en de doorgaans gebruikte benadering, de zogenaamde generaliseerde gradiënt benadering (GGB), is niet accuraat genoeg voor molecuul-oppervlak systemen.

Om deze hindernis te overwinnen, is het mogelijk om een semi-empirische en systeem-specifieke dichtheidsfunctionaal te ontwikkelen met behulp van de specifieke reactieparameter (SRP) aanpak voor DFT. Als men begint met twee GGB dichtheidsfunctionalen welke, gekoppeld met *ab initio* moleculaire dynamica (AIMD), respectievelijk de resultaten van moleculaire bundel experimenten onder- en overschatten, dan is het mogelijk een SRP functionaal te ontwerpen met een gewogen gemiddelde van deze functionalen die afgestemd kan worden om de experimentele resultaten te reproduceren binnen chemische nauwkeurigheid (of-

tewel met fouten kleiner dan 1 kcal/mol).

Het doel van dit proefschrift is om te onderzoeken wat het effect van de keuze van E_{UC} is op de molecuul-oppervlakte interactie, en hoe deze beschrijving verbeterd kan worden door een SRP functionaal te ontwikkelen. Wanneer de SRP functionaal ontwikkeld en getest is, kan het gebruikt worden om waardevolle informatie te verkrijgen over het systeem dat onderzocht wordt zoals bijvoorbeeld chemische nauwkeurige barrière hoogtes en dynamische inzichten in het reactie mechanisme.

In hoofdstuk 3 wordt een verslag gegeven van een typische molecuul-oppervlakte reactie: de dissociatie van N_2 op W(110). Deze reactie is belangrijk vanwege de relevantie van het verbreken van de moleculaire binding voor het Haber-Bosch proces, dat gebruikt wordt in de productie van ammonia. Daarnaast is kwantitatieve overeenstemming tussen theorie en experimenten voor de dissociatie van N_2 op W(110) nog niet bereikt. De studie beschreven in hoofdstuk 3 richt zich op het testen van de vdW-DF2 dichtheidsfunctionaal, welke, in tegenstelling tot standaard GGB functionalen, de lange-afstand van der Waals (vdW) interactie modelleert. Het modelleren van de attractieve vdW contributie verbetert de beschrijving van de molecuul-oppervlakte interactie, geeft doorgaans ondiepere adsorptie putten, en de barrières zijn in betere overeenstemming met experiment in vergelijking met standaard GGB functionalen zoals PW91, PBE en RPBE, welke gebruikt zijn in eerder werk aan dit systeem. Ondanks deze verbetering, falen AIMD berekeningen die gebruik maken van de vdW-DF2 functionaal in het kwantitatief reproduceren van experimentele resultaten. Ook al vermindert de indirecte reactiekans door het gebruik van de vdW-DF2 functionaal, de barrières voor de directe dissociatie zijn mogelijk nog steeds te hoog om accuraat moleculaire bundel experimenten te kunnen modelleren en om de afhankelijkheid van hun resultaten van de botsingsenergie te reproduceren.

Om de overeenstemming tussen experiment en theorie voor dit systeem te verbeteren, is zowel theoretische als experimentele inspanning nodig. Een SRP functionaal ontwikkeld van meta-GGB functionalen kan wellicht de beschrijving van dit systeem verbeteren, terwijl nieuwe en betere gekarakteriseerde experimenten

zullen helpen met het opzetten en uitvoeren van nauwkeurige berekeningen voor een meer betekenisvolle vergelijking.

Hoofdstuk 4 geeft verslag van een studie aan de dissociatie van een methaan isotopoloog (oftewel CHD_3) op verschillende platina oppervlakken. Van de SRP functionaal ontwikkeld in eerder werk voor CHD_3 op Ni(111) (genaamd SRP32-vdW), verkregen door het mengen van de RPBE en PBE uitwisselingsfunctionalen met een lange-afstandscorrelatiefunctionaal die de vdW interactie modelleert, is aangetoond dat die de dissociatie van hetzelfde molecuul op Pt(111) kan modelleren met chemische nauwkeurigheid. Naast de overdraagbaarheid tussen de dissociatie op het (111) oppervlak van nikkel en platina, is de SRP32-vdW functionaal ook met succes overgedragen naar het verbreken van CHD_3 op het gestapte Pt(211) oppervlak.

De overdraagbaarheid van een SRP functionaal tussen verschillende facetten van hetzelfde metaal maakt een aanpak te definiëren, welke we "reactiebarriometrie" noemen, die kan helpen de materiaal kloof in heterogene katalyse te overbruggen. Deze strategie bevat het uitvoeren van goed gedefinieerde moleculaire bundel experimenten waarbij een molecuul dissocieert op een laag-index facet van een overgangsmetaal. Vervolgens is het mogelijk om twee dichtheidsfunctionalen te kiezen die, wanneer gecombineerd met AIMD, de experimentele resultaten onder- en overschatten, respectievelijk. Een kandidaatsfunctionaal is dan gedefinieerd als een gewogen gemiddelde van deze twee dichtheidsfunctionalen die afgestemd kan worden door een parameter te wijzigen totdat, met behulp van een "gissen en missen" procedure, deze functionaal de experimentele resultaten reproduceert met chemische nauwkeurigheid. Ten slotte is de SRP functionaal getest op een ander experiment om zijn nauwkeurigheid te valideren. Wanneer de SRP functionaal gedefinieerd en getest is, is het mogelijk om de overdraagbaarheid tussen verschillende facetten te gebruiken om chemische nauwkeurige barrières te verkrijgen op alle posities en defecten die mogelijk belangrijk zijn in echte katalytische condities.

In hoofdstuk 5 wordt de SRP32-vdW functionaal gebruikt om dynamische inzichten te krijgen in de dissociatie van CHD_3 op Pt(111) en Pt(211), waar-

bij vooral gekeken wordt naar het effect van de stap op de dissociatieve reactie. Hierbij wordt opgemerkt dat, ook al zijn de barrières op het Pt(211) oppervlak aanzienlijk lager dan degene op het Pt(111) oppervlak, het dissociatie mechanisme zeer vergelijkbaar is op de twee oppervlakken. Daarnaast is gevonden dat de energie overdracht naar de fononen groter is voor het gestapte oppervlak en dat dit, samen met de energie overdracht naar parallelle beweging veroorzaakt door het gestapte oppervlakgeometrie, er voor zorgt dat sommige moleculen op het oppervlak kunnen gevangen bljiven, d.w.z., tijdelijk geadsorbeerd. Deze moleculen behouden een grote snelheid in de richting parallel aan het macroscopische oppervlak, wat suggereert dat, in experimenten, deze langere afstanden kunnen afleggen en een groter deel van het oppervlak verkennen, wat de kans vergroot om een hogere orde defect te vinden zoals een "*kink*" waarop zij eventueel kunnen dissociëren.

Hoofdstuk 6 rapporteert een vergelijking van dynamische resultaten van de dissociatie van CHD_3 op Pt(111) waarbij gebruikt gemaakt wordt van twee verschillende dichtheidsfunctionalen: de veel gebruikte PBE functionaal en de SRP32-vdW functionaal. Ondanks het feit dat de minimum barrière die berekend is met de twee functionalen opmerkelijk vergelijkbaar is in geometrie en energie, geven zij redelijk verschillende reactiekanskrommen, waarbij de SRP32-vdW functionaal experimentele resultaten met chemische nauwkeurigheid kan reproduceren, en de PBE functionaal grotendeels de reactiekans overschat. Het grootste verschil in de beschrijving van de molecuul-oppervlak interactie is de aanwezigheid van een van der Waals put die gemodelleerd wordt door de SRP32-vdW functionaal en niet door de PBE functionaal. Er is waargenomen dat deze put de moleculen versnelt op hun weg naar het oppervlak waardoor zij minder tijd hebben om te verdraaien naar de overgangstoestandgeometrie, en dus wordt de kans om te dissociëren kleiner. Daarnaast, zoals beschreven door het aangepaste Baule model, vergroot de aanwezigheid van een attractieve interactie tussen het molecuul en oppervlak de energie overdracht naar de oppervlakfononen, waardoor minder energie beschikbaar is voor de dissociatie en dus de reactiviteit lager wordt. Onze waarnemingen kunnen gedeeltelijk het verschil verklaren tussen de

reactiviteit beschreven door de twee functionalen, maar verdere studie is nodig om potentiële andere dynamische effecten te ontwarren die de reactiviteit kunnen beïnvloeden van CHD_3 op Pt(111) zoals beschreven door de PBE en SRP32-vdW functionalen.

In hoofdstuk 7 geven we verslag van een voorspellende studie over de dissociatie van enkel gedeutereerd water (HOD) op het Ni(111) oppervlak, waarvoor nog geen experimentele resultaten beschikbaar zijn. Deze reactie is belangrijk voor de industriële "water-gas-shift-reactie" en, tot nu toe, is kwantitatieve overeenstemming tussen experiment en theorie nog niet bereikt. In dit hoofdstuk worden AIMD simulaties beschreven van plausibele HOD moleculaire bundel experimenten, uitgevoerd met de SRP32-vdW functionaal. We observeren dat rotationele sturing een belangrijke rol speelt in de reactiviteit omdat, anders dan wat voor CHD_3 geobserveerd is, de moleculen kunnen reageren onafhankelijk van hun initiële oriëntatie. De vergelijking van de resultaten van de simulaties met die van experimenten op een vergelijkbaar systeem (D_2O op Ni(111)) suggereert dat de SRP32-vdW functionaal de reactiviteit misschien overschat. Echter, zodra nieuwe experimenten beschikbaar komen, zal het mogelijk zijn om de onderliggende uitdrukking aan te passen om een kandidaats-SRP-functionaal te verkrijgen, zodat chemische nauwkeurigheid behaald wordt in de theoretische beschrijving van deze relevante reactie. Nadere studie is tevens nodig om volledig het effect van de pre-oriëntatie van het molecuul op de reactiekans te begrijpen.

Curriculum Vitae

Davide Migliorini was born on January, 28 1990 in Crema (Italy). In 2009 he graduated at the G. Gandini high school in Lodi (Italy). From 2009 to 2014 he attended the Università degli Studi in Milano (Italy) where he obtained a bachelor degree and master degree *cum laude* in Chemistry. During his undergraduate studies he started working in theoretical chemistry and materials science focusing on the simulation of the interaction between hydrogen atoms and graphene nanoribbons under the supervision of Prof. dr. Gian Franco Tantardini and Prof. dr. Rocco Martinazzo. In 2015 he moved to Leiden (the Netherlands) to work as a PhD candidate in the group of Prof. dr. Geert-Jan Kroes at the Leiden Institute of Chemistry of Leiden University. There the focus of his work has been on the AIMD simulation of polyatomic molecules interacting with transition metal surfaces, as described in this Thesis.

List of Publications

- F. Nattino, D. Migliorini, M. Bonfanti and G. J. Kroes, "Methane Dissociation on Pt(111): Searching for a Specific Reaction Parameter Density Functional", *J. Chem. Phys.*, 144, 044702 (2016).

- D. Migliorini, F. Nattino and G. J. Kroes,"Application of van der Waals Functionals to the Calculation of Dissociative Adsorption of N_2 on W(110) for Static and Dynamic Systems", *J. Chem. Phys.*, 144, 084702 (2016).

- F. Nattino, D. Migliorini, G. J. Kroes, E. Dombrowski, E. A. High, D. R. Killelea and A. L. Utz, "Chemically Accurate Simulation of a Polyatomic Molecule-Metal Surface Reaction", *J. Chem. Phys. Lett.*, 7, 2402 (2016).

- D. Migliorini, H. Chadwick, F. Nattino, A. Gutiérrez-González, E. Dombrowski, E. A. High, H. Guo, A. L. Utz, B. Jackson, R. D. Beck, and G. J. Kroes, "Surface Reaction Barriometry: Methane Dissociation on Flat and Stepped Transition-Metal Surfaces", *J. Chem. Phys. Lett.*, 8, 4177 (2017).

- H. Chadwick, D. Migliorini and G. J. Kroes, "CHD_3 Dissociation on Pt(111): A Comparison of the Reaction Dynamics Based on the PBE Functional and on a Specific Reaction Parameter Functional", *J. Chem. Phys.*, 149, 044701 (2018).

- H. Chadwick, A. Gutiérrez-González, D. Migliorini, R. D. Beck and G. J. Kroes, "Incident Angle Dependence of CHD_3 Dissociation on the Stepped Pt(211) Surface", *J. Phys. Chem. C*, 122, 19652 (2018).

- D. Migliorini, H. Chadwick and G. J. Kroes, "Methane on a Stepped Surface: Dynamical Insights on the Dissociation of CHD_3 on Pt(111) and Pt(211)", *J. Chem. Phys.*, 149, 094701 (2018).

- N. Gerrits, D. Migliorini and G. J. Kroes, "Dissociation of CHD_3 on Cu(111), Cu(211) and single atom alloys of Cu(111)", *J. Chem. Phys*, 149, 224701 (2018).

- D. Migliorini, F. Nattino, A. K. Tiwari and G. J. Kroes, "HOD on Ni(111): Ab Initio Molecular Dynamics Prediction of Molecular Beam Experiments", *J. Chem. Phys*, 149, 244706 (2018).